MARTIN MARIETTA ENERGY SYSTEMS LIBRARIES
3 4456 0361221 3

cy. 5
CENTRAL RESEARCH LIBRARY
DOCUMENT COLLECTION

ORNL-2430
Physics and Mathematics
TID-4500 (13th ed. rev.)

# PHYSICS DIVISION

# SEMIANNUAL PROGRESS REPORT

## FOR PERIOD ENDING SEPTEMBER 10, 1957

**OAK RIDGE NATIONAL LABORATORY**
operated by
UNION CARBIDE CORPORATION
for the
U.S. ATOMIC ENERGY COMMISSION

CENTRAL RESEARCH LIBRARY
DOCUMENT COLLECTION
LIBRARY LOAN COPY
DO NOT TRANSFER TO ANOTHER PERSON
If you wish someone else to see this document, send in name with document and the library will arrange a loan.

Printed in USA. Price $3.25 cents. Available from the

Office of Technical Services
U. S. Department of Commerce
Washington 25, D. C.

LEGAL NOTICE

This report was prepared as an account of Government sponsored work. Neither the United States, nor the Commission, nor any person acting on behalf of the Commission:

A. Makes any warranty or representation, express or implied, with respect to the accuracy, completeness, or usefulness of the information contained in this report, or that the use of any information, apparatus, method, or process disclosed in this report may not infringe privately owned rights; or

B. Assumes any liabilities with respect to the use of, or for damages resulting from the use of any information, apparatus, method, or process disclosed in this report.

As used in the above, "person acting on behalf of the Commission" includes any employee or contractor of the Commission to the extent that such employee or contractor prepares, handles or distributes, or provides access to, any information pursuant to his employment or contract with the Commission.

ORNL-2430
Physics and Mathematics
TID-4500 (13th ed. rev.)

Contract No. W-7405-eng-26

# PHYSICS DIVISION

# SEMIANNUAL PROGRESS REPORT

## for Period Ending September 10, 1957

J. L. Fowler, Director
E. O. Wollan, Associate Director

DATE ISSUED

MAR 11 1958

OAK RIDGE NATIONAL LABORATORY
Oak Ridge, Tennessee
Operated by
UNION CARBIDE CORPORATION
for the
U.S. ATOMIC ENERGY COMMISSION

MARTIN MARIETTA ENERGY SYSTEMS LIBRARIES
3 4456 0361221 3

## TABLE OF CONTENTS AND SUMMARY

*CONCEPTUAL DESIGN OF A HIGH-INTENSITY PROTON SYNCHROTRON*
T. A. Welton ..... 1

The general specifications for a high-intensity proton synchrotron have been worked out. High-energy injection is used to yield very high intensity at 12 bev.

*BEAM EXTRACTION STUDIES FOR THE 900-Mev CYCLOTRON*
M. M. Gordon and T. A. Welton ..... 6

A report is given on an investigation into the properties of the $\nu_r = 8/4$ nonlinear resonance, with special emphasis on its effectiveness in facilitating beam extraction from the proposed ORNL 900-Mev spiral-ridged cyclotron.

*COULOMB EXCITATION OF STATES IN $Pt^{195}$*
F. K. McGowan and P. H. Stelson ..... 13

Yields and angular distributions of gamma rays from coulomb excitation of states in $Pt^{195}$ have been measured. Direct excitation of levels in $Pt^{195}$ is observed at 99, 130, 210, and 240 kev.

*COULOMB EXCITATION OF THE SECOND $2^+$ STATE IN EVEN-EVEN MEDIUM-WEIGHT NUCLEI*
P. H. Stelson and F. K. McGowan ..... 19

The location of the second $2^+$ state has been established for ten even-even medium-weight nuclei by means of coulomb excitation produced by 8-, 9-, and 10-Mev alpha particles.

*DECAY OF $Nb^{90}$*
N. H. Lazar, G. D. O'Kelley, L. M. Langer, and W. G. Smith ..... 22

Beta- and gamma-ray spectroscopy, utilizing both single and coincident NaI(Tl) crystals and a magnetic spectrometer, has been carried out on the gamma and the electron radiations from $Nb^{90}$. The level structure of $Zr^{90}$ has been determined and may qualitotively be understood in terms of an independent-particle model.

*LEVEL STRUCTURE OF $N^{14}$ FROM $C^{13} + p$ REACTIONS*
J. K. Bair, H. O. Cohn, and H. B. Willard ..... 26

Angular distributions of the 3.09- and 3.68-Mev gamma rays resulting from the inelastic scattering of protons from $C^{13}$ are given, as are distributions of the neutrons from the reaction $C^{13}(p,n)N^{13}$. New values are given for the proton energies at which maximums appear in the neutron yield.

*PROTON STRENGTH FUNCTIONS FROM (p,n) CROSS SECTIONS*
C. H. Johnson, A. Galonsky, and J. P. Ulrich ..... 28

The $(p,n)$ excitation functions for 12 intermediate nuclei have been described by the use of a complex potential model for prediction of the formation of the compound nucleus and by the use of the statistical model of the compound nucleus for prediction of the decay.

*THE (p,n) REACTION CROSS SECTIONS FOR $Li^7$ AND $H^3$*
R. L. Macklin and J. H. Gibbons ..... 30

Absolute cross sections for $(p,n)$ reactions in lithium and tritium have been measured from threshold to 5 Mev. Yields near threshold are in agreement with values calculated from the inverse reactions.

*NEUTRON RESONANCE PARAMETERS OF $Sm^{151}$ AND $Pm^{147}$*
J. A. Harvey, R. C. Block, and G. G. Slaughter ..... 32

Parameters for low-energy resonances in $Sm^{151}$ and $Pm^{147}$ have been determined from transmission measurements with the fast-chopper time-of-flight spectrometer.

*ANGULAR DISTRIBUTION OF NEUTRONS SCATTERED BY THE 2.80-kev RESONANCE IN SODIUM*
R. C. Block ..... 32

The angular distribution of neutrons scattered by the 2.80-kev resonance in sodium has been measured with a reactor beam and various combinations of boron and sodium filters. This distribution is found to be isotropic within the accuracy of these data.

*KILOVOLT NEUTRON CROSS SECTIONS*
J. H. Gibbons, W. M. Good, and J. H. Neiler ..... 34

Neutron total cross sections for $K^{41}$ and $Y^{89}$ have been completed up to 20 kev and for $Rb^{87}$ up to 15 kev.

*BERYLLIUM DIFFERENTIAL NEUTRON SCATTERING*
H. O. Cohn and J. L. Fowler ..... 37

Data are presented for differential elastic neutron scattering from beryllium for neutron energies of 0.73, 1.00, 1.21, 1.50, 1.75, and 2.15 Mev.

*ELASTIC SCATTERING OF NEUTRONS BY $C^{12}$*
H. B. Willard, J. K. Bair, and H. O. Cahn ..... 37

Phase shifts for neutrons scattered elastically by $C^{12}$ have been fitted to the data previously reported. Neutron polarizations have been calculated from these phase shifts.

*DIFFERENTIAL ELASTIC SCATTERING OF NEUTRONS FROM ZERO-SPIN LIGHT NUCLEI*
J. L. Fowler and H. O. Cohn ..... 39

Experimental measurements on the scattering of neutrons from $C^{12}$, $O^{16}$, and $Ne^{20}$ are summarized, and this information is examined in terms of simple single-particle phenomenological nuclear potentials for the neutron-nucleus interaction.

*CROSS SECTION AS A FUNCTION OF ENERGY FOR THE REACTION $S^{32}(n,\alpha)Si^{29}$*
H. W. Schmitt ..... 42

The $S^{32}(n,\alpha)Si^{29}$ cross section has been measured as a function of neutron energy in the range $1.4 \leqq E_n \leqq 3.0$ Mev.

*EXPERIMENTAL L-SHELL FLUORESCENCE YIELDS*
N. H. Lazar and W. S. Lyon ..... 44

The fluorescence yields in the $L$ shell have been measured for a number of heavy $Z$ elements, using a novel coincidence gamma-ray spectroscopy approach. The results are in essential agreement with the early work of H. Lay, who used photographic techniques.

*GAMMA RADIATION IN THE DECAY OF $Xe^{133}$*
F. Pleasonton ..... 46

Three new gamma rays have been found in the decay of $Xe^{133}$ with energies of about 160, 305, and 385 kev. Their intensities relative to 1, for the well-established 81-kev gamma ray, are $10^{-3}$, $10^{-4}$, and $5 \times 10^{-5}$, respectively.

*CHARGE SPECTROMETRY FOR $Xe^{133}$*
A. H. Snell and F. Pleasonton ..... 47

The charge spectrum associated with the decay of the 5.3-day activity in $Xe^{133}$ has been measured, and the results have been analyzed to yield a total conversion coefficient in rough agreement with the value obtained by other methods.

*MOLECULAR DISSOCIATION OF MONOTRITIATED METHANE FOLLOWING RADIOACTIVE DECAY*
A. H. Snell and F. Pleasonton ..... 49

When $CH_3T$ undergoes beta decay, the main molecular consequence is that the product $He^3$ leaves as a neutral atom. Less frequently, the molecule is dissociated by loss of hydrogens, usually but not always as neutral atoms. In extreme cases, bare $C^+$ and $C^{++}$ ions are left.

*ALPHA EMISSION FROM $U^{234}$ AND ORIENTED $U^{235}$ NUCLEI*
J. W. T. Dabbs, L. D. Roberts, and G. W. Parker ..... 50

Measurements show an anisotropy very similar to that previously found in oriented $U^{233}$ nuclei; $U^{234}$ nuclei (spin 0) show no anisotropy, as expected.

*FISSION OF ORIENTED NUCLEI*
L. D. Roberts, J. W. T. Dabbs, and G. W. Parker ..... 51

A theoretical calculation of the angular distribution of fission fragments from oriented $U^{233}$ nuclei is presented and is compared with observed results.

*NEUTRON DIFFRACTION STUDY OF THE MAGNETIC PROPERTIES OF $MnBr_2$*
E. O. Wollan, W. C. Koehler, and M. K. Wilkinson ..... 56

The antiferromagnetic structure and the domain properties of $MnBr_2$ ($T_N = 2.16°K$) have been determined by measurements on a single crystal at pumped-helium temperatures and with applied magnetic fields. Effects of magnetic fields on the Néel temperature have also been observed.

*NEUTRON DIFFRACTION INVESTIGATIONS OF THE TWO ANTIFERROMAGNETIC STRUCTURES OF $MnCl_2$*
M. K. Wilkinson, J. W. Cable, E. O. Wollan, and W. C. Koehler ..... 65

Neutron diffraction results are presented which prove that $MnCl_2$ has two distinct antiferromagnetic transitions at low temperatures. The single-crystal magnetic reflections from both antiferromagnetic structures have been explained by complex unit cells which form a domain pattern along the hexagonal axes of the chemical unit cell.

*TYPES OF MAGNETICALLY ORDERED CONFIGURATIONS ON SIMPLE LATTICES*
H. A. Gersch and W. C. Koehler ..... 75

A scheme for enumerating possible magnetically ordered configurations on simple lattices is described, and a system of nomenclature descriptive of the arrangement is proposed. Examples of the method as applied to simple cubic, face-centered cubic, body-centered cubic, and hexagonal layer lattices are given.

*ANTIFERROMAGNETIC STRUCTURE OF IRON-GROUP TRIFLUORIDES*
H. R. Child, E. O. Wollan, W. C. Koehler, and M. K. Wilkinson ..... 87

The trifluorides of chromium, iron, and cobalt have been found to order antiferromagnetically with a structure of the same type as that observed in similar perovskite-type compounds. No magnetic ordering was observed in $VF_3$.

*ATOMIC-BEAM SPECTROSCOPY*
J. E. Sherwood ..... 91

The atomic-beam magnetic resonance apparatus has been used to measure the nuclear spin of $I^{128}$. A value of 1 was obtained, thus confirming predictions based on the decay of this isotope.

*STUDY OF THE ENERGY LEVELS OF SOME ATOMS AND IONS OF THE SECOND LONG PERIOD*
G. W. Charles ..... 92

Results are presented of a comparison of some of the energy levels of atoms and ions of the second long period with predictions of simple theory, neglecting perturbations. Predictions of same levels in iodine(VI), iodine(IV), and iodine(III) are made.

*PURITY OF $Hg^{198}$ PRODUCED BY NEUTRON IRRADIATION OF $Au^{197}$*
J. R. McNally, Jr. ..... 93

Calculations made under extremely pessimistic conditions for the allowable impurity of $Hg^{199}$ in reactor-produced $Hg^{198}$, to be used as a possible primary standard of length, show that the 99.6%-or-better $Hg^{198}$ produced in the ORNL Graphite Reactor satisfactorily meets the rigid design criterion.

*CLASSIFICATION OF SINGLY IONIZED PLUTONIUM, Pu(II)*
J. H. Wise, P. M. Griffin, and J. R. McNally, Jr. ..... 96

The resolved Zeeman patterns of 129 spectrum lines of Pu(II) were measured and the *g* factors computed. Three new high-energy states have been determined, and 14 new high levels have been tentatively established as a result of the new data.

*INFRARED SPECTRA OF THE ISOTOPICALLY SUBSTITUTED AMMONIA MOLECULES*
H. W. Morgan, P. A. Staats, and J. H. Goldstein ..... 96

The vibrational spectra of the nine isotopic ammonia molecules formed by D and T substitution and of the $N^{15}H_3$ molecule have been studied, and the observed frequencies have been assigned to the normal modes of vibration.

*IMPROVED SWEEPING PULSE GENERATOR AND TIMER FOR MULTICHANNEL ANALYZERS*
G. G. Kelley and C. C. Harris ..... 102

An improved sweeping pulse generator for the MC5 and similar multichannel analyzers is described.

*LIFE TESTS OF FILAMENTARY SUBMINIATURE TUBES*
C. C. Harris and G. G. Kelley ..... 104

Continuing life tests on filamentary subminiature tubes show that the life can be considered to be 20,000 hr. Tests show clearly the correct filament voltage for longest life in one emission-current condition.

*DEVELOPMENTS IN FOCUSING COLLIMATORS FOR BRAIN TUMOR DIAGNOSIS*
J. E. Francis, P. R. Bell, and C. C. Harris ..... 104

Various focusing gamma-ray collimators have been field-tested in order to obtain an optimum design for brain tumor diagnosis.

*DEVELOPMENT OF FAST-PULSE TECHNIQUES FOR MEASUREMENT OF TRANSIT-TIME SPREAD IN PHOTOMULTIPLIER TUBES*
H. O. Eason and G. G. Kelley ..... 112

Equipment is being developed for accurate measurement of transit-time spread in photomultiplier tubes through utilization of fast-coincidence techniques. Description of the method and equipment is included, together with details of a coincidence unit having a resolution time of $10^{-9}$ sec and a distributed amplifier having a stage bandwidth of 600 Mc with a gain of 4.

*MEDICAL SCANNER*
D. P. Hamblen, J. E. Francis, C. C. Harris, and G. G. Kelley ..... 114

The mechanical design has been completed for a sconning device that will be used to move a focusing collimator over a patient in order to determine the distribution of radioactivity within the body.

# PHYSICS DIVISION SEMIANNUAL PROGRESS REPORT

## CONCEPTUAL DESIGN OF A HIGH-INTENSITY PROTON SYNCHROTRON

T. A. Welton

A very qualitative description of a high-intensity proton synchrotron has been given previously.[1,2] The novel features of this accelerator are as follows:

1. high-energy injection from the 900-Mev AVF cyclotron presently under development at the Laboratory,
2. the resulting small frequency swing required in the synchrotron,
3. the very rapid pulsing which then becomes possible, and which is realized by use of alternating-gradient focusing and condenser storage of magnetic field energy,
4. the large number of turns of injected current which can be obtained by virtue of the expected high density in the phase space of the injected beam,
5. the relatively low cost which can be achieved, with apparently high performance.

It is essential in planning such a machine to have clearly in mind a conceptual design in order that the approximate performance requirements for the various components of the system can be clearly seen. Such a design has been assembled and is presented here for future reference. No optimization has been attempted, except that of the most intuitive variety. The performance is nevertheless very promising, and the cost is attractive. The solutions suggested for the various technical problems involved are certainly not unique, but it is at least reassuring to have definite solutions in mind.

Certain assumptions are necessary at the start. It will be assumed that a proton beam is available from the cyclotron with a phase-space density not grossly inferior to that delivered by an electrostatic accelerator. The density in the energy-time space can be separately estimated on an elementary basis. The final proton energy delivered by the synchrotron has been set at 12 bev, this figure being extremely reasonable from the viewpoint of the production thresholds of the known particles. The alternating-gradient type of accelerator has been chosen in preference to two competitors (the constant-gradient and the spiral FFAG machines) on the basis of approximate economic arguments. To get comparable performance, the constant-gradient machine would need a much more expensive magnet and power supply. The FFAG principle allows acceleration with pulsing of the radio-frequency only. The magnet cost to achieve this, however, seems to be much higher than for the AG magnet complete with power supply. The pulse repetition rate has been chosen to be 60 per second. This appears to be compatible with the radio-frequency requirements, and makes for a magnet power supply with minimum complication.

In its gross features, the machine will then be rather similar to the Brookhaven AGS, and very great reliance must be placed on the experience at Brookhaven thus far. The magnet power supply will be one of the types considered by the Harvard-MIT and the Princeton-Pennsylvania groups, so that its requirements can be estimated without much difficulty. The radio-frequency system is, however, unique, although certain qualitative features are clear. The injector (AVF cyclotron) is unique, but its problems are being separately considered in great detail at ORNL. Finally, the proposed injection scheme (resonant inflection) is unique, but seems to be capable of reasonably good theoretical treatment.[1,2]

So far as general features go, we have approximately a "half-AGS." It is then convenient to use the very carefully designed AGS magnet as the basis for our magnet considerations. Two essential modifications in the conditions exist, which will lead to some differences in the detailed design. The two modifications are as follows:

1. The magnet is to be operated at 60 cps.

[1] F. T. Howard *et al.*, *Proposal for a Southern Regional Accelerator*, ORNL CF-57-4-30 (April 9, 1957).

[2] T. A. Welton, *Phys. Semiann. Prog. Rep. March 10, 1957*, ORNL-2302, p 1.

2. The bulk of the adiabatic damping will already have taken place in the injector.

The first modification implies that

1*a*. a good transformer grade of high-silicon sheet steel must be used for the magnet laminations,

1*b*. the magnet coils must consist of more turns than are conventionally used, each of smaller size,

1*c*. the magnet iron must be cooled,

1*d*. a reduced radial and vertical gap is desirable in order to decrease energy storage.

The second modification implies that

2*a*. the aperture of the magnet does not have to be so large as in the AGS, since the nonrelativistic acceleration with diffuse beam occurs in the cyclotron,

2*b*. the region of good field cannot contract very much with increasing energy.

Items 1*d* and 2*a* are compatible. Items 1*b* and 1*c* are not serious. Item 1*a*, together with 2*b*, indicates strongly that the maximum field at the orbit should be held below 10,000 gauss.

It seems quite reasonable to assume that the magnet is ⅓ straight section. For a mean field of $\bar{B}$ kiloguass, the mean radius $R$ is given by

$$R = \frac{3130p}{\bar{B}} \text{ cm} , \tag{1}$$

where $p$ is the proton momentum in $Mc$ units. For 12 bev,

$$p = \sqrt{\left(\frac{12}{0.938} + 1\right)^2 - 1} = 13.75 ,$$

and, using $\bar{B} = 2/3 \times 10.000 = 6.667$, we obtain

$$R = 6455 \text{ cm} \cong 6500 \text{ cm} \cong 213 \text{ ft} .$$

In a really careful study, a sophisticated magnet structure like the AGS arrangement would no doubt prove to be desirable. We might, for example, take half the AGS magnets arranged into 30 periods and 6 superperiods. For present purposes it is adequate to consider a more elementary structure. We arbitrarily choose 32 identical sectors, arranged in the (+0 −0) pattern. It is more convenient to split each magnet section into two equal halves, so that we obtain single magnet sections and straight sections of equal length. The circumference is about 40,800 cm, and one sector is 40,800/32 = 1275 cm. A single section, magnet or straight, is then 1275/6 = 212 cm ≅ 7.0 ft. We then have 128 magnet sections and 64 straight sections, each of which is 7.0 ft in length. These figures are convenient and do not differ markedly from what might be termed standard practice in the AGS field.

It seems reasonable to use a fractional field gradient $[(1/B_0)\, dB_0/dx]$, which is close to that for the Brookhaven AGS magnet. For simplicity we make it identical, so that

$$\frac{B_0'}{B_0} = 0.0425 \text{ cm}^{-1} . \tag{2}$$

The mean field index $n$, which enters the focusing equations, is given by

$$n = R\frac{B_0'}{B_0} = 276 . \tag{3}$$

An elementary calculation for the focusing frequencies yields

$$\nu_x \cong \nu_y = \nu = 7.30 . \tag{4}$$

With slight adjustments this becomes an adequate operating point, and $\nu_x$ can easily be moved to 7.25 for purposes of injection and extraction.

The Brookhaven AGS magnet has a radial extent for the region of good $n$ of about 17 cm. It is felt that in view of items 1*d* and 2*b*, it would be desirable to narrow this to about 12 cm. This is compatible with existing injection calculation[1] and is apparently adequate from that point of view as well as for the accommodation of the synchrotron oscillations. Likewise, the vertical scale of the Brookhaven gap profile can safely be reduced by a factor of ¾. The resulting gap is 6.67 cm at the equilibrium orbit and 5.32 cm for $x = \pm 6.0$ cm. The minimum gap becomes about 4.25 cm, and the pole width should clearly be about 27 cm. It is visualized that 3 cm of the available 5.32-cm vertical space will be used for actual orbit oscillations. Of the residue, perhaps 1 cm (which is certainly adequate) should be used for error allowance, and the rest for the thinnest portion of the vacuum chamber. Of radial extent, about 3 cm is visualized for orbit oscillations. Most of the rest will be used for injection and extraction, although errors and synchrotron oscillation will use a small amount.

A simple layout of the magnet cross section, following closely the AGS layout, yields a lamination which is 74 cm wide and 84 cm high (29 × 33 in.), with cutout for gap and coils. These dimensions can be obtained economically in the iron grade necessary (Armco Tran-Cor M-14, 29-gage, for example). The approximate weight of the core of a single magnet is 9.3 tons, or 1200 tons for 128 magnets. The cost of these magnets apparently turns out to be in the neighborhood of $1200 per ton, or $1.4 \times 10^6$ dollars.

If such iron is carried between −5 and +5 kilogauss at 60 cps with a roughly sinusoidal wave form, there will be a power loss in the iron of about 0.2 w/lb. We assume that this figure holds when the same amplitude of variation is retained, but the mean field is raised to 5 kilogauss by a d-c bias. We thus obtain a simple estimate for power dissipation in the iron (eddy current and hysteresis):

$$W_{Fe} = 0.50 \text{ Mw.}$$

Although this is not an important amount of power to buy, it may require cooling ducts and forced air circulation through the magnet sections.

The electrical properties of the magnet can easily be estimated. For simplicity, we assume excitation by a single-turn coil, although in practice the 310 $cm^2$ (approximate) of copper cross section must be split up into many turns (perhaps a hundred) to minimize skin effect at 60 cps. The peak flux per magnet is given by

$$\phi = k_2 B_0 A \ , \tag{5}$$

where $B_0$ is the peak field at the center of the vacuum chamber, $A$ is the area of good field (projected on the median plane), and $k_2$ is an empirical constant to allow for the fringing field. Brookhaven experience suggests a value of 1.40 for $k_2$. The peak field is given by

$$B_0 = \frac{4\pi}{k_1 g} I \ , \tag{6}$$

where $k_1$ is another empirical constant (which we take as 1.10), $g$ is the gap at the center of the vacuum chamber, and $I$ is the single-turn exciting current. All units are absolute cgs (mixed Gaussian). By using a length of 212 cm and a width of 13 cm for the good field region of one magnet, a gap of 6.66 cm, and a peak field of 10 kilogauss, we obtain

$$I = \frac{k_1 g}{4\pi} B_0 = 5.84 \times 10^3 \text{ abamp} \tag{7}$$

$$= 5.84 \times 10^4 \text{ amp}$$

for the required peak exciting current. The inductance is

$$L = 6.64 \times 10^{-6} \text{ henry/magnet} \ . \tag{8}$$

The peak stored energy is

$$\tfrac{1}{2} L I^2 = 1.13 \times 10^4 \text{ joules/magnet} \ , \tag{9}$$

or a total of

$$128 \times 1.13 \times 10^4 = 1.45 \times 10^6 \text{ joules} \ . \tag{10}$$

The peak ac is $\frac{1}{2}I$ or $2.92 \times 10^4$ amp. This gives a peak a-c voltage across a magnet of

$$\omega L \frac{I}{2} = 73 \text{ v} \ , \tag{11}$$

which must be multiplied by the square of the number of turns in the coil to get the actual voltage.

The power factor of the a-c supply must be brought to unity by some sort of capacitive energy storage. The simplest and most economical procedure appears to be the use of condensers for storing about one quarter of the peak magnet energy, with a choke for storing the other three quarters. Simultaneously, a-c voltage can be kept out of the d-c supply by one of several simple systems. The peak condenser energy storage is then

$$\tfrac{1}{4} \times 1.45 \times 10^6 = \tfrac{1}{2} QV \tag{12}$$

$$= 0.36 \times 10^6 \text{ joules} \ ,$$

where $Q$ is the peak stored charge in coulombs, and $V$ is the voltage raging of the condenser bank. The peak charging current is

$$I_c = 377\, Q \ , \tag{13}$$

so that

$$\tfrac{1}{2} I_c V = 1.36 \times 10^8 \text{ va} \ ,$$

or

$$\frac{I_c}{\sqrt{2}} \frac{V}{\sqrt{2}} = 1.36 \times 10^8 \text{ va} \ . \tag{14}$$

Division by $\sqrt{2}$ yields the effective quantities, so that the rating of the condenser bank must be $1.36 \times 10^5$ kva at 60 cps. A reasonable cost allowance is \$8 per kva, giving a total cost of $1.1 \times 10^6$ dollars.

In addition to the condensers, chokes must also be supplied. These must store a quantity of magnetic energy comparable with that stored in the accelerator and must handle this energy without greatly adding to the losses of the system. At first sight the choke required for a single magnet section would seem to compare in cost with the magnet itself. Fortunately, however, the chokes do not have to accelerate particles, and several economies are therefore possible in their construction. The experience gained at Cambridge and at Princeton indicates that the choke cost will be about one-fifth of the cost of accelerator magnet cores plus coils. By anticipating our coil estimates, we arrive at about $0.5 \times 10^6$ dollars as a reasonable choke cost.

A potentially embarassing problem in the power supply is the variation of the required capacitance with temperature peak and magnetic field. Such discrepancies, unless continuously compensated, can easily cause serious power-factor variations in the a-c supply. An obvious procedure is to supply a small part of the required capacitance in the form of a synchronous condenser, whose effective capacitance can be continuously varied by varying its field excitation. This in turn can be controlled directly from the power factor, which should make startup and operation of the magnet very smooth.

As mentioned previously, the construction of the magnet coils must follow conventional power-transformer practice. They should be composed of many separately insulated conductors, each of which should probably have a cross section of only 1 $cm^2$ in order to minimize skin effect. These turns can be connected in multiple as desired in order to adjust the magnet voltage. If desired, the windings can be split into two differently wound halves, one half for ac and the other for dc.

In the magnet cross section previously specified, there is room for a coil with about 310 $cm^2$ of copper. For one magnet, this single-turn coil has a length of about 484 cm. The copper weight (neglecting cooling channels) is about 1.40 tons/magnet, or a total of about 180 tons. Such coils are estimated to cost about $5 \times 10^3$ dollars/ton, so that a reasonable coil cost is $0.90 \times 10^6$ dollars.

The resistance of one magnet (single-turn) is easily calculated to be $0.27 \times 10^{-5}$ ohm, and the resistance loss in the coils at full magnetic-field amplitude is 0.42 Mw.

The vacuum chamber presents a real problem arising from the rapid pulsing of the machine. Suppose we were to assume a thin-walled, Inconel vacuum chamber, like the Brookhaven-AGS chamber. Eddy currents will disturb the AGS, principally near injection, when the field is low (150 gauss) and the rate of field rise, which is proportional to eddy-current density and also to the resulting error field, is high (13,000 gauss/sec). We define a parameter $\dot{B}/B$ whose maximum value is clearly proportional to the maximum fractional-field perturbation. For the AGS, this maximum value is 87 $sec^{-1}$. In our case, the maximum eddy-current effect occurs about halfway through the acceleration cycle, since $B$ is given by

$$B = 5.6 - 4.4 \cos 377t \text{ (kilogauss)} . \tag{15}$$

From this,

$$\dot{B} = 377 \times 4.4 \sin 377t \text{ (kilogauss/sec)} ,$$

and

$$\frac{\dot{B}}{B} = \frac{377 \times 4.4 \sin 377t}{5.6 - 4.4 \cos 377t} \text{ sec}^{-1} . \tag{16}$$

The maximum comes when $\cos 377t = 4.4/5.6$, so that in our case the eddy-current parameter becomes

$$\frac{\dot{B}}{B} = 480 \text{ sec}^{-1}. \tag{17}$$

This is over five times as large as for the AGS, so that an Inconel chamber is clearly quite undesirable. Either glass (preferably tempered) or molded resin will be required. The outgassing problem with the resin can be minimized by use of a thin metallic lining, and the reduction of vertical orbit space by use of the relatively thick, nonmetallic chamber can probably be avoided by making the chamber thick only where vertical space is being wasted. As a result, a complicated molding job is necessary in order to yield a chamber which fits snugly in the magnet gap and has a strictly rectangular inner cross

section. No simple cost estimate is possible for this component at the present preliminary stage.

The last major component of the accelerator (aside from the injector cyclotron, which is considered separately) is the radio-frequency system. Here the essential problem is to obtain sufficient voltage gain per turn by taking advantage of the small frequency modulation required. If sinusoidal variation of the magnetic field is assumed, the required energy gain per turn is zero both at injection and extraction, with a maximum of 3 Mev/turn halfway through the acceleration. In a more conventional accelerator, a peak voltage of something like twice this figure would be required to give good phase stability. In our machine, 3 Mev/turn gives excellent phase stability over the first and last thirds of the acceleration cycle. In the middle third, the normal excess voltage requirement is mitigated by the fact that the transition energy comes at 5.9 bev. In this neighborhood, phase stability vanishes anyway, and the r-f phase must be changed from one side to the other of the voltage wave. Thus excess voltage is of no advantage in this region, and we set as the peak voltage requirement 4 Mev/turn.

If no frequency modulation were necessary, this voltage could easily be supplied by 16 cylindrical resonators powered by klystron amplifiers (as in the Cambridge electron accelerator). These resonators, with the beam direction along their axes, would be 75 cm long and 176 cm in radius. Each would have a peak voltage of 250 kv and a theoretical $Q$ of about $2 \times 10^5$. The total stored energy would be 240 joules, and it seems reasonable to suppose that a $Q$ of $10^3$ could be kept, even with the required frequency modulation. With these assumptions the r-f power would be 0.5 Mw.

It is doubtful whether a $Q$ of $10^3$ can be achieved if ferrite is used for the full 15% of frequency modulation. A much more attractive scheme is to insert into each cavity a copper paddle which, by rotation, can change the frequency of the cavity without depressing its $Q$ unduly. Rotation would be accomplished by means of a synchronous motor driven at 60 rps from the magnet supply. The paddle would be so shaped that its rotation would supply all but a very small fraction of the desired frequency program. The residue would probably be supplied by ferrite loading, with control current being supplied by a circuit using information on beam phase and radius supplied by pickup electrodes. It is probably simplest to make each cavity a self-sufficient unit with its own pickup electrodes and control circuit. This avoids the problem of phasing the cavities.

Some miscellaneous problems should at least be mentioned. Normally, correcting coils would be supplied on the pole faces in order to take care of changes in magnetic-field shape arising from variations of permeability with flux density. We require the full region of good $n$ for injection,[3] which is at a reasonable flux density (1200 gauss – one of the advantages of high-energy injection), so that correction coils would not be required. On the other hand, the most promising extraction scheme requires also a large region of good $n$ at full field, which would conventionally require sizable correction coils. A much superior scheme seems to be the use of a pole face contour which varies from lamination to lamination in such a way that the effective pole contour varies with flux density as required, in order to compensate for the saturation effects. This promising technique was recently proposed by the Saclay magnet group,[4] and seems likely to render obsolete the use of correction windings.

We require quadrupoles, in some of the straight sections, capable of moving the operating point once per cycle by $\Delta\nu_x$, $\Delta\nu_y \cong \pm 0.1$ in order to accomplish injection and extraction. Coarser permanent adjustment of the $\nu$ values for initial tuneup should probably be done by slight changes in magnet positions. We require also the usual complement of sextupole and octupole magnets for introducing controlled aberrations at extraction. Finally, some additional r-f equipment is required for injection,[3] at a cost which seems to be very small, compared with the main r-f cost.

---

[3] F. T. Howard *et al.*, *Proposal for a Southern Regional Accelerator*, ORNL CF-57-4-30 (April 9, 1957).

[4] E. Regenstreif (ed.), *CERN Symposium on High Energy Accelerators and Pion Physics Proceedings, Geneva, 11th–23rd June 1956*, vol 1, European Organization for Nuclear Research, Geneva, 1956.

## BEAM EXTRACTION STUDIES FOR THE 900-Mev CYCLOTRON

M. M. Gordon T. A. Welton

The main features of the 900-Mev cyclotron being developed at ORNL have already been described. One of the principal problems connected with this machine is that of beam extraction. Since this beam is to be injected into a synchrotron ring, it is important that it have not only well-defined energy and high intensity, but also that it be concentrated in as small a phase-space area as possible (high quality). Thus it is essential that a large fraction of the internal beam be extracted, and also that the extraction process itself should not disturb the quality of the beam.

Beam extraction will be accomplished at the radial integral resonance $\nu_r = 2$, which is reached at a beam energy of 850 Mev or thereabouts, depending on the details of the magnetic field. The vertical-oscillation frequency at this point must be chosen with care in order to avoid the deleterious effects of the $\nu_r = 2\nu_z$ ("Walkinshaw") resonance on the vertical stability of the beam during extraction. The extraction process requires a large buildup in amplitude of the radial oscillations, and in the neighborhood of the $\nu_r = 2\nu_z$ resonance such a buildup tends to drive the operating point into this resonance ($\nu_z \longrightarrow 1$), so that effective vertical instability results. The effects of this resonance can be weakened by choosing a suitably small value for $\nu_z$ so as to be, at least initially, as far from $\nu_z = 1$ as is feasible, and also by reducing the "spiral" to a minimum, since it is known that the strength of this resonance increases with the degree of spiral. These considerations have led us to choose a value of $\nu_z \cong 0.25$, which is achieved by maximizing the amount of "flutter" while minimizing the amount of "spiral." Under these conditions we have found that vertical stability can be maintained for radial-oscillation amplitudes up to about 25 cm, which seems to be adequate for our purposes.

For an eight-sector machine, the point for which $\nu_r = 2$ coincides with the quarter-integral essential resonance ($\nu_r = N/4$). This resonance is driven by cubic terms in the equation for the radial oscillation, and, according to both theoretical and empirical studies, this type of resonance may or may not lead to unstable motions, depending on the relative magnitudes of the $x^3$ and $x^3 \cos N\theta$ terms in the equations of motion. For the spiral-sector cyclotron, the $\nu_r = 8/4$ resonance leads to radial instability, and the possibility then arises of making use of this instability to help extract the beam at $\nu_r = 2$. This report is concerned mainly with the results of an investigation into this possibility.

The instability arising from the 8/4 resonance is nonlinear in nature, and it is because of this that the instability looks attractive from a beam-extraction point of view. For efficient beam extraction it is necessary that the beam acquire a large radius gain per turn such that it can miss a septum on one turn and then clear this septum on the next turn in order to enter the extractor channel. For a quarter-integral resonance, one can expect an amplitude gain per turn which is proportional to the cube of the amplitude, so that, as the amplitude increases, the rate of increase will rise very rapidly.

The numerical calculations of orbit properties to be described below were carried out on the Oracle by using a code (No. 289) specifically designed for this type of work.

### PROPERTIES OF THE 8/4 RESONANCE

The magnetic field in the median plane of the eight-sector machine was taken in the following form (cyclotron units):

$$B_z = -\frac{1}{\sqrt{1 - r^2}}\,[1 + f(r)\cos 8(\theta - \xi)] \ ,$$

where the spiral $\xi = r^2$ for simplicity, and

$$f(r) = r^2 + 0.590r - 0.166 \ .$$

This value of the flutter was chosen by a "cut and try" method such that $f \cong 1$ and $\nu_z = 0.25$ near $\nu_r = 2$.

After setting up the form of the field, a study of orbit properties in this field was then carried out. The first part of this study consisted of

a series of runs by which orbits were calculated exactly at resonance ($\nu_r = 2$) for particles of constant energy. For each of these runs a particle was started with given initial $r$ and $p_r$, and its orbit was calculated for 30 revolutions or until an overflow stop occurred. For each run the computer output gave values once per sector for $r$ and $p_r$. The curves of Fig. 1 were drawn from these results. In this figure each point on a curve represents an $(r,p_r)$ set obtained at a particular sector in a given run. The individual curves are obtained by connecting all the points for a given run. These curves can be understood qualitatively in terms of the theory of nonlinear resonances. According to this theory, for the $\nu = N/4$ resonance,

$$K = A^4(C_1 + C_2 \cos 4\phi) ,$$

where $(A,\phi)$ are essentially polar coordinates in the $(r,p_r)$ phase space, $C_1$ and $C_2$ are constants depending on the coefficients of the $x^3$ and $x^3 \cos N\theta$ terms in the equation of motion, and $K$ is a constant (invariant) of the motion depending only on the specific initial conditions. Comparison of this invariant ($C_2 > C_1$) with the curves of Fig. 1 shows good agreement, considering the approximate nature of the theory.

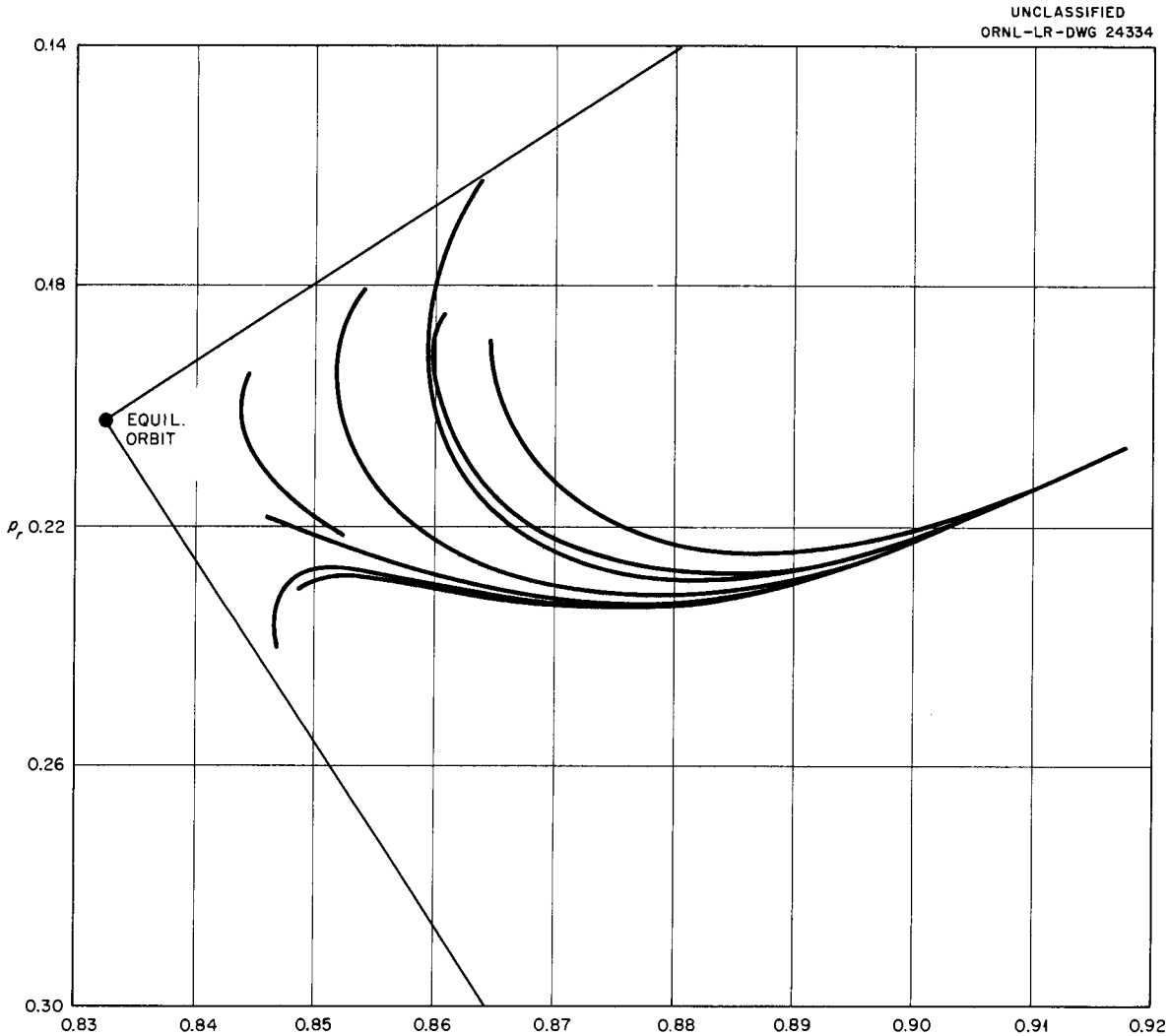


**Fig. 1. Phase Curves for 8/4 Resonance.**

Curves in Fig. 1 are shown for only one quarter of the total phase space (that portion of specific interest for beam extraction, namely, where $r$ increases); the corresponding curves for the remaining portions of phase space may be obtained from the given curves by successive rotations through 90 deg (the invariant $K$ above has period $\pi/2$ in $\phi$).

One of the curves in Fig. 1 can be seen to lie quite close to the asymptote along which $r$ increases monotonically. In examining the numerical data for this run, it was found that they could be fitted very well to the equation

$$\frac{dA}{dn} = CA^3, \qquad C = 176 ,$$

where $A$ is the difference between $r$ and the equilibrium-orbit value, and $dA/dn$ is the increase of $r$ per revolution. Such an equation for $A$ is expected from the theory for the quarter-integral resonance for a phase curve along which $\phi$ is essentially constant. If we take 600 cm as the cyclotron unit, then this equation predicts the following:

| $A$ (cm) | $dA/dn$ (cm) |
|---|---|
| 1 | $5 \times 10^{-4}$ |
| 2 | $4 \times 10^{-3}$ |
| 4 | $3 \times 10^{-2}$ |
| 8 | 0.25 |
| 16 | 2 |
| 24 | 6.8 |

Thus we see that this resonance can be used to obtain beam extraction, since it provides sufficient radius gain per turn at the larger amplitudes to allow efficient channel entry. The effect of the resonance is hardly noticeable for small amplitudes. Hence, for extraction, it will be necessary to induce appreciable radial amplitude in the beam going into the resonance in order that the nonlinear, quarter-integral resonance be effective. This procedure is discussed in the next subsection.

The nonlinear resonance theory indicates that the width of this resonance should vary as $A^2$. By using the data described above, we have estimated a width $\delta\nu_r = 0.003$ (about 3 Mev in energy) for an amplitude $A$ of 6 cm. This result serves to emphasize the conclusion that the 8/4 resonance will be ineffective unless a sufficiently large radial amplitude is induced as the resonance is approached.

### 8/4 RESONANCE PLUS INTEGRAL RESONANCE

The curves of Fig. 1 were obtained from values taken from the computed data at a specific $\theta$ value within each sector. These values were so chosen that the increase in $r$ per revolution was a maximum ($p_r$ nearly constant). Because of the eightfold azimuthal symmetry of the field, it is then possible to effect extraction at any one of these eight $\theta$ positions around the machine. Indeed, if some care is not exercised in steering the beam into the 8/4 resonance properly, the beam may spill out at all eight positions.

The method utilized for "steering" the beam into the 8/4 resonance bears some resemblance to that of the LeCouteur scheme. We imagine an auxiliary set of field coils which change the median-plane field given above by an amount

$$\Delta B_z = \xi r^2 \sin 2(\theta + \gamma) ,$$

where $\xi$ and $\gamma$ are constants. Such an addition to the field serves to displace the $(r,p_r)$ point of a particle at a given $\theta$ value by an approximately uniform amount for each revolution near resonance ($\nu_r = 2$). The amount of the displacement is controlled mainly by $\xi$, while the direction of the displacement is controlled by the choice of $\gamma$. Such an effect is characteristic of the "integral" resonance produced by this $\Delta B_z$. The above form for $\Delta B_z$ was chosen for its simplicity; although it is not very realistic, the results obtained from it are nevertheless qualitatively valid.

The value of $\xi$ was chosen by setting

$$\xi r_0^2 = \epsilon \bar{B}(r_0) = \frac{\epsilon}{\sqrt{1 - r_0^2}} ,$$

where $r_0 = 0.8328$ is the mean equilibrium-orbit radius at $\nu_r = 2$, and was set equal to $10^{-3}$ so that $|\Delta B_z|$ was $10^{-3}$, the average guide field at $r = r_0$. The value of $\gamma$ was chosen by optimizing the action of $\Delta B_z$ in steering the beam into the 8/4 resonance so that extraction would occur in a specified sector.

The extraction process was simulated by a series of runs under the following conditions. For each run a proton was started 15 Mev (16 revolutions) below the energy at which $\nu_r = 2$ and was accelerated at the rate of $10^{-3} Mc^2$ per revolution.

The first run was for a particle initially in the equilibrium orbit. The results of this run are shown graphically in Fig. 2, where $A$ is the value of $r$ minus the initial value. As expected, $dA/dn = \alpha = 1.1$ cm/turn is constant for small $A$, where the integral resonance effect of

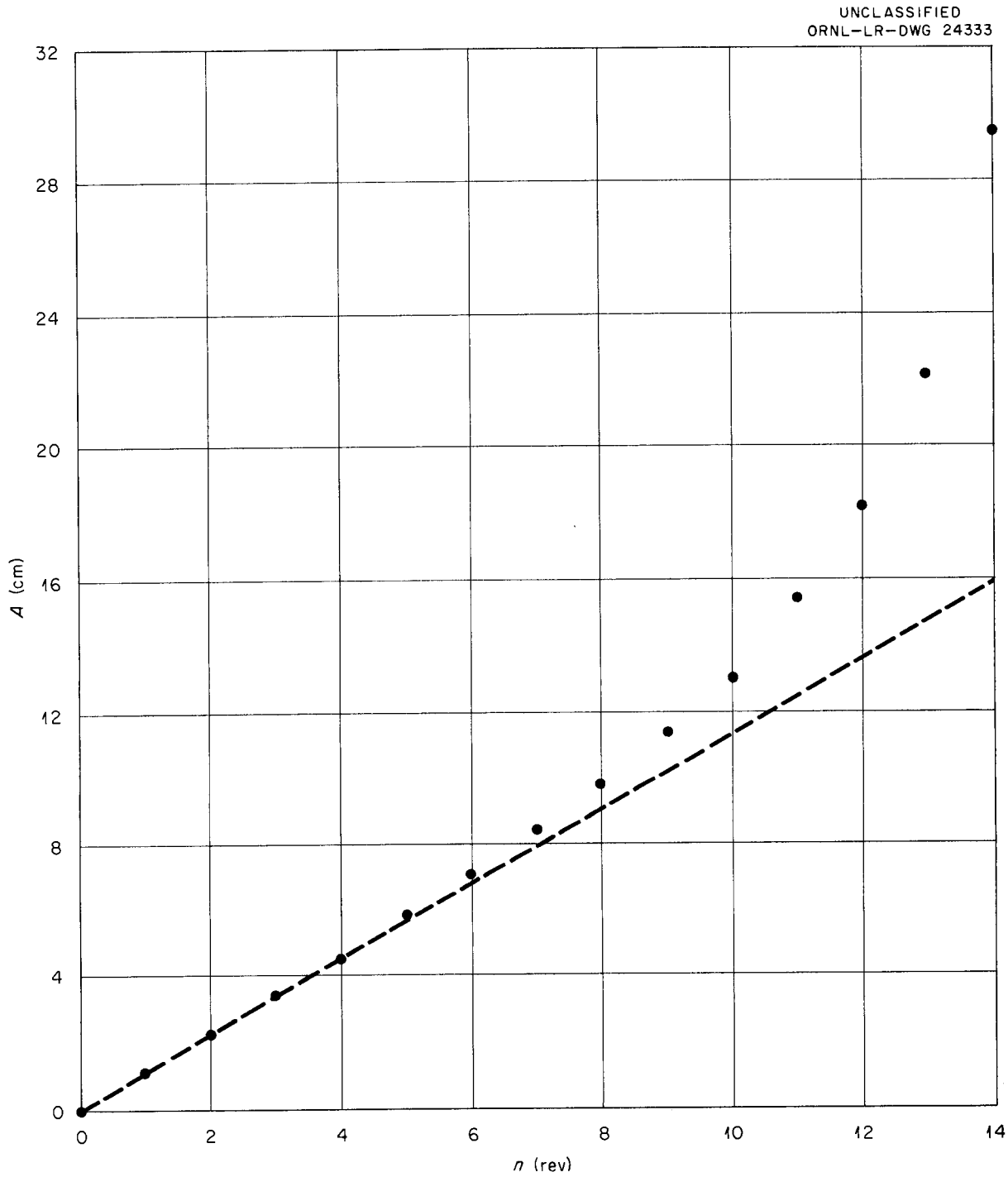


**Fig. 2. The 8/4 Resonance Driven by $\xi \bar{B} \cos 2\theta$.**

$\Delta B_z$ controls the situation. For large amplitudes the 8/4 resonance takes over. We found, as expected, that this curve can be fitted to the equation

$$\frac{dA}{dn} = \alpha \left[ 1 + \left( \frac{A}{a} \right)^3 \right],$$

with $a = 14.6$ cm. It is possible to draw some useful conclusions from this result. If the beam consists of particles with initial radial spread $\Delta r = \Delta_0$ about the equilibrium-orbit value of $r$, then this radial spread grows during extraction such that

$$\Delta r = \Delta_0 \left[ 1 + \left( \frac{A}{a} \right)^3 \right].$$

For an initial spread of $\Delta_0 = 0.5$ cm, one finds then, from this equation and from Fig. 2, the following information:

| $n$ (turns) | $A$ (cm) | $\Delta r$ (cm) |
|---|---|---|
| 10 | 13.1 | 0.86 |
| 11 | 15.3 | 1.13 |
| 12 | 18.1 | 1.45 |
| 13 | 22.1 | 2.23 |
| 14 | 29.5 | 4.62 |

From results of this kind one can determine the efficiency with which the beam will enter the extraction channel.

The purpose of the other runs of this kind that were made was to determine the effect of beam extraction on the vertical quality of the beam. As noted before, as the radial amplitude increases, the vertical frequency $\nu_z$ tends to increase as a result of the effect of the $\nu_r = 2\nu_z$ resonance. For example, in a run in which the particle was given a small vertical-oscillation amplitude initially, the vertical frequency behaved as follows:

| $n$ (turns) | $A$ (cm) | $\nu_z$ |
|---|---|---|
| 0–6 | 0–7 | 0.25 |
| 6–8.5 | 7–10.5 | 0.28 |
| 8.5–11.5 | 10.5–16.5 | 0.33 |
| 11.5–14 | 16.5–29.5 | 0.4–0.55 |

Up to the 15th revolution the vertical amplitude held steady, but during the 15th revolution, while the radial amplitude climbed to over 50 cm, $\nu_z$ reached the value $\nu_z = 1$ and, at the same time, the vertical amplitude began to climb rapidly.

In order to study the effect of extraction on the vertical quality more fully, the following procedure was adopted. Eight values of $(z,p_z)$ were found on an invariant ellipse; that is, this ellipse is such that, as long as the radial amplitude remains small, and if the particle starts out with a $(z,p_z)$ on this ellipse, the succession of $(z,p_z)$ values which the particle attains will lie on the ellipse. These eight $(z,p_z)$ values were used as initial conditions for a series of runs with a given initial $(r,p_r)$ value. In this way the behavior of the invariant ellipse in the $(z,p_z)$ phase space can be traced through the extraction process. A series of such sets of eight runs for initial $(r,p_r)$ values, which themselves lie on an invariant $r$ ellipse, would then completely depict the effect on the vertical quality of the beam. Actually, to save time, only two different $(r,p_r)$ values were used, each with the initial $r$ displaced from the equilibrium orbit by 0.3 cm – one +0.3 cm, the other –0.3 cm. Since these two cases have the greatest difference in radial amplitude growth, they should provide an adequate test of the behavior of the vertical quality. The results of these runs are displayed partly in Fig. 3; the two $z$ ellipses are shown superimposed at $n = 0$, 8, 10, and 12 turns. Good-quality preservation would be indicated by good overlapping of the two ellipses. As can be seen, there is a considerable degree of overlapping even out to $n = 12$, where $A = 18$ cm, although it is evident that the amount of overlapping is progressively decreasing as $n$ increases. Thus it seems quite reasonable to expect that the vertical quality of the beam can be preserved during extraction, provided that the beam is extracted before too large a radial amplitude is achieved, and provided the initial radial spread of the beam is not too great (in the above case this radial spread was 0.6 cm).

## CONCLUSIONS

At the time this work was begun, there was some question as to whether the cyclotron should have 8 or 12 sectors. The 12-sector choice was

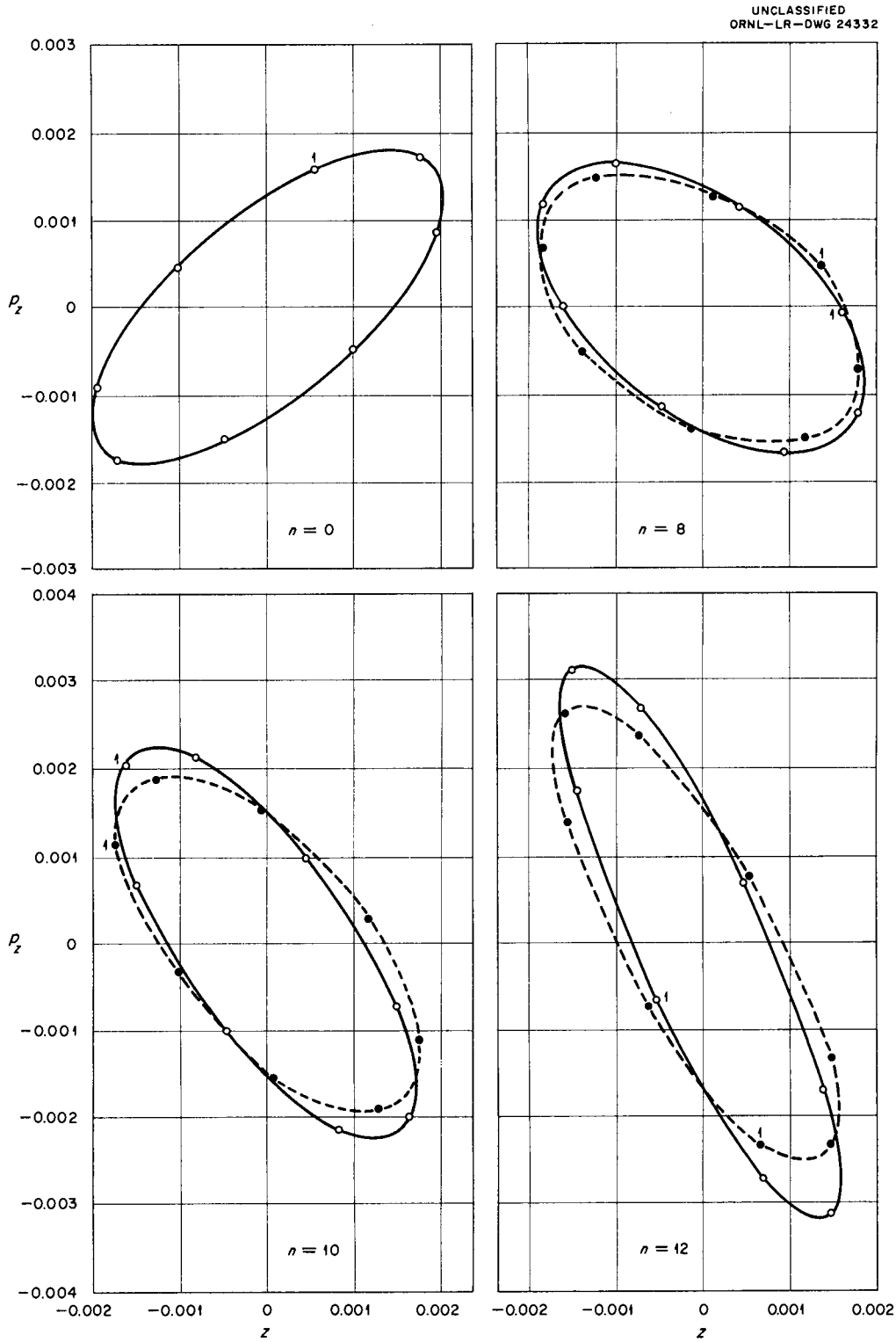


**Fig. 3. Invariant $z$ Ellipse During Extraction.**

favored because the energy of the $\nu_r = 2$ resonance is about 50 Mev higher than for 8 sectors, and, in addition, it was found that the 8/4 resonance would interfere with the possibility of actually accelerating past the $\nu_r = 2$ resonance. Our investigations have shown, however, that the eight-sector machine has greater stability against the deleterious effects of the $\nu_r = 2\nu_z$ resonance. Furthermore, the 8/4 resonance turns out to be so weak for small radial amplitudes that it should not interfere with an attempt to accelerate through the $\nu_r = 2$ resonance. Finally, the 8/4 resonance can be used for beam extraction, while the 12/6 resonance is completely ineffective in this respect. As a result of these considerations, it is now planned that the cyclotron have eight sectors.

Two general extraction schemes have been thought of, and each will be pursued further. The first involves the construction of a "programed" machine with very tight control over the r-f voltage and the starting conditions at the center of the machine. In such a machine every particle would have an identical history, within narrow limits, from beginning to end. The extraction route for these particles would then be very well defined, and high-efficiency extraction would result. In this scheme the radial quality of the beam would be optimized for efficient injection into the synchrotron ring; the vertical quality is not so important, since the ring will have ample vertical aperture. In addition, such high extraction efficiency looks very attractive from the point of view of preventing activation of the machine structure by the unextracted high-energy protons.

The second scheme is based on the following considerations. A cyclotron beam naturally tends to have good vertical quality, but poor radial quality. On the other hand, for efficient injection into the ring, high radial quality is required. Now this scheme proposes to extract the cyclotron beam on a statistical basis (as in the LeCouteur extractor) but with great care toward maintaining the good vertical quality. The emergent beam would then be passed through a solenoid which would interchange "radial" and "vertical" directions before injection of the beam into the ring. In this way the good vertical quality of the cyclotron beam is transformed into good radial quality for ring injection. The use of statistical extraction cuts down on the extraction efficiency; however, with an amplitude gain per turn of 4 cm (at $A$ = 18 cm in Fig. 2) and a septum width of about 0.5 cm, it should be possible to achieve an efficiency of 80% for entry into the extraction channel.

The investigations reported above are preliminary in nature; their aim was to explore the feasibility of utilizing the 8/4 resonance for extraction and to evaluate the difficulty of the various problems that are involved. The results indicate that an effective beam extraction mechanism could be based on the 8/4 resonance. Further investigations are planned into such matters as effects of changes in the degree of spiral and the amount of flutter; also, it is planned to use more realistic fields.

## COULOMB EXCITATION OF STATES IN $Pt^{195}$

F. K. McGowan P. H. Stelson

Gamma rays of 99, 130, 210, and 240 kev have been observed from coulomb excitation of $Pt^{195}$ with protons and alpha particles.[1] Transitions of 31, 99, and 130 kev have been observed[2] in the $\epsilon$-capture decay of $Au^{195}$. From intensity measurements of the internal-conversion electrons by Gillon *et al.*,[3] there is strong evidence that the levels in $Pt^{195}$ are at 99 and 130 kev, with a 31-kev cascade transition between them. Recently, Bernstein and Lewis[4] measured the excitation functions of the internal-conversion electrons from coulomb excitation of states in $Pt^{195}$, and they concluded that the levels in $Pt^{195}$ are at 31 and 130 kev, with a 99-kev cascade transition between them.

We have made additional studies of coulomb excitation in $Pt^{195}$ with protons and alpha particles, using a target enriched in $Pt^{195}$ (60.1%). A typical pulse-height spectrum of the gamma rays is shown in Fig. 1 for alpha-particle bombardment of the $Pt^{195}$ target. The peak at 400

[1] P. H. Stelson and F. K. McGowan, *Phys. Rev.* 99, 112 (1955).

[2] A. de-Shalit, O. Huber, and H. Schneider, *Helv. Phys. Acta* 25, 279 (1952).

[3] L. P. Gillon *et al.*, *Phys. Rev.* 93, 124 (1954).

[4] E. M. Bernstein and H. W. Lewis, *Phys. Rev.* 100, 1345 (1955).

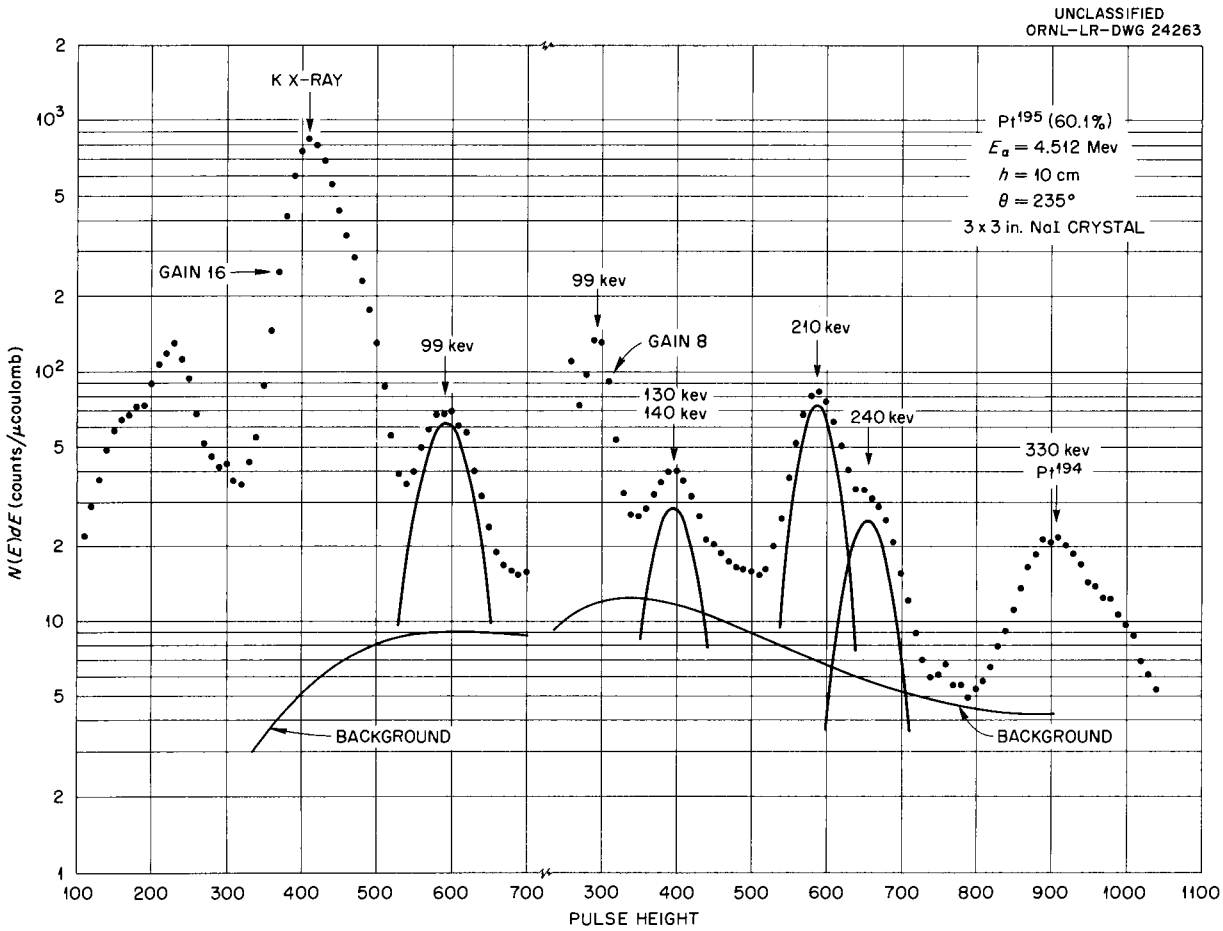


**Fig. 1. Differential Pulse-Height Spectrum of the Gamma Radiation for Alpha-Particle Bombardment of $Pt^{195}$.**

pulse-height units is too wide for a single gamma ray of 130 kev. Coincidence spectrum measurements have revealed an additional gamma ray of 140 kev in coincidence with the 99-kev gamma ray. Since our measured value of the $K$-shell internal-conversion coefficient of the 99-kev transition is 5.8 ± 1.5, the $K$ x rays from internal conversion of the 99-kev transition should also be in coincidence with the 140-kev gamma ray. A coincidence pulse-height spectrum of the 140-kev gamma ray in coincidence with the $K$ x rays is shown in Fig. 2. According to the level scheme proposed by Bernstein and Lewis, the 140-kev gamma should also be in coincidence with the 130-kev gamma; that is, the relative intensities of 99- and 130-kev gamma rays in coincidence with the 140-kev gamma ray should be identical with those observed in the singles spectrum. A spectrum of the 99- and 130-kev gamma rays in coincidence with the 140-kev gamma ray was taken at $E_\alpha$ = 4.96 Mev. The intensity of the 130-kev gamma ray relative to the 99-kev gamma

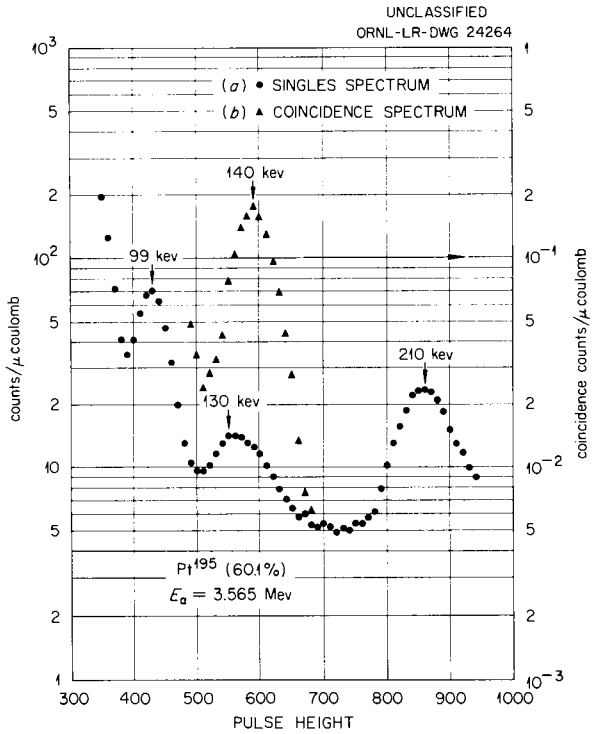


**Fig. 2. (*a*) Portion of the Pulse-Height Spectrum of the Gamma Radiation for Alpha-Particle Bombardment of $Pt^{195}$. (*b*) Spectrum of Gamma Radiation in Coincidence with $K$ X Rays from Internal Conversion of the 99-kev Transition.**

ray was found to be at least 20 times smaller than the intensity observed in the singles spectrum. This result provides evidence that the levels are at 99 and 130 kev in $Pt^{195}$, with the 140-kev cascade transition between levels at 240 and 99 kev. To verify this assignment, we have measured the energy dependence of the 140-kev gamma-ray yield in coincidence with the $K$ x rays from internal conversion of the 99-kev transition. The relative yield of the 140-kev gamma ray as a function of $E_\alpha$ is shown in Fig. 3. The solid curve is the predicted yield for an excitation of a level at 240 kev. Agreement between the experimental yield and the predicted yield for the direct excitation of a state at 240 kev is good.

In Table 1 we have listed the gamma-ray yields from coulomb excitation of states in $Pt^{195}$ with alpha particles. The relative gamma-ray yields as a function of $E_\alpha$ are shown in Figs. 3 and 4. The solid curves are the predicted energy dependence of the yields for various excitation energies $\Delta E$ above the ground state of $Pt^{195}$. The theoretical curves for excitation of levels at 210 and 240 kev and the experimental data for the 210-kev gamma ray are all normalized at $E_\alpha$ = 4.022 Mev. From the good agreement between the experimental and predicted yields with $\Delta E$ = 210 kev, we conclude that there is direct excitation of a level at 210 kev in $Pt^{195}$. If there were a state at 31 kev in $Pt^{195}$, the 210-kev transition might have been a cascade transition between levels at 240 and 31 kev. However, the energy dependence of the yield of 210-kev gamma rays excludes this interpretation. The measured excitation functions shown in Figs. 3 and 4 indicate direct excitation of levels in $Pt^{195}$ at 99, 130, 210, and 240 kev. The 99-kev transition is not a cascade transition between levels at 130 and 31 kev, as suggested by Bernstein and Lewis, for the following reasons: (1) The 140-kev gamma ray is not in coincidence with the 130-kev gamma ray. (2) Energy dependence of the yield for the 240- and 140-kev gamma rays is in accordance with the prediction for $\Delta E$ = 240 kev instead of 270 kev. (3) Energy dependence of the yield for the 99-kev gamma ray lies between the prediction for $\Delta E$ = 99 and 130 kev instead of at $\Delta E$ = 130 kev. When the small contribution from direct excitation of the 240-kev state to the yield of 99-kev gamma rays

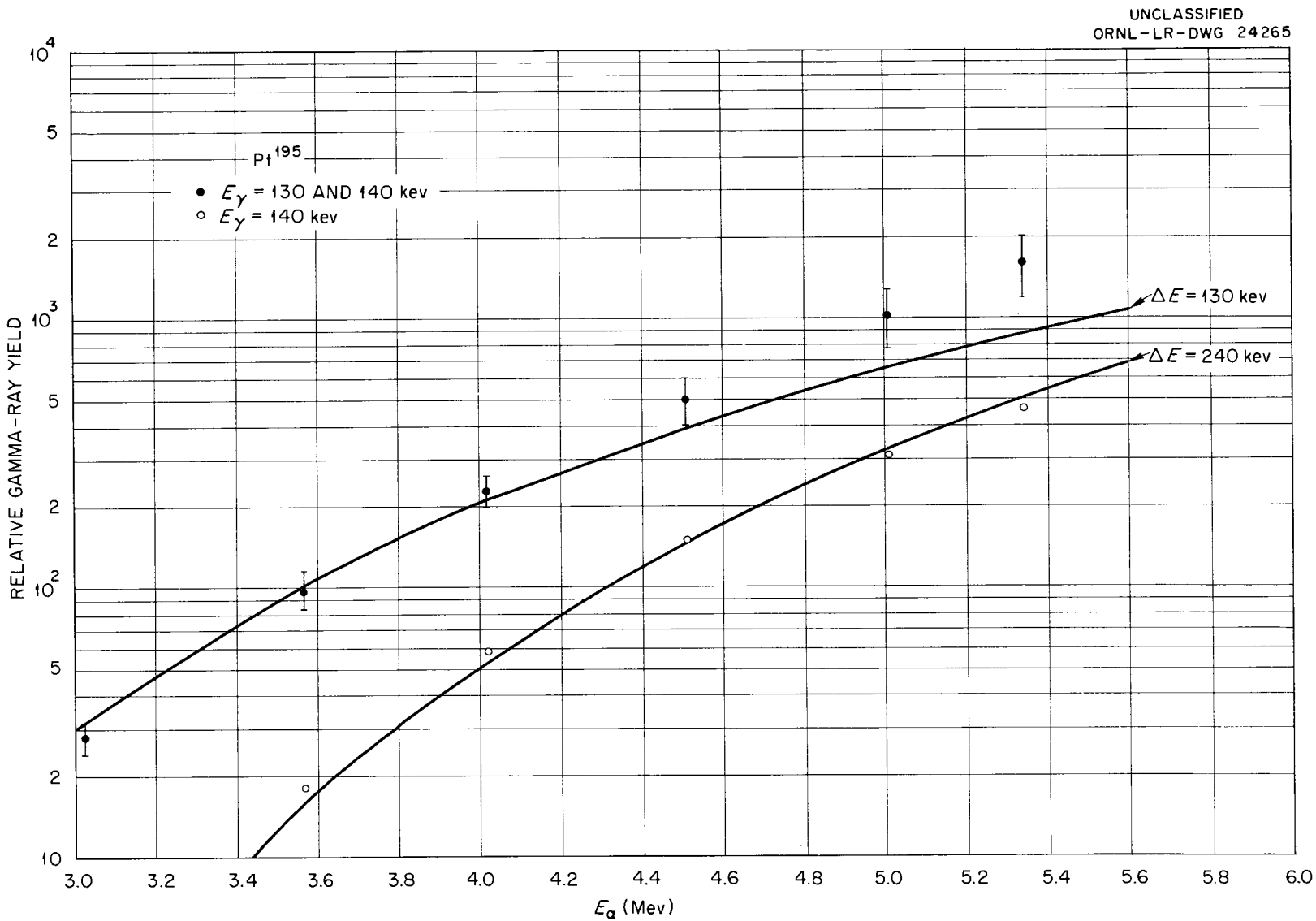


**Fig. 3. Relative Gamma-Ray Yields as a Function of $E_\alpha$.** The solid curves are the predicted energy dependence of the yields for various excitation energies $\Delta E$ above the ground state of $Pt^{195}$.

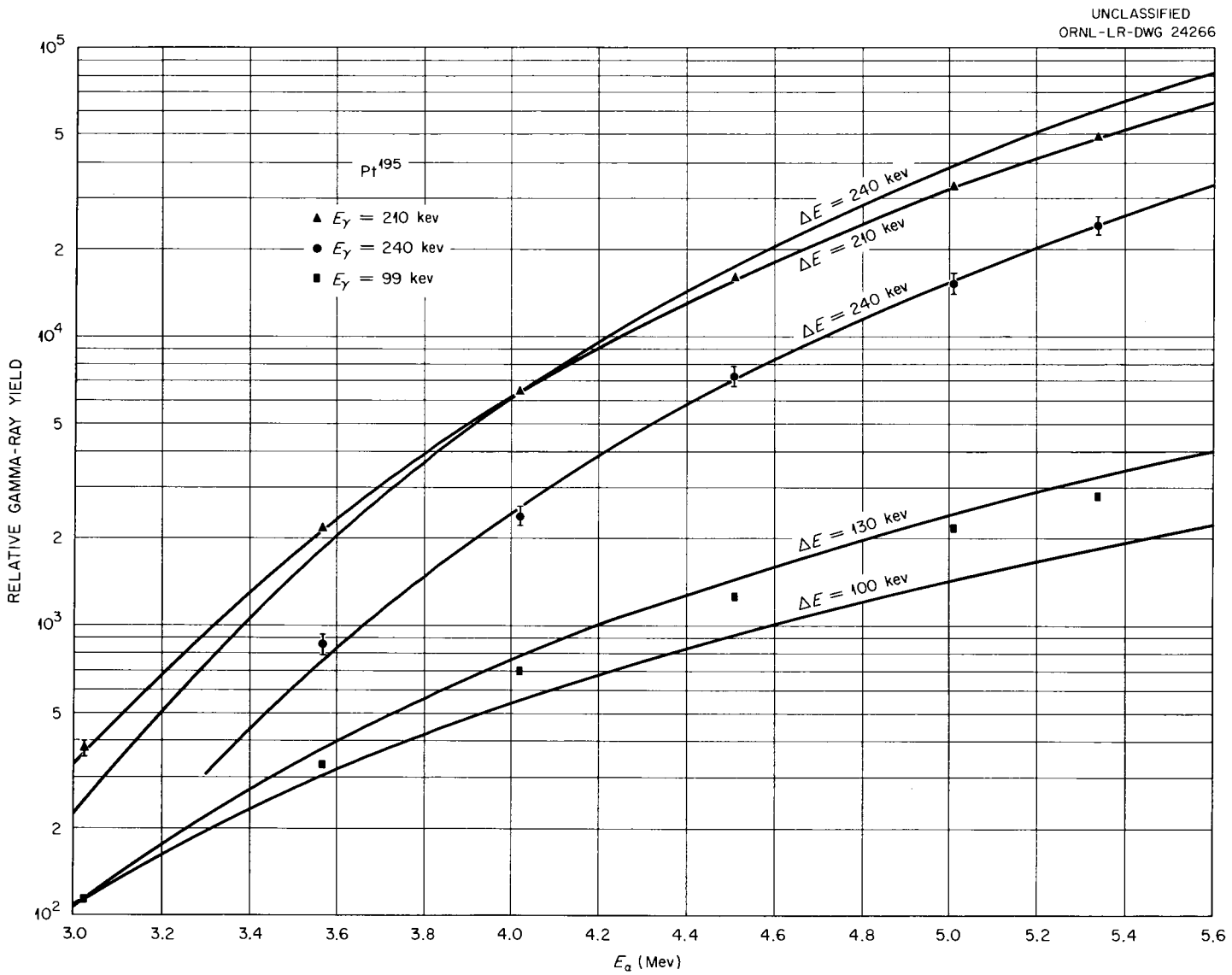


**Fig. 4. Relative Gamma-Ray Yields as a Function of $E_\alpha$.** The solid curves are the predicted energy dependence of the yields for various excitation energies $\Delta E$ above the ground state of $Pt^{195}$.

Table 1. Yield of Gamma Rays from Coulomb Excitation of States in $Pt^{195}$

| $E_\gamma$ (kev) | $E_\alpha$ (Mev) | Yield of Gamma Rays per Microcoulomb |
|---|---|---|
| 240 | 3.565 | $(8.94 \pm 0.90) \times 10^2$ |
| | 4.022 | $(2.48 \pm 0.17) \times 10^3$ |
| | 4.512 | $(7.67 \pm 0.62) \times 10^3$ |
| | 5.008 | $(1.59 \pm 0.13) \times 10^4$ |
| | 5.341 | $(2.57 \pm 0.16) \times 10^4$ |
| 210 | 3.026 | $(4.29 \pm 0.60) \times 10^2$ |
| | 3.565 | $(2.44 \pm 0.17) \times 10^3$ |
| | 4.022 | $(7.73 \pm 0.46) \times 10^3$ |
| | 4.512 | $(1.87 \pm 0.09) \times 10^4$ |
| | 5.008 | $(3.87 \pm 0.20) \times 10^4$ |
| | 5.341 | $(5.81 \pm 0.29) \times 10^4$ |
| 140 and 130 | 3.565 | $(1.02 \pm 0.15) \times 10^3$ |
| | 4.022 | $(2.39 \pm 0.36) \times 10^3$ |
| | 4.512 | $(5.20 \pm 1.04) \times 10^3$ |
| | 5.008 | $(1.06 \pm 0.25) \times 10^4$ |
| | 5.341 | $(1.68 \pm 0.42) \times 10^4$ |
| 140 | 3.565 | $(3.02 \pm 0.33) \times 10^2$ |
| | 4.022 | $(8.64 \pm 0.94) \times 10^2$ |
| | 4.512 | $(2.59 \pm 0.28) \times 10^3$ |
| | 5.008 | $(5.28 \pm 0.58) \times 10^3$ |
| | 5.341 | $(7.85 \pm 0.86) \times 10^3$ |
| 99 | 3.026 | $(1.66 \pm 0.10) \times 10^3$ |
| | 3.565 | $(5.00 \pm 0.30) \times 10^3$ |
| | 4.022 | $(1.06 \pm 0.06) \times 10^4$ |
| | 4.512 | $(1.94 \pm 0.12) \times 10^4$ |
| | 5.008 | $(3.06 \pm 0.18) \times 10^4$ |
| | 5.341 | $(4.01 \pm 0.24) \times 10^4$ |

is removed from the total yield of 99-kev gamma rays (shown in Fig. 4), the energy dependence of the 99-kev gamma ray deviates even more from the prediction for $\Delta E = 130$ kev.

The angular distributions of the 240- and 210-kev gamma rays have been measured with respect to the incident ion beam on a thick target of $Pt^{195}$ at $E_p = 2.4$, 2.7, and 3 Mev and $E_\alpha = 4.96$ Mev. The measured distributions agree with an assignment of $5/2(E2)1/2$ for the 240-kev transition and $3/2(E2 + M1)1/2$ with $(E2/M1)^{1/2} = -(6.5 \pm 0.5)$ or $0.375 \pm 0.015$ for the 210-kev transition. Only the latter value for the ratio $(E2/M1)^{1/2}$ is consistent with the $K/L = 6$ measured by Bernstein and Lewis.[4] The angular distribution of the 140-kev gamma is peaked at 90 deg with respect to the ion beam, which is consistent with a transition assignment of $5/2(E2 + M1)3/2$ and predominately $M1$ radiation. The 130-kev gamma-ray distribution is peaked at 0 deg, which is consistent with a transition assignment of $5/2(E2)1/2$. At $E_\alpha = 4.08$ Mev the observed angular distribution of the 99-kev gamma radiation was found to be

$$W(\theta) = 1 - (0.142 \pm 0.006)\, P_2(\cos\theta) ,$$

which yields $(A_2)_{\gamma\gamma} = -(0.195 \pm 0.008)$. Since this distribution is a composite resulting from excitation of states at 240, 130, and 99 kev, no attempt has been made to interpret the observed coefficient $(A_2)_{\gamma\gamma}$. The measured $K$-shell internal coefficient mentioned above for the 99-kev transition agrees with the prediction for an $M1$ transition ($\beta_1^K = 5.65$ by Sliv). Since the ground-state spin of $Pt^{195}$ is 1/2, $E2$ excitation of a state at 99 kev and decay of the state predominately by $M1$ radiation uniquely assign a spin of 3/2 to this state.

A summary of quantities obtained from $B(E2)_{exc}$ of states in $Pt^{195}$ is given in Table 2, and a level diagram of transitions observed from coulomb excitation of $Pt^{195}$ is shown in Fig. 5. The ratio of cascade/crossover for the decay of the 130-kev state was taken from the work by de-Shalit *et al.*[2]

**Table 2. Summary of Quantities Obtained from $B(E2)_{exc}$ of States in $Pt^{195}$**

| $E_\gamma$ (kev) | $B(E2)_{exc} \times 10^{49}$ ($cm^4$) | Transition | $B(E2)_d \times 10^{49}$ ($cm^4$) | Cascade / Crossover | $(E2/M1)^{1/2}$ | $\alpha_T$ | $T_{1/2}$ (sec) | $B(M1)_d$ | $B(E2)_d / B(E2)_{sp}$ |
|---|---|---|---|---|---|---|---|---|---|
| 240 | 3.72 ± 0.40 | 5/2 → 1/2 | 1.24 | 1.0 | ∞ | 0.197 | $2.39 \times 10^{-10}$ | | 18 |
| 140 | | 5/2 → 3/2 | | | ~0 | 2.55 | | $0.85 \times 10^{-2}$ | |
| 210 | 4.28 ± 0.34 | 3/2 → 1/2 | 2.14 | ~0 | 0.375 ± 0.015 | 0.77 | $4.49 \times 10^{-11}$ | $4.7 \times 10^{-2}$ | 32 |
| 130 | 3.0 ± 0.7 | (5/2 → 1/2) | 1.0 | ~9 | (∞) | 1.64 | $5.8 \times 10^{-10}$ | | 15 |
| 31 | | (5/2 → 3/2) | | | (~0) | 47 | | $4.3 \times 10^{-2}$ | |
| 99 | 1.83 ± 0.36 | 3/2 → 1/2 | 0.92 | | (~0) | 6.86 | | | 14 |

UNCLASSIFIED
ORNL-LR-DWG 24267

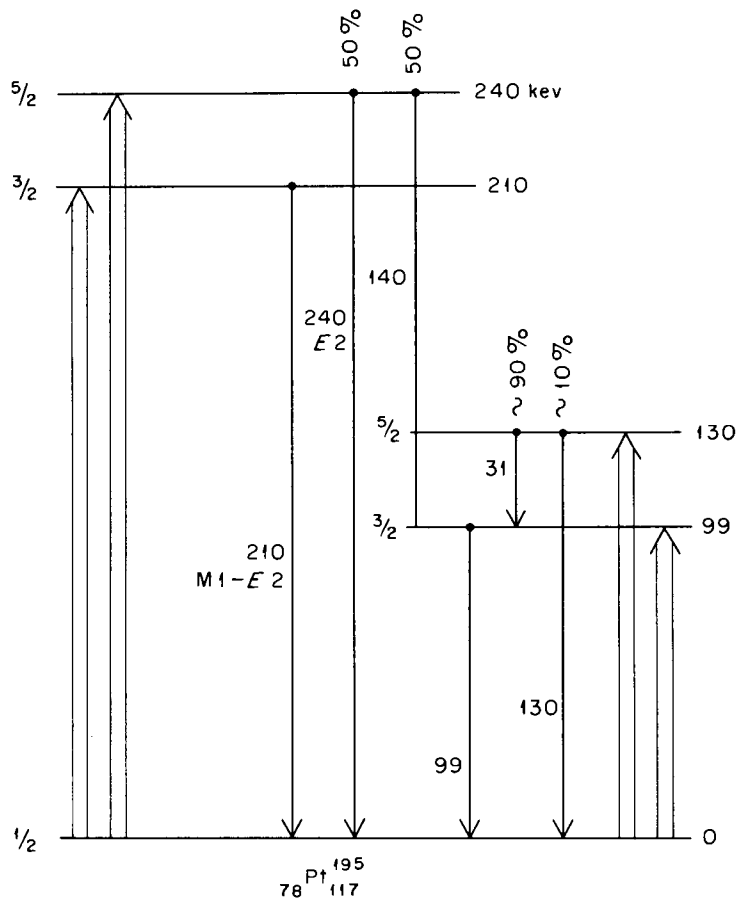


**Fig. 5. Energy-Level Diagram of Transitions Observed from Coulomb Excitation of $Pt^{195}$.**

# COULOMB EXCITATION OF THE SECOND $2^+$ STATE IN EVEN-EVEN MEDIUM-WEIGHT NUCLEI

P. H. Stelson F. K. McGowan

Coulomb excitation measurements have shown that for even-even medium-weight nuclei the $E2$ transition rates for the decay of the first $2^+$ state to the ground state are 10 to 60 times the Weisskopf independent-particle estimate. This information, together with the recognition of systematic trends in the ratio of level positions, spins of second excited states, and relative transition rates, has led to the proposal that these excited states result from a collection motion which generates "near harmonic" spectra.[1] This model predicts that at roughly twice the excitation energy of the first $2^+$ state there should be a close-lying triplet of states of the type $0^+$, $2^+$, and $4^+$. Almost no information is available on the existence of these triplets. However, this lack of information does not contradict the model, because most of our knowledge is based on the excitation of these states by beta decay, with its concomitant strong selection rules. Furthermore, if, in a given case, beta decay did appreciably excite a second member of the triplet, this fact might have been missed because of the limited experimental resolution.

The vibrational model predicts that the reduced $E2$ transition probability from the second $2^+$ state to the first $2^+$ state should be twice as large as that for the decay of the first $2^+$ state to the ground state. It is also predicted that the crossover $E2$ from the second $2^+$ state to the ground state is forbidden. The available information on the relative transition rates supports these predictions. For the medium-weight nuclei there are no absolute determinations of these transition rates.[2]

One expects that the direct coulomb excitation of the second $2^+$ state is quite weak, both because the cross section decreases rapidly with increasing excitation energy and because the cross section depends directly on the $E2$ matrix element, which is expected to be small. We have not been able to obtain evidence for the excitation of these states by the examination of gamma-ray spectra. However, by making a coincidence measurement on the cascade gamma rays, one can achieve a considerable increase in sensitivity. We wish to report measurements which give the positions of higher $2^+$ states for ten medium-weight nuclei.

A diagram of the experimental arrangement is given in Fig. 1. Targets of enriched isotopes were mounted on 5-mil nickel backings. The two gamma-ray detectors were 3 × 3 in. NaI(Tl) cylindrical crystals. The crystals were beveled to achieve larger solid angles. The distance from the source of gamma rays to the front face of the crystal was 4 cm. The tapered lead shield was placed between the crystals to reduce background coincidences resulting from Compton scattering of gamma rays from one crystal to the other. Doubly ionized helium ions of 8, 9, and 10 Mev accelerated by the 5.5-Mv Van de Graaff were used to produce coulomb excitation. A fast-slow coincidence circuit was used which had a resolving time, $2\tau$, of 0.12 $\mu$sec. Pulses

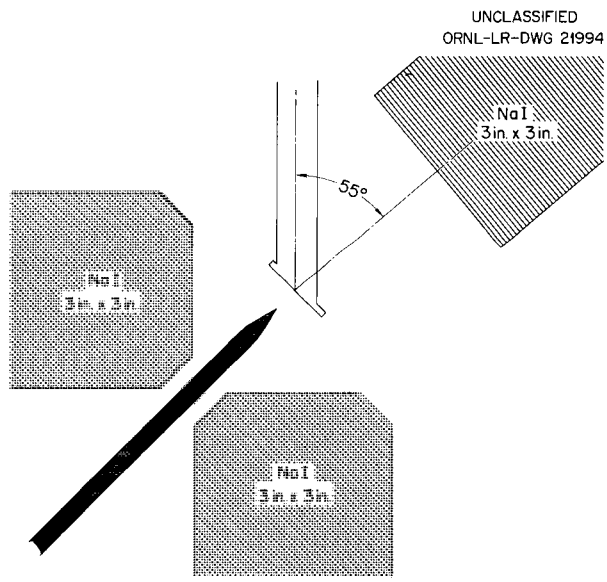


**Fig. 1. Schematic Diagram of Experimental Arrangement.** The 3 × 3 in. NaI crystal detector located in the upper right corner of the diagram was not used in this experiment.

[1] G. Scharff-Goldhaber and J. Weneser, *Phys. Rev.* 98, 212 (1955).

[2] Absolute determinations have been made for the heavy nucleus $Pt^{194}$. See F. K. McGowan and P. H. Stelson, *Phys. Rev.* 106, 522 (1957).

from the detector located at 0 deg to the beam were fed into a single-channel analyzer whose window was placed on the full energy peak of the gamma ray resulting from excitation of the first $2^+$ state. The coincidence spectrum from the detector located at 90 deg to the beam was displayed on a 20-channel pulse-height analyzer.

Figures 2 and 3 show examples of coincidence spectra observed. The large peak at 358 kev in the $Ru^{104}$ spectrum is the result of chance coincidences. The 535-kev peak represents the upper cascade gamma ray. The small peak on the low-energy side of the 535-kev peak is believed to result from annihilation gamma rays from $\beta^+$ activities generated in the impurities of the target. The $Cd^{114}$ spectrum, shown in Fig. 3, represents an exceptional case in which two gamma rays with energies of 645 and 808 kev are found to be in coincidence with the 555-kev transitions.

A summary of the results of these measurements is given in Table 1. The term $E_1$ is the energy of the first $2^+$ state, and $E_2$ is the energy of the upper cascade gamma ray. Consequently, $E_1 + E_2$ is the energy of the upper $2^+$ state. The $B(E2)_{exc}$ is the reduced electric quadrupole transition probability for excitation of the upper $2^+$ state. The last column gives the ratio of the observed crossover $B(E2)_d$ to that for an independent-particle transition $B(E2)_{sp}$.

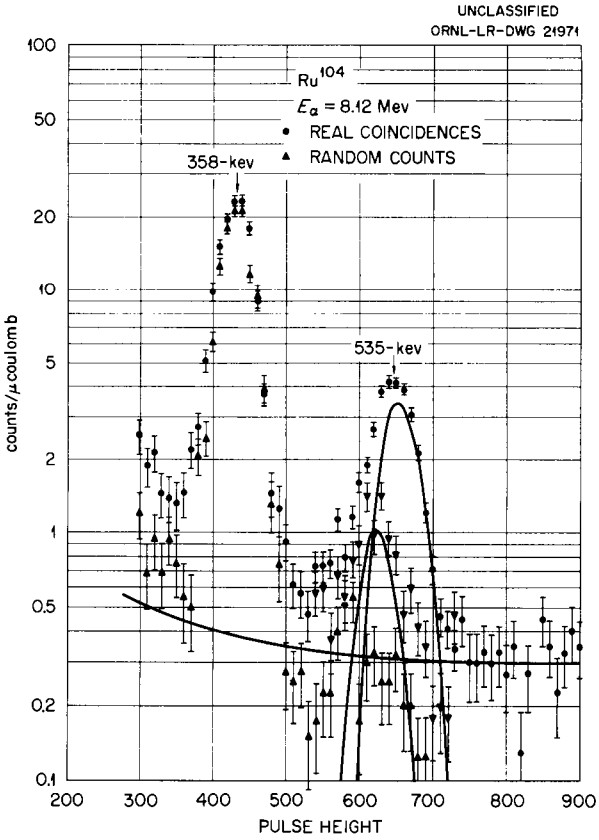


Fig. 2. Coincidence Spectrum for $Ru^{104}$.

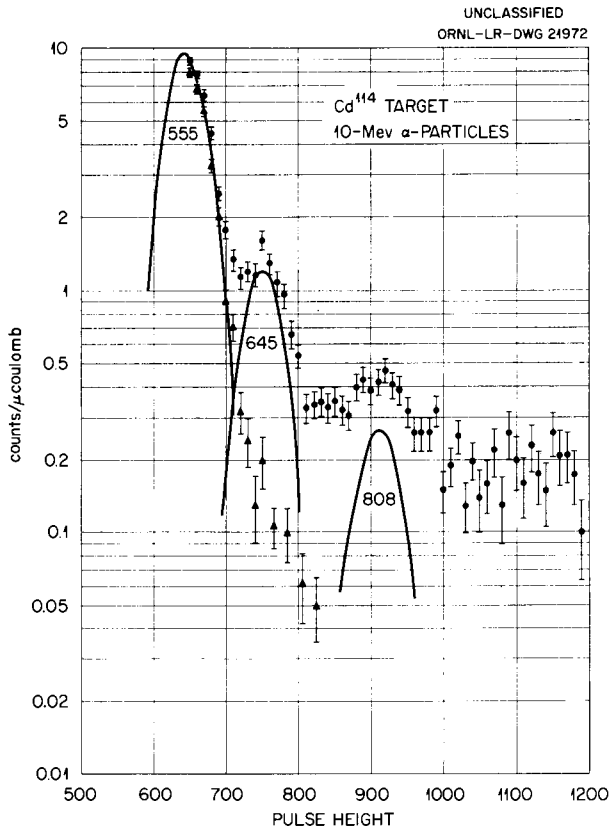


Fig. 3. Coincidence Spectrum for $Cd^{114}$.

There is no other information on the second $2^+$ state for most of the nuclei investigated. Since we cannot measure the intensity of the crossover transition, the ratio of cascades/crossover is not known for most of these states. This ratio is needed to determine the $B(E2)_d$ for the cascade and the crossover transitions. Where this is not known, the $B(E2)_{exc}$ listed in Table 1 for the crossover transition is based on the assumption that the ratio cascades/crossover is very large. Judging from known cases, this assumption should not introduce a large error in the $B(E2)_{exc}$ for the crossover transition. By excluding this source of uncertainty, it is believed that the $B(E2)_{exc}$ are accurate to ±20%.

Table 1. Summary of Information Obtained from Coulomb Excitation of Second $2^+$ States in Even-Even Nuclei

| Nucleus | $E_1$ (kev) | $E_2$ (kev) | $(E_1+E_2)/E_1$ | $B(E2)_{exc}$ (cm$^4$) | $B(E2)_d/B(E2)_{sp}$ |
|---|---|---|---|---|---|
| | | | | $\times 10^{-50}$ | |
| $Ru^{100}$ | 540 | 815 | 2.51 | 1.45 | 1.00 |
| $Ru^{102}$ | 475 | 625 | 2.31 | 1.12 | 0.77 |
| $Ru^{104}$ | 358 | 535 | 2.49 | 1.25 | 0.83 |
| $Pd^{106}$ | 513 | 607 | 2.18 | 1.09 | 0.73 |
| $Pd^{108}$ | 433 | 508 | 2.17 | 0.71 | 0.46 |
| $Pd^{110}$ | 374 | 438 | 2.17 | 0.87 | 0.56 |
| $Cd^{110}$ | 656 | 820 | 2.25 | 1.38 | 0.88 |
| $Cd^{112}$ | 610 | 685 | 2.12 | 0.82 | 0.51 |
| $Cd^{114}$ | 555 | 645 | 2.16 | 1.25 | 0.76 |
| $Cd^{114}$ | | 808 | | 1.10 | 0.67 |
| $Cd^{116}$ | 517 | 700 | 2.35 | 1.30 | 0.77 |

Additional information is available on the higher levels of $Cd^{114}$ and $Pd^{106}$. These level schemes are given in Fig. 4. From the study of the gamma rays following neutron capture in $Cd^{113}$, Motz[3] was able to establish the positions and branching ratios of states in $Cd^{114}$. The state at 1286 kev is also excited by the decay of $In^{114}$, and gamma-gamma angular correlation measurements have established the spin as 4. Our values for the positions of $2^+$ states at 1200 and 1363 kev agree with those determined by Motz. Using his branching ratios we are able to determine the values for $B(E2)_d$ for the upper cascade transitions on the assumption that these are pure $E2$ transitions. The ratio of these $B(E2)_d$ to those for an independent particle are given in Fig. 4.

The beta decay of $Rh^{106}$ excites a state in $Pd^{106}$ at 1137 kev. Gamma-gamma angular correlations have shown that the spin of this state is 0. We find a $2^+$ state at 1120 ± 8 kev.

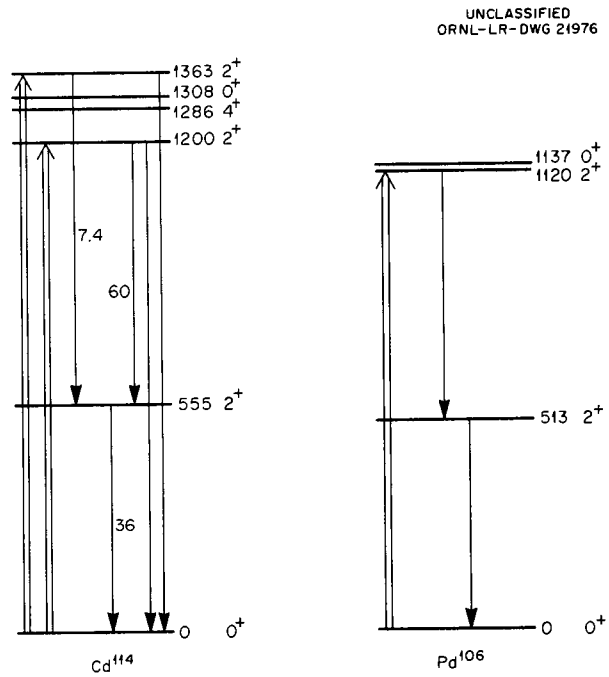


Fig. 4. Level Diagrams for $Cd^{114}$ and $Pd^{106}$.

[3] H. T. Motz, *Phys. Rev.* 104, 1353 (1956).

## DECAY OF $Nb^{90}$

N. H. Lazar
G. D. O'Kelley[1]
L. M. Langer[2]
W. G. Smith[2]

The levels in $Zr^{90}$ are expected to show independent-particle characteristics, since the nucleus contains 50 neutrons and 40 protons. Thus a study of the gamma rays following the decay of $Nb^{90}$ was undertaken and was followed, in the summer of this year, by a study of the electron spectrum, with the assistance of the group at Indiana University and their 40-cm radius, shaped-field, high-resolution magnetic spectrometer.

Sources were prepared by irradiation of enriched $Zr^{90}$ (98%) with protons in the ORNL 86-in. cyclotron. After chemical purification, pulse-height spectra were obtained with the 3-in.-dia, 3-in.-high NaI(Tl) scintillation spectrometer (Fig. 1). Analysis was carried out by fitting the known associated Compton distribution to the peak height for each gamma ray. These distributions were determined from sources with only one or two gamma rays which had been measured under the same conditions. The intensities of the gamma rays could be obtained from the area in the full energy peak, using the peak efficiency determined previously for these crystals. The energy and the intensity of each of the gamma rays determined in this manner are given in Table 1.

In addition, coincidence experiments were carried out with two 3-in.-dia, 3-in.-high scintillation spectrometers. Coincidence rates were obtained with all the major peaks, and several other gamma rays could be identified and their intensities determined. In Table 1 we also list these gamma rays. For example, it may be noted that two gamma rays of nearly the same energy (0.14 Mev, 1.1 Mev) were observed in some cases but were identified as separate transitions from a consideration of the relative intensities in the single-crystal spectrum, as compared with the coincidence results. Although a good deal of effort and time was spent in the analysis of the various coincidence experiments, the technique has been described previously,[3] and the results may most concisely be expressed in terms of the decay scheme of $Nb^{90}$ given in Fig. 2.

To determine the spins and parities of the various levels, the conversion coefficients and *K/L* conversion ratios were determined. For this purpose, samples of purified $Nb^{90}$ were

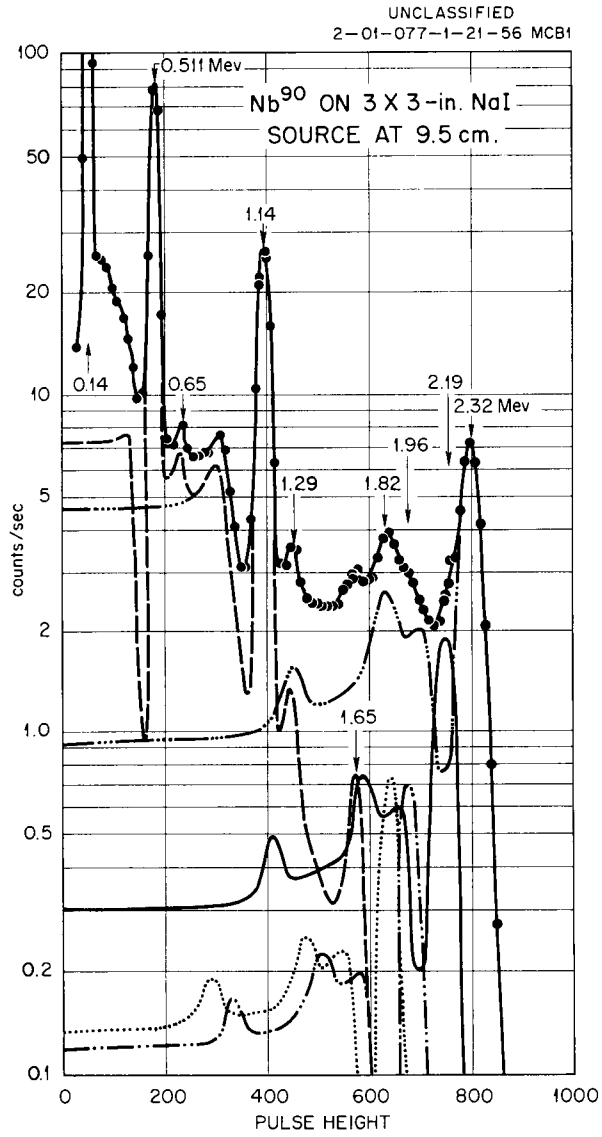


**Fig. 1. Gamma Rays from Decay of $Nb^{90}$ on 3-in.-high, 3-in.-dia NaI(Tl) Crystal.**

[1]Chemistry Division.

[2]Indiana University, Bloomington.

[3]N. H. Lazar and E. D. Klema, *Phys. Rev.* 98, 710 (1955).

Table 1. Energies and Intensities of Gamma Rays in Decay of $Nb^{90}$

| $E_\gamma$ | $I_\gamma$ | $\alpha_K$ Experimental | $\alpha_K$ Theoretical | Observed $K/L$ Ratio | Multipole Radiation | Multipole Assignment |
|---|---|---|---|---|---|---|
| 2.32 | 0.79 | $4.03 \times 10^{-4}$ | $4.10 \times 10^{-4}$ | | $E5$ | $E5$ |
| 2.19 | 0.13 | | | | | |
| 2.00 | 0.010* | | | | | |
| 1.85 | 0.013* | | | | | |
| 1.60 | 0.032* | | | | | |
| 1.48 | Weak* | | | | | |
| 1.27 | 0.032* | | | | | |
| 1.13 | 0.95 | $1.83 \times 10^{-4}$ | $2.0 \times 10^{-4}$ | | $E1$ | $E1$ |
| 1.1 | 0.018* | | | | | |
| 0.89 | 0.012* | | | | | |
| 0.372 | 0.012* | $1.35 \times 10^{-2}$ | $0.93 \times 10^{-2}$<br>$3.85 \times 10^{-2}$ | 5.6 | $E2$<br>$M3$ | $E2 + 0.13M3$ |
| 0.43 | $1.2 \times 10^{-4}$** | | | | | |
| 0.142 | 0.570 | 0.297 | 0.293 | 6.5 | $E2$ | |
| 0.133 | 0.028* | 2.91 | 2.20<br>33.5 | 3.5 | $E3$<br>$M4$ | $E3 + 0.025M4$ |
| 1.75 | None observed | $e^-/\beta^+ = 1.09 \times 10^{-4}$ | | 3.8<br>4.5<br>5.5 | | $E0$ |

*Denotes intensity determined from analysis of coincidence results.

**Assume $(K/L)_{1.75} = 4.0$ and $(e^-/\pi)_{1.75} = 2.6$.

transported to Indiana University, and electron and positron spectra were obtained with the magnetic spectrometer. The $K$ and $L$ internal-conversion lines were observed for gamma rays at 0.132 and 0.142 Mev, confirming the interpretation of the coincidence results of a doublet at 0.14 Mev. In addition, the $K$ and $L$ internal-conversion lines were obtained for 0.372-, 1.13-, and 1.75-Mev transitions. Finally, a weak conversion peak (intrepreted as a $K$-conversion line) was observed at an energy consistent with a gamma ray at 2.32 Mev. Now, since all these gamma rays (except the 1.75-Mev transition) were observed with the scintillation spectrometer and their intensities were known relative to the positron intensity, and since these conversion-line intensities were also determined relative to the positron spectrum, $K$ internal-conversion coefficients, $\alpha_K(\gamma)$, could be experimentally determined with fairly high precision. Table 1 lists these results and the theoretical values in best agreement as determined from interpolation of Rose's tables.[4] Since assignments could be made as to multipolarity, the spins of most of the levels could also be defined.

The conversion lines observed at 1.75 Mev are interpreted as the 0+ to 0+ transition previously identified[5] in $Zr^{90}$ in the decay of $Y^{90}$. For such a transition the expected ratio of $K$ conversion to $L$ conversion is 9.0. The best source yielded a $K/L$ conversion ratio of 3.8,

[4] M. E. Rose, *Tables of Conversion Coefficients*, privately distributed.

[5] O. E. Johnson, R. G. Johnson, and L. M. Langer, *Phys. Rev.* 98, 1517 (1955).

UNCLASSIFIED
2-01-077 DS90

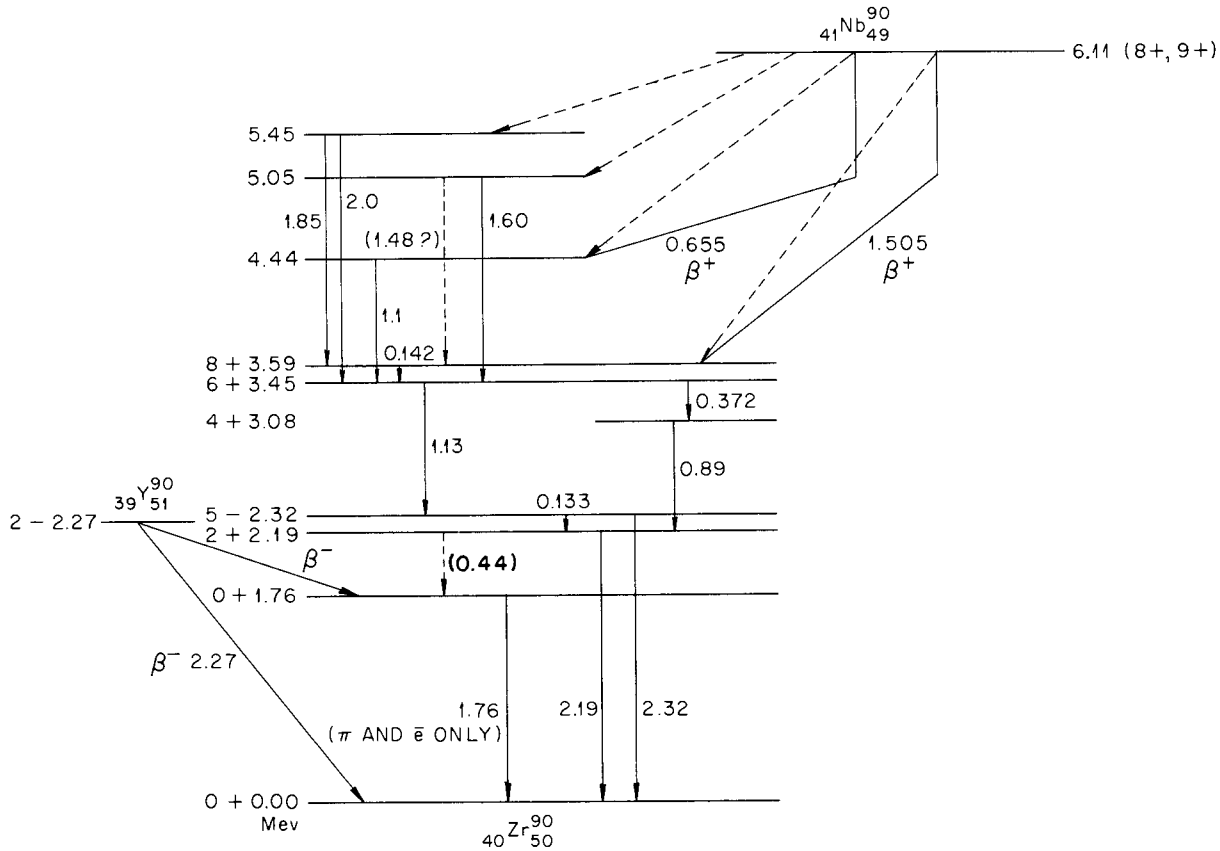


**Fig. 2. Decay Scheme of $Nb^{90}$ and Level Structure of $Zr^{90}$.**

while the other sources gave values of 4.5 and 5.5. Both these latter sources also showed poorer resolution – probably because the $Nb^{90}$ appeared to wet the Zapon films enough to flow outside the insulin line previously inscribed on the film – and hence are not to be regarded as reliable as the first run with a good source. This anomalous $K/L$ ratio is, as yet, not understood. The lifetime for this state has been measured by Day[6] and is found to be anomalously long. The transition thus shows evidence of being hindered by a selection rule on the orbital angular momentum, and this may be the cause for the anomalous $K/L$ ratio as well. This may be a theoretical point well worth investigating further in view of Weneser and Church's theory[7] of $E0$ transitions.

The conversion coefficient of the 2.32-Mev transition is consistent with an assignment of $E5$ radiation. Previously, Campbell *et al.*[8] identified an isomer with a half life of 0.8 sec in $Zr^{90}$ produced in $(n,n')$ reactions. The isomer decays with the emission of a 2.32-Mev gamma ray, in agreement with the present results.

The 0.133-Mev transition appears to be a mixture of $E3$ and $M4$ radiation, with $M4/E3 = 0.025$.

[6]R. B. Day, private communication.

[7]E. L. Church and J. Weneser, *Phys. Rev.* 103, 1035 (1956).

[8]E. C. Campbell *et al.*, *Phys. Rev.* 98, 1172 (1955).

This is consistent with both $\alpha_K$ and the $K/L$ conversion ratio. The apparent hindrance of the $E3$ transition is expected to be interpretable in terms of an orbital angular-momentum selection rule operating because of the particle configurations of the 2.19- and 2.32-Mev states.

The 0.142-Mev transition is essentially pure $E2$ radiation. It is interesting that the conversion coefficient could be determined from the gamma-ray intensity in coincidence with the 1.13-Mev gamma ray, as well as from a direction comparison of $e^-/\beta^+$ and $I/\beta^+$. These determinations are in good agreement.

As was mentioned above, $Zr^{90}$ has 40 protons and 50 neutrons in the nucleus. If the last two protons couple to give the observed structure, the ground-state configuration, from the simplest point of view, is expected to be $(p_{1/2})^2_{0+}$, and the next most probable pure states are $(p_{1/2} - g_{9/2})_{5-\text{ or }4-}$ and $(g_{9/2})_{0+,\,2+,\,4+,\,6+,\text{ or }8+}$. One may calculate the splitting[9] of the $(g_{9/2})^2$ configuration, assuming only a $\delta$-function interaction between the protons, and the results are given in Table 2. It is clear that, qualitatively, the results reproduce the experimental ordering, if the states are interpreted as shown, but that the quantitative spacings are not reproduced. This is not unexpected because (1) the $\delta$-function interaction is probably only a fair approximation for such low $Z$, and (2) the states cannot be pure configurations. This last statement may be understood in terms of the predicted relative intensities of some of the gamma rays. In particular, consider the 1.13- and the 0.372-Mev transitions. Since the angular momentum and parity of the 1.13-Mev radiation is 1−, while that for the 0.372-Mev radiation is 2+, their relative intensities would be expected to be

$$I(0.372):I(1.13) = 1.5 \times 10^{-7} .$$

The observed intensity is $1.7 \times 10^{-2}$, indicating a hindrance of the 1.13-Mev transition of at least $9 \times 10^4$. By referring to the orbital assignment for the pure states involved, it is clear that a proton must make a jump from a $g_{9/2}$ to a $p_{1/2}$ orbital in the transition. Since this involves $\Delta j = 4$, the $E1$ transition would be absolutely forbidden for pure configurations. The 0.372-Mev transition, on the other hand, merely involves a reorientation of the two $g_{9/2}$ protons and hence should proceed normally. However, the 0.372-Mev transition is not pure $E2$, as seen from the conversion coefficient, indicating further admixtures of other states at least in the 3.45-Mev state. It is clear that a complete description of all the transition probabilities in terms of all possible configurations would be very complicated indeed.[10] However, other qualitative arguments supporting the fact that the pure configurations almost (but not quite) determine the various states may be made in terms of the relative intensities of other gamma rays such as 1.27 vs 0.142 Mev, 2.19 vs 0.49 Mev (feeding the first excited level), etc.

The states at energies greater than 4.5 Mev have not been assigned spins, although their parity is almost surely (+) because of the low $ft$ values for the electron capture branches feeding them.

[9]The method for calculating the splitting was taken from notes from a series of lectures given by A. M. Lane at ORNL in the summer of 1956. See also A. de-Shalit, *Phys. Rev.* 91, 1479 (1953). The author is indebted to Dr. Lane for several interesting conversations on this subject.

**Table 2. Theoretical and Experimental Energy Splittings of Levels in $Zr^{90}$, Assuming o $(g_{9/2})^2$ Configuration for the Last Two Protons and a $\delta$-Function Interaction Between the Particles**

| Energy Levels | Experimental (Mev) | Theoretical (Mev) |
|---|---|---|
| $E(8+) - E(6+)$ | 0.142 | 0.142* |
| $E(8+) - E(4+)$ | 0.517 | 0.355 |
| $E(8+) - E(2+)$ | 1.40 | 0.854 |
| $E(8+) - E(0+)$ | 1.84 | 3.96 |

*Theory normalized to $E(8+) - E(6+)$.

[10]R. K. Sheline, Florida State University, hos also worked with this nucleus and obtained similar results. He is attempting to interpret the results in terms of mixtures of configurations for several of the levels (private communication).

## LEVEL STRUCTURE OF $N^{14}$ FROM $C^{13}$ + $p$ REACTIONS

J. K. Bair H. O. Cohn H. B. Willard

Yield curves for the reaction $C^{13}(p,p'\gamma)C^{13}$ have previously been given[1] in preliminary form. The yield of the reaction $C^{13}(p,n)N^{13}$ has been published.[2] The present work reports measurements of the angular distribution of the inelastic-scattering gamma rays, angular distributions of the neutrons, and new determinations of the proton energies at which maximums appear in the neutron yield. Experimental techniques, except where otherwise noted, are essentially those for the reactions cited.[1,2]

Angular distributions of the 3.09-Mev gamma ray were taken at 12 proton energies between 3.7 and 4.2 Mev, and of the 3.68-Mev gamma ray at 10 proton energies distributed over the 4.5-Mev resonance. The shield-detector combination[1] subtended a half angle of 7½ deg or less at the target. All the low-energy gamma-ray distributions were isotropic, and are not shown. The fact that these distributions were isotropic, independent of proton energy, can be considered as a confirmation of the previously known[3] $J = \frac{1}{2}$ spin of the 3.09-Mev state in $C^{13}$. Figure 1 shows the angular distribution of the 3.68-Mev gamma ray at the peak of the 4.5-Mev resonance. The solid curve is of the form $1 - A\cos^2\theta$, with $A = 0.35$.

[1] H. O. Cohn, J. K. Bair, and H. B. Willard, *Phys. Semiann. Prog. Rep. Sept. 10, 1956*, ORNL-2204, p 26.

[2] J. K. Bair, J. D. Kington, and H. B. Willard, *Phys. Rev.* **90**, 575 (1953).

[3] F. Ajzenberg and T. Lauritsen, *Revs. Modern Phys.* **27**, 77 (1955).

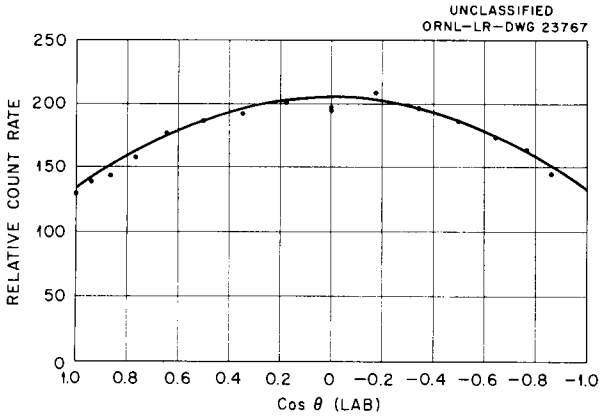


**Fig. 1. Experimental Angular Distribution of the 3.68-Mev Inelastic Gamma Ray Taken at the Peak of the 4.5-Mev Resonance.** The solid curve is a plot of $1 - 0.35\cos^2\theta$.

Since the published[2] yield curve for the $C^{13}(p,n)N^{13}$ reaction has its energy scale based, in part, on the older, incorrect energy of the $F^{19}(p,\alpha\gamma)O^{16}$ resonances now known to be located at 1347 and 1374 kev, and since the energy scale was also based on analyzing magnet current, it was felt worth while to redetermine the energies of the maximums with the better techniques[4] now available. In order to tie these measurements into the gamma-ray measurements, runs were made over the four most prominent maximums in the neutron yield curve, measuring simultaneously the 90-deg gamma-ray yield, the 0-deg neutron yield as measured with a long counter, and the 170-deg neutron yield as measured with a suitably biased propane recoil counter. Figure 2 gives the 0-deg neutron yield. Table 1 lists, in columns 1 and 2, the energies corresponding to maximums in the 3.09- and 3.68-Mev gamma rays, respectively, while column 3 estimates their width. Columns 4 and 5 give the new energies for the 0-deg neutron yield maximums and their differences from the old value.[2] The new values are, as expected, lower than the old values, and the differences are of abaut the expected magnitude. Column 6 gives the energy of the maximum of the backward neutron yield, and column 7 gives an estimate of the experimental width.

Neutron angular distributions were taken at ten proton energies between 3.5 and 4.6 Mev. These data were obtained by means of a 1 × 4 in. propane (½ atm) recoil counter at a distance of about 3 in. from the target to the front face of the counter. Figure 2 shows a curve of the yield of neutrons in the forward direction and the neutron angular distributions (as a function of the cosine of the center-of-mass angle $\phi$). The arrows indicate the proton energy at which the distribution was measured. The open points on the distribution at 3.98 Mev were taken some years ago with the long counter used as the detector. The open points on the distributions at 4.30 and 4.51 Mev were taken with the propane recoil counter but in a somewhat different experimental arrangement.

[4] J. D. Kington *et al.*, *Phys. Rev.* **99**, 1393 (1955).

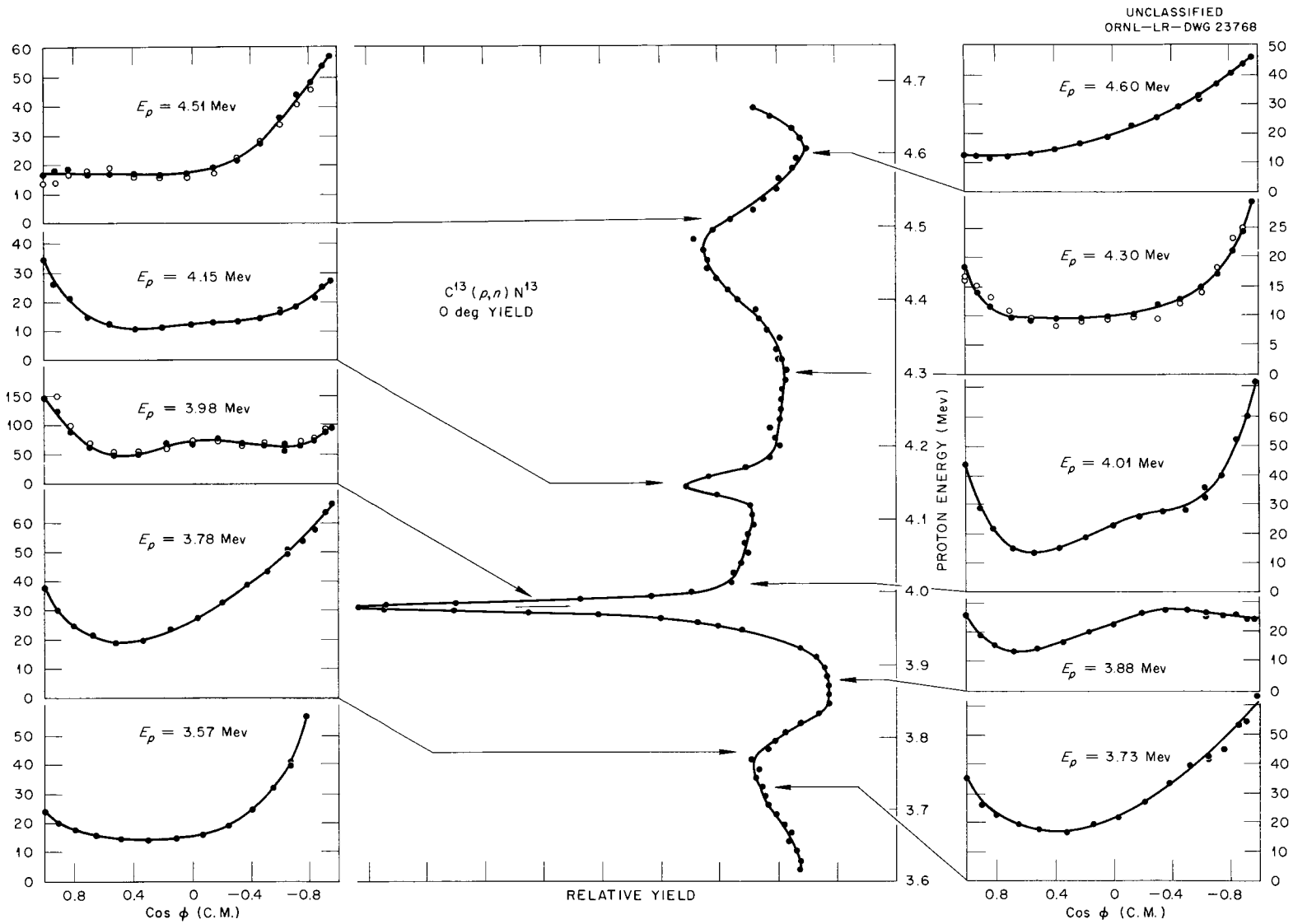


**Fig. 2. A Section of the $C^{13}(p,n)N^{13}$ 0-deg Yield Curve. The inserts are the angular distributions taken at the proton energies indicated by the arrows.**

Table 1. Parameters for the Levels of $N^{14}$

| $E_p$ (Mev) For 3.09-Mev Gammas | $E_p$ (Mev) For 3.68-Mev Gammas | $W_{1/2}$ (kev) | $E_p$ (Mev) for 0-deg Neutrons | $\Delta E$ (kev) | $E_p$ (Mev) for "180-deg" Neutrons | $W_{1/2}$ (kev) |
|---|---|---|---|---|---|---|
| 3.80 | | 100 | 3.77 | 9 | 3.79 | 100 |
| | | | 3.98 | 26 | 3.99 | 15 |
| 4.1 | | 150 | 4.1 | | 4.1 | 150 |
| 4.14 | | | 4.15 | 31 | 4.13 | 30 |
| | 4.52 | 150 | 4.47 | 52 | 4.51 | 150 |

## PROTON STRENGTH FUNCTIONS FROM $(p,n)$ CROSS SECTIONS

C. H. Johnson A. Galonsky J. P. Ulrich

The $(p,n)$ cross sections for 12 intermediate nuclei with $37 \leq A \leq 93$ were previously reported[1] for proton energies from threshold to about 500 kev above threshold. It was shown that the gross variations in cross section (a factor of $5 \times 10^7$ from $Nb^{93}$ to $Cl^{37}$) could be attributed to the effect which the coulomb barrier has on the cross section for formation of the compound nucleus. This cross section was written as

$$\sigma_c = \sum_l \sigma_c^l = \pi \lambda\!\!\!^{-2} \sum_l (2l + 1)\, T_l(p) \ ,$$

where $T_l(p)$ is a proton penetration factor. Curves of $\sigma_c$ were presented for a totally absorbing square-well model of the nucleus. It was found that the observed average cross sections, although agreeing roughly with the theory, showed systematic deviations both in shape and in magnitude. These deviations have now been studied in detail.

The deviations in shape result from competition of neutron emission with proton and gamma-ray emission. The statistical theory of the compound nucleus[2,3] has been used to predict this competition. It is found, for example, that for reactions involving no spin change from initial to final nucleus the neutron experiences little competition; the $(p,n)$ cross section rises nearly to $\sigma_c$ within 50 kev of threshold. For reactions involving spin change of two units, neutron emission is inhibited, and the $(p,n)$ cross section rises slowly toward $\sigma_c$ for several hundred kev. This theory gives a good account of all the average $(p,n)$ excitation functions except those for $Ga^{71}$, $As^{75}$, and $Se^{77}$. In these cases it is possible that the parameters may be reasonably adjusted to give more competition near threshold. It is suggested, however, that the statistical assumption may be inaccurate and that direct interaction may be significant.

These $(p,n)$ cross sections were calculated from the $\sigma_c$ which is predicted by a 40-Mev totally absorbing square well with a radius of $1.45A^{1/3}$ fermis. Although these cross sections agree generally in shape with the experimental curves, they are usually too small in magnitude. Figure 1 shows the ratio of the observed cross section to the predicted value plotted as a function of the target mass numbers. Each point is an average over the range (~500 kev) of each measurement. For the three above-mentioned reactions, which show discrepancies in predicted shape, the ratio was obtained in the upper energy region, where competition is of minor importance.

[1] C. H. Johnson and A. Galonsky, *Phys. Semiann. Prog. Rep. March 10, 1957*, ORNL-2302, p 13.

[2] W. Hauser and H. Feshbach, *Phys. Rev.* 87, 366 (1952).

[3] B. Margolis, *Phys. Rev.* 88, 327 (1952).

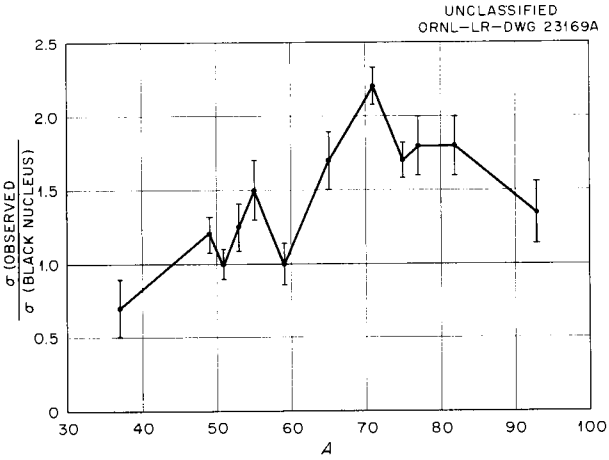


**Fig. 1. Ratio of the Observed Average $(p,n)$ Cross Section to the Black-Nucleus Cross Section for a 40-Mev Square Well and a Radius of 1.45 $A^{1/3}$ Fermis.** In each case the average proton energy is ~250 kev above threshold; the thresholds lie between 1.0 and 2.2 Mev. Vertical heights of the symbols are uncertainties estimated roughly within the framework of the statistical theory of the compound nucleus.

Figure 1 shows a systematic deviation from the black-nucleus prediction. It has been shown[4] that the complex potential model gives an improved description of very similar measurements.[5]

We have made a very approximate square-well calculation of the strength functions for $s$-, $p$-, $d$-, and $f$-wave protons, using a proton energy in the middle of our experimental range, namely, 2 Mev. The complex well depth is $V_0(1 + i\zeta) - V_c$, where $V_0$ and $\zeta$ are independent of $A$, and $V_c = 4/3\,(Z/A^{1/3})$ Mev is the radial average of the coulomb energy for a uniform charge distribution inside the well whose radius is taken as $R = 1.45A^{1/3}$ fermis. Making the coulomb potential constant inside the nucleus is a big approximation, but it does lead to a simple calculation. The choice of the radial rather than the volume average comes from consideration of the WKB solution.[4]

The well depth may now be rewritten as $V_0'(1 + i\zeta')$, where $V_0' = V_0 - V_c$, and $\zeta' = \zeta[V_0/(V_0 - V_c)]$. Since this is exactly the form of the well depth for neutrons, the neutron formulas[6] may be, and actually were, used in calculating[7] the internal logarithmic derivatives, $f_l$. It is to be noted, however, that because of the dependence on $V_c$ the well depth is changing throughout the periodic table. The strength functions computed from

$$\frac{\langle \gamma_l^2 \rangle}{D} \cong \left(\frac{R}{\pi}\right) \frac{-Imf_l}{(Imf_l - s_l)^2 + (R_e f_l - \Delta_l)^2},$$

with $V_0 = 46$ Mev and $\zeta = 0.04$, are shown in Fig. 2. Although $s_l$ is negligible, $\Delta_l$, the real part of the logarithmic derivative of the external wave function,

[4] B. Margalis and V. F. Weisskopf, *Phys. Rev.* 107, 641 (1957).

[5] J. P. Schiffer and L. L. Lee, Jr., *Phys. Rev.* 107, 640 (1957).

[6] H. Feshbach, C. E. Porter, and V. F. Weisskopf, *Phys. Rev.* 96, 448 (1954).

[7] We thank L. Dresner of this Laboratory for calculating $f_l$ on the Oracle.

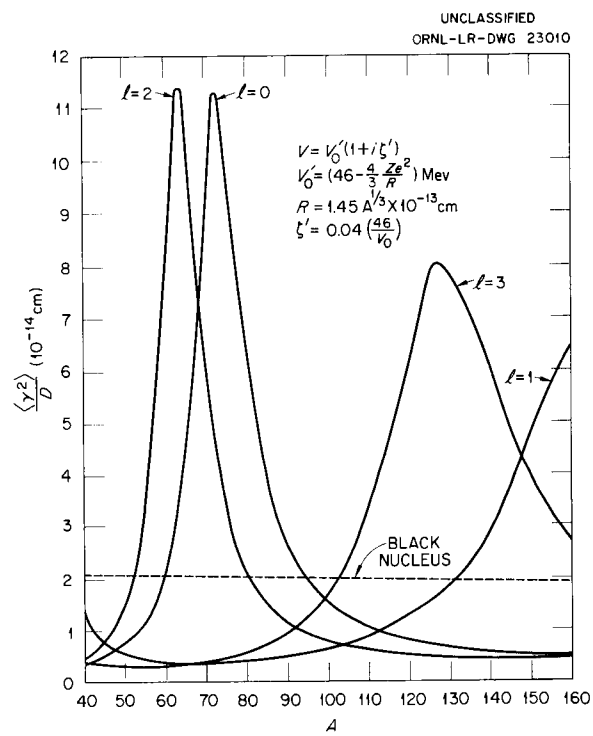


**Fig. 2. Strength Functions for 2-Mev $s$-, $p$-, $d$-, and $f$-Wave Protons vs Mass Number.** The calculations are for a complex square well of depth $[46(1 + 0.04i) - V_c]$ Mev and radius $R = 1.45A^{1/3} \times 10^{-13}$ cm; $V_c$, the coulomb potential inside the well, is approximated by a constant for each nucleus: $4Ze^2/3R$.

is very important in locating the peaks. The inclusion of $\Delta_l$ always shifts the peaks to higher mass numbers, the shift increasing with $l$ and with $A$. The $s$-wave peak in Fig. 2 was shifted up by 12 mass units, in contrast with the case of $s$-wave neutrons for which $\Delta = 0$.

The values of $V_0$ and $\zeta$ were chosen to fit the peak in Fig. 1. To see that this has been accomplished we note that at $A \sim 72$ the values of $\sigma_c^l/\sigma_c$ for a black nucleus are approximately 0.35, 0.47, and 0.16 for $s$-, $p$-, and $d$-wave protons, respectively. Multiplying these by the strength functions (divided by the black-nucleus value) in Fig. 2 at $A \sim 72$, we get

$$\frac{\sigma_c}{(\text{black-nucleus } \sigma_c)} \cong (0.35)(5.5) + (0.47)(0.19) + (0.16)(2.5) = 2.4 ,$$

in good agreement with the value of the observed peak. Since the sensitivity of the position of the calculated peak to the value of $V_0$ is ~5 mass units per Mev, it appears that the proton well (46 Mev) is significantly deeper than the neutron well (42 Mev in ref 6), and the difference is about the same as that found in studies of the bound states of nuclei in this mass region.[8]

[8] A. E. S. Green, *Phys. Rev.* **102**, 1325 (1956); *Phys. Rev.* **104**, 1617 (1956).

## THE $(p,n)$ REACTION CROSS SECTIONS FOR $Li^7$ AND $H^3$

R. L. Macklin J. H. Gibbons

A flat-response $4\pi$ neutron counter for use in the kilovolt energy range with neutrons from charged-particle reactions has been designed and constructed. It consists of a 5-ft sphere of reactor-grade graphite with $B^{10}F_3$ counters placed near the surface. Thin targets for Van de Graaff accelerated protons have been used at the center of the sphere, and the cross sections for several $(p,n)$ reactions have been measured, for incident proton energies up to 5 Mev.

The $Li^7(p,n)Be^7$ reaction (Fig. 1) has been studied carefully near threshold, where the cross section can be ascribed in detail to a broad $2^-$ level in $Be^8$. This assignment also gives agreement with the thermal-neutron $Be^7(n,p)Li^7$ cross section for the expected $\frac{1}{2}^-$ ground state of $Be^7$. The well-known resonance at 2.25 Mev is $3^+$, as in previous analyses, but for both resonances we find a good fit to the cross section (Fig. 2) only for reduced neutron widths several times the reduced proton widths.

The $H^3(p,n)$ reaction cross section (Fig. 3) follows the form prescribed by either resonance

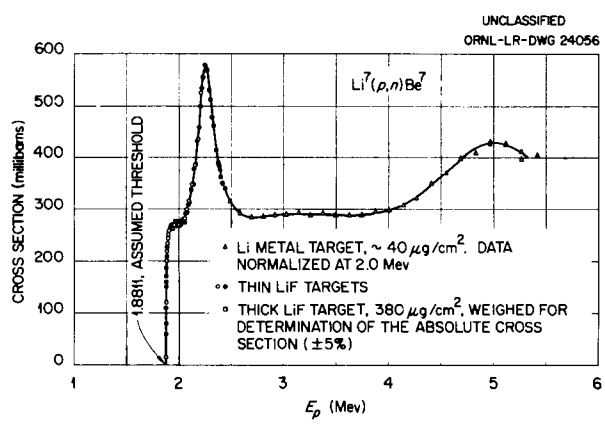


**Fig. 1. The $Li^7(p,n)Be^7$ Reaction Cross Section as a Function of Proton Energy.** Natural lithium fluoride targets were used for quantitative weighing and stability, below 2.5 Mev. At high energies a lithium metal target was used and was normalized to the LiF data at 2 Mev.

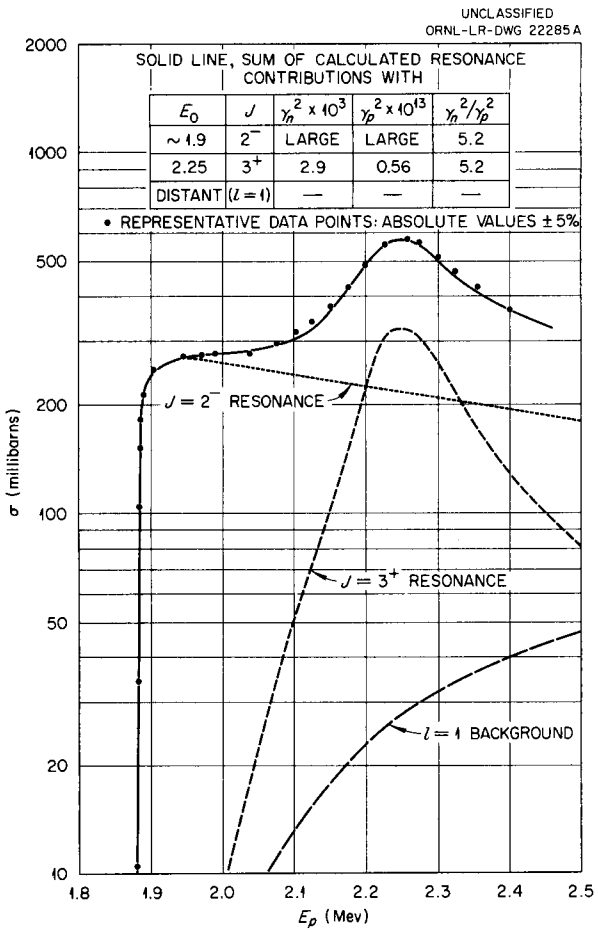


**Fig. 2. Calculated Resonance Contributions to the $Li^7(p,n)Be^7$ Reaction Cross Section as a Function of Laboratory Proton Energy.**

theory or direct interaction from 1.1 to 2.4 Mev. From threshold to 1.1 Mev the cross section is larger than that predicted, but extrapolates to the value deduced by reciprocity from the $He^3(n,p)H^3$ thermal cross section. Above 2.4 Mev the $H^3(p,n)$ cross section peaks rather sharply and has not yet been analyzed.

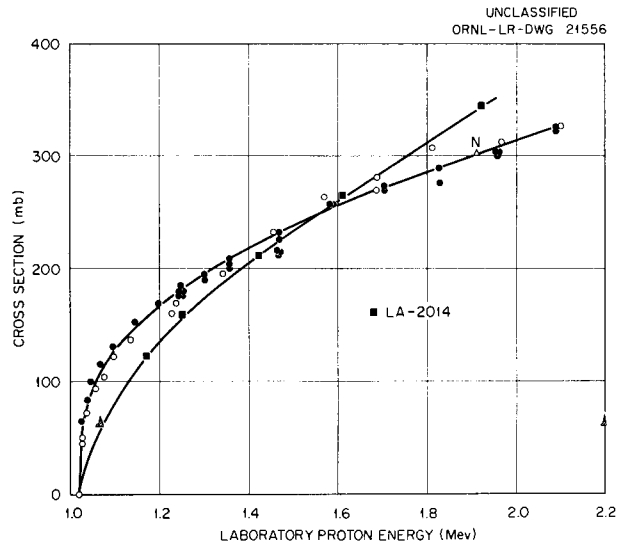


**Fig. 3. The $H^3(p,n)He^3$ Cross Section as a Function of Incident Proton Energy. Data near threshold were obtained with a thin Zr-$H^3$ target whose energy loss was measured by a neutron time-of-flight method. The Zr-$H^3$ results were normalized to the $H_2^3$ gas cell measurements at 1.9 Mev. The earlier long-counter results of Jarvis are included for comparison.**

## NEUTRON RESONANCE PARAMETERS OF $Sm^{151}$ AND $Pm^{147}$

J. A. Harvey R. C. Block G. G. Slaughter

The fast-chopper time-of-flight spectrometer at the LITR has been used to measure the total neutron cross sections of samples of fission-product samarium and promethium prepared by G. W. Parker and W. J. Martin of the Chemistry Division. The fission-product samarium sample contained only 3 mg of $Sm^{151}$, which has a 100-year half life. Several resonances were observed in the energy range from 0.2 to 20 ev. Samples enriched in $Sm^{147}$ and $Sm^{149}$ have also been measured. After corrections were made for the $Sm^{147}$ and $Sm^{149}$ contributions to the cross section of the fission-product sample, four resonances were assigned to $Sm^{151}$ in the energy range from 0.2 to 5 ev. Parameters for the resonances in $Sm^{151}$ are given below:

| $E_0$ (ev) | $\Gamma_n^0$ ($10^{-3}$ ev) |
|---|---|
| 1.10 | 0.58 ± 0.12 |
| 1.70 | 0.20 ± 0.07 |
| 2.04 | 0.34 ± 0.09 |
| 4.10 | 0.25 ± 0.08 |
| 6.30 | 1.3 ± 0.4 |

The level spacing per spin state and the $\overline{\Gamma}_n^0/D$ ratio of $Sm^{151}$ are 2.1 ± 0.8 ev and (2.2 ± 1.0) × $10^{-4}$, respectively, which are smaller than those of $Sm^{149}$ and $Sm^{147}$.

Transmission measurements have been made up to 50 ev on two samples of $Pm^{147}$ (6.8 and 27 mg). The data were corrected for the 3% $Am^{241}$ impurity and for about 8% $Sm^{147}$ which had grown in from the decay of the 2.5-year $Pm^{147}$. Parameters for the resonances assigned to $Pm^{147}$ are given below:

| $E_0$ (ev) | $\Gamma_n^0$ ($10^{-3}$ ev) |
|---|---|
| 1.04 | 0.0054 |
| 5.12 | 3.3 |
| 5.92 | 2.3 |
| 6.71 | 4.6 |
| 15.0 | 0.57 |
| 18.7 | 1.5 |
| 30.4 | 2.0 |
| 39.3 | 0.76 |
| 47.1 | 12.5 |

The level spacing per spin state and the $\overline{\Gamma}_n^0/D$ ratio based on the data up to 20 ev are 7 ± 2 ev and (3.0 ± 1.1) × $10^{-4}$, respectively.

---

## ANGULAR DISTRIBUTION OF NEUTRONS SCATTERED BY THE 2.80-kev RESONANCE IN SODIUM

R. C. Block

The angular distribution of neutrons scattered out of a filtered beam from the LITR by a thin sodium sample was measured in an effort to assign the neutron orbital angular momentum of the 2.80-kev level in sodium. The sodium scatterer was prepared by pressing clean metallic sodium between two 0.0005-in.-thick aluminum foils to a thickness of about 0.016 in. in a flat-plate hydraulic press. The aluminum foils were left in place, and their edges were sealed together to provide an airtight container for the sodium. Thin scattering samples of lead and carbon were also prepared and measured to aid in the interpretation of the data. The apparatus used is illustrated in Fig. 1. A collimated neutron beam from hole HB-1 of the LITR impinged upon the scatterer, and the scattered neutrons were detected by five detectors placed at 30, 60, 90, 120, and 150 deg with respect to the beam axis. Each counter consisted of a $BF_3$ proportional counter placed in a shielded paraffin cylinder. Various combinations of sodium and enriched $B^{10}$ filters were placed in the beam to modify the energy spectrum of the reactor beam. The counters were intercalibrated with a Po-Be source rotated

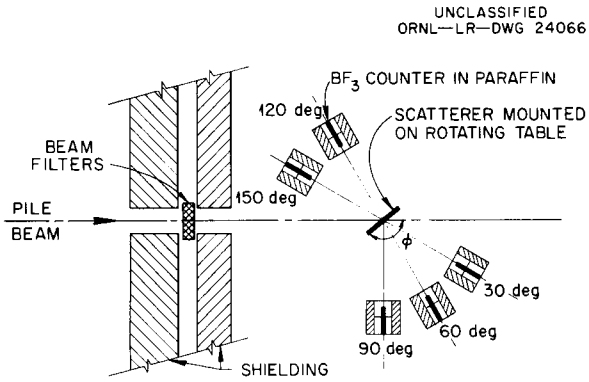


**Fig. 1. Floor Plan of Scattering Apparatus.**

about the scattering center. The scatterers were placed at angles, $\phi$, of 135 and 315 deg (see Fig. 1), and the counts from these two angles were averaged for each measurement in order to reduce errors due to misalignment. The data have been converted to center-of-mass values and are plotted in Figs. 2 and 3. The limits on the experimental points in Figs. 2 and 3 are standard deviations based on the counting statistics only.

It is observed in the lead and sodium distributions in Figs. 2 and 3 that a large component of the neutrons is scattered toward forward angles. The carbon distribution in Fig. 2 exhibits a large $P_2(\cos\theta)$ component. Thus it appears that there were many neutrons with energies greater than 0.5 Mev in the reactor beam; this interpretation is also consistent with a thick-thin boron filter measurement. Also, the over-all characteristics of these distributions are just about what are to be expected from measured distributions[1-7] averaged over a $dE/E$ and fission neutron energy spectrum. Since this large component of high-energy neutrons in the beam produced such highly anisotropic

[1] H. B. Willard, J. K. Bair, and J. D. Kington, *Phys. Rev.* 98, 669 (1955).

[2] J. E. Wills, *Bull. Am. Phys. Soc.* 1, 175 (1956).

[3] R. Budde and P. Huber, *Helv. Phys. Acta* 28, 49 (1955).

[4] R. Ricamo, *Nuovo cimento* 10, 1607 (1953).

[5] W. J. Rhein, *Phys. Rev.* 98, 1300 (1955).

[6] M. Walt and H. H. Barschall, *Phys. Rev.* 93, 1062 (1954).

[7] A. Langsdorf, Jr., R. O. Lane, and J. E. Monahan, *Neutron Scattering Angular Distribution*, ANL-5567 (June 1956).

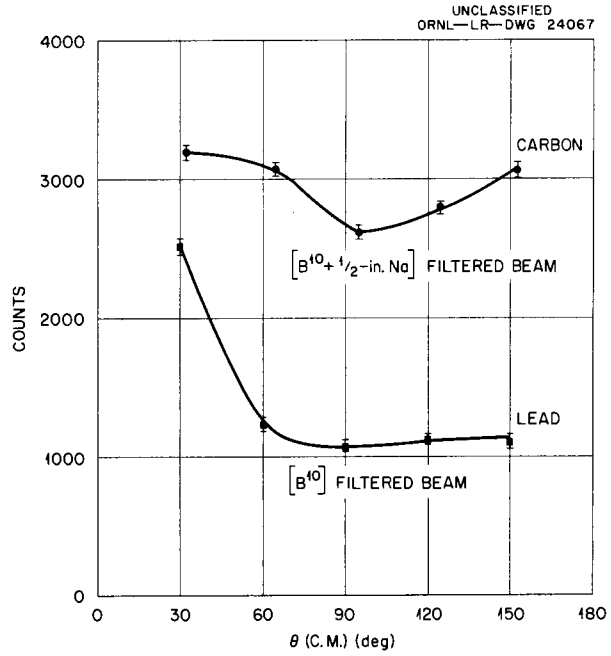


**Fig. 2. Scattering of Neutrons from Filtered Reactor Beam by Carbon and Lead. The $B^{10}$ filter consisted of 0.260 g of $B^{10}$ per square centimeter.**

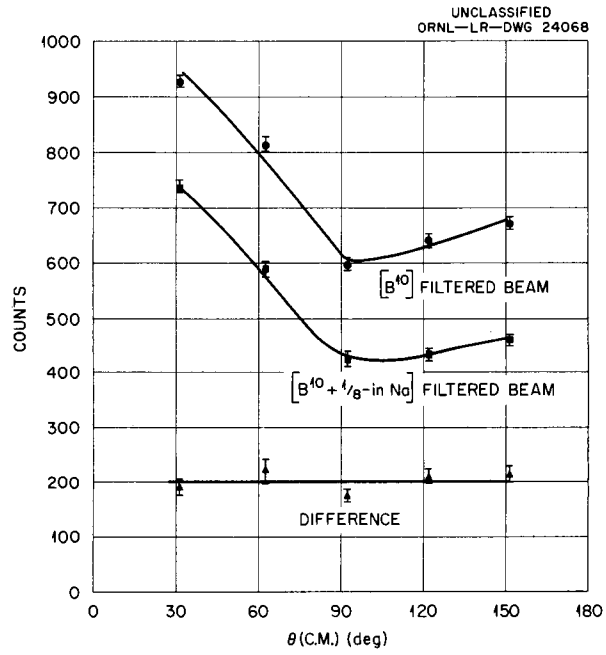


**Fig. 3. Scattering of Neutrons from Filtered Reactor Beam by Sodium. The lower curve is the difference between the upper two curves and primarily represents the scattering from the 2.80-kev resonance. The $B^{10}$ filter consisted of 0.260 g of $B^{10}$ per square centimeter.**

scattering from sodium, the neutrons scattered by the 2.80-kev resonance had to be separated from the total scattering before an analysis of the angular distribution could be made. This was accomplished by placing a sodium filter in the boron-filtered beam which was thick to neutrons near the 2.80-kev resonance but which was thin to all neutrons at other energies. Then the difference in the scattering between the boron-filtered and the boron-plus-sodium-filtered beam would be almost completely due to the 2.80-kev resonance scattering. These results are plotted at the bottom in Fig. 3. It is noted that within an accuracy of about 10% the angular distribution from this resonance is isotropic. Recent high-resolution total cross-section measurements[8,9] have assigned to this level a total angular momentum of 1, and it appears from the isotropy of this measurement that the level is formed by $s$-wave neutrons. However, it is possible for this level to be formed by $p$-wave neutrons and still have this angular distribution. By applying the analysis of Blatt and Biedenharn[10] for the case of $p$-wave resonance elastic scattering and $s$-wave potential scattering, anisotropies in the angular distribution of less than 10% would be observed if the partial width for formation (or decay) of this state in channel spin 2 was anywhere from 50 to 100% of the total neutron width. (Channel spin is defined as the vector sum of the neutron and target nucleus spins. In the case of $Na^{23}$ the ground-state spin is 3/2, and the two possible channel spins are 1 and 2. Since a $J = 1$ state can be formed in $Na^{24}$ by $p$-wave neutrons with both channel spins, the total neutron width $\Gamma$ is equal to the sum of the two partial widths $\Gamma_1$ and $\Gamma_2$ for formation of the state in channel spins 1 and 2, respectively.) Thus, out of all the possible ways of forming the $J = 1$ state in $Na^{24}$ with $p$-wave neutrons, only half of these possibilities are ruled out by this experiment. Therefore, although most of the experimental evidence tends to favor an $s$-wave assignment of this level, a $p$-wave assignment is by no means ruled out. A monoenergetic angular distribution measurement will probably be required in order to resolve this ambiguity.

[8] J. E. Lynn, F. W. K. Firk, and M. C. Moxon, *The Low Energy Cross Section of Sodium*, TNCC(UK) No. 18 (May 20, 1957).

[9] W. M. Good, J. H. Neiler, and J. H. Gibbons, submitted to *Phys. Rev.*

[10] J. M. Blatt and L. C. Biedenharn, *Revs. Modern Phys.* **24**, 258 (1952).

## KILOVOLT NEUTRON CROSS SECTIONS

J. H. Gibbons W. M. Good J. H. Neiler

The millimicrosecond flight-time spectrometer study of kilovolt neutron cross sections has continued. Measurements on $K^{41}$ and $Y^{89}$ have been completed up to 20 kev and on $Rb^{87}$ up to 15 kev. Figures 1, 2, and 3 show the results obtained. At the present state of the technique being used, the instrumental resolution is still several times the resonance width. Therefore the resonance widths are extracted by a standard method of area analysis. Table 1 gives a summary of the work done thus far, including $\Gamma_n^0/D$ ratios uncorrected for excitation energy.

The nuclides selected thus far have been purposely chosen for their wide level spacing. As a result, the number of individual levels studied has been rather too small for statistics on levels to be significant. However, even for the rather wide spacings studied, the improved resolution of the new instrument has led to some changes in the existing level schemes. In $K^{39}$ and $K^{41}$ several resonances previously observed[1] below 30 kev have been shown to consist, up to 16 kev, of a single resonance in $K^{39}$ at 9.2 kev and resonances in $K^{41}$ at 5.4 and 16.2 kev. In the case of $Rb^{87}$, the resonances at 6.6 and 7.35 kev reported here split a resonance previously observed[2] a little above 7 kev. In $Y^{89}$, a resonance previously reported[3] at 5.5 kev fails to show up in the present

[1] A. L. Toller and H. W. Newson, *Phys. Rev.* (to be published).

[2] H. W. Newson *et al.*, "Total Cross Sections Near Neutron Magic Numbers," to be submitted to *Phys. Rev.*

[3] H. W. Newson *et al.*, *Phys Rev.* 105, 198 (1957).

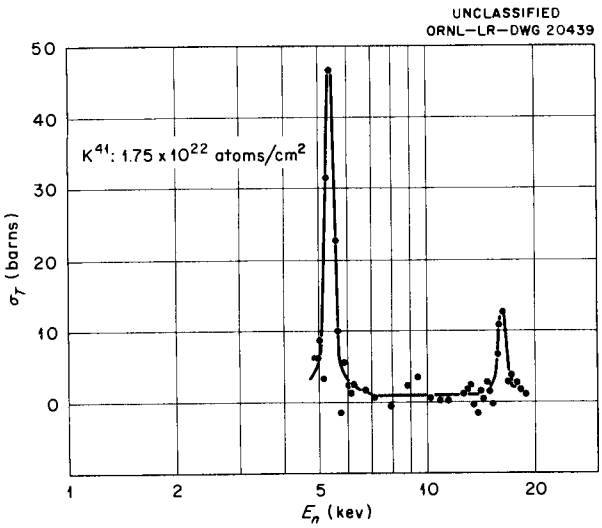


**Fig. 1. Total Cross Section of $K^{41}$ as a Function of Energy.**

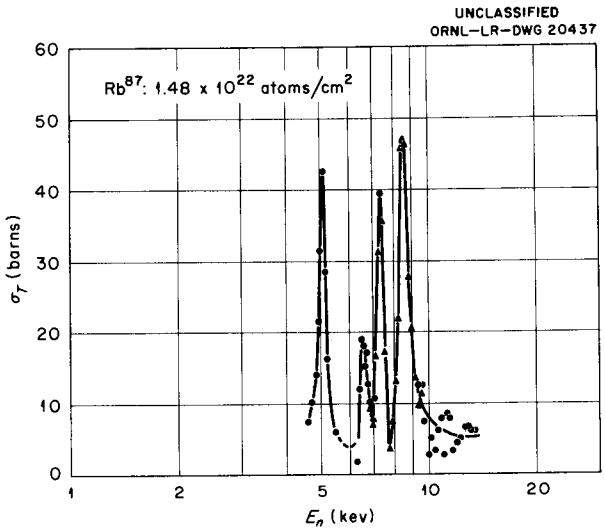


**Fig. 2. Total Cross Section of $Rb^{87}$ as a Function of Energy. The close spacing of levels and their relatively large widths, as exhibited by the observed peak cross section, indicate an appreciable strength function. Two runs are shown.**

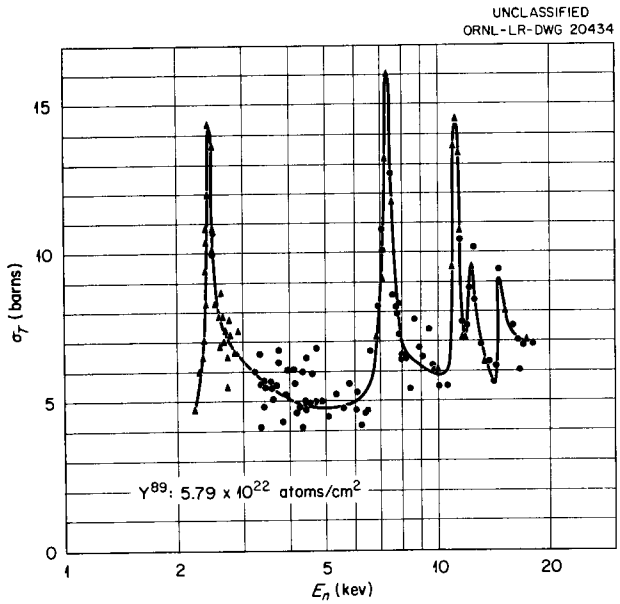


**Fig. 3. Total Cross Section of $Y^{89}$ as a Function of Energy. In contrast with the results for $Rb^{85}$ and $Rb^{87}$, this nuclide exhibits rather narrow resonance widths and surprisingly large level spacing. Two runs are shown.**

investigation, while a single resonance that previously appeared at 12 kev now appears to consist of two resonances at 11.25 and 14.0 kev.

Sodium-23 deserves special mention because its resonance at 2.80 kev has been studied on various occasions with conflicting results as to the peak cross section, and hence the $J$ value. The total cross section was re-examined in collaboration with Macklin and Block, with a resolution as good as or better than that obtained in any previous measurement. A peak cross section of 380 ± 10 barns was measured which is in agreement with that determined by Lynn, Firk, and Moxon.[4] This establishes $J = 1$ for this resonance.

---

[4] J. E. Lynn, F. W. K. Firk, and M. C. Moxon, *The Low Energy Cross Section of Sodium*, TNCC(UK) No. 18 (May 20, 1957).

**Table 1. Summary of Kilovolt Neutron Cross-Section Measurements**

| Nuclide | Atoms ($cm^{-2}$) | Isotopic Purity (%) | Energy Interval Studied (kev) | $E_0$ (kev) | $\Gamma$ (ev) | $D_{obs}$ (kev) | $\overline{\Gamma}_n^0/D_0$ | Remarks |
|---|---|---|---|---|---|---|---|---|
| | $\times 10^{22}$ | | | | | | $\times 10^{-4}$ | |
| $Na^{23}$ | 6.41 | (100) | 2.4 – 8 | 2.80 | 420 ($l = 0$) | | | $J = 1$, $\sigma_0 = 380 \pm 10$ barns |
| | 0.265 | | | | 370 ($l = 1$) | | | |
| | 0.11 | | | | | | | |
| $Al^{27}$ | 7.65 | (100) | 5 – 6.2 | 5.6 | 20 | | | $l$ probably > 0 |
| $P^{31}$ | 6.10 | (100) | 6 – 20 | | | | | $\sigma$ decreases smoothly from 5.0 barns at 8 kev to 4.0 barns at 20 kev |
| $K^{39}$ | 2.27 | 99.7 | 3 – 10 | 3.4 | 12 | 10 | 0.9 | |
| | | | | 9.2 | 60 | | | |
| $K^{41}$ | 1.75 | 98.3 | 5 – 20 | 5.4 | 35 | 10 | 1.0 | |
| | | | | 16.2 | 60 | | | |
| Ti | 3.65 | Natural | 3 – 20 | 3.0 | 50 | | | Resonances at 17.5 kev and probably the one at 3.0 kev are due to $Ti^{48}$ |
| | 0.767 | | | 3.7 | | | | |
| | | | | 17.5 | 7000 | | | |
| Se | 1.19 | Natural | 3.8 – 9 | 4.25 | 35 | | | Width assignments assumed $s$-wave neutrons on $Se^{80}$ |
| | | | | 4.95 | 35 | | | |
| | | | | 5.85 | | | | |
| | | | | 6.8 | | | | |
| | | | | 8.6 | | | | |
| $Rb^{85}$ | 2.04 | 99.1 | 3 – 9 | 3.3 | | 1.0 | 1.8 | $N = 48$ |
| | | | | 4.1 | 18 | | | |
| | | | | 4.9 | 34 | | | |
| | | | | 5.8 | 33 | | | |
| | | | | 6.9 | 17 | | | |
| | | | | 9? | | | | |
| $Rb^{87}$ | 1.48 | 94.9 | 4.5 – 15 | 5.0 | 46 | 1.7 | 2.4 | $N = 50$ |
| | | | | 6.6 | 17 | | | |
| | | | | 7.35 | 54 | | | |
| | | | | 8.55 | 170 | | | |
| $Sr^{86}$ | 1.50 | 88.6 | 3 – 15 | 3.0 | | 4 | | $N = 48$ |
| | | | | 4.3 | | | | |
| | | | | 11.3 | | | | |
| $Sr^{88}$ | 2.09 | 99.6 | 7 – 20 | 13.6 | 400 | 15 | | $N = 50$ |
| $Y^{89}$ | 5.79 | (100) | 2.2 – 18 | 2.5 | 6 | 3.0 | 0.25 | $N = 50$ |
| | 1.93 | | | 7.35 | 55 | | | |
| | | | | 11.25 | 60 | | | |
| | | | | 14 | | | | |
| | | | | 17 | | | | |
| Pb | 10.48 | Natural | 20 – 34 | | | | | No fluctuations > 10% of $\sigma_{pot}$ (= 10.2 barns) were observed |
| $Bi^{209}$ | 2.42 | (100) | 2.2 – 2.6 | 2.3 | 24 | 7 | | $D_{obs}$ includes resonance at 0.8 kev |
| | | | | 12.5 | | | | |
| | | | | 15.5 | | | | |
| | | | | 33 | | | | |

## BERYLLIUM DIFFERENTIAL NEUTRON SCATTERING

H. O. Cohn J. L. Fowler

Differential elastic neutron scattering from beryllium was measured at neutron energies of 0.73, 1.00, 1.21, 1.50, 1.75, and 2.15 Mev. These data were obtained simultaneously with the neutron-scattering angular distribution from oxygen reported earlier.[1] Beryllium cylinders 4½ in. high and 0.45 and 0.63 in. in diameter served as scattering samples. Monoenergetic neutrons of ~50-kev resolution were produced in a tritium gas target by bombarding it with protons from the 5.5-Mv ORNL Van de Graaff generator. Scattered neutrons were detected by a propane recoil counter shielded from the direct beam by a lithiated paraffin wedge.[2] The experimental points are plotted in Fig. 1 after having been corrected for counter efficiency, angular resolution, and multiple scattering in the sample, and transferred to the center-of-mass system. The absolute measured differential cross section agreed within experimental error with the total elastic scattering cross section reported in the literature.[3] The solid curves were calculated from *s*, *p*, and *d* phase shifts giving the best fit to the experimental points. The artificial simplifying assumption was made that the phase shifts for the two possible channel spins are identical.

[1] J. L. Fowler and H. O. Cohn, *Bull. Am. Phys. Soc.* 2, 32 (1957); *ibid.*, p 286; and J. L. Fowler and H. O. Cohn, *Phys. Rev.* (to be published).

[2] H. B. Willard, J. K. Bair, and J. D. Kington, *Phys. Rev.* 98, 669 (1955).

[3] D. J. Hughes and R. B. Schwarts, *Neutron Cross Sections*, BNL-325, Supp. 1 (Jan. 1, 1957).

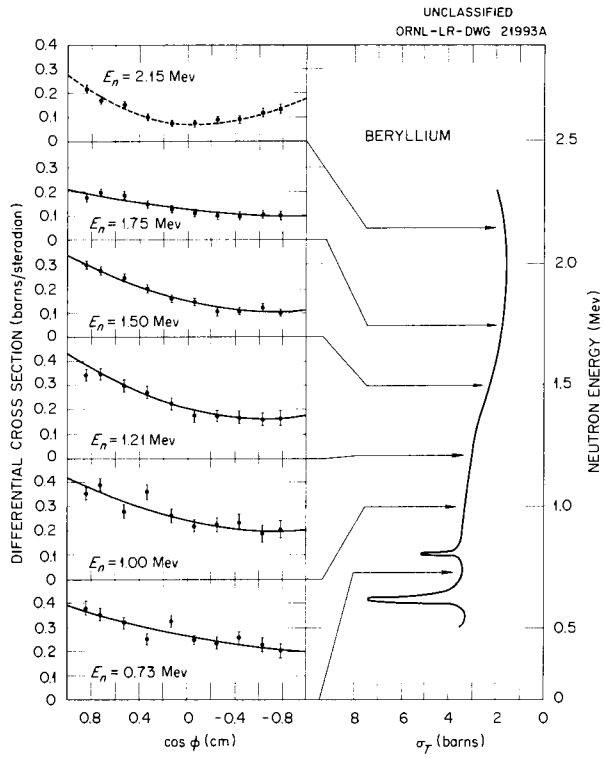


**Fig. 1. Differential Elastic Neutron Scattering Cross Sections for Beryllium. On the right side is the beryllium total cross section (D. J. Hughes and R. B. Schwartz, *Neutron Cross Sections*, BNL-325, Supp 1 (Jan. 1, 1957). Statistical errors are shown.**

## ELASTIC SCATTERING OF NEUTRONS BY $C^{12}$

H. B. Willard J. K. Bair H. O. Cohn

The data presented in the last progress report[1] have been fitted with *s*-, *p*-, and *d*-wave phase shifts. Explicit formulas for this analysis of spin-zero nuclei appear in the paper by Meier, Scherrer, and Trumpy,[2] while the generalization can be found in the work by Blatt and Biedenharn.[3] Results are shown in Fig. 1 and are listed in Table 1. The $d_{3/2}$ phase shift exhibits a resonance behavior which can be fitted quite well if it is assumed that the levels at 2.95 and 3.67 Mev have widths of 90 kev and 1.69 Mev, respectively. A nuclear

[1] H. B. Willard, J. K. Bair, and H. O. Cohn, *Phys. Semiann. Prog. Rep. March 10, 1957*, ORNL-2302, p 23.

[2] R. W. Meier, P. Scherrer, and G. Trumpy, *Helv. Phys. Acta* 27, 577 (1954).

[3] J. M. Blatt and L. C. Biedenharn, *Revs. Modern Phys.* 24, 258 (1952).

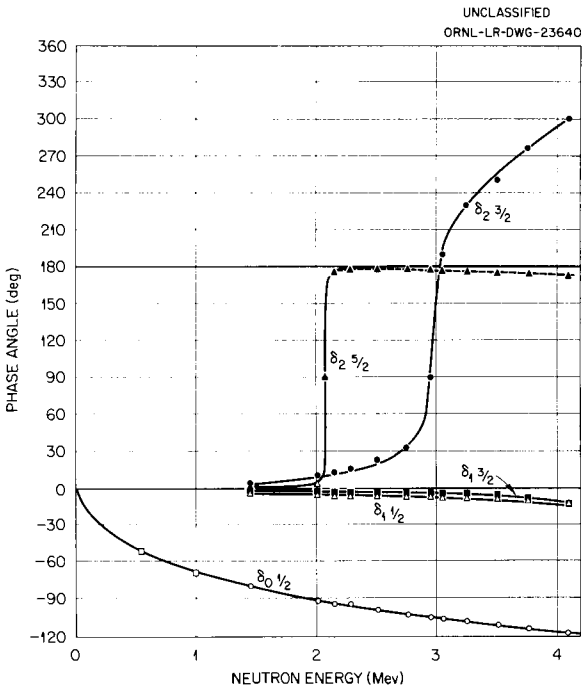


**Fig. 1. Phase Shifts for Neutrons Scattered Elastically by $C^{12}$ as a Function of Bombarding Energy.**

**Table 1. Experimentally Determined Phase Shifts for Neutrons Scattered Elastically by $C^{12}$**

| $\bar{E}_n$ (Mev) | Phase Shifts (deg) | | | | |
|---|---|---|---|---|---|
| | $\delta_{0,1/2}$ | $\delta_{1,1/2}$ | $\delta_{1,3/2}$ | $\delta_{2,3/2}$ | $\delta_{2,5/2}$ |
| 1.451 | −80 | −4 | −2 | 3 | 0 |
| 2.015 | −92 | −6 | −3 | 10 | 4 |
| 2.150 | −94 | −6 | −3 | 13 | 176 |
| 2.283 | −95 | −6.5 | −3.5 | 16 | 177 |
| 2.505 | −99 | −6.5 | −3.5 | 23 | 178 |
| 2.758 | −103 | −7 | −3.5 | 34 | 178 |
| 2.946 | −105 | −7.5 | −3.5 | 90 | 178 |
| 3.052 | −106 | −8.0 | −4.0 | 190 | 177 |
| 3.254 | −108 | −8.5 | −4.0 | 230 | 176 |
| 3.505 | −111 | −9.0 | −5.0 | 252 | 175 |
| 3.762 | −114 | −10.0 | −8.0 | 277 | 174 |
| 4.100 | −118 | −12.0 | −12.0 | 300 | 173 |

interaction distance of 4.61 fermis was used in the calculation of the barrier penetration and level shift facts, and the tangents of the phase shifts of the two individual resonances were added to give the tangent of the resultant $d_{3/2}$ phase shift, which appears as a solid curve in Fig. 1.

The $d_{5/2}$ phase shift is due almost entirely to the 2.076-Mev level (7-kev natural width), although the deviation from resonance behavior, shown as a dotted curve in Fig. 1, is probably due to potential $d$-wave scattering.

This reaction has often been used as a polarization analyzer for neutrons between 2.5 and 3.5 Mev.[2,4-6] Therefore the energy dependence of the polarization at center-of-mass angles $\theta = 45$ and 135 deg was calculated by use of the above phase shifts. As Fig. 2 indicates, this reaction is strongly polarized at some energies. However, it should be cautioned that the polarization depends more sensitively on the phase shifts than on the angular distributions, with the result that the errors are correspondingly larger.

[4] R. Budde and P. Huber, *Helv. Phys. Acta* 28, 49 (1955).

[5] B. M. McCormac *et al.*, *Phys. Rev.* 104, 718 (1956).

[6] W. Haeberli and W. W. Rolland, *Bull. Am. Phys. Soc.* 2, 234 (1957).

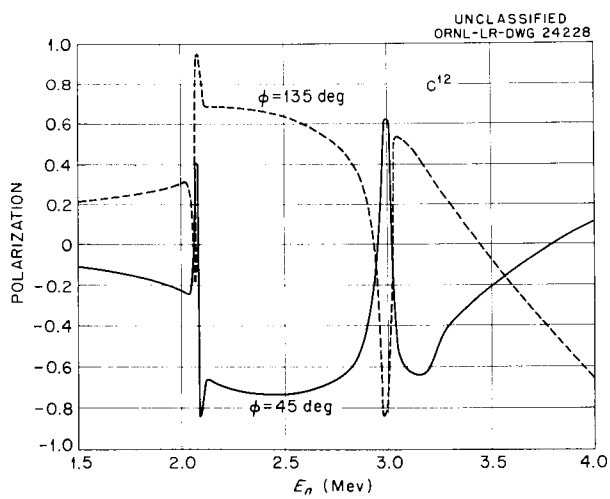


**Fig. 2. Calculated Values of the Polarization of Neutrons Scattered Elastically by $C^{12}$ for Center-of-Mass Angles $\phi$ = 45 and 135 deg.**

# DIFFERENTIAL ELASTIC SCATTERING OF NEUTRONS FROM ZERO-SPIN LIGHT NUCLEI

J. L. Fowler H. O. Cohn

Differential neutron scattering involving light nuclei with zero spin is of special interest. In such cases as $He^4$, $C^{12}$, $O^{16}$, and $Ne^{20}$ the situation is uncomplicated by the possibility of two-channel spin states, so that a unique phase-shift analysis of the data is possible. Because $O^{16}$ is a doubly closed shell nucleus, the scattering data here permit a simple interpretation in terms of phenomenological nuclear potentials.[1] A somewhat similar analysis[2] in terms of a phenomenological interaction in the case of scattering of neutrons from $He^4$ has been found[3] to give the experimental *s*-, *p*-, and *d*-wave phase shifts in the energy range 0 to 10 Mev.

Figure 1 gives the differential cross section of oxygen in the region of the 1-Mev resonance. Neutrons were scattered from BeO and Be samples and were detected with a shielded propane counter; $H^3(p,n)$ neutrons of ~50-kev energy spread were used.[4] On the right side of the figure is plotted the total cross section of oxygen taken from the paper of Bockelman *et al.*[5] The arrows indicate the energy at which the differential cross section on the left side was measured. The abscissa on the left side is the cosine of the center-of-mass angle. The solid curves are theoretical differential cross sections calculated with the set of phase shifts given beside each curve. A change of any phase shift by 5 deg gives an appreciably worse fit to the data.

Figure 2 shows a continuation of the measurements up to 2.15 Mev. Notice that the effect of the $d_{3/2}$ level at 1 Mev, as indicated by the difference of the $d_{3/2}$ phase shift from 180 deg, extends for over 1 Mev above the level. The *s* level, which shows up as a dip at 2.37 Mev, indicates that the *s*-potential scattering phase shift at this energy is about 90 deg.

In Fig. 3 these phase shifts are plotted as a function of energy. Below 700 kev the phase shifts are taken from the measurements of Okazaki.[6] For the $p_{3/2}$ phase shifts, the lines go through 90 and 270 deg with a slope which gives the width of the level. These levels are compound nucleus levels – the reduced width is small compared with a single-particle level. For the 1.00-Mev level, the reduced width is approximately that of a single-particle level. Other levels in $O^{17}$ with large reduced widths are the ground-state $J = 5/2+$ and the first excited state $J = 1/2+$. Since $O^{16}$ is a doubly closed shell nucleus, we may expect to be able to describe much of its interaction with a neutron in terms of an average

[1] J. L. Fowler and H. O. Cohn, *Bull. Am. Phys. Soc.* 2, 286 (1957).

[2] E. Van der Spuy, *Nuclear Phys.* 1, 381 (1956).

[3] J. D. Seagrave, *Phys. Rev.* 92, 1222 (1953); P. Huber and E. Baldinger, *Helv. Phys. Acta* 25, 435 (1952).

[4] H. B. Willard, J. K. Bair, and J. D. Kington, *Phys. Rev.* 98, 669 (1955); J. L. Fowler and C. H. Johnson, *Phys. Rev.* 98, 728 (1955).

[5] C. K. Bockelman *et al.*, *Phys. Rev.* 84, 69 (1951).

[6] A. Okazaki, *Phys. Rev.* 99, 55 (1955).

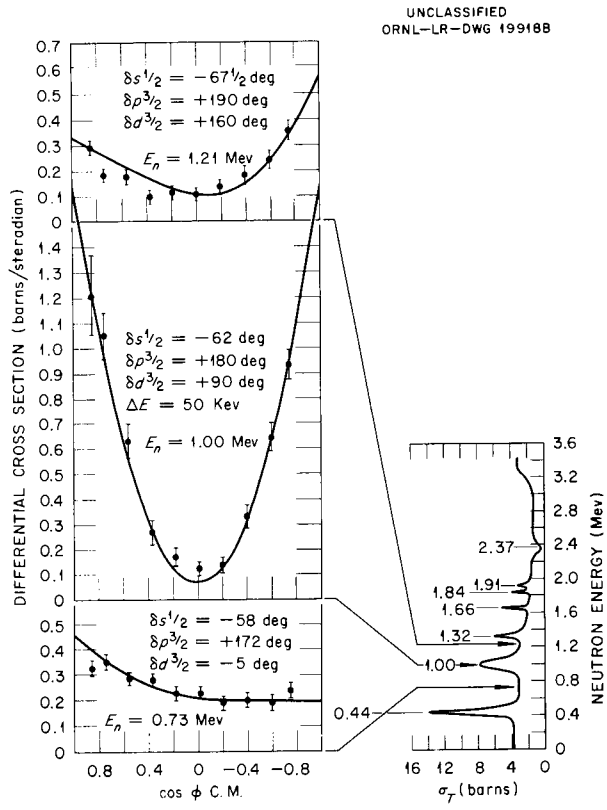


**Fig. 1. Differential Cross Section of Neutron Scattering from $O^{16}$ in the Region 0.73 to 1.21 Mev.**

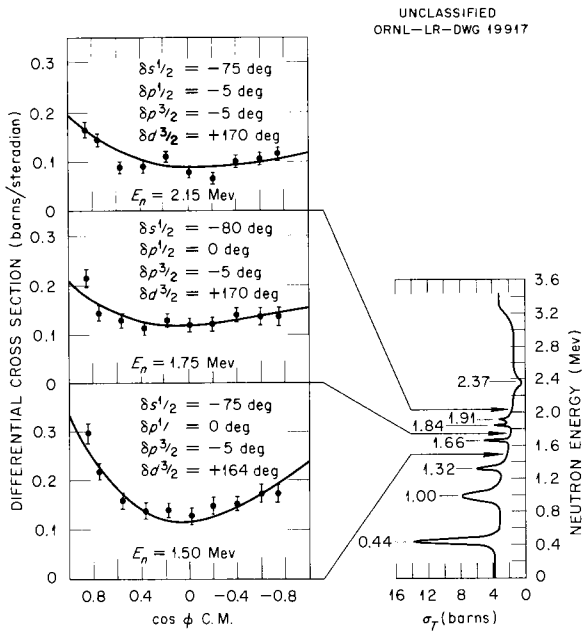


**Fig. 2. Differential Cross Section of Neutron Scattering from $O^{16}$ in the Region 1.50 to 2.15 Mev.**

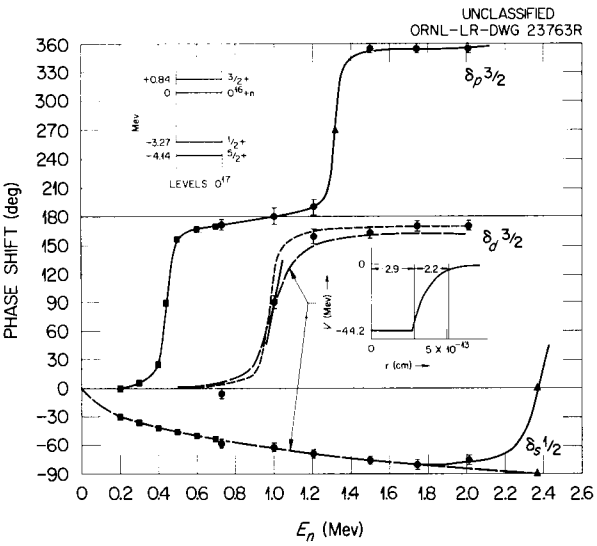


**Fig. 3. Phase Shifts for Elastic Scattering of Neutrons from $O^{16}$.**

potential. In particular, we may try to fit the levels listed in the upper insert of Fig. 3 in terms of the single-particle picture.

Although the $s$-wave phase shifts and the $2s$ state can be fitted simultaneously with a square well,[7] such a well is not suitable for the $d$ states. With the potential shown as the lower insert of Fig. 3, one obtains the correct energy for the $2s$ state, as well as the dashed curve for the $s$ phase shifts. With the depth of the well decreased slightly, corresponding to velocity dependence, and with a surface spin orbit energy about 35 times the Thomas term, the correct ground-state energy is found, as well as the dashed curve for the $d_{3/2}$ phase shift. The well has slightly too diffuse a boundary – reducing the diffuseness by 25% gives the dotted curve. These two cases bracket the experimental situation. Furthermore, the parameters used here are very similar to those used to order the bound-state levels for magic-number nuclei of much higher mass.[8]

In the case of $C^{12}$ neutron scattering, a similar analysis is possible. Here the scattering phase shifts were obtained by Willard *et al.* (see "Elastic Scattering of Neutrons by $C^{12}$," this report). The $2s$ state of $C^{13}$ and the $s$-wave phase shifts are fitted by a well similar to the one which gives the dotted curve in Fig. 3, but with the central core region reduced in the ratio of $A^{1/3}$. The $d$-wave analysis is complicated by the fact that the narrow compound nucleus, $d_{3/2}$ level at 2.95 Mev makes the single-particle interpretation of the 3.67-Mev $d_{3/2}$ level inappropriate.

The next zero-spin nucleus which can be investigated from this viewpoint is $Ne^{20}$. Since neon is a gas, the differential scattering experiment is more difficult. Figure 4 illustrates how it

[7] H. O. Cohn and J. L. Fowler, *Phys. Semiann. Prog. Rep. March 10, 1957*, ORNL-2302, p 7, Fig. 4.

[8] A. A. Ross, H. Mark, and R. D. Lawson, *Phys. Rev.* **102**, 1613 (1956); A. E. S. Green, *Phys. Rev.* **104**, 1617 (1956); and A. A. Ross, R. D. Lawson, and H. Mark, *Phys. Rev.* **104**, 401 (1956).

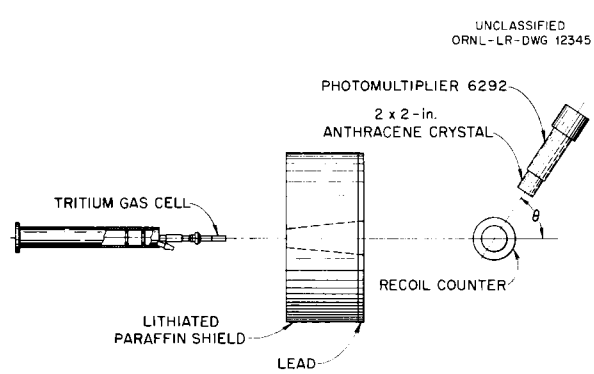


**Fig. 4. Apparatus for Measuring Differential Elastic Scattering of Neutrons from Neon.**

was performed.[9] An anthracene crystal detects neutrons in coincidences with neon recoils which occur in a proportional counter. Direct-source neutrons are shielded out by the combination of lithiated paraffin and lead shields.

Figure 5 shows three resonances in the region of 1.2 to 1.45 Mev. From the asymmetry about 90 deg, one concludes that the 1.31-Mev level is of odd parity. There is an even-parity level at 1.38 Mev – probably a $d_{3/2}$ level. Below this energy region shown here, one more odd-parity level at 0.91 Mev was found between 0.82 and 1.25 Mev.

Figure 6 shows the situation from 1.57 to 1.75 Mev. Here the cross-section data are on an absolute scale. The solid lines are theoretical curves for a $p_{3/2}$ level at 1.62 Mev and a $d_{3/2}$ level at 1.68 Mev, calculated under the assumption that the $s$-wave potential scattering phase shift is about –50 deg. Attempts to fit this $s$-wave information, together with a prominent $s_{1/2}$ state in $Ne^{21}$, with a potential extrapolated from the types used for carbon and oxygen have been unsuccessful. Due to configuration mixing of $d$ and $s$ states here, one should not expect a simple single-particle model to apply to a case which is as far removed from a closed shell as $Ne^{21}$.

[9] H. O. Cohn and J. L. Fowler, *Bull. Am. Phys. Soc.* I, 175 (1956).

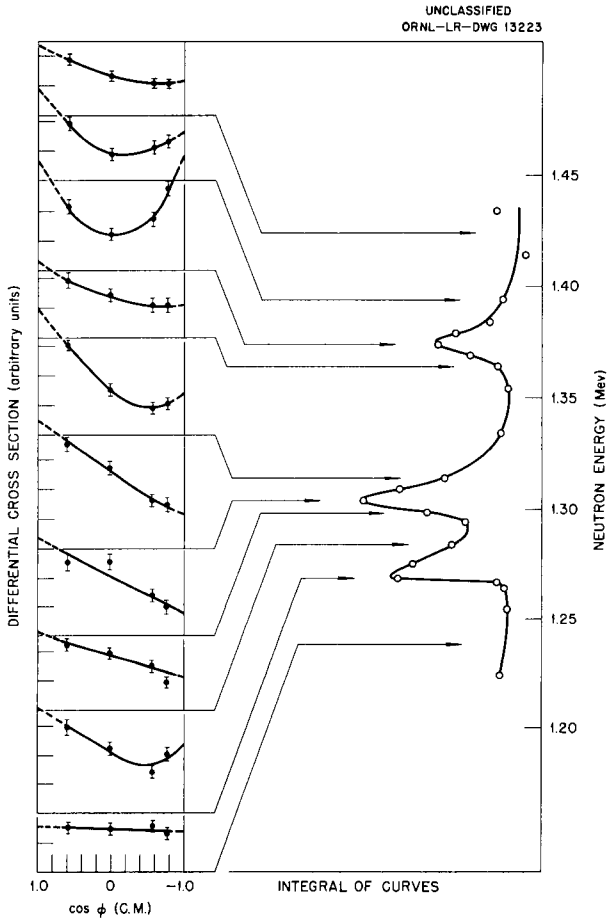


**Fig. 5. Differential Scattering of Neutrons from Neon in the Region 1.22 to 1.43 Mev.**

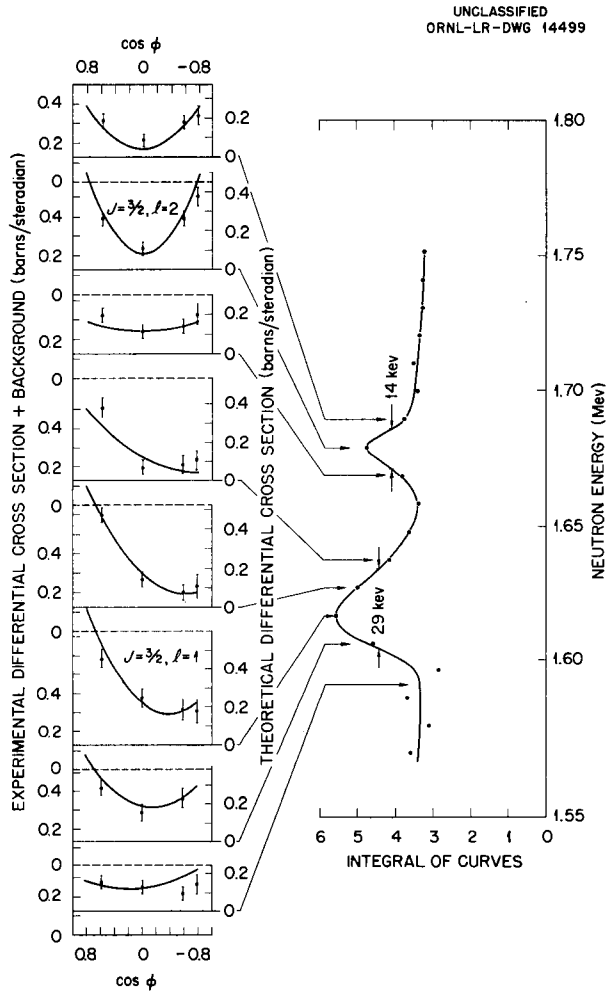


**Fig. 6. Differential Cross Section of Neutrons Scattered from Neon in the Region 1.57 to 1.75 Mev.**

## CROSS SECTION AS A FUNCTION OF ENERGY FOR THE REACTION $S^{32}(n,\alpha)Si^{29}$

H. W. Schmitt

The $S^{32}(n,\alpha)Si^{29}$ cross section has been measured as a function of energy in the range $1.4 \leq E_n \leq 3.0$ Mev. A double back-to-back ionization chamber, shown schematically in Fig. 1, was used with krypton gas. Monoenergetic neutrons from the $H^3(p,n)He^3$ reaction were incident on the sulfur and the $U^{238}$ deposits, situated back-to-back in the center plate of the chamber, and fragments from neutron fission of the $U^{238}$ were counted to determine the number of neutrons incident on the sample. A long counter was used as a secondary neutron monitor, and the results agreed, within the accuracy of the measurement, with those obtained with $U^{238}$ fission counting and the known[1] fission cross section of $U^{238}$.

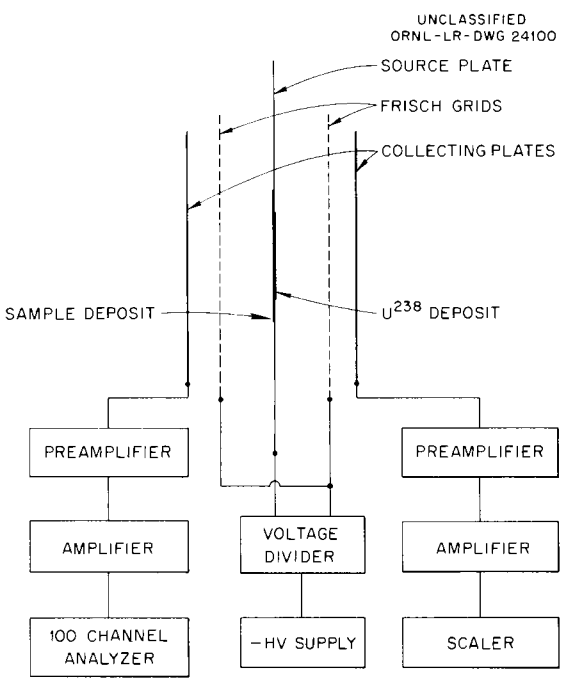


**Fig. 1. Back-to-Back Ionization Chamber for $(n,\alpha)$ Cross-Section Measurements.**

The $U_3^{238}O_8$ deposit was prepared by electroplating; the amount of material on the foil was determined by alpha counting and by weighing. Uncertainty in the mass of $U^{238}$ in the deposit was ±3%. The isotopic purity of the $U^{238}$ was at least $10^5$:1. Lead sulfide (PbS) was evaporated on platinum backings to provide the sulfur samples. The perpendicular thickness of the PbS deposit was equal to about 5% of the range of a 3.5-Mev alpha particle – alpha-particle energies in these measurements ranged from ~2.5 to ~4.5 Mev; corrections were made for alpha-particle counting losses. The amount of lead sulfide in the deposit was determined by weighing; the accuracy in the sulfur mass determination was ±4%. One PbS foil was used throughout these measurements, and a second foil half as thick was used in a check measurement at one neutron energy. Good agreement was obtained.

A typical alpha-particle spectrum is shown in Fig. 2, together with the corresponding background spectrum. The chamber was plated with gold, and pure krypton gas was used to keep the background low. Effects such as neutron scattering from the chamber and surroundings, neutron attenuation in the foil backings, competing reactions, etc., were considered and were collectively estimated to be less than 1%.

The $S^{32}(n,\alpha)Si^{29}$ cross section was determined only for those events in which the $Si^{29}$ was left

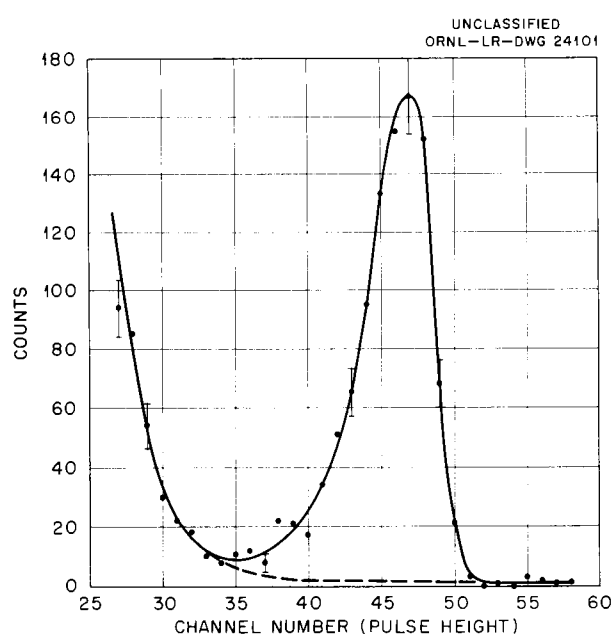


**Fig. 2. Typical Pulse-Height Spectra.** Solid line gives spectrum with sulfur sample in chamber; dashed line gives background spectrum ($E_n$ = 2.09 Mev).

[1] R. W. Lamphere, *Phys. Rev.* 104, 1654 (1956).

in its ground state. Results for alpha-particle emission at 0 to 90 deg with respect to the neutron beam in the laboratory system are shown in Fig. 3. Results for alpha-particle emission at 90 to 180 deg are shown in Fig. 4. Because of the use of a tritium gas target and occasional breakage of foils, the energies of the datum points in Figs. 3 and 4 are not necessarily the same. Hence a point-by-point addition of the curves drawn in Figs. 3 and 4 was done to give the total $(n,\alpha)$ cross section shown in Fig. 5. Also shown in Fig. 5 are typical neutron energy spreads at various neutron energies, and typical statistical uncertainties at various values of $\sigma_{n,\alpha}$. The latter averaged about ±6%.

The uncertainty in the absolute values of the cross section arises largely in the mass determinations of the $U^{238}$ and sulfur deposits discussed above; smaller uncertainties appear in correcting for alpha-particle losses. The combined accuracy in the absolute value determinations is approximately ±8%. One further uncertainty may arise in a few regions of the curve where the cross section is very rapidly varying, for example, at $E_n = 2.3$,

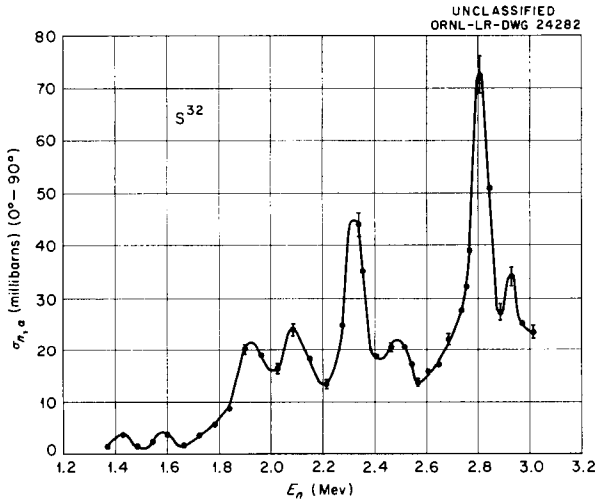


**Fig. 3. Cross Section for the $S^{32}(n,\alpha)Si^{29}$ Reaction, Where Alpha Particles Are Emitted at 0 to 90 deg with Respect to the Neutron Beam in the Laboratory System.**

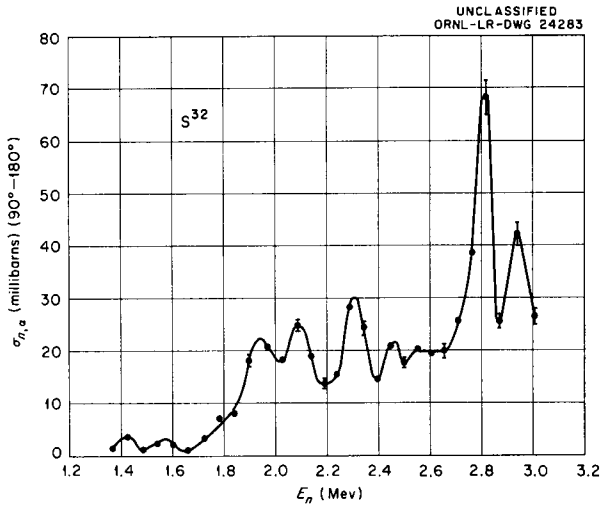


**Fig. 4. Cross Section for the $S^{32}(n,\alpha)Si^{29}$ Reaction, Where Alpha Particles Are Emitted at 90 to 180 deg with Respect to the Neutron Beam in the Laboratory System.**

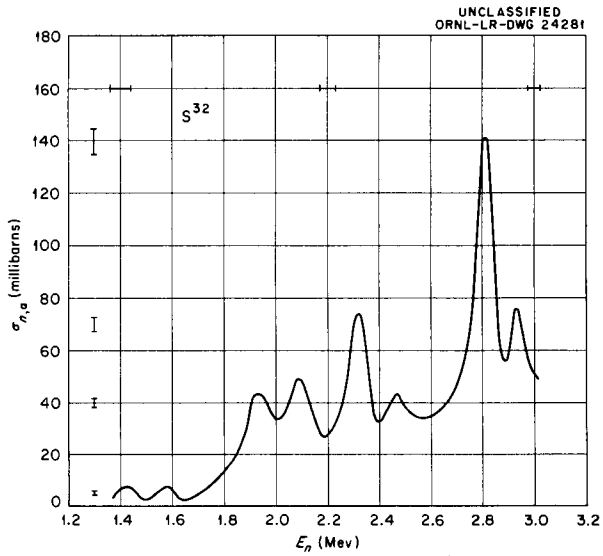


**Fig. 5. Cross Section for the $S^{32}(n,\alpha)Si^{29}$ Reaction. Typical statistical uncertainties and neutron energy spreads are shown. Uncertainty in absolute values of $\sigma_{n,\alpha}$ is ±8%.**

2.8, and 2.9 Mev. Since datum points were taken approximately every "resolution width," there may be some uncertainty in the heights of a few of the peaks as drawn.

The $S^{32}(n,\alpha)Si^{29}$ cross section has been measured previously by Hürlimann and Huber[2] for neutrons in the energy range $2.2 \leqq E_n \leqq 4.1$ Mev. In the region of overlap of the two measurements, $2.2 \leqq E_n \leqq 3.0$ Mev, there is general agreement in the shape of the curve, although the appearance of the two curves is as though the neutron energy resolution is somewhat higher in the present measurements. Direct comparison of absolute values of $\sigma_{n,\alpha}$ is difficult because of this apparent difference in neutron energy resolution.

[2]T. Hürlimann and P. Huber, *Helv. Phys. Acta* 28, 33 (1955).

## EXPERIMENTAL *L*-SHELL FLUORESCENCE YIELDS

N. H. Lazar W. S. Lyon

Information about certain nuclear events may be obtained in terms of the relative number of vacancies created in the $K$ and $L$ electron shells of the atom during the event. A convenient method of determining this ratio, particularly for heavy nuclei, is to measure the intensity of $K$ and $L$ x rays (e.g., with a scintillation counter) following the event. Then, if the fluorescent yields of the various subshells are known, the number of vacancies in each of the shells can be determined. Since it is a difficult task to compute these fluorescence yields, recourse to an experimental measurement has been taken.

In 1934, Lay[1] measured the fluorescence yield in the $L$ shell of a series of elements, using the beam of an x-ray machine to produce ionization of the atom. The intensity of the succeeding x rays was determined by the blackening of photographic plates. His results are plotted in Fig. 1. Since that time a number of people[2] have attempted to measure $\bar{w}_L$, the average $L$-shell fluorescence yield, following various nuclear processes (internal conversion, $K$ and $L$ capture), and their results have been consistently lower than Lay's values. These experiments usually were designed to measure the Auger yield ($\bar{a}_L = 1 - \bar{w}_L$), but since the energy of the Auger electrons is usually extremely low, the experimental difficulty is not negligible.

The present technique is somewhat novel in concept. Vacancies in the $L$ shell are produced by two different processes in, say, internal conversion. Either the vacancy is created directly by conversion in the $L$ shell or the vacancy may be created by de-excitation of an atom following a vacancy in the $K$ shell. In the latter case, a

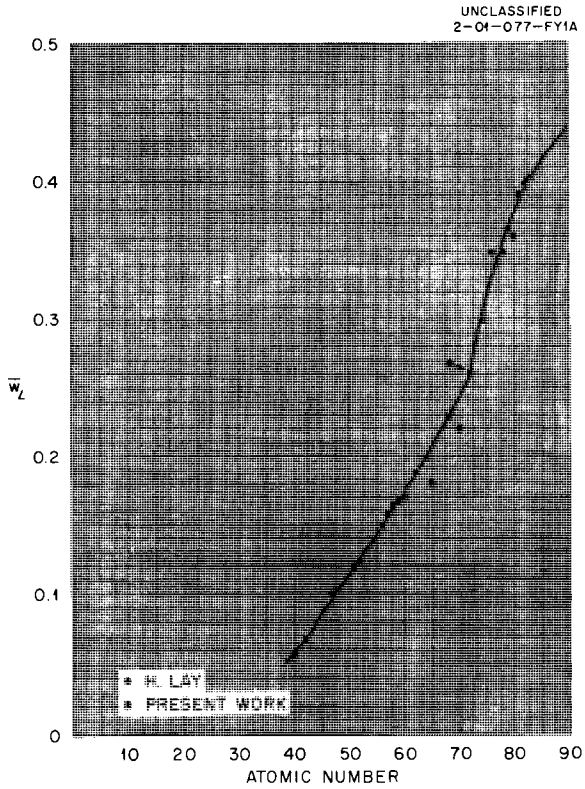


**Fig. 1. Average Fluorescence Yield in the *L* Shell ($\bar{w}_L$) Shown as a Function of Atomic Number. The solid line is drawn through the points of H. Lay.**

[1]H. Lay, *Z. Physik* 91, 533 (1934).

[2]For a review of earlier data see R. W. Fink, *Phys. Rev.* 106, 266 (1957) and B. L. Robinson and R. W. Fink, *Revs. Modern Phys.* 27, 424 (1955).

vacancy in the $L$ shell is labeled by the emission of a $K\alpha$ x ray. The probability of emission of an $L$ x ray per $K\alpha$ x ray is just the fluorescence yield in the $L$ shell. Now, one may determine this probability by a coincidence experiment between $K$ and $L$ x rays, since the number of $K\alpha$ x rays per $K$ x ray has been measured.[3]

The experimental arrangement consists of two NaI(Tl) detectors; one, 3 in. in diameter by 3 in. high in 0.005-in.-thick aluminum, is used to detect $K$ x rays; the other, 1 ½ in. in diameter and 3.4 mm thick in a beryllium can with one face 0.137 g/cm$^2$, is used to detect the $L$ x rays. Coincidences are taken with a single-channel analyzer selecting the $K$ x rays. In some cases, the single-channel window was narrowed to ensure proper time relationships with all the channels of the multichannel analyzer used for pulse-height analysis of the $L$ x rays, and it was then moved through the $K$ x-ray region successively. In these cases, the number of coincidence counts in the $L$ x-ray peak, $P(L)$, is given by

$$P(L) = C(K)\ \epsilon_p \frac{\Omega}{4\pi} A\, f_{LK} ,$$

where $C(K)$ represents the number of counts in the window due to $K$ x rays and does not include counts from events like bremsstrahlung from stopping of electrons, possible Compton electron counts from higher-energy gamma rays, etc., which may give pulses at the $K$ x-ray pulse height; $\epsilon_p$ is the peak efficiency of the 1 ½-in. by 3.4-mm crystal and was taken as unity; $\Omega/4\pi$ is the solid angle subtended by the front face of the thin crystal; $A$ represents the transmission of the $L$ x rays through the beryllium absorbers which were inserted to remove beta rays; $f_{LK}$ is the probability of having an $L$ x ray per $K$ x ray. The absorption by the beryllium foils was experimentally determined through the measurement of the attenuation of x rays from various substances. In all cases the attenuation was less than 60%. An attenuation of the lowest-energy $L$ x rays by air was avoided by filling the volume between the source and the crystal with a helium atmosphere. The sources used and the results obtained are given in Table 1. The results are also plotted in Fig. 1. The average thicknesses of all the sources were less than 1 mg/cm$^2$ and most were invisible. The results, particularly for terbium, could, however, be influenced by nonuniform source distribution, and further work is planned to determine the magnitude of such an effect.

The main sources of error are (1) the uncertainty in the beryllium absorption coefficient, since the $K$ x rays used in the determination of this coefficient are made up of various energies, a characteristic somewhat different from that of the $L$

[3] A. H. Compton and S. K. Allison, *X-Rays in Theory and Experiment*, 2d ed., p 640, Van Nostrand, New York, 1935.

**Table 1. Average Fluorescence Yields in the $L$ Shell**

| Isotope | Atomic Number of Daughter | $\bar{w}_L$ | Remarks |
|---|---|---|---|
| $Bi^{207}$ [a] | 82 | 0.40 | $K$ x rays arise mostly from $K$ capture; no coincidences of $K$ x rays with gamma rays observed |
| $Hg^{203}$ | 81 | 0.39 | $K$ x rays from internal conversion of 0.279-Mev gamma ray |
| $Tl^{204}$ | 80 | 0.36 | X rays from ~3% electron capture branch |
| $Lu^{176}$ [a] | 72 | 0.26 | X rays from internal conversion of 0.089-Mev gamma ray |
| $Tm^{170}$ [a] | 70 | 0.22 | X rays from internal conversion of 0.084-Mev gamma ray |
| $Gd^{159}$ | 65 | 0.18 | X rays from noncoincident gamma rays of various energies |

[a] The material for preparation of these sources was supplied by F. K. McGowan.

x rays, and (2) the determination of $C(K)$ in isotopes such as $Lu^{176}$ and $Tm^{170}$, where counts from the gamma rays fall in the region of the $K$ x ray. This factor was determined in $Tm^{170}$ by absorbing the x ray with lead in the manner described by McGowan and Stelson[4] and fitting the shape of the gamma ray to the data. In $Lu^{176}$, the gamma ray was fitted with the same curve (the energy difference is only 5 kv). In all cases, the over-all accuracy is thus assigned a value of 10%.

[4]F. K. McGowan and P. H. Stelson, *Phys. Rev.* (to be published).

## GAMMA RADIATION IN THE DECAY OF $Xe^{133}$

F. Pleasonton

In the course of investigating the charge spectrum of the product atom following the decay of $Xe^{133} \rightarrow Cs^{133}$, a small sample of our source gas was examined with a scintillation spectrometer[1] (NaI). Several gamma rays, of very weak intensity, were found with energies higher than the expected 81 kev, namely, at about 160, 235, 305, and 385 kev. The last of these agrees closely with the 380-kev gamma ray reported by Ketelle and Brosi.[2]

The decay rates of the 81- and 160-kev peaks were followed carefully over a period of 36 days, and it was found that the 81-kev gamma ray yielded a half life of 5.65 days. The 160-kev peak, however, decayed at a rate consistent with a mixture, at the time of initial observation, of 4 parts to 1 of 5.7- and 12.3-day activities, respectively.

For intensity reasons the other peaks were not followed so closely, but over a period of ten days the 235-kev peak decayed at a rate consistent with a mixture of $Xe^{133m}$ (2.3 days) and $Xe^{135}$ (9 hr). All that can be said of the higher-energy peaks is that they decayed somewhat more rapidly than did the 160-kev peak, but less rapidly than the 235-kev peak.

With the exception of the 235-kev gamma ray, the others agree nicely in energy with the levels found in coulomb excitation studies of cesium, as reported by Temmer and Heydenburg[3] (81 and 163 kev) and by Fagg[4] (82, 160, 302, and 379 kev). These transitions can, therefore, be presumed to be characterized as $E2$, $M1$, or some admixture of the two.

After appropriate corrections were made for internal conversion and absorption, the following relative intensities were derived for the gamma rays, in order of increasing energy: 1, $10^{-3}$, $10^{-4}$, and $5 \times 10^{-5}$.

[1]Available through the courtesy of N. H. Lazar.

[2]Cited in I. Bergström, *Arkiv Fysik* 5, 191 (1952).

[3]G. M. Temmer and N. P. Heydenburg, *Phys. Rev.* 104, 967 (1956).

[4]L. W. Fagg, *Bull. Am. Phys. Soc.* 2, 207 (1957).

## CHARGE SPECTROMETRY FOR $Xe^{133}$

A. H. Snell F. Pleasonton

The 5.3-day activity of $Xe^{133}$ consists predominantly of a 0.345-Mev beta decay followed by an 81-kev gamma transition that has a *K*-shell internal-conversion coefficient of about 1.5. (For some new features in the decay scheme, representing branches of low intensity, see "Gamma Radiation in the Decay of $Xe^{133}$," this report.) This means that $Xe^{133}$ should be an interesting candidate for charge spectrometry, because the atoms that escape internal conversion should contribute one kind of charge distribution, and the atoms that undergo internal conversion should contribute another kind of charge distribution; so the total charge spectrum should exhibit an almost balanced combination of the two.

Strong samples of $Xe^{133}$ are available in fission-product separation, and we are indebted to R. E. McHenry of the Operations Division for providing us with two. We allowed the activity to decay for about ten days before starting our measurements, to permit the 9.2-hr $Xe^{135}$ to disappear and to de-emphasize the already feeble 2.3-day $Xe^{133}$ isomer. On the other hand, the readings had to be taken before the weak 12-day $Xe^{131}$ activity could become of appreciable relative importance. By narrowing the slits of the spectrometer, we increased the resolution from 2.8% to 1.9% in energy, full width at half maximum; although this is still insufficient for a clean resolution of masses 131, 133, and 135 at a given charge, it did permit good separation of the charge peaks in the region of charge 20, where they are 5% apart.

The measurements presented difficulties with respect to charges 1 and 2, which did not reproduce well from run to run. Suspecting that the variations were due to collisions in the residual gas and that these collisions would be most probable at the start of the trajectory where the ions are moving slowly and spend most of their time, we performed an experiment in which the large, low-field end of the collecting volume was rendered ineffective. This was done by insertion of a barrier foil halfway along the ring electrodes inside which the ions were being collected. This reduced the effective volume for collecting to 11% of its previous value and also reduced the total number of ions collected to 21% of its previous value. However, it ensured that ions would be collected only from a region of comparatively strong electric field. Two runs of the charge spectrum were taken under this arrangement, which agreed moderately well with a third run taken from the whole collecting volume but disagreed badly with a fourth run also taken from the whole collecting volume under experimental conditions which, so far as we could see, were identical. This last set of observations did, however, show signs of charge degradation in that charges above 8 were all more weakly represented and charges below 8 were all more strongly represented than in the other three sets of data. Consequently we have given this run a weight of one-half in averaging it in with the other three runs. The results thus evaluated are given in Table 1 and in Fig. 1. The indicated errors take into account the lack of reproducibility between the four runs. Statistical errors in counting were much smaller.

The charge spectrum shows very prettily the division into two groups, an initial decline to charge 4 reminiscent of the spectrum for pure beta

**Table 1. The $Xe^{133}$ (5.3-Day) Charge Spectrum**

| Charge | Abundance (%) | Charge | Abundance (%) |
|---|---|---|---|
| 1 | 37.2 ± 7.2 | 12 | 3.03 ± 0.17 |
| 2 | 4.2 ± 0.7 | 13 | 1.61 ± 0.07 |
| 3 | 2.45 ± 0.22 | 14 | 1.00 ± 0.08 |
| 4 | 2.16 ± 0.15 | 15 | 0.63 ± 0.04 |
| 5 | 2.97 ± 0.18 | 16 | 0.31 ± 0.02 |
| 6 | 3.97 ± 0.11 | 17 | 0.13 ± 0.02 |
| 7 | 5.66 ± 0.29 | 18 | 0.049 ± 0.005 |
| 8 | 9.15 ± 0.15 | 19 | 0.019 ± 0.002 |
| 9 | 11.12 ± 0.44 | 20 | 0.008 ± 0.004 |
| 10 | 8.72 ± 0.31 | 21 | 0.005 ± 0.003 |
| 11 | 5.56 ± 0.08 | | |

emission exemplified by $Kr^{85}$ (ref 1) and a subsequent peak reminiscent of that formed by pure internal conversion in $Xe^{131}$ (ref 2). The maximum

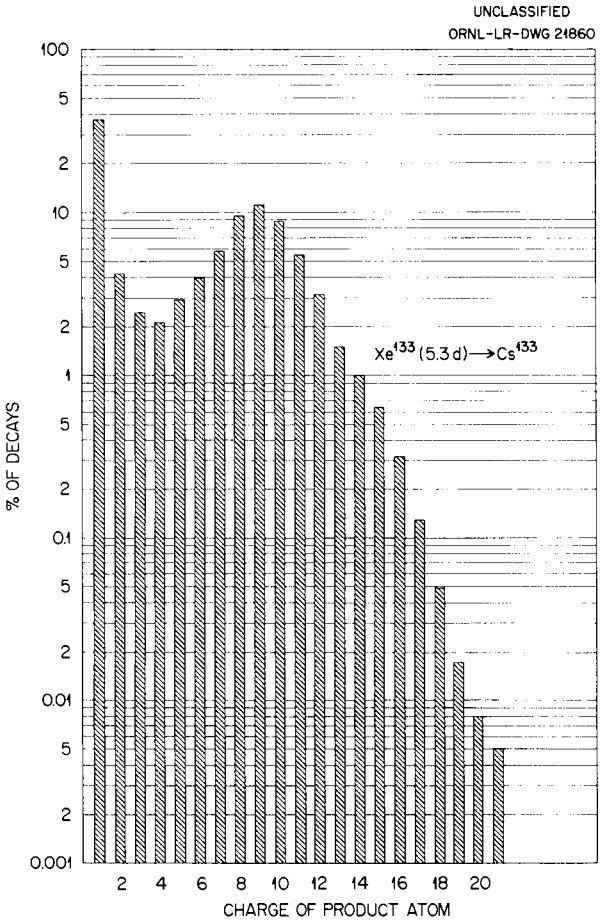


**Fig. 1. Charge Spectrum Following Decay of $Xe^{133}$(5.3-day) → $Cs^{133}$.**

of the internal-conversion peak has shifted from charge 8 in $Xe^{131}$ to charge 9 here, because an additional charge is contributed by the beta particle.

If we use the relative intensities of the two parts of the spectrum to derive an internal-conversion coefficient, using a guess as to how the intensities overlap in the region of the valley, we obtain a value 1.3 ± 0.3. It seems natural to identify this number with the summed internal-conversion coefficients for the *K*, *L*, and *M* shells. Other values of this quantity may be derived from the scintillation work of Bergstrom *et al.*[3] and of Graham and Bell;[4] they are 1.71 and 2.07, respectively. The rough agreement may be gratifying as a test of our interpretation of the charge spectrum, but one would like the numbers to come out more closely. In view of the nonreproducibility of the charge-1 intensity in the present work, it seems probable at this time that some little-understood factors in the new technique may be the main source of the discrepancy.

The barrier experiment showed as a by-product that the ion collecting system is three times as efficient in the small-volume, narrow end of the core as it is in the large-volume, weak field region. Evidently if more voltage could be applied, a healthy increase in intensity could be expected.

---

[1] A. H. Snell and F. Pleasonton, *Phys. Rev.* 107, 740 (1957).

[2] F. Pleasonton and A. H. Snell, *Proc. Roy. Soc.(London)* A241, 141 (1957).

[3] I. Bergström *et al.*, *Arkiv Fysik* 7, 260 (1954).

[4] R. L. Graham and R. E. Bell, *Can. J. Phys.* 31, 377 (1953).

# MOLECULAR DISSOCIATION OF MONOTRITIATED METHANE FOLLOWING RADIOACTIVE DECAY

A. H. Snell F. Pleasonton

The work on the radioactive dissociation of molecules has been continued from TH and $C^{14}O_2$ to the case of $CH_3T$. The monotritiated methane was obtained from the New England Nuclear Company, who stated that it was prepared "by reacting methyl magnesium iodide with carrier-free tritiated water to yield monotritiated methane." The radioactive methane was diluted to a concentration of 5% in ordinary methane, so that under equilibration in its own beta radiation field there would be little chance of more than one tritium atom occurring in combination in a given methane molecule. The specific activity of 1.5 curies per mole was ample for the experiment. The results of the measurements are given in Table 1.

Looking at the weakness of mass 18, we see that a very few of the molecules remain bound, and looking at the strength of mass 15, we see that the dominating process is the one in which the $He^3$ takes its quota of two electrons and departs from the molecule. It does not often leave one of its electrons with the molecule, as indicated by the intensity of charge 3. The ions of mass 16 represent for the most part the $C^{13}$ counterpart of the abundant mode of decay, but their abundance relative to mass 15 seems a little too high to be accounted for by the 1.1% natural abundance of $C^{13}$. Then there is a group of fragments represented by $(CH_2)^+$, $(CH)^+$, and $(C)^+$ which in sum far outweigh the abundance of $H^+$, showing that when hydrogens are dissociated from the $(CH_3)^+$ radical they usually take an electron with them. The weak ions of mass 17 and 18, together with the just-mentioned overabundance of mass 16, seem to imply a small probability that the $He^3$ remain attached at least for the length of time required for passage through the spectrometer. Finally, doubly charged ions of mass 12 and 14 are observed, but not of mass 13 or 15.

These results have a striking parallel in some recent measurements on monotritiated ethane by Hess and Wexler.[1]

The results resemble those for TH and $C^{14}O_2$ in the general aspect that in these cases of pure beta decay the molecular damage is not large in most events, but occasionally disruptions occur that are more drastic than one would perhaps have expected.

[1] D. C. Hess and S. Wexler, *Bull. Am. Phys. Soc.* **2**, 304 (1957).

**Table 1. Molecular Dissociation Following Radioactive Decay in $CH_3T$**

| *e/m* | Ion | Abundance (%) |
|---|---|---|
| 1/1 | $H^+$ | 2.4 ± 0.1 |
| 1/2 | $H_2^+$ | 0.14 ± 0.01 |
| 1/3 | $(He^3)^+$, $H_3^+$ | 0.12 ± 0.01 |
| 1/4 | $(He^3H)^+$ | 0.15 ± 0.02 |
| 1/12 | $(C^{12})^+$ | 4.9 ± 0.1 |
| 1/13 | $(C^{12}H)^+$, $(C^{13})^+$ | 4.0 ± 0.1 |
| 1/14 | $(C^{12}H_2)^+$, $(C^{13}H)^+$ | 4.9 ± 0.1 |
| 1/15 | $(C^{12}H_3)^+$, $(C^{13}H_2)^+$ | 82.0 ± 1.5 |
| 1/16 | $(C^{13}H_3)^+$, $(C^{12}H\,He^3)^+$ | 1.3 ± 0.1 |
| 1/17 | $(C^{12}H_2He^3)^+$ | 0.06 ± 0.01 |
| 1/18 | $(C^{12}H_3He^3)^+$ | 0.06 ± 0.01 |
| 2/12 | $C^{++}$ | 0.08 ± 0.01 |
| 2/14 | $(CH_2)^{++}$ | 0.06 ± 0.01 |

## ALPHA EMISSION FROM $U^{234}$ AND ORIENTED $U^{235}$ NUCLEI

J. W. T. Dabbs L. D. Roberts G. W. Parker

In the semiannual report of September 1956[1] we reported final results on the anisotropy of alpha emission from aligned $U^{233}$ nuclei as a function of the absolute temperature $T$. The experimental results could be summarized by the expression

$$(1) \qquad W(\theta) = 1 - \frac{0.0625}{T} P_2(\cos\theta) ,$$

where $\theta$ is the angle of emission of the alpha particles relative to the $c$ axis of the $UO_2Rb(NO_3)_3$ crystal which was cooled to produce nuclear alignment by quadrupole (Pound) coupling.

This work has now been extended to two new nuclei, $U^{234}$ and $U^{235}$. The method was the same as that described previously.[1,2] For the $U^{234}$ measurements, a single crystal (~1 cc) of (normal U) $UO_2Rb(NO_3)_3$ was grown from solution, and a thin layer of highly diluted $U^{234}$ was grown on this substrate crystal, as before. Measurements were made at 77, 4.2, and 1.15°K of the emission at 0 and 90 deg to the $c$ axis. In the case of $U^{234}$, an even-even nucleus, one expects no anisotropy, since one expects no nuclear alignment in zero-spin nuclei. Thus the measurements served as a check on the methods used in this type of observation. Figure 1 shows the results, where the ratio $W(0 \text{ deg})/W(90 \text{ deg})$ as a function of $1/T$ is plotted in comparison with the results of similar measurements on $U^{233}$ reported previously[3] (also Eq. 1 above). It is seen that, within the statistical errors, no anisotropy was observed, as expected.

In the $U^{235}$ measurements, a similar crystal was prepared, except that a somewhat thicker layer of undiluted $U^{235}$ salt was grown on the substrate crystal, because of the much lower alpha activity of $U^{235}$. The $U^{235}$ used was designated as sample WR-1 and contained only 0.0013% $U^{234}$, 0.004% $U^{236}$, and 0.001% $U^{238}$, and was obtained from the Stable Isotopes Division. In order to provide a magnetic relaxation mechanism, 0.1% of $Np^{237}$ was added to the coating solution, as discussed previously. However, most of this was removed in subsequent ion exchange column processing, and an alpha pulse-height analysis of the actual material showed less than 9% of the total alpha activity to be due to $U^{234}$ and $Np^{237}$ combined (the peaks from these two nuclides are superimposed in such an analysis). If we take the value of 0.0013% $U^{234}$, we calculate that 3.7% of the alpha activity would be due to $U^{234}$. If the 0.1% Np had been retained, the total activity would have been 36.1%; we therefore conclude that the actual sample contained ~0.016% Np, and, judging from the results obtained, this was sufficient to provide an adequate relaxation mechanism.

The uncorrected results of the measurements on $U^{235}$ at 77, 4.2, 1.75, and 1.18°K are shown in Fig. 2. After correcting for the isotropic $U^{234}$ alpha background and the anisotropic $Np^{237}$ alpha activity,[4] we find that the results are consistent with an angular distribution given by

$$(2) \qquad W(\theta) = 1 - \frac{0.073}{T} P_2(\cos\theta) ,$$

[1] L. D. Roberts, J. W. T. Dabbs, and G. W. Parker, *Phys. Semiann. Prog. Rep. Sept. 10, 1956*, ORNL-2204, p 60.

[2] For essentials of the apparatus, see L. D. Roberts, J. W. T. Dabbs, and G. W. Parker, *Phys. Semiann. Prog. Rep. March 10, 1956*, ORNL-2076, Fig. 1, p 3.

[3] L. D. Roberts, J. W. T. Dabbs, and G. W. Parker, *Phys. Semiann. Prog. Rep. March 10, 1957*, ORNL-2302, p 31.

[4] L. D. Roberts, J. W. T. Dabbs, and G. W. Parker, *Phys. Semiann. Prog. Rep. March 10, 1956*, ORNL-2076, p 3–6; *Phys. Semiann. Prog. Rep. Sept. 10, 1956*, ORNL-2204, p 60.

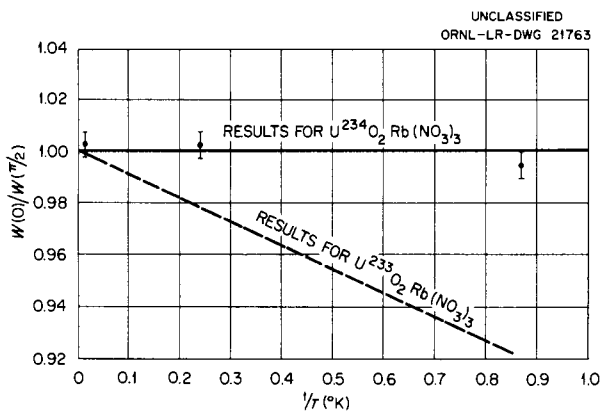


**Fig. 1. The Anisotropy of Alpha Emission from $U^{234}O_2Rb(NO_3)_3$ Between 77 and 1.15°K.**

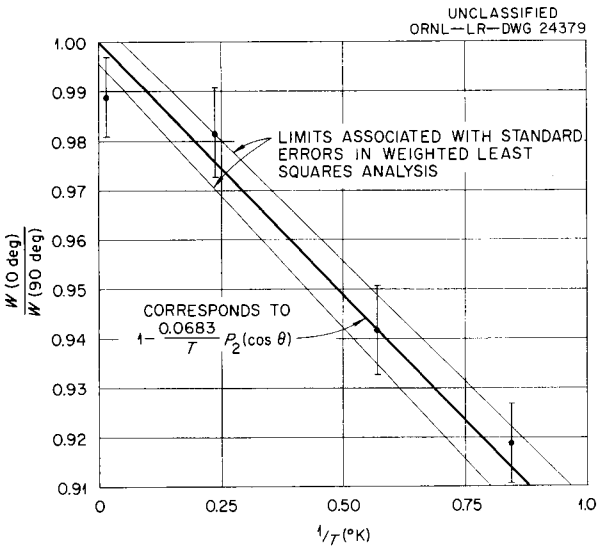


**Fig. 2. The Anisotropy of Alpha Emission from Aligned $U^{235}$ Nuclei.** (Data taken September 1957.)

which is very similar to the $U^{233}$ result (Eq. 1). It is here assumed that no higher terms than $P_2(\cos\theta)$ enter, since $P_4(\cos\theta)$ must enter[5] as $(q/kT)^2$, and here the lowest temperatures involved are such as to make this quantity very small ($\sim$0.001); $q$ is the quadrupole coupling parameter involved in the nuclear alignment.

[5] M. E. Rose, *Phys. Semiann. Prog. Rep. March 10, 1956*, ORNL-2076, p 1.

No analysis of this result in terms of angular momentum theory has been attempted thus far, because of lack of knowledge of the decay scheme of $U^{235}$. Three alpha groups are known to exist.[6,7] The intensities and energies clearly do not fit, for example, a simple Bohr-Mottelson rotational band structure; and no other information is presently available as to the spins and parities of the states in the daughter nucleus, $Th^{231}$. At present, one can only make the observation that we have found three cases ($U^{233}$, $U^{235}$, and $Np^{237}$) in which a strong disagreement exists with the expected result. For this, one assumes the barrier penetration picture of Hill and Wheeler,[8] together with a moderately uniform alpha-particle formation probability over the nuclear surface, and the results of Eisenstein and Pryce[9] relative to the electronic structure of the $UO_2$ bond in $UO_2Rb(NO_3)_3$. The latter result determines the sign of the quadrupole coupling parameter $q$, and hence the direction of the major nuclear axis in the aligned nuclear system.

[6] A. Ghiorso, *Phys. Rev.* 82, 979 (1951).

[7] E. Würger, K. P. Meyer, and P. Huber, *Helv. Phys. Acta* 30, 157 (1957).

[8] D. L. Hill and J. A. Wheeler, *Phys. Rev.* 89, 1102 (1953).

[9] J. C. Eisenstein and M. H. L. Pryce, *Proc. Roy. Soc. (London)* A229, 20 (1955).

## FISSION OF ORIENTED NUCLEI

L. D. Roberts J. W. T. Dabbs G. W. Parker

In the last semiannual report[1] we described the results of an experiment on the thermal fission of aligned $U^{233}$ nuclei. In this experiment it was found that the anisotropy in the angular distribution of the fission fragments from the oriented nuclei was much smaller than that observed for the alpha emission. As we indicated,[1] Bohr has presented[2] a qualitative discussion of fission which is the only model thus far seriously proposed that can be compared with our experiment. In the following, we have formulated the Bohr picture quantitatively and have also applied the methods of angular-momentum theory, as given by Rose,[3] to calculate quantitative predictions.

[1] L. D. Roberts, J. W. T. Dabbs, and G. W. Parker, *Phys. Semiann. Prog. Rep. March 10, 1957*, ORNL-2302, p 31.

[2] A. Bohr, *Proc. Intern. Conf. Peaceful Uses Atomic Energy, Geneva, 1955* 2, 151 (1956).

[3] M. E. Rose, *Phys. Semiann. Prog. Rep. March 10, 1956*, ORNL-2076, p 1; *Elementary Theory of Angular Momentum*, Wiley, New York, 1957.

Bohr suggests that the compound nucleus formed upon the capture of a neutron has a long life compared with a rotation period; that is, the compound state at the saddle point for fission is one of good angular momentum. The nucleus $U^{233}$ has spin $j = 5/2$ and presumably positive parity. For *s*-wave capture with compound-state angular momentum $I = j - 1/2 = 2$, one would expect that the angular momentum of the lowest state would correspond to pure core rotation, while for $I = j + 1/2 = 3$, to conserve parity, the ground state should involve the coupling of an excited nucleon state with possible core rotation. Bohr then assumes that fission will occur along the major nuclear axis. Thus for an aligned nuclear spin system the state of pure core rotation, $I = 2$, should lead to a high degree of anisotropy in the angular distribution with the maximum intensity perpendicular to the axis of alignment, while the anisotropy for the $I = 3$ state might be expected to be less strong, since the nucleon-core coupling would lead to a more complex (i.e., less well-defined) core motion. We will now present a formulation of these ideas.

In Fig. 1 we define, in accord with Bohr, the angular-momentum quantum numbers for a strongly deformed nucleus possessing axial symmetry. The coupling scheme is characterized by the three

UNCLASSIFIED
ORNL-LR-DWG 24593

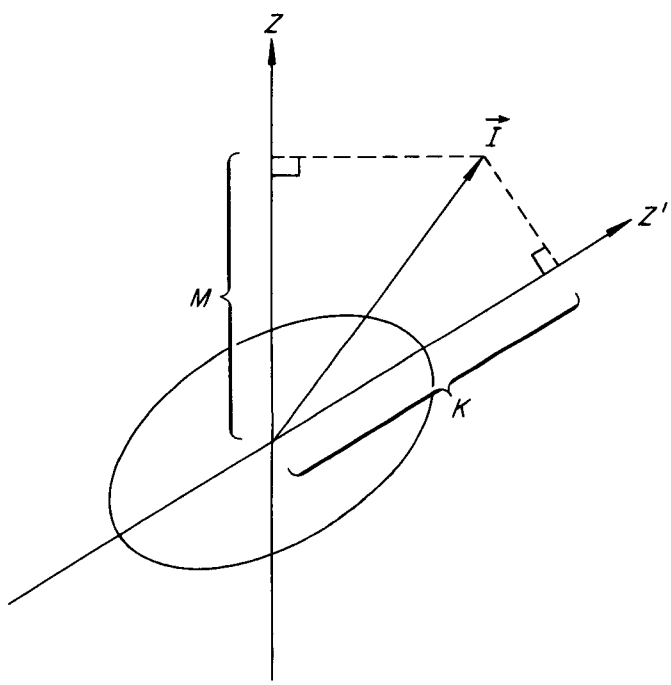


**Fig. 1. Angular Momentum Quantum Numbers for a Strongly Deformed Nucleus.**

constants of motion: the total angular momentum, $I$, its projection, $M$, on an axis fixed in space (the axis of nuclear alignment), and its projection, $K$, on the nuclear symmetry axis, $Z'$. The separation of the nuclear motion into rotational and intrinsic modes corresponds to the existence of approximate solutions

of the nuclear wave equation of the type

$$\psi = \sqrt{\frac{2I+1}{16\pi^2}} \left[ \phi_{\tau,K} D^I_{M,K}(\alpha,\beta,\gamma) + (-)^I \phi_{\tau,-K} D^I_{M,-K}(\alpha,\beta,\gamma) \right] , \tag{1}$$

where $\alpha$, $\beta$, $\gamma$ are the Eulerian angles, the $D^I_{M,K}$ are symmetric top wave functions, and $\phi_{\tau,K}$ represents the intrinsic structure characterized by $K$ and the remaining set of quantum numbers $\tau$. Here, we require only that

$$(\phi^*_{\tau',K'}, \phi_{\tau,K}) = \delta_{\tau',\tau} \delta_{K',K} .$$

We associate $\psi$ with the nuclear compound state after neutron capture but, of course, before fission. In our nuclear alignment experiment, however, the nuclei with wave functions $\chi_{jm}$ were oriented in a known way before neutron capture, and we must now relate this orientation to that of the compound-state system. The respective populations would be $P(m)$ and $P(M)$. In the aligned compound-state system the angular distribution $W(\alpha,\beta,\gamma)$ of the nuclear symmetry axis is given by

$$W(\beta) = \sum_M \iint |\psi|^2 \, d\alpha \, d\gamma \, P(M) \propto \sum_M |D^I_{M,K}|^2 \, P(M) . \tag{2}$$

In the capture of a neutron of spin projection $\mu$ this reduces to

$$W(\beta) \propto \sum_{m,\mu} |D^I_{M,K}|^2 \cdot |C(j, \tfrac{1}{2}, I; m, \mu)|^2 \, P(m) , \tag{3}$$

with $M = m + \mu$. However,

$$\begin{aligned} |D^I_{M,K}|^2 &= (-)^{M-K} D^I_{M,K} D^I_{-M,-K} \\ &= \sum_\nu (-)^{M-K} C(I,I,\nu; M,-M) \, C(I,I,\nu; K,-K) \, P_\nu(\cos\beta) . \end{aligned} \tag{4}$$

In the above expressions the $C$'s are Wigner coefficients, and $P_\nu(\cos\beta)$ is the $\nu$th Legendre polynomial with $\beta$ measured from the $Z$ axis, Fig. 1.

By combining these relations, one obtains

$$W(\beta) \propto \sum_{m,\mu,\nu} (-)^{m-K+\mu} C(I,I,\nu; K,-K) \, C(I,I,\nu; M,-M) \cdot |C(j, \tfrac{1}{2}, I; m, \mu)|^2 \, P(m) \, P_\nu(\cos\beta) . \tag{5}$$

We may now recouple the angular momenta and sum over $\mu$ to obtain

$$\sum_\mu (-)^{m-K+\mu} C(I,I,\nu; M,-M) \cdot |C(j, \tfrac{1}{2}, I; m, \mu)|^2 = (-)^{m-K+2j+\frac{1}{2}-\nu} (2I+1) \, W(j,I,j,I; \tfrac{1}{2},\nu) \, C(j,j,\nu; m,-m) , \tag{6}$$

where $W(j,I,j,I; \frac{1}{2},\nu)$ is a Racah coefficient. Then the angular distribution becomes

$$W(\beta) \propto \sum_\nu (-)^{j+\frac{1}{2}-K-\nu} C(I,I,\nu; K,-K) \, W(j,I,j,I; \tfrac{1}{2},\nu) \, S_\nu P_\nu , \tag{7}$$

where, in a similar notation to that of Rose,[3] we define $S_\nu$ as

$$S_\nu = \sum_m (-)^{j+m} C(j,j,\nu; m,-m) \, P(m) . \tag{8}$$

Equation 7 gives the angular distribution of the nuclear symmetry axis. Bohr identifies the angular distribution of the fragments after fission with this distribution of the $Z'$ axis before fission. Thus within this identification Eq. 7 gives the angular distribution of the fragments.

A possible alternative treatment would proceed directly from angular-momentum theory. In the following we use this theory to treat, somewhat arbitrarily, the case in which one fragment may have an intrinsic spin $\sigma$, with the other fragment having intrinsic spin zero. We make the basic assumptions that the wave function describing the fission fragments is a spherical harmonic, $Y_L^M$, and that the interaction energy, $H'$, leading to fission is of the form

$$H' = \sum_M (-)^M Y_L^{-M} T_L^M \quad . \tag{9}$$

Here the tensor $T_L^M$ will contain the internal nuclear coordinates, and $L$ is the orbital angular momentum of the fragments. Proceeding from this point without further assumption, we obtain the angular distribution

$$W_L(\beta) \propto (2I+1) \sum_\nu (-)^{I+j-\frac{1}{2}-\nu} C(L,L,\nu;0,0)\ W(I,I,L,L;\nu,\sigma)\ W(j,I,j,I;\tfrac{1}{2},\nu) \cdot G_\nu P_\nu(\cos\beta) \ , \tag{10}$$

where

$$G_\nu = \sum_m (-)^{j-m}\ C(j,j,\nu;m,-m)\ P(m) \ , \tag{11}$$

in accord with the notation of Rose.[3]

If we consider the case in which all the angular momentum is carried away in orbital motion (i.e., $\sigma = 0$ and $L = I$), Eq. 10 reduces to

$$W_I(\beta) \propto \sum_\nu (-)^{j-I-\frac{1}{2}}\ C(I,I,\nu;0,0)\ W(j,I,j,I;\tfrac{1}{2},\nu)\ G_\nu P_\nu(\cos\beta) \ . \tag{12}$$

We note that $G_\nu$ is equal to $S_\nu$ within a phase and that for the case $K = 0$, Eqs. 12 and 7 are the same within a normalization factor (which includes a phase). Thus in the case where the compound nucleus is in a state of pure core rotation, the picture of Bohr corresponds exactly to this direct angular-momentum-theory calculation where the fragments carry off no intrinsic angular momentum.

In the angular-momentum-theory result (Eq. 12) we now note that, to terms in $\nu = 2$, $W_I(\beta)$ is the same for both compound states, that is, for $I = j + 1/2$ and for $I = j - 1/2$. Then for either value of $I$ we obtain

$$W_I(\beta) \propto 1 - \frac{(2j-1)(2j+2)}{12}\left[\frac{180(2j-2)!}{(2j+2)!}\right]^{1/2} \sqrt{2j+3}\ G_2 P_2(\cos\beta) \ . \tag{13}$$

In Bohr's picture, for a nucleus of even parity, the compound state will go over the saddle point in fission with $K = 0$ for $I$ even, but will require $K \neq 0$ for $I$ odd. Similarly for odd parity we would expect that $K = 0$ for $I$ odd but that $K \neq 0$ for $I$ even. Thus to terms in $\nu = 2$ the Bohr model predicts a different angular distribution of the fragments for the two values of $I$, whereas the simple angular-momentum-theory calculation based on $I = L$ gives a result independent of $I$.

For $U^{233}$ the nuclear alignment arises from electric quadrupole coupling, with a spin Hamiltonian

$$\mathcal{H} = q[j_z^2 - \tfrac{1}{3}j(j+1)] \quad , \tag{14}$$

where $q$ is the quadrupole coupling constant. From specific-heat experiments,[4] we have a tentative value of $q = -0.027\ \mathrm{cm}^{-1}$. With $j = \frac{5}{2}^+$ for $U^{233}$, Eq. 11 gives

$$G_2 = -\frac{2}{3}\sqrt{\frac{7}{3}}\,\frac{q}{kT} \quad . \tag{15}$$

Then for the case $I = j - 1/2$ and $K = 0$, to terms in $\nu = 2$, either Eq. 7 or Eq. 13 gives

$$\begin{aligned} W_I(\beta) &\propto 1 + \frac{8}{3}\frac{q}{kT}P_2(\cos\beta) \\ &\propto 1 - \frac{0.104}{T}P_2(\cos\beta) \quad . \end{aligned} \tag{16}$$

Similarly, Eq. 7 becomes, for the case $I = j + 1/2$,

$$W_I(\beta) \propto 1 - \frac{[3K^2 - I(I+1)]}{I(I+1)} \cdot \frac{(2j-1)(2j+2)}{12}\left[\frac{180(2j-2)!}{(2j+2)!}\right]^{1/2}\sqrt{2j+3}\cdot G_2 P_2(\cos\beta) \quad . \tag{17}$$

This equation is the same as Eq. 13, except for the multiplying factor $\alpha = [3K^2 - I(I+1)]/I(I+1)$. For our case of $I = j + 1/2 = 3$, $K^2$ may take the values 9, 4, 1. The corresponding values of $\alpha$ are $+5/4$, 0, and $-3/4$. As indicated above, $K$ presumably cannot be zero for parity reasons. Using our calculated value for $G_2$, Eq. 15, Eq. 17 becomes

$$K^2 = 9; \quad W_I(\beta) \propto 1 + \frac{0.13}{T}P_2(\cos\beta) \quad , \tag{18a}$$

$$K^2 = 4; \quad W_I(\beta) = \text{const; (isotropic distribution)} \quad , \tag{18b}$$

$$K^2 = 1; \quad W_I(\beta) \propto 1 - \frac{0.078}{T}P_2(\cos\beta) \quad . \tag{18c}$$

Thus our observation that the anisotropy is very small could be fitted into the Bohr picture by assuming that $I = j + 1/2 = 3$, with the rather high intrinsic spin $K = 2$. We also note that the angular-momentum-theory calculation leading to Eq. 10 would lead to isotropy for $L = 0$, $I = \sigma$. Wheeler has suggested that fission occurs predominantly through one channel, and within the framework of the Bohr model our result would suggest this channel as $I = 3$, $K = 2$ for the thermal fission of $U^{233}$. If we should assume that in thermal fission several channels are involved, it is clear that a suitable linear combination of these (i.e., a suitable linear combination of Eqs. 16 and 18*a*) would also give isotropy.

---

[4] L. D. Roberts, J. W. T. Dabbs, and G. W. Parker, *Phys. Semiann. Prog. Rep. Sept. 10, 1956*, ORNL-2204, p 60.

Note added in proof: Using a new type of fission counter which gives quite good resolution even near 1°K, we find a large anisotropy in the fragment angular distribution for the theoretical fission of oriented $U^{233}$ nuclei. It is comparable in magnitude to that observed for alpha-particle emission *but of opposite sign*. With the use of the above theory, this suggests that the fission process has a substantial contribution from the state $K = I$.

---

## NEUTRON DIFFRACTION STUDY OF THE MAGNETIC PROPERTIES OF $MnBr_2$

E. O. Wollan W. C. Koehler M. K. Wilkinson

### INTRODUCTION

Manganous bromide crystallizes in the $CdI_2$ layer type of hexagonal structure with one molecule per unit cell with the $Mn^{++}$ ion at (000) and the two $Br^-$ ions at $\left(\frac{1}{3}, \frac{2}{3}, u\right)$ and $\left(\frac{2}{3}, \frac{1}{3}, u + \frac{1}{2}\right)$, in which $u \cong 0.25$, $a_0 = 3.868$ Å, and $c_0 = 6.272$ Å.

Measurements by Stout have shown this compound to have a very pronounced specific-heat anomaly at about 2.16°K, indicating an antiferromagnetic transition at this temperature.

Neutron diffraction measurements by the powder method were carried out about two years ago on this and a number of other layer-type compounds of the iron group which were shown to have layer-type antiferromagnetic structures in which the spins in each hexagonal layer are ferromagnetically aligned and the spins in neighboring layers oppositely aligned. The powder pattern of $MnBr_2$ was also consistent with this interpretation, the most prominent magnetic reflection at $2\theta \cong 5$ deg being indexable as $(00l)$ type. There was observed, however, in $MnBr_2$, short-range order above the Néel temperature that was suggestive of antiferromagnetic ordering in the hexagonal layers, whereas in the other bromide compounds studied this short-range order had a ferromagnetic character consistent with this type of ordering within the layers. As a result of these uncertainties it was decided to make a single-crystal neutron diffraction study of this compound. The magnetic structure has now been found to be of a more complicated type than was first proposed.

### CRYSTAL SAMPLE AND GONIOMETER MOUNTING

The neutron spectrometer with single-crystal goniometer and magnet which was used in this study was briefly described in a previous report,[1] to which the reader is referred for construction details.

The $MnBr_2$ crystal was grown by the method of slowly moving the material held in a sealed-off quartz crucible through the heated region of a specially constructed furnace.[2] Several attempts were made before a satisfactory crystal was obtained. The best results seem to be obtained for crystals of this type when the inner walls of the crucible are coated with Aquadag.

Since this material forms very soft crystals, care must be taken in the process of cutting them to the proper size. Therefore a thin, circular, aluminum template of the desired size ($\frac{5}{16}$ in. in diameter) was glued to a smooth cleavage plane of a rather large piece of the boule. A fine jeweler's saw was then used to cut a cylinder of the diameter of the template. The desired thickness was then achieved by cleaving thin layers from the back of this cylinder. The aluminum template was left in place, and the cylinder was fitted into a thin-walled, internally threaded (No. 80), cylindrical, aluminum box into which was screwed a thin cover plate to hold the crystal firmly in place. The box, which was made with a small stud in its back, was firmly

[1] E. O. Wollan *et al.*, *Phys. Semiann. Prog. Rep. Sept. 10, 1956*, ORNL-2204, p 49.

[2] We are indebted to J. Manning for growing the the crystals used in this study.

screwed in place in the center of the gear plate of the goniometer.

The crystal was mounted with the $c$ axis horizontal and perpendicular to the axis of rotation of the gear. Any $(hkl)$ plane can thus be brought into a vertical position by rotation about the horizontal axis. For convenience the orientations about this axis will be referred to as the angle $\beta$. After a given plane has been brought into the vertical position, it can be turned to the proper reflecting angle relative to the incident beam by rotation about the vertical axis within the cryostat. This orientation will be referred to as the angle $\alpha$, the angle $\theta$ being reserved for the readings of the spectrometer table which orients the magnet and cryostat as a whole.

## THE ANTIFERROMAGNETIC STRUCTURE

The early powder data, as mentioned above, were first interpreted in terms of an antiferromagnetic sheet structure with the moments aligned ferromagnetically within each hexagonal layer and with oppositely directed spins in alternate layers.

From the single-crystal measurements it was, however, quickly ascertained that the first reflection referred to above was not of the $(00l)$ type; later it was identified as an $(h0l)$ type of reflection. Several other reflections of this type were also observed and were all found to have 120-deg symmetry about the $c$ axis of the crystal. A concerted effort was then made to devise an antiferromagnetic array of moments which would account for the spacing and symmetry of the observed reflections. This met with no success, and it was not until effects on the reflected intensity of magnetic fields applied to the sample were investigated that the character of the antiferromagnetic structure became understandable.

It was observed that if a magnetic field of about 1000 oersteds or greater was applied along the scattering vector of a given $(h0l)$ type of reflection the intensity of that reflection increased by a factor of about 3 and that if this field was then turned off most of the increase of intensity remained frozen in. It was also observed that after the intensity had been frozen in for a particular $(h0l)$ reflection all other $(h0l)$ reflections in the same plane (i.e., for a given value of the angle setting $\beta$ of the goniometer, e.g., $\beta$ = 35 deg) possessed about the same permanent increase in intensity, a factor of about 3, over their original no-applied-field values. It was then further observed that the other sets of $(h0l)$ reflections at 120-deg intervals ($\beta$ = 155 and 275 deg) around the $c$ axis were essentially extinguished. It thus became evident that the antiferromagnetic structure did not possess threefold symmetry about the $c$ axis of the crystal but only a onefold axis, which, in the absence of an applied magnetic field, could grow with equal probability along any one of three $[h0]$ directions. There is thus indicated a type of antiferromagnetic domain growth in this compound, the nature of which is different from that normally associated with this term in that it involves the direction of growth of the antiferromagnetic structure rather than the orientation of the spins within the structure.

The domain properties of this system and their behavior under applied magnetic fields are discussed in more detail in the following section. For the purposes of determining the unit cell of the antiferromagnetic structure, it was necessary to determine the structure of a single domain, and the fact that in this compound the crystal could be permanently prepared below $T_N$ as a single antiferromagnetic domain was a simplifying factor in the determination of the structure.

From the spacing values and the crystal orientations of the most intense reflections, which were of the $(h0l)$ type, it was possible to determine the projection of the unit cell perpendicular to the plane of the $c$ axis and the $[h00]$ direction.

In determining the indices of the crystal reflections, the powder data were used to ascertain the counter setting $(2\theta)$ for a given reflection in those cases where resolved magnetic peaks had been observed. When the crystal was so adjusted as to bring intensity into the counter at a given $2\theta$, the counter was scanned over the peak to obtain the optimum $2\theta$ value for the reflection. This gives directly the spacing value for the reflection.

The orientation of some of the observed $(h0l)$ type of reflecting planes is shown in the upper part of Fig. 1. At this stage of the magnetic structure determination there was no information available on the orientation of the spins of the various manganese atoms relative to the crystal axes, and it was necessary to make deductions on the basis of phase relationships only. Since the smallest angle reflection which was observed, indexed as (101) on a hexagonal cell $4 \times 4 \times 4$ times larger

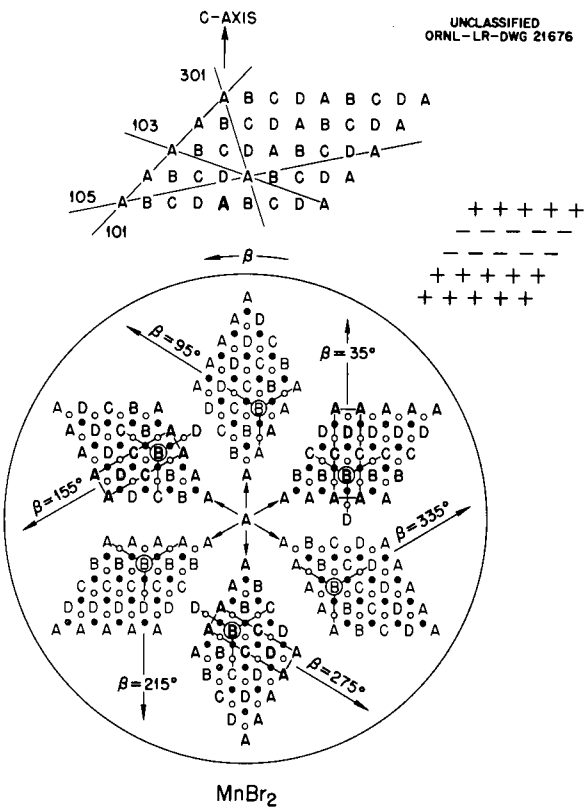


**Fig. 1. Magnetic Structure and Related Domains in $MnBr_2$.** The upper part of this figure shows the projection of the magnetic cell on an $(h0l)$ plane. The lower part shows the hexagonal layers for the six possible directions of domain growth. The bolder regions represent the actual domain growth directions. Two layers of bromine ions above the plane of metal atoms are shown by the open and shaded circles. The upper right corner shows the actual spin assignments. Other features are discussed in the text.

than the chemical cell, it was logical to assume that these planes passed through atoms of like spin orientation. The spins (or phases) of these atoms were thus labeled $A$, and the intervening atomic layers were correspondingly assumed to be of like spin and were labeled $B$, $C$, and $D$. It should be noted that Fig. 1 represents the projection of atoms on the plane, atoms $B$ and $D$ being in a different plane than atoms $A$ and $C$. From the characteristics of the cell represented by this figure it became possible to predict the presence or absence of certain $(h0l)$ types of reflections. It is interesting to note from the figure that planes of index $(\bar{1}01)$ are of a different type than those of index $(101)$, in that the former pass through both $A$ and $C$ types of atoms. As will be seen, the reflections are observed for planes of the $(\bar{1}01)$ type. This fact has significance not only for the antiferromagnetic structure of a single domain but also for the domain properties associated with the structure. Also, as can be noted in Fig. 1, all $(h0l)$ planes for which reflections are observed have the same structure factor, since they correspond to spacings which always have the spin sequence $ABCDA$.

Having thus determined certain properties of the magnetic cell from reflections of the $(h0l)$ type, it is necessary to show the other cell dimension from the more general $(hkl)$ type of reflections. The results up to this point are suggestive of a cell having a spin arrangement in the hexagonal layers corresponding to that shown in, for example, the upper right section of the lower part of Fig. 1. If this is the proper spin arrangement, the antiferromagnetic structure can be represented in terms of an orthorhombic cell, whose $a$ and $b$ axes are outlined in Fig. 1 in the hexagonal layers.

The observed reflections, shown in the first column of Table 1, agree in angle of orientation and spacing value with the orthorhombic cell referred to in connection with Fig. 1 and for which a half of the cell is represented by the atoms outlined by the dashed lines in Fig. 2.

The second step in obtaining the actual antiferromagnetic structure involves a determination of the orientation of the spins relative to the axes of the crystal. This can be obtained from a determination of the relative intensities of the various reflections which are dependent on the values of $q^2 = 1 - (\bar{e} \cdot \bar{S})^2$, where $\bar{e}$ is the unit scattering vector and $\bar{S}$ is a unit vector parallel to the atomic spin vector, the assumption being made in this representation that all spins are parallel or antiparallel to a single direction in the crystal. To make significant relative intensity measurements on the magnetic reflections, it was first required that a check be made of the importance of absorption and extinction in the crystal. To do this, several nuclear reflections were studied, and it was found that for $MnBr_2$ crystals of the size used neither absorption nor extinction had a significant effect on the observed intensities. The cross-section

UNCLASSIFIED
ORNL-LR-DWG 22136R

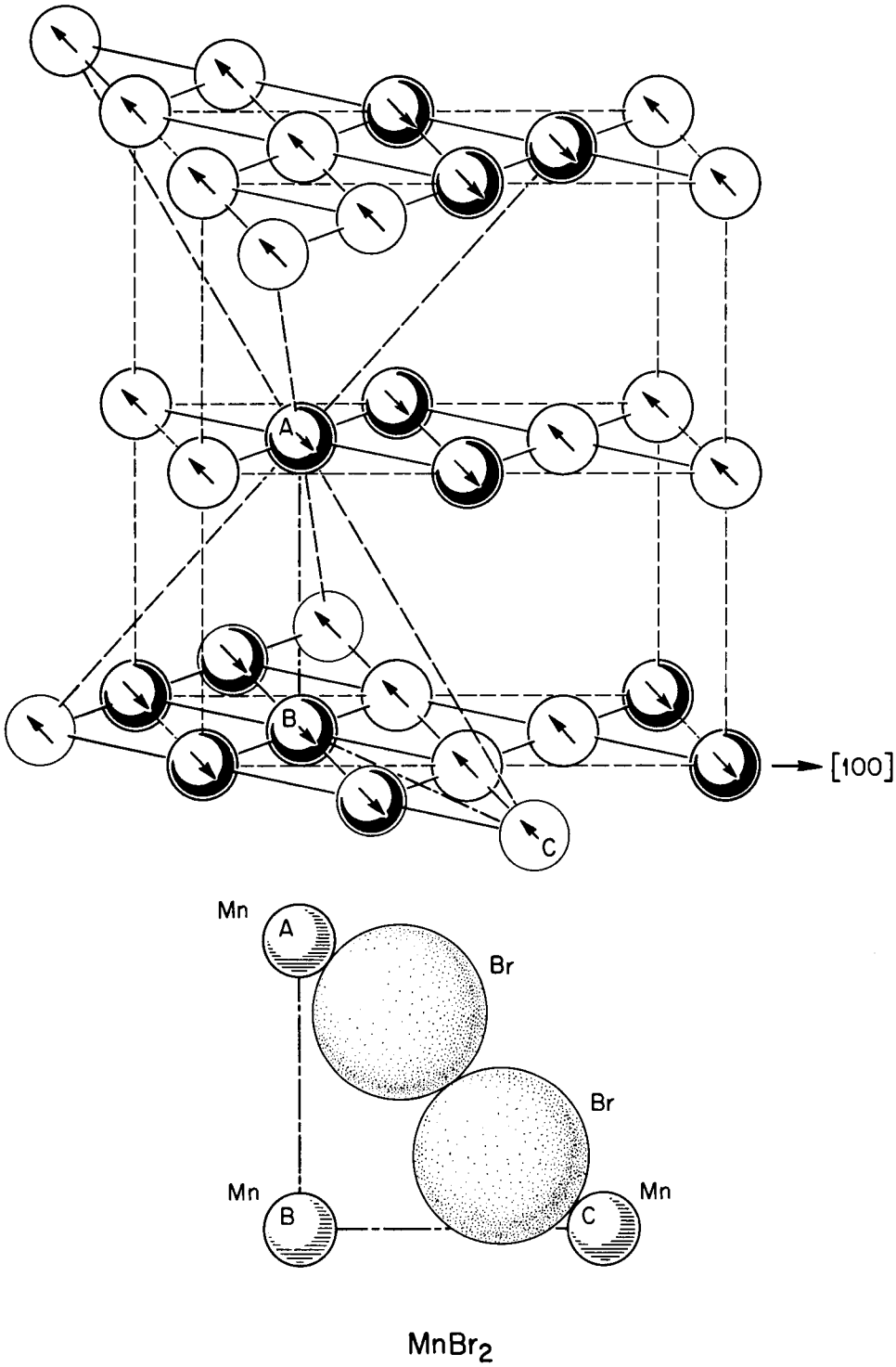


**Fig. 2. Possible Coupling Mechanism for $MnBr_2$.** Upper part of figure shows half of the orthorhombic antiferromagnetic cell. The radial lines indicate a means of antiferromagnetic coupling along lines of bromine ions as shown in the lower part of figure.

Table 1. Comparison of Observed and Calculated Intensities for $MnBr_2$

| Orthorhombic ($bkl$) | $2\theta$ | $\gamma$ | $q^2$ | 70% Saturation | |
|---|---|---|---|---|---|
| | | | | $F^2_{obs}$ (barns) | $F^2_{calc}$ (barns) |
| 101 | 5° 14′ | 61° 56′ | 1 | 0.56 | 0.61 |
| 103 | 8° 42′ | 31° 58′ | 1 | 0.54 | 0.56 |
| 105 | 13° 8′ | 20° 30′ | 1 | 0.44 | 0.50 |
| 107 | 17° 52′ | 14° 44′ | 1 | 0.35 | 0.39 |
| 301 | 14° 4′ | 79° 54′ | 1 | 0.49 | 0.47 |
| 303 | 15° 42′ | 61° 52′ | 1 | 0.41 | 0.42 |
| 305 | 18° 36′ | 48° 15′ | 1 | 0.39 | 0.36 |
| 307 | 22° 12′ | 51° 19′ | 1 | 0.35 | 0.30 |
| 111 | 16° 48′ | 81° 34′ | 0.07 | 0.028 | 0.039 |
| 113 | 18° 12′ | 66° 1′ | 0.31 | 0.092 | 0.085 |
| 115 | 20° 44′ | 53° 26′ | 0.35 | 0.110 | 0.126 |
| 117 | 24° 4′ | 46° 4′ | 0.45 | 0.130 | 0.169 |
| 311 | 21° 20′ | 83° 21′ | 0.43 | 0.134 | 0.134 |

values, $F^2$, for the magnetic reflections as determined without any correction for these effects are tabulated in column 5 of Table 1. These quantities are in good accord with corresponding relative values calculated on the basis of the spins being parallel to the short $b$ axis of the orthorhombic cell. This point is further verified (see "Domain Structure," which follows) by magnetic field measurements made on the crystal prepared as a single antiferromagnetic structure domain.

The third step in determining the antiferromagnetic structure involves the identification of the spin orientation sequence associated with the letters $ABCDA$, which up to now have been used to identify the various spins in the cell. To do this, it was necessary to make absolute intensity measurements of the magnetic reflections, which were accomplished by determining these intensities relative to those of a number of nuclear reflections for which the absolute scattering power could be directly deduced from the known coherent neutron scattering cross sections of manganese and bromine. It was required, however, that the parameters of the bromine ion positions in the crystal be accurately known. A check of several nuclear reflections involving different bromine ion contributions gave good consistency on the basis of the listed bromine parameters and provided the instrumental constants from which the intensities of the magnetic reflection could be determined on an absolute basis. An additional factor is involved in the absolute intensity determination: the degree of saturation of the spin system. It is to be expected that the $Mn^{++}$ ion will have a magnetic moment associated with a spin only value of 5/2. The low Néel temperature in this compound, however, makes it impossible for saturation of the spin system to be obtained at the lowest temperature (1.35°K) reached in this experiment. A reasonable estimate based on the temperature saturation curve of Fig. 6 would suggest that one is within about 20% of saturation at 1.35°K; the field saturation of a single domain was found to be incomplete to about 10%. To within a reasonable limit of accuracy, then, the intensity saturation can be expected to be about 30% higher than the measured values. The measured absolute intensities of the various reflections listed in column 5 of Table 1 were used in determining the magnetic cross-section values, $F^2$. These values can be compared with the calculated values listed in the last column of Table 1, which have been arbitrarily reduced to take account of the lack of saturation.

These calculations are based on the spin assignment shown in the upper right corner of Fig. 1, in which the spins $ABCDA$ in each hexagonal layer have been taken in the sequence $++--+$, where the + and − signs represent the spins parallel and antiparallel to the short $b$ axis of the orthorhombic antiferromagnetic cell. Half the cell for this structure is shown in Fig. 2. It is evident that a smaller monoclinic cell could be used to describe this structure, but indexing on the basis of the orthorhombic cell is somewhat simpler.

## DOMAIN STRUCTURE

When the $MnBr_2$ crystal is lowered in temperature below the Néel point (2.16°K) in the absence of a magnetic field, it develops a threefold symmetry about the $c$ axis which, as has been implied in the previous section, is associated with the formation of antiferromagnetic structure domains. These domains have been found to grow with equal probability along three of the hexagonal axes of the crystal. Most of the properties of these domains can be studied by the application of a magnetic field along the scattering vector of an $(h0l)$ type of magnetic reflection. For convenience the strong (101) type of reflection has been used in most cases.

When the crystal is brought to a low temperature in the absence of a field and a particular set of (101) planes (at $\beta$ = 35 deg, e.g.) is brought into position to reflect, the effect of magnetic fields of varying magnitude on the intensity of this reflection is represented by the data plotted in the upper curve of Fig. 3. For small fields there is at first no noticeable increase in intensity, but after some critical field has been reached, which for this reflection is of the order of 400 oersteds, there is an abrupt increase in intensity associated with this reflection which levels off at something like three times the no-field value. If the field is then turned off, a major fraction of this increase in intensity remains frozen in. An investigation of the (101) type of reflections at 120 deg in $\beta$ ($\beta$ = 155 and 275 deg) away from this position, whose intensities before the application of the field were comparable with those at $\beta$ = 35 deg, reveals that their intensities have dropped to essentially zero value. The fact that the crystal remains as a single antiferromagnetic domain after the field has been removed is undoubtedly associated with the fact that there appears to be a definite energy associated

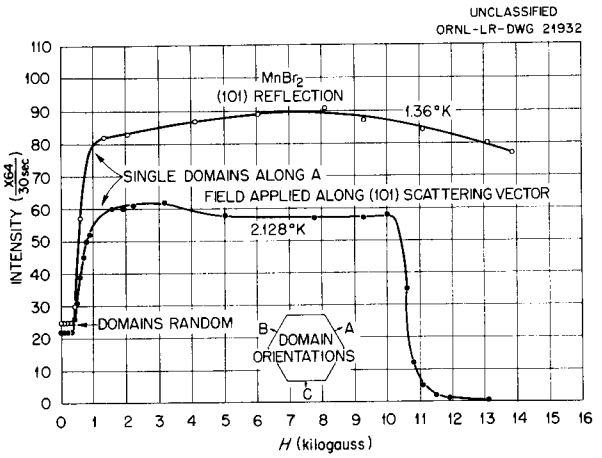


**Fig. 3. Domain Behavior and Intensity Changes as a Function of Applied Magnetic Field for Two Temperatures.** Drop in lower curve at 10.5 kilogauss corresponds to point at which $T > T_N(H)$.

with the structure domain reorientation, as evidenced by the requirement of a minimum field value to bring about the change. The fact that the over-all intensity increase was not exactly equal to three is evidence that the distribution of the domains among the three orientations was not exactly equal. It should also be pointed out that the very abrupt change in intensity shown in Fig. 3 is not always realized. If the crystal has remained at low temperatures during a process of study in which many cyclic changes in domain orientation have been effected, there is a tendency for the beginning of the magnetization curve to be rounded off. This may well be associated with the physical size of the domains associated with their respective distributions along one or the other of the threefold axes.

Curves similar to those of Fig. 3 were also obtained for other reflections of the $(h0l)$ type. Reflections of the $(hkl)$ type were, however, found to disappear with the application of a field along their respective scattering vectors. This is readily accounted for by the field direction along the scattering vector of these planes being more optimally oriented to stabilize another domain direction than that associated with the particular $(hkl)$ reflection in question.

It was shown in the previous section on the basis of intensity measurements that the spins are parallel to the short axis of the magnetic structure, that is, perpendicular to a [100] hexagonal direction.

It was thus of interest to determine the effectiveness of a magnetic field in reorienting the domains as a function of the orientation of the field in the plane perpendicular to the [100] direction. Accordingly, the crystal was prepared, by initial field application, as a single domain oriented along, for example, $\beta$ = 155 deg. The (101) reflection at $\beta$ = 35 deg was then studied. The intensity was observed with no field, and in one case the crystal was tilted in a angle to bring the field vector along the [100] direction, with $\beta$ still equal to 35 deg and a small field applied and then turned off. The crystal was returned to its (101) reflecting position and the intensity measured. This process was repeated for various field values, and for this case the results are represented by the upper curve of Fig. 4. Similar curves were obtained with various orientations of the field vector $H$ relative to the hexagonal plane of the crystal. Successive curves obtained are also shown in Fig. 4. An analysis of these data shows that the field which is effective in orienting domains from one threefold axis to another is given by $H_{eff} = H \cos \gamma$. This seems to be a reasonable result and substantiated the spin orientation assignment obtained from the relative intensity measurements discussed previously.

Another domain study was made by determining the intensity associated with each of the three domain directions as a function of the angle $\beta$ at which a magnetic field was applied. The measurements were made on the (101) reflection for which the scattering vector makes an angle of 28 deg with the hexagonal layers, and the magnetic field ($H$ = 4 kilo-oersteds) was always applied at this same angle of inclination. The various (101) magnetic reflections appear at $\beta$ = 35, 155, and 275 deg. The field was applied at a given value of $\beta$, say 30 deg; it was then turned off, and the intensities of the reflections at all three $\beta$ angles were determined. This operation was repeated with the field successively turned on and off

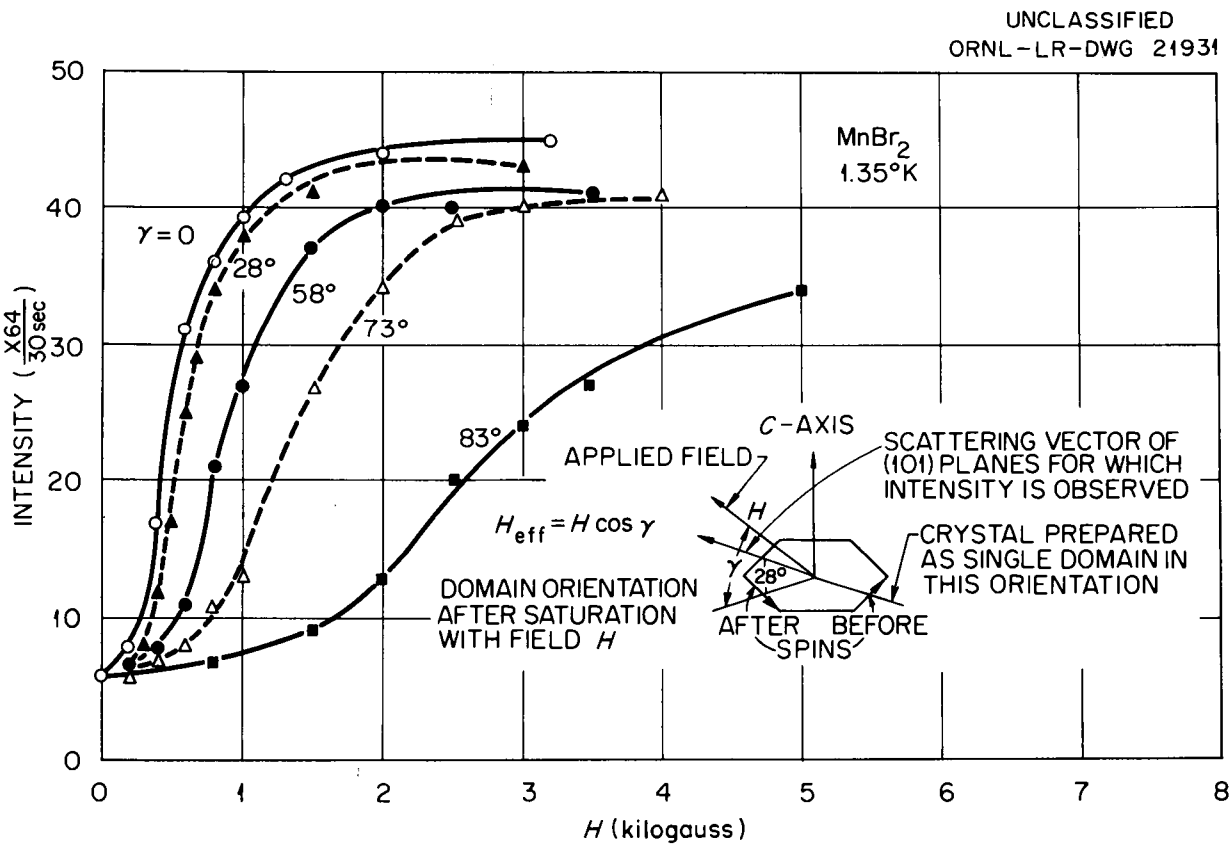


**Fig. 4. Effect of Magnetic Field as a Function of Angle $\gamma$ of Inclination with Hexagonal Layers.** Field effective in flipping domains $H_{eff} = H \cos \gamma$.

at other $\beta$ orientations of the crystal. The resultant data are represented in Fig. 5. It is observed that a single domain direction is stable as long as the field is applied within a range of $\beta$ of approximately 30 deg on either side of the direction of the scattering vector for the particular domain in question. The fact that the intensity data show pronounced irregularities is not too surprising, since there may be statistical fluctuations in the sizes of domains which develop, and these effects may be influenced by minor distortions which were present in the crystal.

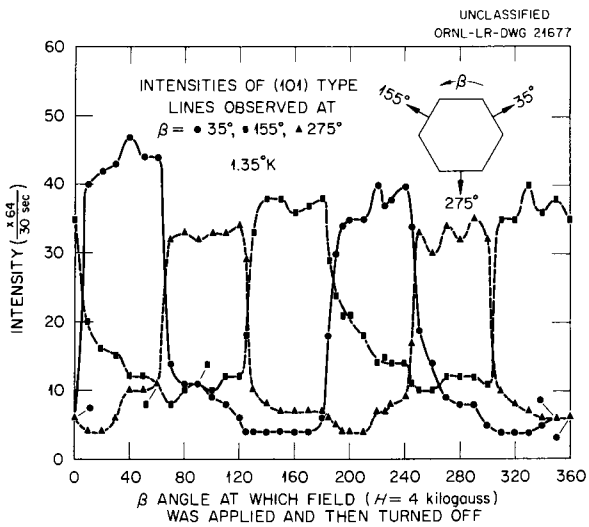


**Fig. 5. Domain Behavior as a Function of Angle $\beta$ Around the $c$ Axis at Which Magnetic Field Is Applied.**

A domain property of this structure which has thus far not been commented on is that these domains grow along only three of the six hexagonal axes of the crystal. This situation is diagrammatically represented by the six domain patterns in the lower part of Fig. 1, in which the three observed directions of domain growth are represented by the bold lines, and the unobserved directions of growth are more lightly represented. When only the magnetic manganese ions are considered, all six directions in the crystal are identical. It is thus suggested that the observed threefold symmetry of domain growth must be associated with the bromine ions in the crystal. As an aid in considering this point, two layers of bromine ions above the hexagonal sheet of metal atoms have been represented in Fig. 1. The layer of $Br^-$ ions at $\left(\frac{121}{334}\right)$ is represented by the open circles, and that at $\left(\frac{213}{334}\right)$ is represented by the shaded circles. Inspection of the diagram shows that the bromine positions relative to the magnetic structure are different in a domain growth direction at, for example, $\beta = 35$ deg than in the directions 60 deg on either side of this direction, that is, $\beta = 95$ or 335 deg. To determine the particular directions in the crystal which relate the bromine positions to the directions of magnetic domain growth it is required that the $\beta$ angles and the intensities of a series of nuclear reflections of the (101) type (chemical cell) be correlated with the $\beta$ angles of the observable magnetic domains. Data of this type were obtained and used in constructing the domain diagram of Fig. 1.

The implications of the dependence of the directions of domain growth on the bromine ion positions will be considered in the section, "Magnetic Coupling."

## ORDERING TRANSITION EFFECT OF MAGNETIC FIELDS

The intensity of the single-crystal reflections from a (101) type of plane as a function of temperature and also of applied magnetic fields in the pumped helium region is shown in Fig. 6. The open squares represent the intensity in the absence of a magnetic field. It is evident from the shape of this curve that the temperature dependence of the magnetic ordering is not of the Brillouin type; in fact, the very sharp rise near the Néel temperature indicates a transition of nearly first order rather than of the usual second-order type. The initial rise does, however, seem to be finite within the accuracy of the determination. The temperatures in these experiments were determined from the vapor pressure and by the use of a calibrated carbon resistor.

When the transition data are obtained with a small field ($H = 2.7$ kilo-oersteds), the same general type of curve is obtained, but in this case the intensity rises to about three times the no-field value. From the discussions in previous sections it is now evident that this increase with applied field arises from the fact that the intensity is distributed among three domains in the absence of a field, whereas with the field the domains are brought into a single orientation.

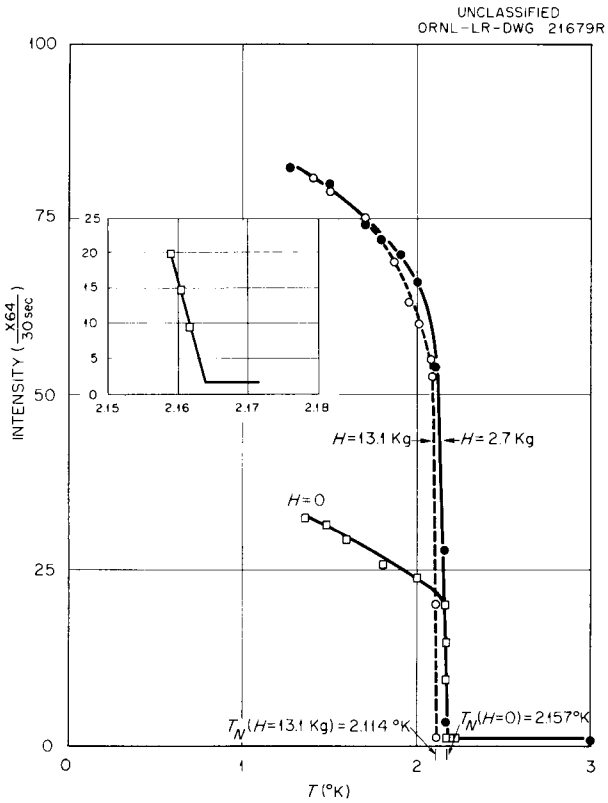


**Fig. 6. Antiferromagnetic Transition vs Temperature and Applied Magnetic Field. The squares ($H = 0$) correspond to three directions of domain growth, whereas circles ($H > 0$) correspond to growth of a single domain.**

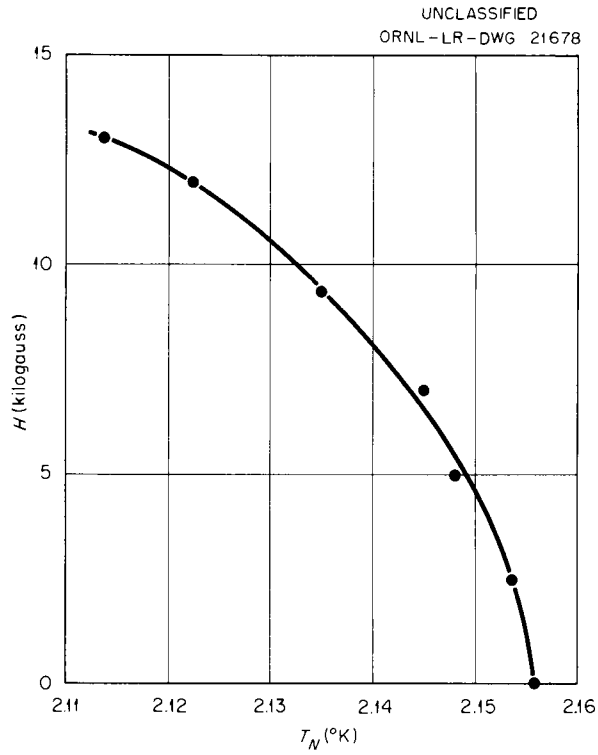


**Fig. 7. Néel Temperature vs Applied Magnetic Field.**

When the strength of the magnetic field applied to the sample is increased, it is observed that the Néel temperature is lowered over the no-field value. This is shown for the maximum field of 13.1 kilo-oersteds in Fig. 6. The dependence on magnetic field strength is shown in more detail in Fig. 7.

Another representation of the field dependence of the antiferromagnetic transition is given in Fig. 3. The upper curve, which represents the intensity of a (101) reflection as a function of magnetic field for an initially random orientation of magnetic domains, shows only a minor decrease of intensity at the maximum value of applied field. This curve was taken at 1.35°K. The lower curve, which was taken at a temperature of 2.128°K, shows a very different behavior in that the intensity falls to zero at a field of about 10.5 kilo-oersteds. Reference to Fig. 7 shows that this is just the value of the magnetic field for which the corresponding Néel temperature becomes equal to the temperature of the sample, and hence for fields above this value no order is to be expected.

## MAGNETIC COUPLING

In a compound such as $MnBr_2$, where the manganese ions are well separated from each other, any magnetic exchange between these ions must be of an indirect type via the intervening bromine ions. Although the over-all picture of magnetic coupling in a relatively complicated situation of this type would be very difficult to interpret in even a qualitative way, some interesting points in this regard have come from the study of the domain characteristics of the system. These are related to the observation that the domain growth follows only three of the six [100] directions in the crystal, all of which are identical for the manganese ions. The relation of the bromine ions to the six [100] directions is shown in projection on the hexagonal planes in Fig. 1. Consider in the domain at $\beta = 35$ deg, for example, the circle drawn around the $B$ atom in the layer. This circle is drawn to represent the $A$ atom in the next

hexagonal layer of metal atoms above the plane of the paper. The three lines radiating out from this circle represent lines which join the $A$ atom in the upper plane to metal atoms in the plane of the paper. These lines pass nearly through the centers of adjacent bromine ions in intervening layers. A three-dimensional representation of these radial lines is given in connection with the diagram of the structure in Fig. 2. It can be seen in this figure that the central $A$ atom is joined by these lines to six metal atoms in adjacent layers and that five of the atoms have spin orientation opposite to that of the central atom and one has like orientation. The disposition of the bromine ions along these lines is shown in the lower part of Fig. 2. At an angle in the crystal in which the domains are found to grow, this particular set of bond directions, which involves a nearly straight-line connection between manganese and bromine ions, is thus to be associated with a preponderance of antiferromagnetic exchange. Now for comparison, if one looks at a direction in the crystal in which domain growth is not observed, for example, $\beta = 95$ deg, in Fig. 1, one observes that the orientation of the radial lines relative to the corresponding domain growth direction is now different than in the previous case. From a study of the arrangement one can readily determine that in this case a central $A$ atom would have a predominance of ferromagnetic coupling along the specified bond directions, there being five ferromagnetic and only one antiferromagnetic relationship to the central atom.

The data thus suggest that indirect antiferromagnetic exchange coupling along nearly linear Mn-Br-Br-Mn bonding linkages is of significance in determining the antiferromagnetic structure in $MnBr_2$. This must, however, be accompanied by some antiferromagnetic coupling within the hexagonal layers.

The authors acknowledge the assistance of H. R. Child in the taking of some of the data in this investigation.

---

## NEUTRON DIFFRACTION INVESTIGATIONS OF THE TWO ANTIFERROMAGNETIC STRUCTURES OF $MnCl_2$

M. K. Wilkinson J. W. Cable E. O. Wollan W. C. Koehler

### INTRODUCTION

Anhydrous $MnCl_2$ belongs to a series of anhydrous iron-group chlorides which crystallize in the rhombohedral or pseudohexagonal structure characteristic of $CdCl_2$ and are actually, therefore, hexagonal layer structures in which the layers of metal atoms are separated by two layers of chlorine atoms. Two of the other chlorides, $FeCl_2$ and $CoCl_2$, were investigated previously by neutron diffraction techniques[1] and were found to order antiferromagnetically at about 25°K. For these compounds the magnetic moments within a metal layer were coupled ferromagnetically, and adjacent layers contained moments which were aligned antiparallel.

The experimental investigations at this Laboratory of the cryomagnetic properties of $MnCl_2$ indicated that this compound has interesting magnetic properties at low temperatures, since both the specific heat[2] and the magnetic susceptibility[3] exhibit unusual behaviors. Specific-heat measurements show two sharp $\lambda$-type anomalies at 1.81 and 1.96°K, while the polycrystalline magnetic susceptibility passed through a plateau between 2 and 1.5°K and was rising again at 1.1°K, which was the lowest temperature obtained during the measurements. These results were interpreted as an indication that there is a double transition in the electron-spin system of the divalent manganese ions and that both transitions involve

[1] M. K. Wilkinson and J. W. Cable, *Phys. Semiann. Prog. Rep. March 10, 1956*, ORNL-2076, p 44.

[2] R. B. Murray, *Phys. Rev.* 100, 1071 (1955).

[3] R. B. Murray and L. D. Roberts, *Phys. Rev.* 100, 1067 (1955).

antiferromagnetic ordering. Presumably, the specific-heat maximum at 1.96°K would represent a transition from the paramagnetic state to a first type of antiferromagnetic ordering, while the maximum at 1.81°K would result from a reorientation of the atomic moments to a second type of antiferromagnetic structure.

## EXPERIMENTAL TECHNIQUES

Investigations were performed on both powdered samples and single crystals of the material, and the specimens were enclosed in a double-jacketed vacuum cryostat at pressures below $10^{-6}$ mm Hg. Since the total neutron cross section for helium is very low[4] (0.73 barns) for neutrons with a wavelength of about 1 Å, the samples were placed within the liquid-helium bath to ensure temperature equilibrium. The temperatures were determined by measurements of the helium vapor pressure and the resistance of calibrated carbon resistances, which were submerged in the helium bath. For the cryostats and pumping system that were used, temperatures down to 1.25°K could be obtained for powdered samples, and single-crystal measurements could be made down to 1.38°K.

In the single-crystal investigations, the specimens were mounted on the low-temperature single-crystal goniometer which was designed and constructed at this Laboratory.[5] With this goniometer, the crystal to be studied can be rotated about either the horizontal or vertical axis so that any set of planes in the crystal can be oriented into a position for Bragg reflection of the incident neutron beam. A crystal with hexagonal symmetry such as $MnCl_2$ can be most conveniently mounted with the hexagonal *c* axis of the crystal aligned parallel to the horizontal axis of rotation. In this orientation a measurement of the angular position of a reflection about the vertical axis gives the geometrical angle between the reflecting plane and the *c* axis. Furthermore, with the vertical axis set at the proper position for a Bragg reflection, rotation of the crystal about the horizontal axis gives the angular positions about the *c* axis where this reflection occurs and therefore gives the symmetry about the *c* axis of the crystal. The $MnCl_2$ crystal was mounted in this manner, and $\alpha$ angles refer to the angular positions about the vertical axis of the goniometer, while $\beta$ angles give similar positions about the horizontal axis.

## EXPERIMENTAL RESULTS

### Results from Powdered Samples

The initial neutron diffraction investigations were made on powdered samples of $MnCl_2$ from room temperature to 1.25°K. Figure 1 represents the difference between diffraction patterns taken at 1.25°K and at 4.18°K, and the diffraction peaks are therefore characteristic only of the magnetic coherent scattering present at 1.25°K which was not present at 4.18°K. The negative background, of course, represents the diffuse scattering present at 4.18°K in excess of that at 1.25°K. This diffuse scattering is predominantly paramagnetic, but the nonuniform background near the large reflection at a scattering angle of 7 deg is representative of a considerable amount of short-range order which was observed at 4.18°K. Several resolved antiferromagnetic reflections are present in the pattern at small angles, and there appear to be many small unresolved reflections at scattering angles greater than 25 deg. It was impossible to determine the magnetic structure from these results. In particular, the reflection near 7 deg could not be indexed on any of the models which

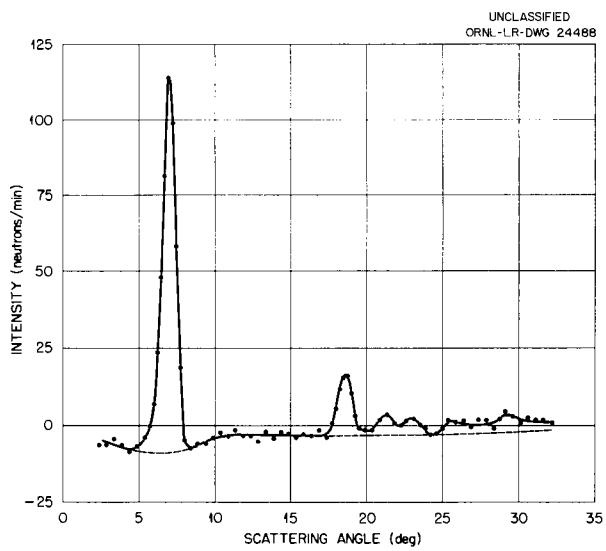


**Fig. 1. Powder Diffraction Pattern Representing the Difference in the Patterns from $MnCl_2$ at 1.25 and 4.18°K.**

[4]D. G. Hurst and D. G. Henshaw, *Phys. Rev.* **100**, 994 (1955).

[5]E. O. Wollan *et al.*, *Phys. Semiann. Prog. Rep. Sept. 10, 1956*, ORNL-2204, p 49.

were tested, and its angular position and intensity suggested a magnetic structure with a large, complex unit cell.

The intensity of this large magnetic reflection was studied as a function of temperature, and the results are shown in Fig. 2. These intensity measurements represent the scattered intensity at a scattering angle of 7 deg in excess of that found at 78°K. This effectively removes all the usual types of diffuse scattering (including paramagnetic scattering) from the data. It is seen that the coherent magnetic scattering follows a Brillouin-type curve and suggests a Néel temperature of about 2.1°K, somewhat higher than the high-temperature peak of the specific-heat measurements. However, there is a large amount of short-range order or critical scattering in the vicinity of the Néel temperature, as indicated by the tail on the data between 2 and 4.18°K. Since the intensity of critical scattering is almost symmetrical about a magnetic ordering temperature, if this scattering were subtracted from the results in Fig. 2, it is probable that the indicated Néel temperature would be slightly below 2°K. The intensity measurements were taken both for increasing and decreasing temperatures, and the results were completely reproducible. While the data are not inconsistent with a transition temperature of 1.96°K, there certainly is no distinct sign of a discontinuity near 1.81°K, the temperature at which the specific-heat data would have suggested a reorientation of the magnetic moments. The reason for this false impression can be understood by an examination of the results obtained from measurements on single crystals.

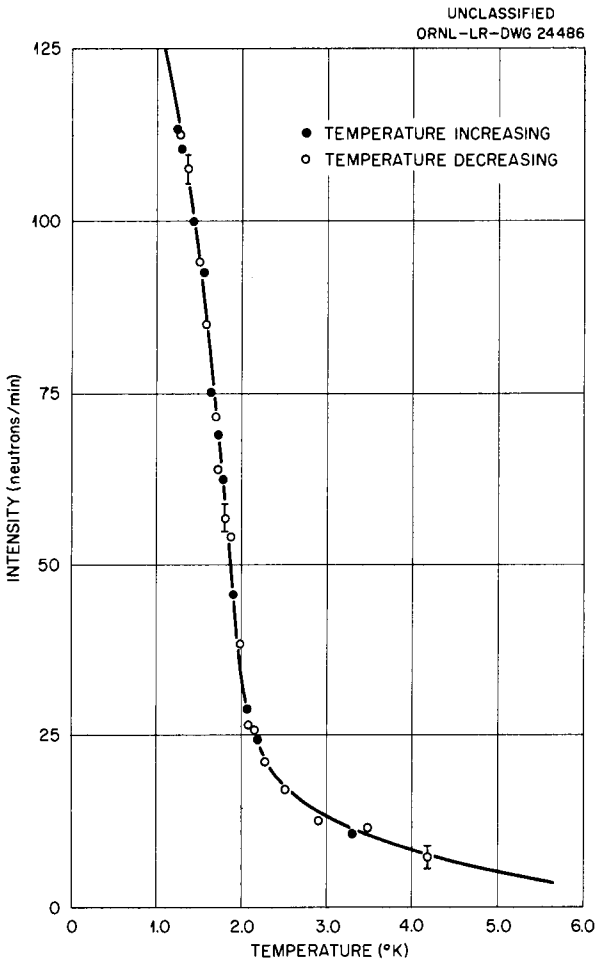


**Fig. 2. Temperature Variation of the Largest Antiferromagnetic Reflection from $MnCl_2$ Powder.**

### Results from Single Crystals

The results from single-crystal measurements show definitely that there are two transitions to different antiferromagnetic structures, as indicated by the specific-heat measurements. Furthermore, they show that both antiferromagnetic structures are quite complex, with large unit cells, and that the magnetic reflections which occur from the two structures are very similar, with nearly the same values of the scattering angles. Because of this situation it would have been impossible to distinguish between the two structures by powder diffraction patterns.

**Magnetic Structure Below the High-Temperature Transition.** – The magnetic structure below the high-temperature transition was studied with the sample temperature at 1.84°K throughout the investigation. Since this temperature was only slightly below $T_N$, the magnetic lattice was not well ordered, and the coherent intensities were small. However, magnetic reflections have been found at 13 different values of the scattering angle up to about 30 deg. The interplanar angles of the reflecting planes contributing these magnetic reflections were determined from the $\alpha$-angle measurements, the symmetry conditions about the $c$ axis were obtained from measurements of the $\beta$ angle, and the relative integrated intensities were measured by the usual type of single-crystal rocking curves. Some of these reflections were observed by scanning, while others were found in testing the predicted models.

The first attempt to determine the structure from the observed magnetic reflections involved the pseudohexagonal symmetry of the chemical unit cell. A magnetic unit cell in which the $a$ axis was 10 times the $a$ axis of the chemical cell and in which the $c$ axis was doubled would predict reflections with satisfactory values for the interplanar angles and the scattering angles, but would not account for the observed symmetry about the $c$ axis. In fact, only one structure has been found which will explain all the data. This magnetic structure is one in which the unit cell has orthorhombic axes and can grow in antiferromagnetic domains along the three axes in the base plane of the chemical hexagonal unit cell as shown in Fig. 3. The unit cell for this structure is very large, containing ten manganese atoms in the base plane and six layers of manganese atoms along the $c$ axis. A smaller triclinic unit cell

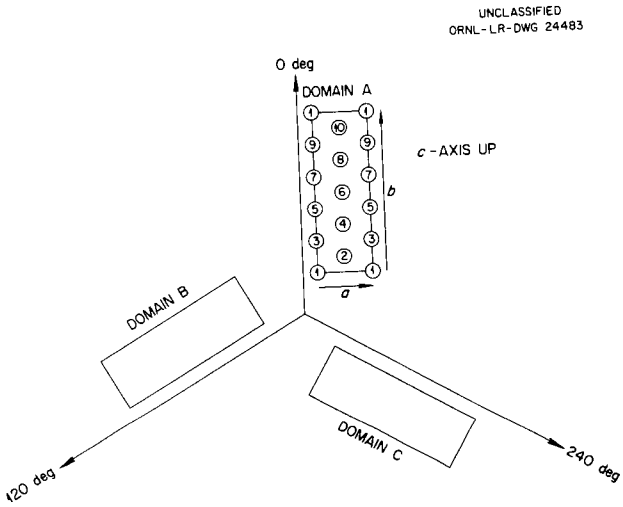


**Fig. 3. Domain Pattern for the Antiferromagnetic Structure of $MnCl_2$ Between 1.82 and 1.96°K.**

exists which contains only the atoms of the base plane, but it was found to be more convenient to index the observed reflections on the basis of the orthorhombic axes. The size and symmetry of this unit cell have been dictated entirely by the positions of the reflecting planes which give rise to the magnetic reflections.

Preliminary measurements have been made of the absolute intensities of the observed reflections in order to determine possible arrangements of the atomic magnetic moments within the cell. With a complex system of this type, it is certainly not possible to claim that there is only one unique arrangement of moments which fits the data. However, with the restriction of a single axis of magnetization, the only type of ordering which has been found to satisfactorily explain the intensities is shown in Fig. 4. The direction of the magnetic moment in this arrangement is closely parallel to the $a$ axis, but accurate calculations have not been completed. The only reflections

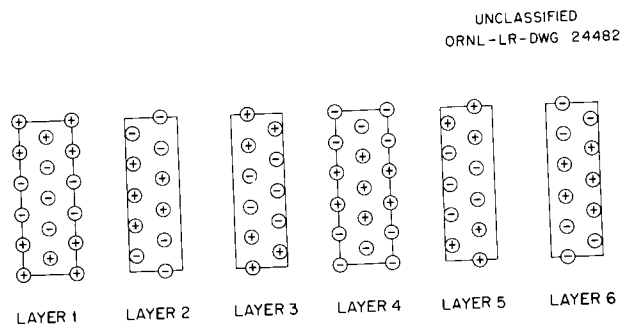


**Fig. 4. Magnetic Unit Cell of $MnCl_2$ Between 1.82 and 1.96°K.**

predicted by this cell which have scattering angles less than about 30 deg for 1.22-Å neutrons and magnetic structure amplitudes sufficiently large to give observable intensities are shown in Table 1. These reflections are listed by their orthorhombic indices, and calculated values are tabulated for the scattering angles, the interplanar angles between the reflecting planes and the $c$ axis ($\gamma$), the $\beta$ angles for the reflections of domain $A$ with the zero angle shown in Fig. 3, and the value of $q^2$ (the fraction of magnetic intensity allowed by the relative orientation of the atomic magnetic moments and scattering vector). Each of these reflections has a structure amplitude per atom of $0.836 \times 10^{-12}$ cm (excluding thermal motion and the magnetic form factor and assuming a spin only moment with $S = 5/2$). Identical reflections in domain $B$ have $\beta$ angles which are 120 deg larger, while for domain $C$, 240 deg must be added to each $\beta$ value listed. All these reflections have been observed except the (211) and (211), and these would not be expected, since the $q^2$ is unfavorable. The agreement between the calculated and experimental values of scattering angles and interplanar angles is well within experimental error, and in each case the observed reflections exhibit the symmetry about the $c$ axis which is predicted by the domain pattern.

Table 1. Calculated Reflections for Magnetic Structure of $MnCl_2$ Between 1.82 and 1.96° K

| Reflection | $2\theta$ ($\lambda$ = 1.22 Å) | $\gamma$ | $\beta$ (Domain $A$) | $q^2$ |
|---|---|---|---|---|
| $(0\,1\,3)$ | 7° 5′ | 57° 46′ | 0° | 1.00 |
| $(0\,\bar{1}\,3)$ | 7° 5′ | 57° 46′ | 180° | 1.00 |
| $(0\,1\,9)$ | 18° 26′ | 78° 8′ | 0° | 1.00 |
| $(0\,\bar{1}\,9)$ | 18° 26′ | 78° 8′ | 180° | 1.00 |
| $(\bar{1}\,4\,1)$ | 18° 50′ | 6° 7′ | 35° 50′ | 0.66 |
| $(\bar{1}\,\bar{4}\,1)$ | 18° 50′ | 6° 7′ | 144° 10′ | 0.66 |
| $(\bar{1}\,4\,5)$ | 21° 15′ | 28° 11′ | 215° 50′ | 0.73 |
| $(1\,4\,5)$ | 21° 15′ | 28° 11′ | 324° 10′ | 0.73 |
| $(2\,\bar{1}\,1)$ | 22° 22′ | 5° 9′ | 260° 11′ | 0.04 |
| $(2\,1\,1)$ | 22° 22′ | 5° 9′ | 279° 49′ | 0.04 |
| $(\bar{1}\,4\,7)$ | 23° 26′ | 36° 52′ | 35° 50′ | 0.78 |
| $(\bar{1}\,\bar{4}\,7)$ | 23° 26′ | 36° 52′ | 144° 10′ | 0.78 |
| $(\bar{2}\,1\,5)$ | 24° 28′ | 24° 14′ | 80° 11′ | 0.19 |
| $(\bar{2}\,\bar{1}\,5)$ | 24° 28′ | 24° 14′ | 99° 49′ | 0.19 |
| $(\bar{1}\,6\,1)$ | 25° 26′ | 4° 32′ | 25° 46′ | 0.81 |
| $(\bar{1}\,\bar{6}\,1)$ | 25° 26′ | 4° 32′ | 154° 14′ | 0.81 |
| $(2\,\bar{1}\,7)$ | 26° 24′ | 32° 16′ | 260° 11′ | 0.31 |
| $(2\,1\,7)$ | 26° 24′ | 32° 16′ | 279° 49′ | 0.31 |
| $(1\,\bar{6}\,5)$ | 27° 18′ | 21° 39′ | 205° 46′ | 0.84 |
| $(1\,6\,5)$ | 27° 18′ | 21° 39′ | 334° 14′ | 0.84 |
| $(\bar{1}\,6\,7)$ | 29° 4′ | 29° 2′ | 25° 46′ | 0.86 |
| $(\bar{1}\,\bar{6}\,7)$ | 29° 4′ | 29° 2′ | 154° 14′ | 0.86 |
| $(1\,\bar{4}\,11)$ | 29° 6′ | 49° 41′ | 215° 50′ | 0.86 |
| $(1\,4\,11)$ | 29° 6′ | 49° 41′ | 324° 10′ | 0.86 |
| $(0\,1\,15)$ | 30° 32′ | 82° 49′ | 0° | 1.00 |
| $(0\,\bar{1}\,15)$ | 30° 32′ | 82° 49′ | 180° | 1.00 |
| $(\bar{2}\,1\,11)$ | 31° 34′ | 44° 45′ | 80° 11′ | 0.51 |
| $(\bar{2}\,\bar{1}\,11)$ | 31° 34′ | 44° 45′ | 99° 49′ | 0.51 |

The length of the orthorhombic $b$ axis is dictated primarily by the (013) group of reflections which occur at a scattering angle of 7° 5′. Measurements on these reflections show that the reflecting planes have a spacing value of 10.0 ± 0.3 Å, form an angle of 58.0 ± 0.5 deg with the hexagonal $c$ axis, and occur at $\beta$ angles corresponding to $(hhl)$ reflections of the chemical hexagonal cell. Hence the orthorhombic $b$ axis which has been chosen not only fits the data but also has the minimum length that these (013) reflections will allow. The length of the orthorhombic $c$ axis (six manganese layers) is not surprising, since it must be remembered that in the $CdCl_2$ crystal structure three layers of metal atoms are required to position one metal atom directly above another. The domain pattern is suggested by the symmetry about the $c$ axis for all the observed $(hkl)$ reflections with no index equal to zero. Each of these reflections exhibits two positions in the $\beta$ angle symmetrically spaced on either side of the proper $\beta$ position for an $(h0l)$ reflection from the chemical hexagonal cell. For example, if the proper $\alpha$ angle is set for the (145) reflection, then according to Table 1, this reflection should occur at a $\beta$ angle of about 324 deg. This reflection is observed; but without changing the $\alpha$ angle, another reflection is observed for a $\beta$ value of about 336 deg; and these two reflections repeat at positions of 120 deg as the $\beta$ angle is changed. This behavior is seen in Fig. 5, where Fig. 5*a* shows the intensity of the reflection as the $\alpha$ angle is changed with the $\beta$ angle set at the proper position, and Fig. 5*b* shows that portion of the $\beta$ dependence near 330 deg for the proper $\alpha$ angle. The absolute values of the $\alpha$ angle are the instrumental values which include an arbitrary zero angle, while the instrumental $\beta$ values have been modified to correspond to the angles in the diagram of Fig. 3. According to the domain pattern and the tabulated $\beta$ angles in Table 1, the two reflections in Fig. 5*b* correspond to the (145) reflection from domain $A$ and the (145) reflection from domain $B$.

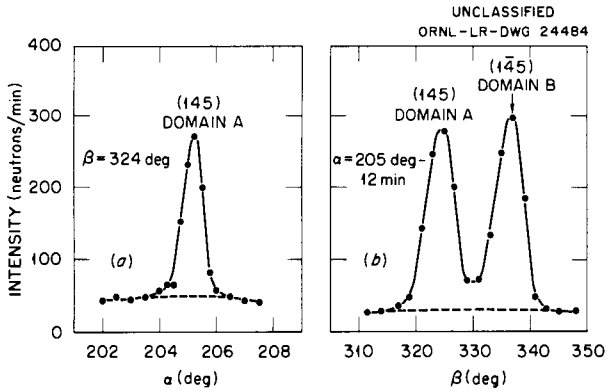


**Fig. 5. Partial Diffraction Patterns Showing the (145) and (145) Reflections from an $MnCl_2$ Single Crystal at 1.84°K.**

The suggestion of antiferromagnetic domains along three of the axes in the hexagonal base plane is quite similar to the domain pattern which has been much better established in the antiferromagnetic structure of $MnBr_2$ (see "Neutron Diffraction Study of the Magnetic Properties of $MnBr_2$," this report). It is substantiated by the effects of an external magnetic field on the intensities of the (013) reflections. When the field is applied parallel to the scattering vector of these reflections, the intensity is increased threefold, which strongly suggests that the field allows only one antiferromagnetic domain to exist. However, unlike the case of $MnBr_2$, it is impossible to "lock in" the structure which is produced by the external field, and when the field is removed, the intensities return to their original values. This effect is believed to be associated with the fact that only a very small degree of long-range magnetic order exists at 1.84°K, since it is only 0.12 deg below the transition temperature.

**Magnetic Structure Below the Low-Temperature Transition.** – The magnetic structure below the low-temperature transition was studied with the sample temperature at 1.38°K throughout the investigation. The reflections from this antiferromagnetic structure were found to be very similar to those from the high-temperature magnetic structure and occurred at almost the same values of the scattering angles. In fact, it was necessary to take data very carefully to be positive that a second structure actually existed. The small differences were first thought to be caused by a change in the chemical crystal structure at the second transition. However, a careful study of the symmetry of the nuclear reflections throughout this temperature region showed that the crystal structure remained the same within limits much less than the variation required to explain the changes in the magnetic reflections.

The most obvious indication for the existence of a second magnetic structure was the different

symmetry about the $c$ axis for the large reflection at a scattering angle of 7 deg. Instead of one reflection which has sixfold symmetry as the $\beta$ angle was varied, there were two reflections separated about 20 deg in $\beta$, and each of these possessed sixfold symmetry. When this different structure had been definitely established, a close examination of the reflections at larger scattering angles showed that some of these were caused by two sets of reflecting planes with slightly different spacing values and interplanar angles.

The only satisfactory model for explaining the observed data below the second transition temperature is also based on the presence of antiferromagnetic domains, but the symmetry conditions require a more complex domain pattern. Two similar unit cells with monoclinic axes are required, and each of these cells must grow in domains along the three axes in the base plane of the chemical hexagonal unit cell as shown in Fig. 6. These unit cells contain 15 manganese atoms in the base plane and include six layers of manganese atoms along the $c$ axis. It is also possible to form a smaller unit cell for this structure which is triclinic and contains the manganese atoms in only two layers. However, the monoclinic axes are more convenient to use, and the indices which are given for the observed reflections are based on these axes.

Preliminary measurements have also been obtained for the magnetic intensities observed at 1.38°K. These measurements can be satisfactorily explained by the assignment of magnetic moments given in Fig. 7. This arrangement, of course, applies to domains twisted like domain $A$-1, and those twisted like domain $A$-2 have a similar arrangement. The suggested magnetic moment direction is closely parallel to the $a$ axis.

Table 2 lists all the magnetic reflections which are predicted by this model with a scattering angle less than about 30 deg for 1.22-Å neutrons and a structure amplitude large enough for the reflection to be observed. This table also lists the scattering angles, the values of $\gamma$, the $\beta$ angles predicted for domain $A$-1 and domain $A$-2 by use of the zero angle of Fig. 6, and the values of $q^2$. Similar reflections are, of course, predicted for the other domains, and again it is necessary merely to add 120 deg to obtain the proper $\beta$ angles for the $B$ domains and to add 240 deg for the $\beta$ values of the $C$ domains. The calculated average structure amplitude per atom for each of these reflections is $0.819 \times 10^{-12}$ cm, very nearly the same as that calculated for the structure existent at 1.84°K. It is interesting to compare the data in this table with those listed in Table 1. The very close similarity of the reflections predicted in the two magnetic structures is immediately obvious. It is also apparent that powder diffraction data could not possibly have distinguished between the two structures, since the scattering angles are so closely the same throughout the angular region where the magnetic intensities in the powder pattern were sufficiently large for accurate measurements. Furthermore, the observations of two reflections with almost the same value of $\alpha$ angle in the low-temperature structure can be explained by the data in Table 2. This model predicts that for every scattering angle in Table 1 corresponding to an $(hkl)$ reflection with no index equal to zero, there

UNCLASSIFIED
ORNL-LR-DWG 24481

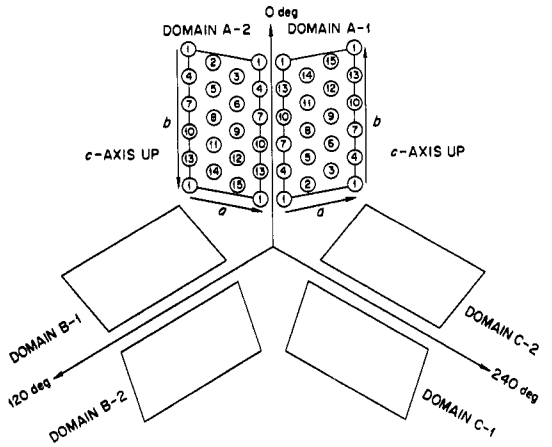


**Fig. 6. Domain Pattern for the Antiferromagnetic Structure of $MnCl_2$ Below 1.82°K.**

UNCLASSIFIED
ORNL-LR-DWG 24480

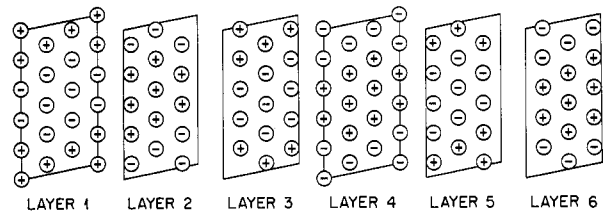


**Fig. 7. Magnetic Unit Cell of $MnCl_2$ Below 1.82°K.**

Table 2. Calculated Reflections for Magnetic Structure of $MnCl_2$ Below 1.82°K

| Reflection | $2\theta$ ($\lambda$ = 1.22 Å) | $\gamma$ | $\beta$ Domain $A$-1 | $\beta$ Domain $A$-2 | $q^2$ |
|---|---|---|---|---|---|
| $(0\,1\,3)$ | 7° 7′ | 57° 18′ | 10° 53′ | 169° 7′ | 1.00 |
| $(0\,\bar{1}\,3)$ | 7° 7′ | 57° 18′ | 190° 53′ | 349° 7′ | 1.00 |
| $(0\,1\,9)$ | 18° 29′ | 77° 57′ | 10° 53′ | 169° 7′ | 1.00 |
| $(0\,\bar{1}\,9)$ | 18° 29′ | 77° 57′ | 190° 53′ | 349° 7′ | 1.00 |
| $(\bar{1}\,4\,1)$ | 18° 25′ | 6° 15′ | 33° 58′ | 146° 2′ | 0.85 |
| $(\bar{2}\,\bar{4}\,1)$ | 19° 14′ | 5° 59′ | 142° 23′ | 37° 37′ | 0.44 |
| $(1\,\bar{4}\,5)$ | 20° 54′ | 28° 42′ | 213° 58′ | 326° 2′ | 0.88 |
| $(2\,4\,5)$ | 21° 37′ | 27° 39′ | 322° 23′ | 217° 37′ | 0.56 |
| $(3\,1\,1)$ | 21° 40′ | 5° 19′ | 280° 9′ | 259° 51′ | 0.01 |
| $(3\,\bar{1}\,1)$ | 23° 6′ | 4° 59′ | 260° 21′ | 279° 39′ | 0.01 |
| $(\bar{1}\,4\,7)$ | 23° 7′ | 37° 28′ | 33° 58′ | 146° 2′ | 0.90 |
| $(\bar{2}\,\bar{4}\,7)$ | 23° 46′ | 36° 16′ | 142° 23′ | 37° 37′ | 0.64 |
| $(\bar{3}\,\bar{1}\,5)$ | 23° 49′ | 24° 58′ | 100° 9′ | 79° 51′ | 0.18 |
| $(\bar{3}\,1\,5)$ | 25° 8′ | 23° 35′ | 80° 21′ | 99° 39′ | 0.16 |
| $(\bar{1}\,6\,1)$ | 25° 43′ | 4° 29′ | 27° 10′ | 152° 50′ | 0.92 |
| $(\bar{2}\,\bar{6}\,1)$ | 25° 7′ | 4° 36′ | 155° 48′ | 24° 12′ | 0.67 |
| $(3\,1\,7)$ | 25° 48′ | 33° 3′ | 280° 9′ | 259° 51′ | 0.30 |
| $(3\,\bar{1}\,7)$ | 27° 2′ | 31° 26′ | 260° 21′ | 279° 39′ | 0.27 |
| $(\bar{1}\,6\,5)$ | 27° 34′ | 21° 25′ | 207° 10′ | 332° 50′ | 0.93 |
| $(2\,6\,5)$ | 27° 1′ | 21° 53′ | 335° 48′ | 204° 12′ | 0.71 |
| $(\bar{1}\,6\,7)$ | 29° 20′ | 28° 47′ | 27° 10′ | 152° 50′ | 0.94 |
| $(\bar{2}\,\bar{6}\,7)$ | 28° 48′ | 29° 21′ | 155° 48′ | 24° 12′ | 0.75 |
| $(1\,\bar{4}\,11)$ | 28° 49′ | 50° 20′ | 213° 58′ | 326° 2′ | 0.94 |
| $(2\,4\,11)$ | 29° 24′ | 49° 2′ | 322° 23′ | 217° 37′ | 0.76 |
| $(0\,1\,15)$ | 30° 32′ | 82° 41′ | 10° 53′ | 169° 7′ | 1.00 |
| $(0\,\bar{1}\,15)$ | 30° 32′ | 82° 41′ | 190° 53′ | 349° 7′ | 1.00 |
| $(\bar{3}\,\bar{1}\,11)$ | 31° 2′ | 45° 42′ | 100° 9′ | 79° 51′ | 0.51 |
| $(\bar{3}\,1\,11)$ | 31° 22′ | 44° 16′ | 80° 21′ | 99° 39′ | 0.49 |

will be two scattering angles slightly displaced to higher and lower values where ($bkl$) reflections will occur at the lowest temperatures. The reflecting planes contributing to these reflections will have interplanar angles which are also displaced to slightly higher and lower values and will have a similar but different symmetry about the $c$ axis. These doublets have been observed for those reflections where the interplanar angles were sufficiently different to allow resolution in the $\alpha$ angles.

As an example of this behavior, consider the ($1\bar{4}5$) and (145) reflections of the high-temperature structure which occur at a scattering angle of 21° 15′ and have the values of $\alpha$ angle and $\beta$ angles shown in Fig. 5. The low-temperature model predicts a ($1\bar{4}5$) reflection and a (245) reflection with scattering angles of 20° 54′ and 21° 37′, respectively, which have interplanar angles that are different by 1° 3′. Figure 8$a$ shows the $\alpha$-angle variation for the angular region around these reflections. These data were obtained by using a detector with a wide slit that was positioned at the average scattering angle for the two reflections. Both reflections are clearly visible and are separated by about 0.9 deg, which is in good agreement with the difference in the calculated values of $\gamma$. It can also be noticed that the $\alpha$ angles for the two peaks are symmetrically displaced from the $\alpha$ position of the reflection in Fig. 5. The scattering angles for the two reflections measured by using a narrow detector slit were also in good agreement with the calculated values. Furthermore, the predicted symmetry about the $c$ axis for these reflections is also observed. According to Tables 1 and 2, the $\beta$-angle positions of the ($1\bar{4}5$) and (245) reflections from the low-temperature structure are different, and both are slightly different from the $\beta$ values of the ($1\bar{4}5$) and (145) reflections at 1.84°K. The variations in the $\beta$ angle around 330 deg for these reflections are shown in Figs. 8$b$ and 8$c$, and similar reflections are also seen when $\beta$ is increased by 120 and 240 deg. The presence of these two pairs of reflections which occur with threefold symmetry about the $c$ axis is explained by the domain pattern suggested for this structure, and the actual values of the $\beta$ angles agree very well with those predicted in Table 2.

The existence of a structure with antiferromagnetic domains below the low-temperature

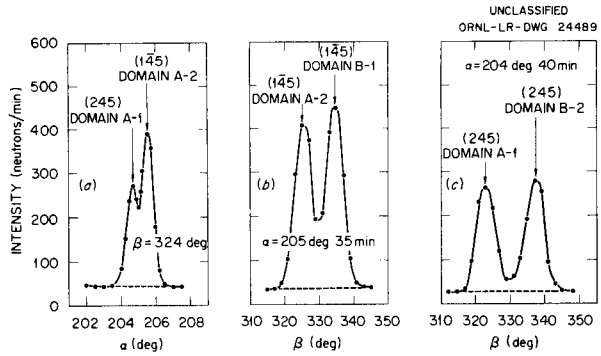


**Fig. 8. Partial Diffraction Patterns Showing the (145) and (245) Reflections from an $MnCl_2$ Single Crystal at 1.38°K.**

transition is substantiated by the intensity changes which are observed when an external magnetic field is applied. However, the details of the intensity changes for this type of domain pattern are not yet understood.

**Transition Temperatures.** – Since the reflections from the two magnetic structures are so similar, there was doubt that the structure which appeared below 1.96°K actually disappeared when the temperature was lowered below the other transition. Therefore, very careful observations were made on the temperature variation of the intensity of the (013) reflections. This study was made with a large detector slit so that scattered intensities could be observed even though they did not have exactly the proper values for the $\alpha$ angle and the $\beta$ angle. With the detector angle and $\beta$ angle fixed, rocking curves were taken around the proper $\alpha$ angles as the temperature was varied. For the particular geometry which was used, a (013) reflection from domain $B$ of the high-temperature structure would occur at an $\alpha$ angle of about 186° 20′, while a ($0\bar{1}3$) reflection from domain $B$-1 together with a (013) reflection from domain $B$-2 of the low-temperature structure would appear at $\alpha$ angles of about 185° 50′ and 187° 45′. Data were obtained in this fashion at approximately 25 different temperatures from 3.05 to 1.38°K, and some of these results are shown in Fig. 9. As the temperature was lowered from 3.05°K, there was an increase in the diffuse scattering level because of the critical scattering. The most rapid increase in this critical scattering, of course, occurs close to the transition temperature, and the low, broad maximum around the proper position for

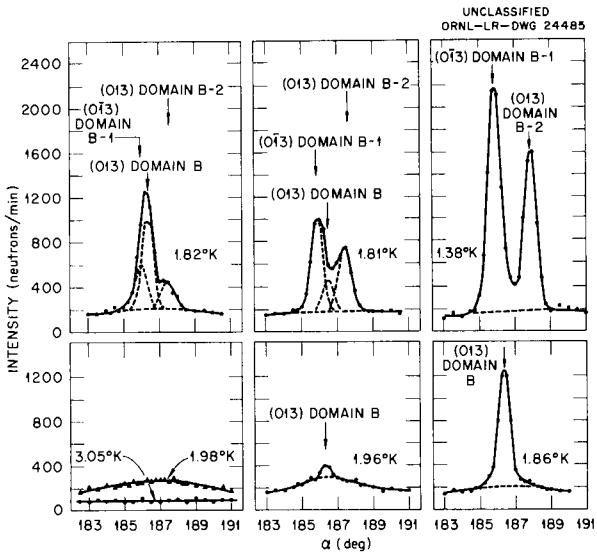


**Fig. 9. Partial Single-Crystal Diffraction Patterns from $MnCl_2$ Which Show the Determination of the Two Antiferromagnetic Transitions.**

coherent scattering from the ordered lattice is clearly indicated in the data at 1.98°K. The first indication of coherent scattering was found at 1.96°K, exactly the same temperature where one of the specific-heat maximums occurred. The intensity of this reflection was observed to increase fairly rapidly with decreasing temperature until about 1.85°K, and in the region around 1.82°K the first structure disappears as the low-temperature structure begins to form. There is a temperature region from about 1.81 to 1.83°K where both structures are present, and below 1.81°K the intensities from the low-temperature structure increase steadily to the intensities observed at 1.38°K.

All the data taken in this manner are summarized in Fig. 10, where the integrated intensities of the reflections are plotted as a function of the temperature. The fairly large difference in intensity between the (0$\bar{1}$3) reflection from domain *B*-1 and the (013) reflection from domain *B*-2 was primarily the result of the geometry of this particular experiment. It is interesting to consider the solid black circles, which represent the total integrated intensity throughout the temperature region where

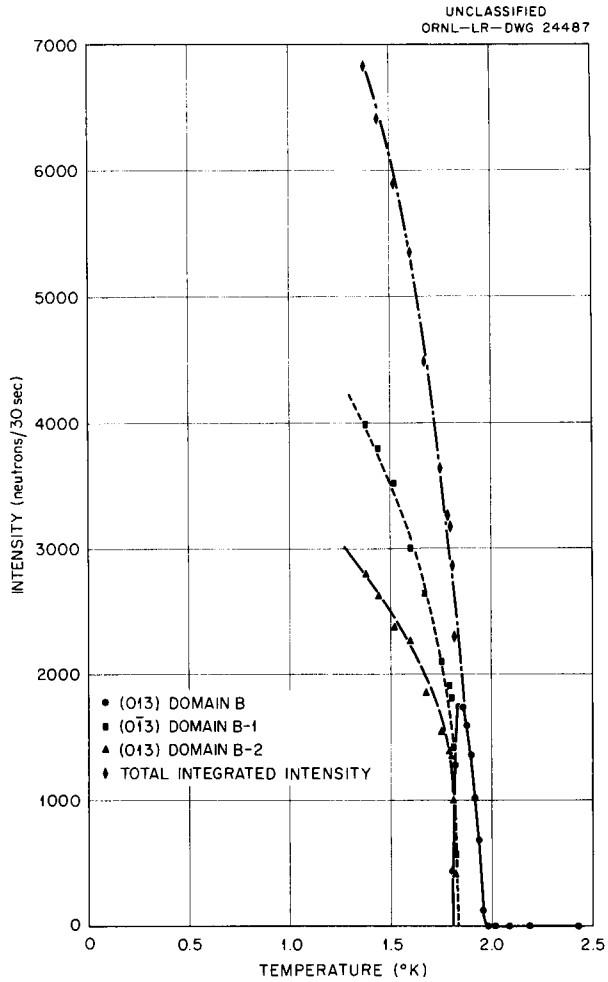


**Fig. 10. Temperature Variation of the (013) Magnetic Reflections from a Single Crystal of $MnCl_2$.**

more than one reflection occurred. Because of the experimental geometry, the intensities of these points would be larger if the data for each reflection had been taken with the proper $\beta$ angle. However, they probably are not more than 25% low, and within this accuracy they show the relative temperature variation of the intensity which would have been obtained with a powdered sample at a scattering angle of 7 deg. The curve through these points follows a logical Brillouin-type dependence for only one transition at 1.96°K, and explains the reason why the powder data in Fig. 2 did not indicate two transition temperatures.

# TYPES OF MAGNETICALLY ORDERED CONFIGURATIONS ON SIMPLE LATTICES

H. A. Gersch[1] W. C. Koehler

## INTRODUCTION

In crystals which contain magnetically active ions or atoms, various ordered arrangements of the moments may exist, depending upon the details of the interactions between the spins and upon the space lattice appropriate for the crystal. Ordered configurations corresponding to energy minimums under simplifying assumptions concerning the interactions (isotropic with specified interactions between nearest and next-nearest neighbors) have been predicted for a number of simple lattices[2-5] and have been found experimentally by neutron diffraction experiments. These latter investigations have also uncovered other types of ordered configurations.

At the present time, neutron-magnetic scattering data are analyzed to a great extent by trial and error methods. It is therefore of some interest to investigate systematically the diffraction effects to be expected from ordered configurations on a number of simple lattices. To this end a consistent scheme for enumerating the structure types possible for a given lattice without regard to energy considerations but subject to a geometrical constraint has been developed, and a system of nomenclature, descriptive of the moment arrangement, is proposed.

## THE CATALOGING SCHEME

The model on which the cataloging scheme is based assumes scalar spins so that at each lattice point there is either a "spin up" (+) or a "spin down" (–), and the ordered configurations are obtained by the imposition of an equivalence condition which is defined precisely below.

Within the above-mentioned approximation the Hamiltonian for the spin system may be written in the form

$$H = \frac{1}{2} \sum_{ij} A_{ij} S_i S_j \ , \tag{1}$$

where $A_{ij}$ represents the interaction between the $i$th and the $j$th spins, and the double sum is over all spins in the lattice. Usually the $A_{ij}$ are assumed to be nonzero between nearest and next-nearest neighbors.

The energy of the spin system is a quadratic form in the spin variables $S_i$, each of which can take on only discrete values which for simplicity are taken as $\pm 1$. Without this restriction to discrete values, the Hamiltonian would be analogous to the potential energy of a crystal lattice expanded about its energy minimum. (Then $S_i$ would refer to the continuous displacement of the $i$th atom from its equilibrium position, and $A_{ij}$ would represent the force on the $j$th atom for a unit displacement of the $i$th atom.) This similarity between spin configurations and atomic vibrations forms the basis for the scheme of cataloging the possible ordered spin arrangements. The spin variables $S_i$ are supposed to be continuous; they can then be represented in terms of normal coordinates. Each normal mode describes a spin configuration with definite phase relations between neighboring spins. The ordered spin states which are sought correspond to those normal modes for which neighboring spins are in phase (spins parallel) or 180 deg out of phase (spins antiparallel). If cyclic boundary conditions are imposed on the $S_i$, then the requirement of equivalence of spins at different lattice sites can be satisfied for all sites, since the effect of this condition is to remove the surface.

### The One-Dimensional Crystal

The details for the simplest case of a one-dimensional chain of $N$ spins will be given by way of illustration. The cyclic boundary condition bends the chain into a circle so that

$$S_j = S_{N+j} \ , \quad j = 1, \ldots, N \ . \tag{2}$$

Let the normal coordinate amplitudes be designated by $q_k$, $k = 1, \ldots, N$. Then the unitary

[1] Summer research participant from Georgia Institute of Technology.

[2] P. W. Anderson, *Phys. Rev.* 79, 705 (1950).

[3] J. M. Luttinger, *Phys. Rev.* 81, 1015 (1951).

[4] J. S. Smart, *Phys. Rev.* 86, 968 (1952); *Phys. Rev.* 90, 55 (1953).

[5] J. H. Van Vleck, *J. phys. radium* 12, 262 (1951).

transformation from the $S_i$ to the $q_k$ is expressed by

$$S_i = \sum_{k=1}^{N} t_{ik} q_k \ , \tag{3}$$

where the transformation coefficients $t_{ik}$, $i$, $k = 1, \ldots, N$ must be chosen to satisfy the cyclic condition (Eq. 2) and to diagonalize the Hamiltonian (Eq. 1) so that

$$H = \frac{1}{2} \sum_{i,k=1}^{N} A_{ik} S_i S_k = \frac{1}{2} \sum_{k=1}^{N} \nu_k^2 q_k^2 \ . \tag{4}$$

The cyclic condition (Eq. 2) requires that

$$t_{ik} = t_{N+i,k} \ , \tag{5}$$

while Eq. 4 requires that

$$\begin{aligned} \sum_{i,k=1}^{N} A_{ik} S_i S_k &= \sum_{i,k=1}^{N} A_{ik} \sum_{l=1}^{N} t_{il} q_l \sum_{m=1}^{N} t_{km} q_m \\ &= \sum_{l,m=1}^{N} q_l q_m \sum_{i,k=1}^{N} A_{ik} t_{il} t_{km} \\ &= \sum_{k=1}^{N} \nu_k^2 q_k^2 \ . \end{aligned} \tag{6}$$

Since the transformation is unitary,

$$\sum_{k=1}^{N} t_{kl} t_{km} = \delta_{m,l} \ , \tag{7}$$

and the desired result is obtained if

$$\sum_{i=1}^{N} A_{ik} t_{il} = \nu_l^2 t_{kl} \ . \tag{8}$$

Equation 8 is the familiar eigenvalue equation for the frequencies $\nu_l$ of the normal modes.

The real transformation coefficients which satisfy Eqs. 5, 7, and 8 are

$$t_{ik} = \frac{1}{N^{1/2}} \left( \cos \frac{2\pi}{N} ik + \sin \frac{2\pi}{N} ik \right) , \tag{9}$$

and the spin configurations expressed in terms of normal modes may be written as

$$S_i = \frac{1}{N^{1/2}} \sum_{k=1}^{N} \left( \cos \frac{2\pi}{N} ik + \sin \frac{2\pi}{N} ik \right) q_k \ . \tag{10}$$

It is now required that the following constraint be satisfied:

$$S_{j+1} \left[ S_{j+1+m} + S_{j+1-m} \right] = S_j \left[ S_{j+m} + S_{j-m} \right] \tag{11}$$

for all $j$, $m = 1, \ldots, N$. In this equation the left side is the correlation between spins at the $(j + 1)$st lattice site and its $m$th neighbors, and the right side is the corresponding correlation between the $j$th site and its $m$th neighbors. The condition expressed by Eq. 11 is required to hold for all $j$ and $m$ from 1 to $N$, and this is possible only because of the imposition of the cyclic boundary conditions. With these as given by Eq. 2, and for $m = N$, condition 11 reduces to

$$S_{j+1}^2 = S_j^2 \ , \quad \text{or} \quad S_{j+1} = \pm S_j \ , \tag{12}$$

so that the constraint has the effect of extracting from the continuous spin configurations only those with discrete spins. It may be noted that condition 11 is equivalent to the requirement that the number of like and unlike $m$th neighbors ($m = 1, \ldots, N$) be the same for all spins.

It is now shown that there are only four distinct possibilities for normal modes which satisfy the constraint. Condition 11 is rewritten, using the fact that it requires $S_{j+1} = \pm S_j$, as

$$S_j \left[ S_{j+m} + S_{j-m} \mp S_{j+1+m} \mp S_{j+1-m} \right] = 0 \ . \tag{13}$$

Expressing the spins $S_j$ in terms of normal coordinates $q_k$ (Eq. 10) brings this into the form

$$\begin{aligned} 0 = \sum_{k=1}^{N} q_k \cos \frac{2\pi}{N} mk \Bigg[ \cos \frac{2\pi}{N} jk \Bigg( 1 \mp \\ \mp \cos \frac{2\pi}{N} k \mp \sin \frac{2\pi}{N} k \Bigg) + \sin \frac{2\pi}{N} jk \Bigg( 1 \mp \\ \mp \cos \frac{2\pi}{N} k \pm \sin \frac{2\pi}{N} k \Bigg) \Bigg] \ . \end{aligned} \tag{14}$$

Multiplying by $\cos 2\pi/N\,(mk)$ and summing $m$ from

1 to $N$ results in

$$(15)\quad 0 = q_\omega[\cos \omega j(1 \mp \cos \omega \mp \sin \omega) + \sin \omega j(1 \mp \cos \omega \pm \sin \omega)] + q_{2\pi-\omega}[\cos \omega j(1 \mp \cos \omega \pm \sin \omega) - \sin \omega j(1 \mp \cos \omega \mp \sin \omega)] ,$$

where $\omega = 2\pi k/N$ ranges from 0 to $2\pi$ as $N \longrightarrow \infty$. This equation is to hold for all $j$ from 1 to $N$, and the choice of plus or minus signs can change arbitrarily with $j$. Clearly, the values $\omega = \pi$, $2\pi$ are solutions of Eq. 15, since for these values every term in parentheses can be made zero. For $\omega = 2\pi$, the upper signs must be chosen for all $j$, corresponding to the ferromagnetic ordering $S_{j+1} = S_j$ for all $j$. (As the number of spins $N \longrightarrow \infty$, the lowest value of $\omega \longrightarrow 0$ and gives the same configuration as $\omega = 2\pi$.) For $\omega = \pi$, the lower signs must be chosen for all $j$, corresponding to the pure antiferromagnetic ordering $S_{j+1} = -S_j$ for all $j$.

In addition to $\omega = \pi$, $2\pi$, there are the solutions $\omega = \pi/2$ or $3\pi/2$, for which the terms in the parentheses can be made equal to zero. For example, Eq. 15 for $\omega = \pi/2$ is

$$(16)\quad 0 = q_{\pi/2}\left[\cos\frac{\pi}{2}j(1 \mp 1) + \sin\frac{\pi}{2}j(1 \pm 1)\right] + q_{3\pi/2}\left[\cos\frac{\pi}{2}j(1 \pm 1) - \sin\frac{\pi}{2}j(1 \mp 1)\right] .$$

This can be satisfied by putting $q_{3\pi/2} = 0$ and choosing the upper sign for even $j$ and the lower sign for odd $j$. Alternatively, $q_{\pi/2}$ can be put equal to zero, and the equation satisfied by the reverse choice of signs. These sign choices generate the two configurations $\omega = \pi/2$, $3\pi/2$, respectively.

Equation 15 is identical if written for $\omega = 3\pi/2$, and leads to the same configurations as those just obtained. No other values of $\omega$ are possible, because the terms in parentheses in Eq. 15 are not zero for any $\omega$ other than 0, $\pi/2$, $\pi$, $3\pi/2$. For if the equation is satisfied for some particular value of $j$ by some other $\omega$, say $\omega_i$, it clearly cannot be satisfied with this $\omega_i$ for all $j$ from 1 to $N$. The configurations generated by these values of $\omega$ are shown in Fig. 1.

UNCLASSIFIED
ORNL-LR-DWG 20195

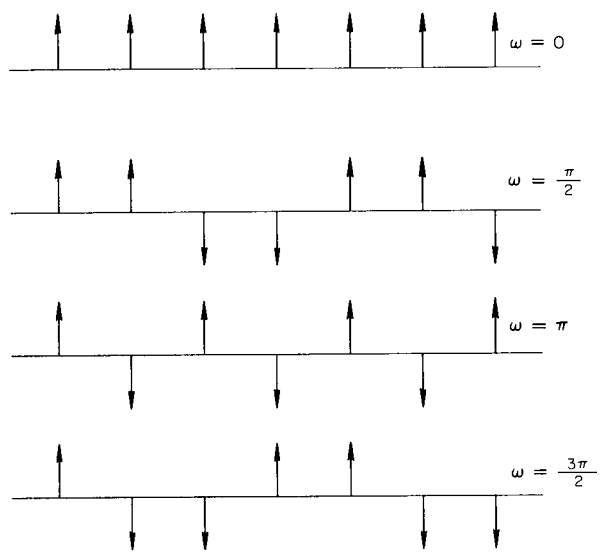


**Fig. 1. Possible Ordered Spin Configurations for a One-Dimensional Chain.**

### Generalization to Three Dimensions

The foregoing discussion is directly applicable to an arbitrary three-dimensional lattice. Positions are described by lattice vectors so that instead of $S_i$, one writes $S_{\vec{R}}$, where

$$(17)\quad \vec{R} = l_1\vec{a}_1 + l_2\vec{a}_2 + l_3\vec{a}_3 ,$$

in which $l_1$, $l_2$, $l_3$ are integers and $\vec{a}_1$, $\vec{a}_2$, $\vec{a}_3$ are basis vectors for the lattice. The transformation coefficients are

$$(18)\quad t_{ik} = \frac{1}{N^{3/2}}(\cos \vec{k}\cdot\vec{R} + \sin \vec{k}\cdot\vec{R}) ,$$

with $\vec{k} = \omega_1\vec{b}_1 + \omega_2\vec{b}_2 + \omega_3\vec{b}_3$, in which $\vec{b}_1$, $\vec{b}_2$, $\vec{b}_3$ is the vector set reciprocal to $\vec{a}_1$, $\vec{a}_2$, $\vec{a}_3$, and $-\pi \leqq \omega_i \leqq \pi$ for $i = 1, 2, 3$.

The constraint which extracts the ordered configurations is written in direct analogy to Eq. 11:

$$(19)\quad S_{\vec{R}}\left[S_{\vec{R}+\vec{A}_L} + S_{\vec{R}-\vec{A}_L}\right] = S_{\vec{R}+\vec{a}_i}\left[S_{\vec{R}+\vec{a}_i+\vec{A}_L} + S_{\vec{R}+\vec{a}_i-\vec{A}_L}\right] ,$$

in which $\vec{R}$ and $\vec{a}_i$ are defined above and $\vec{A}_L$ is any lattice vector. Although Eq. 19 is the obvious

generalization of the one-dimensional constraint, there is the following important difference in the two cases. The constraint for the one-dimensional case is equivalent to requiring the number of like and unlike $m$th neighbors to be the same for all spins and for all $m$. The corresponding statement is not true in the three-dimensional case. The condition expressed by Eq. 19 is more restrictive than one which demands equal numbers of like and unlike neighbors. Clearly, Eq. 19 demands equivalence of spins with respect to any lattice vector $\vec{A}_L$, so that a configuration which satisfies the condition will automatically satisfy the requirement of equal numbers of like and unlike neighbors. This may be seen, from Eq. 19, by summing the $\vec{A}_L$ over fixed magnitudes. The converse is not true, for configurations can be found which satisfy an equivalence condition with respect to neighbor relations but which do not satisfy the more restrictive condition above.

It may be pointed out, however, that once the configurations have been enumerated which satisfy condition 19 it is a relatively easy matter to obtain from them others which satisfy the less restrictive requirement.

It is now shown that the condition of Eq. 19 restricts the $\omega_i$ to the values

$$\omega_i = 0 \ , \quad \pm\frac{\pi}{2} \ , \quad \pi \ , \tag{20}$$

where the range $-\pi$ to $\pi$ for each of the $\omega_i$ has been chosen rather than the range 0 to $2\pi$, to allow propagation vectors in all directions.

The proof that the configurations given by Eq. 20 are the only ones satisfying the equivalence requirement as expressed by Eq. 19 exactly parallels the steps used for the one-dimensional chain. Since again the constraint requires that $S^2_{\vec{R}+\vec{a}_i} = S^2_{\vec{R}}$, it is written in the form

$$S_{\vec{R}}\left[S_{\vec{R}+\vec{A}_L} + S_{\vec{R}-\vec{A}_L} \mp S_{\vec{R}+\vec{a}_i+\vec{A}_L} \mp \mp S_{\vec{R}+\vec{a}_i-\vec{A}_L}\right] = 0 \ . \tag{21}$$

Expressing the spins appearing here in terms of normal coordinates gives

$$0 = \sum_{\vec{k}} q_{\vec{k}} \cos \vec{k}\cdot\vec{A}_L \Big[\cos \vec{k}\cdot\vec{R}(1 \mp \mp \cos \vec{k}\cdot\vec{a}_i \mp \sin \vec{k}\cdot\vec{a}_i) + \sin \vec{k}\cdot\vec{R} \times \times (1 \mp \cos \vec{k}\cdot\vec{a}_i \pm \sin \vec{k}\cdot\vec{a}_i)\Big] \ , \tag{22}$$

where $\vec{k} = 2\pi(k_1\vec{b}_1 + k_2\vec{b}_2 + k_3\vec{b}_3)/N^{1/3}$, the $\vec{b}_i$ are basis vectors of the reciprocal lattice, and the triple sum is over $1 \leq k_1 \leq N^{1/3}$, $i = 1, 2, 3$. Multiplying by $\cos \vec{k}'\cdot\vec{A}_L$ and summing over all lattice vectors $\vec{A}_L$ results in the equation

$$0 = q_{k'}\Big[\cos \vec{k}'\cdot\vec{R}(1 \mp \cos \vec{k}'\cdot\vec{a}_i \mp \mp \sin \vec{k}'\cdot\vec{a}_i) + \sin \vec{k}'\cdot\vec{R}(1 \mp \cos \vec{k}'\cdot\vec{a}_i \pm \sin \vec{k}'\cdot\vec{a}_i)\Big] + + q_{\vec{K}-\vec{k}'}\Big[\cos \vec{k}'\cdot\vec{R}(1 \mp \cos \vec{k}'\cdot\vec{a}_i \pm \sin \vec{k}'\cdot\vec{a}_i) - - \sin \vec{k}'\cdot\vec{R}(1 \mp \cos \vec{k}'\cdot\vec{a}_i \mp \sin \vec{k}'\cdot\vec{a}_i)\Big] \ , \tag{23}$$

with $\vec{K} = 2\pi(\vec{b}_1 + \vec{b}_2 + \vec{b}_3)$. There are three such equations, one for each of the basis vectors of the real lattice, $\vec{a}_1$, $\vec{a}_2$, $\vec{a}_3$, and again each equation must be satisfied for all lattice positions $\vec{R}$. By exactly the same reasoning as for the one-dimensional chain, their solution is the set

$$\omega_i = \frac{2\pi k_i}{N^{1/3}} = 0 \ , \ \pm\frac{\pi}{2}, \ \pi \ ; \qquad i = 1, 2, 3 \ . \tag{24}$$

Again these are the only values for $\omega$ for which Eq. 24 can be satisfied for all lattice positions $\vec{R}$, because the terms in the parentheses in Eq. 23 cannot be made zero for any other choice of $\omega$.

Since there are four possible values for each of the $\omega_i$, there are, in all, 64 possible ordered arrangements. To each choice of the $\omega_i$ there corresponds a spin configuration which is described by

$$S_{l_1 l_2 l_3} \propto \cos(\omega_1 l_1 + \omega_2 l_2 + \omega_3 l_3) + + \sin(\omega_1 l_1 + \omega_2 l_2 + \omega_3 l_3) \ . \tag{25}$$

One may note that the propagation vector $\vec{k} = \omega_1\vec{b}_1 + \omega_2\vec{b}_2 + \omega_3\vec{b}_3$ is normal to planes of like spin. The manner in which these planes alternate

in sign is determined from the wavelength $\lambda = 2\pi/|\vec{k}|$, which gives the distance along $\vec{k}$ for one complete cycle of (+) or (−) planes.

If isotropic first- and second-nearest-neighbor interactions are assumed, the energy of a configuration may be obtained from Eq. 4 by setting $q_k^2 = N$ for the particular configuration, yielding the energy per spin $E$:

$$E = \frac{1}{2}\,\nu^2_{\omega_1\omega_2\omega_3}\,, \tag{26}$$

with $\nu_{\omega_1\omega_2\omega_3}$ obtained from Eq. 8. This procedure is equivalent to writing the energy in the form

$$E = \frac{1}{2}\,\alpha \sum_{l_1 l_2 l_3} S_{l_1 l_2 l_3} \sum_{\mathrm{NN}} S_{l_1' l_2' l_3'} + \frac{1}{2}\,\beta \sum_{l_1 l_2 l_3} S_{l_1 l_2 l_3} \sum_{\mathrm{NNN}} S_{l_1' l_2' l_3'}\,, \tag{27}$$

where $\alpha$ and $\beta$ are nearest- and next-nearest-neighbor interaction energies, which are positive if antiferromagnetic (AF) and negative if ferromagnetic (F); $S_{l_1 l_2 l_3}$ is (±1) as above; and the sums are taken over the first- and second-nearest-neighbor configuration for each spin.

## APPLICATIONS TO SIMPLE LATTICES

### Simple Cubic Lattice

To illustrate the variety of types of ordered spin configurations, we first give results for the simple cubic lattice in Table 1. The choice of lattice vectors is illustrated in Fig. 2*a*. Of the 64 configurations which result from all possible choices of $\omega_i$, only 10 are distinctly different. (The remaining 54 can be derived from these by cyclic permutation of the basis vectors, by shift in origin, or by rotation.)

The quantity $E/|\alpha|$ for the case that both interactions are AF as calculated from Eq. 26 is

**Table 1. Ordered Spin Configurations on a Simple Cubic Lattice**

| No. | $\omega_1\,\omega_2\,\omega_3$ | Number of Configurations | Neighbors | | | | $E/\lvert\alpha\rvert$ |
|---|---|---|---|---|---|---|---|
| | | | NN | | NNN | | |
| | | | Like | Unlike | Like | Unlike | |
| 1 | 0 0 0 | 1 | 6 | 0 | 12 | 0 | $3+6\rho$ |
| 2 | $0\,0\,\frac{\pi}{2}$ | 6 | 5 | 1 | 8 | 4 | $2+2\rho$ |
| 3 | $0\,0\,\pi$ | 3 | 4 | 2 | 4 | 8 | $1-2\rho$ |
| 4 | $0\,\frac{\pi}{2}\,\frac{\pi}{2}$ | 12 | 4 | 2 | 6 | 6 | 1 |
| 5 | $\frac{\pi}{2}\,\frac{\pi}{2}\,\frac{\pi}{2}$ | 8 | 3 | 3 | 6 | 6 | 0 |
| 6 | $0\,\frac{\pi}{2}\,\pi$ | 12 | 3 | 3 | 4 | 8 | $-2\rho$ |
| 7 | $0\,\pi\,\pi$ | 3 | 2 | 4 | 4 | 8 | $-1-2\rho$ |
| 8 | $\frac{\pi}{2}\,\frac{\pi}{2}\,\pi$ | 12 | 2 | 4 | 6 | 6 | $-1$ |
| 9 | $\frac{\pi}{2}\,\pi\,\pi$ | 6 | 1 | 5 | 8 | 4 | $-2+2\rho$ |
| 10 | $\pi\,\pi\,\pi$ | 1 | 0 | 6 | 12 | 0 | $-3+6\rho$ |

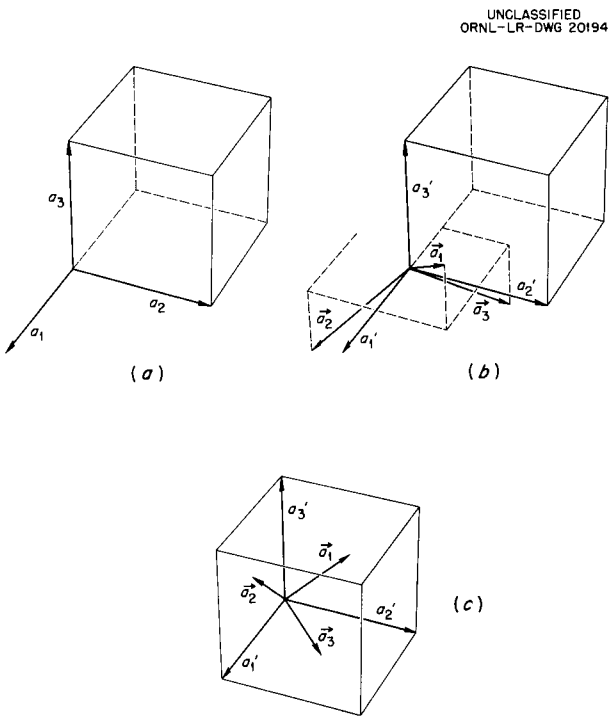


**Fig. 2. Choice of Lattice Vectors.** (*a*) Simple cubic lattice; (*b*) body-centered cubic lattice; (*c*) face-centered cubic lattice.

$$(28)\quad \frac{E}{|\alpha|} = \cos\omega_1 + \cos\omega_2 + \cos\omega_3 + 2\rho[\cos\omega_1\cos\omega_2 + \cos\omega_1\cos\omega_3 + \cos\omega_2\cos\omega_3] .$$

In Table 1, values of $E/|\alpha|$ are given for this case, and the three cases $\alpha > 0, \beta > 0$; $\alpha < 0, \beta > 0$; and $\alpha > 0, \beta < 0$ are illustrated in Fig. 3, where $E/|\alpha|$ is plotted as a function of $\rho = |\beta|/|\alpha|$ for the ten configurations.

The results of considerations given in the literature[6–9] are that two types of ordering are energetically possible if isotropic nearest- and next-nearest-neighbor AF interactions are assumed. These are illustrated in Fig. 3*a*, where for $\rho < 0.25$ the $(\pi\ \pi\ \pi)$ configuration is favored, and for $\rho > 0.25$ the $(0\ \pi\ \pi)$ is predicted. These correspond respectively to configurations (1) in which each spin has six antiferromagnetically aligned nearest neighbors and (2) in which chains of like spin are surrounded by four oppositely oriented chains of like spin. In Fig. 3*b* ($\alpha < 0$, $\beta > 0$) the ferromagnetic (0 0 0) configuration is favored if $\rho < 0.25$ and if the alternating ferromagnetic sheet configuration $(0\ 0\ \pi)$ for $\rho > 0.25$. In the final case only the $(\pi\ \pi\ \pi)$ configuration is stable.

Experimentally, the perovskite-like compounds $ABO_3$, which contain magnetically active A- or B-site cations, provide examples of magnetic ions on a simple cubic lattice. To a fair approximation the A- and B-site cations in the manganese perovskites, for example, (La,Ca) $(Mn^{3+},Mn^{4+})O_3$, in the rare-earth orthoferrites, and in the rare-earth orthochromites form simple cubic lattices, and magnetic-ordering configurations for a number of these compounds have now been reported.[10,11] Of the configurations listed in Table 1, four have been observed: in the mixed-oxides series the pure compounds $LaMnO_3$ and $CaMnO_3$ exhibit ordering of the types $(0\ 0\ \pi)$ and $(\pi\ \pi\ \pi)$, respectively, and for certain concentrations of $Mn^{4+}$ the (0 0 0) and $(0\ \pi\ \pi)$ configurations are also found. In the rare-earth orthoferrites $AFeO_3$ (ref 12) (A = La, Nd, Er, Ho) and in $LaCrO_3$, the $Fe^{3+}$ and $Cr^{3+}$ order at high temperatures in the $(\pi\ \pi\ \pi)$ arrangement, and $Er^{3+}$ and $Ho^{3+}$ appear to order at very low temperatures in the $(0\ \pi\ \pi)$ configuration. These four structure types were originally designated as types *A*, *B*, *C*, *G*; in the present notation they are respectively $(0\ 0\ \pi)$, (0 0 0), $(0\ \pi\ \pi)$, and $(\pi\ \pi\ \pi)$. This latter notation will be adopted for the balance of this discussion, it being more descriptive of the spin arrangement in the several structures.

### Face-Centered Cubic Lattice

The basis vectors for the face-centered cubic lattice and their relationship to a convenient

[6] P. W. Anderson, *Phys. Rev.* 79, 705 (1950).

[7] J. M. Luttinger, *Phys. Rev.* 81, 1015 (1951).

[8] J. S. Smart, *Phys. Rev.* 86, 968 (1952); *Phys. Rev.* 90, 55 (1953).

[9] J. H. Van Vleck, *J. phys. radium* 12, 262 (1951).

[10] E. O. Wollan and W. C. Koehler, *Phys. Rev.* 100, 545 (1955).

[11] W. C. Koehler and E. O. Wollan, *Phys. and Chem. Solids* 2, 100 (1957).

[12] W. C. Koehler, E. O. Wollan, M. K. Wilkinson, and J. W. Cable, *Phys. Rev.* (to be published).

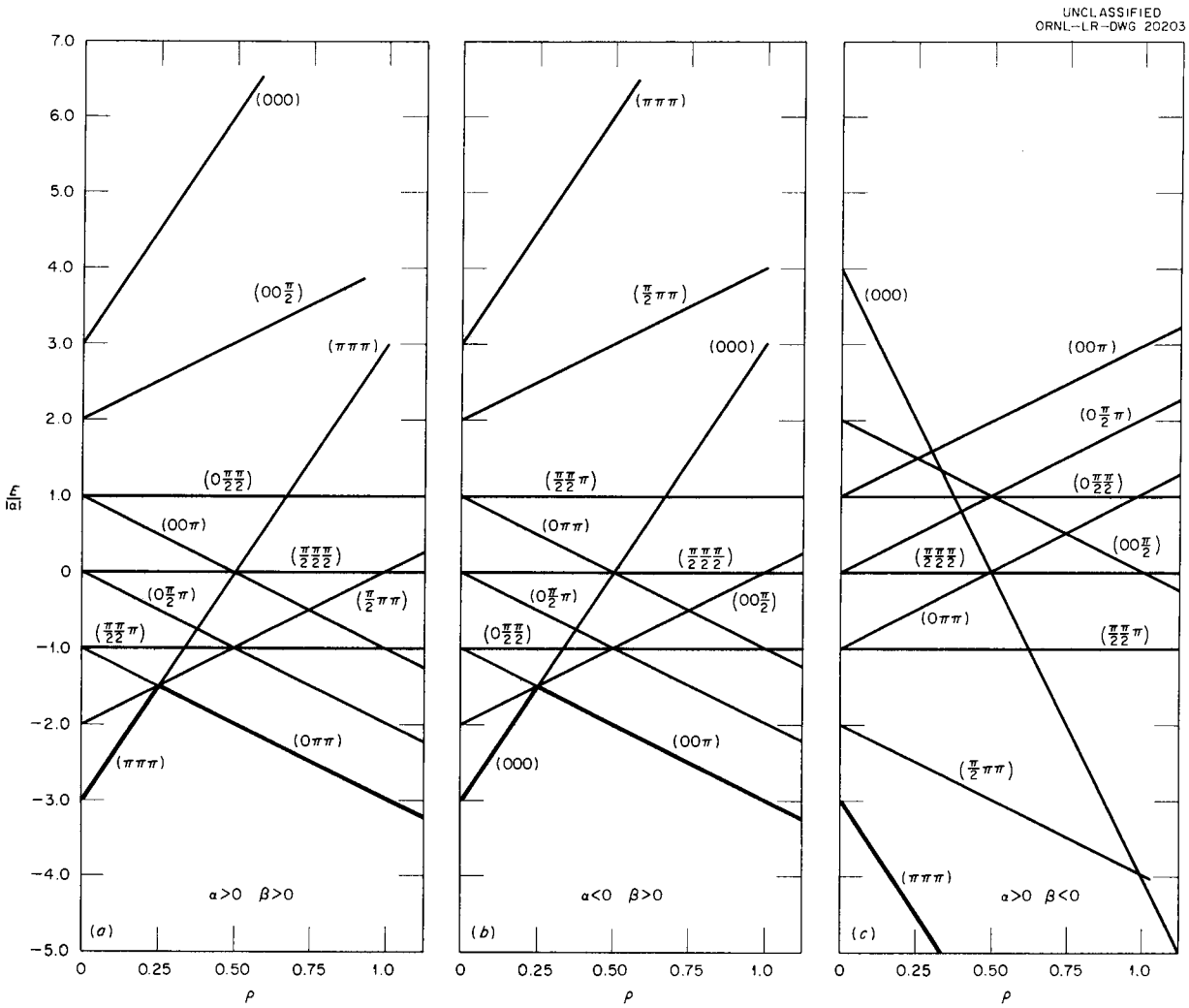


**Fig. 3.** $E/|\alpha|$ **vs** $\rho = |\beta|/|\alpha|$ **for Simple Cubic Lattice.** (*a*) Both interactions antiferromagnetic $\alpha > 0$, $\beta > 0$; (*b*) $\alpha < 0$, $\beta > 0$; (*c*) $\alpha > 0$, $\beta < 0$. Favored configurations (*a*) $\rho < 0.25$ ($\pi\pi\pi$), $\rho > 0.25$ ($0\pi\pi$); (*b*) $\rho < 0.25$ (000), $\rho > 0.25$ ($00\pi$); (*c*) ($\pi\pi\pi$).

orthogonal coordinate system are illustrated in Fig. 2*c*. As in the previous case, there is a total of 64 possible configurations corresponding to the 64 possible combinations of $\omega_1$, $\omega_2$, $\omega_3$. Of these, again, 40 may be excluded as arising from cyclic permutations of existing combinations, and of the remaining 24, eight may be considered as distinct. The eight configurations listed in Table 2 may be more graphically described by giving the configurations of the simple cubic sublattices into which the face-centered cubic lattice naturally divides. The notation adopted is the following: the origins of the four sublattices are taken at 0 0 0, $(\vec{a}_1' + \vec{a}_2')/2$, $(\vec{a}_2' + \vec{a}_3')/2$, and $(\vec{a}_1' + \vec{a}_3')/2$, as indicated in Fig. 2*c*, and the sublattice is designated as positive or negative, as the spin at its origin is up (+) or down (–). In accordance with the requirement of equivalence, each sublattice configuration must be the same one of the ten simple cubic configurations described above. In Table 2 the sublattice configurations are given in the above-mentioned sequence.

For each configuration the number of like and unlike nearest and next-nearest neighbors is

tabulated. The energy $E/|\alpha|$ for isotropic AF interactions expressed in terms of the $\omega_i$ is

$$(29)\quad \frac{E}{|\alpha|} = \cos\omega_1 + \cos\omega_2 + \cos\omega_3 + \cos(\omega_1 - \omega_3) + \cos(\omega_1 - \omega_2) + \cos(\omega_2 - \omega_3) + \rho[\cos(\omega_1 + \omega_2 - \omega_3) + \cos(\omega_1 - \omega_2 + \omega_3) + \cos(-\omega_1 + \omega_2 + \omega_3)] .$$

These values are given in the table and displayed graphically in Fig. 4*a*. The other two cases of interest are also plotted in the figure.

When $\alpha$ and $\beta$ are both positive, the $\left(\pi\frac{\pi}{2}\frac{\bar{\pi}}{2}\right)$ configuration is favored if $\rho < 0.5$, and the $(0\ 0\ \pi)$ configuration is favored if $\rho > 0.5$. The $(0\ 0\ \pi)$ arrangement may be alternatively viewed as consisting of four interpenetrating $(\pi\ \pi\ \pi)$ simple cubic configurations so oriented that the propagation vector $\vec{k}$ is normal to (111) planes of the

**Table 2. Ordered Spin Configurations on a Face-Centered Cubic Lattice***

| No. | $\omega_1\,\omega_2\,\omega_3$ | Number of Configurations | Neighbors NN Like | NN Unlike | NNN Like | NNN Unlike | $E/\lvert\alpha\rvert$ |
|---|---|---|---|---|---|---|---|
| 1 | $0\,0\,0$ <br> $[0\,0\,0;\ 0\,0\,0;\ 0\,0\,0;\ 0\,0\,0]$ | 1 | 12 | 0 | 6 | 0 | $6+3\rho$ |
| 2 | $0\,\pi\pi$ <br> $[0\,0\,0;\ -(0\,0\,0);\ 0\,0\,0;\ -(0\,0\,0)]$ | 3 | 4 | 8 | 6 | 0 | $-2+3\rho$ |
| 3 | $0\frac{\pi}{2}\frac{\pi}{2}\left(0\frac{\bar{\pi}}{2}\frac{\bar{\pi}}{2}\right)$ <br> $[\pi 0\,0;\ \pi 0\,0;\ \pi 0\,0;\ \pi 0\,0]$ | 6 | 8 | 4 | 4 | 2 | $2+\rho$ |
| 4 | $\pi\frac{\pi}{2}\frac{\bar{\pi}}{2}\left(\pi\frac{\bar{\pi}}{2}\frac{\pi}{2}\right)$ <br> $[\pi 0\,0;\ -(\pi 0\,0);\ -(\pi 0\,0);\ \pi 0\,0]$ | 6 | 4 | 8 | 4 | 2 | $-2+\rho$ |
| 5 | $0\frac{\pi}{2}\frac{\bar{\pi}}{2}\left(0\frac{\bar{\pi}}{2}\frac{\pi}{2};\ \frac{\pi}{2}\frac{\pi}{2}\pi;\ \frac{\bar{\pi}}{2}\frac{\bar{\pi}}{2}\pi\right)$ <br> $[0\,\pi\pi;\ -(0\,\pi\pi);\ 0\,\pi\pi;\ 0\,\pi\pi]$ | 12 | 6 | 6 | 2 | 4 | $-\rho$ |
| 6 | $0\,0\,\pi\ (\pi\pi\pi)$ <br> $[\pi\pi\pi;\ \pi\pi\pi;\ -(\pi\pi\pi);\ \pi\pi\pi]$ | 4 | 6 | 6 | 0 | 6 | $-3\rho$ |
| 7 | $\frac{\pi}{2}\frac{\pi}{2}\frac{\pi}{2}\left(\frac{\bar{\pi}}{2}\frac{\bar{\pi}}{2}\frac{\bar{\pi}}{2};\ 0\,0\frac{\pi}{2};\ 0\,0\frac{\bar{\pi}}{2}\right)$ <br> $\left[\frac{\pi}{2}\frac{\pi}{2}\frac{\pi}{2};\ \frac{\bar{\pi}}{2}\frac{\bar{\pi}}{2}\frac{\bar{\pi}}{2};\ \frac{\bar{\pi}}{2}\frac{\bar{\pi}}{2}\frac{\bar{\pi}}{2};\ \frac{\bar{\pi}}{2}\frac{\bar{\pi}}{2}\frac{\bar{\pi}}{2}\right]$ | 8 | 9 | 3 | 3 | 3 | 3 |
| 8 | $\frac{\bar{\pi}}{2}\frac{\bar{\pi}}{2}\frac{\pi}{2}\left(\frac{\pi}{2}\frac{\pi}{2}\frac{\bar{\pi}}{2};\ 0\,\pi\frac{\pi}{2};\ 0\,\pi\frac{\bar{\pi}}{2};\ 0\frac{\pi}{2}\pi;\ 0\frac{\bar{\pi}}{2}\pi;\ \pi\pi\frac{\pi}{2};\ \pi\pi\frac{\bar{\pi}}{2}\right)$ <br> $\left[\frac{\pi}{2}\frac{\pi}{2}\frac{\pi}{2};\ \frac{\bar{\pi}}{2}\frac{\bar{\pi}}{2}\frac{\bar{\pi}}{2};\ -\left(\frac{\bar{\pi}}{2}\frac{\bar{\pi}}{2}\frac{\bar{\pi}}{2}\right);\ -\left(\frac{\bar{\pi}}{2}\frac{\bar{\pi}}{2}\frac{\bar{\pi}}{2}\right)\right]$ | 24 | 5 | 7 | 3 | 3 | $-1$ |

*Equivalent configurations are given in parentheses. The four-sublattice designation is given in brackets, where the origins are taken at 000, $(a_1' + a_2')/2$, $(a_2' + a_3')/2$, and $(a_1' + a_3')/2$, respectively.

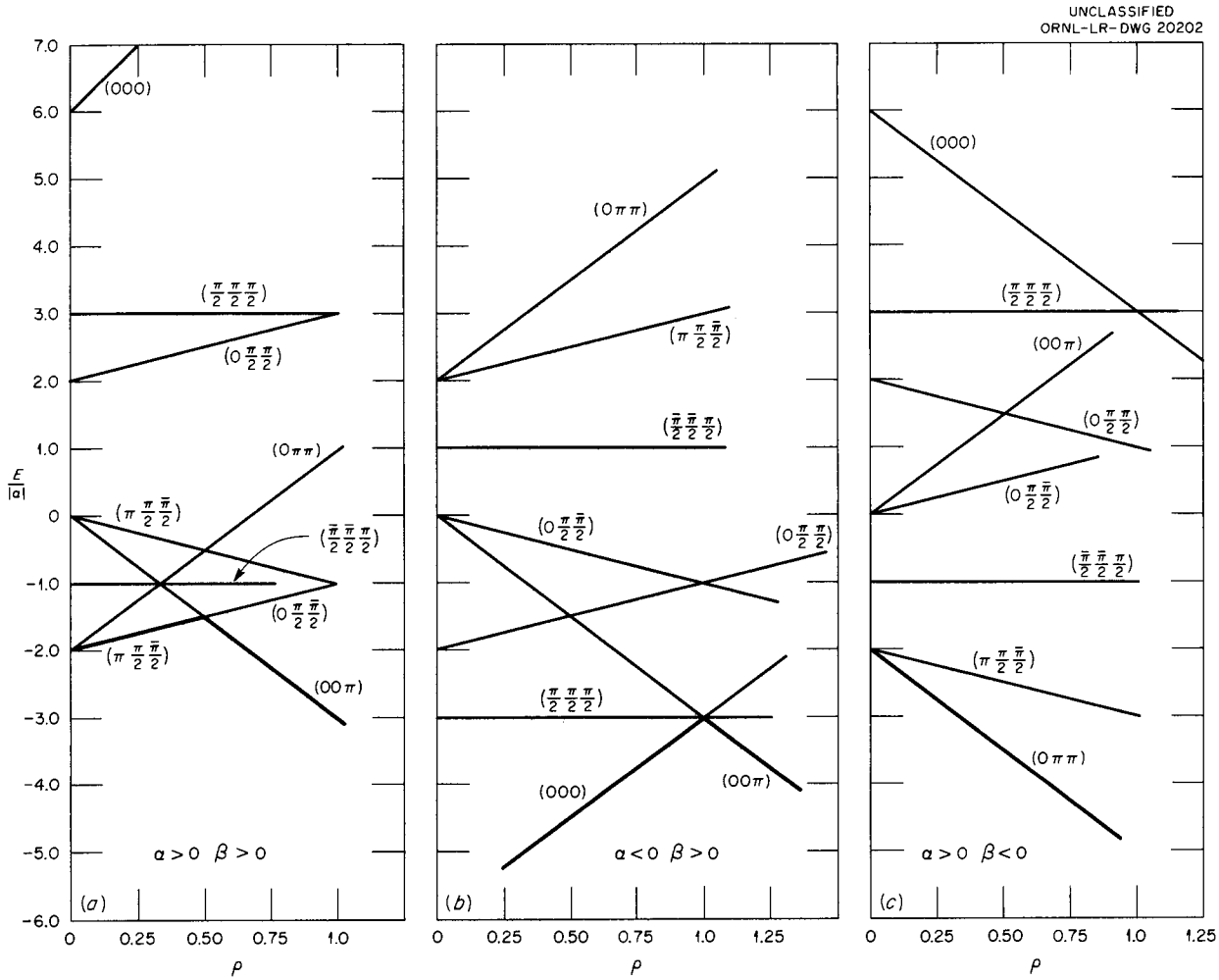


**Fig. 4.** $E/|\alpha|$ **vs** $\rho = |\beta|/|\alpha|$ **for Face-Centered Cubic Lattice.** (*a*) **Both configurations antiferromagnetic** $\alpha > 0$, $\beta > 0$; (*b*) $\alpha < 0$, $\beta > 0$; (*c*) $\alpha > 0$, $\beta < 0$. **Favored configurations** (*a*) $\rho < 0.50 \left(\pi \frac{\pi}{2} \frac{\bar{\pi}}{2}\right)$, $\rho > 0.50$ $(00\pi)$; (*b*) $\rho < 1.00$ (000), $\rho > 1.00$ $(00\pi)$; (*c*) $(0\pi\pi)$.

face-centered cubic lattice. Ordering of this type has previously been designated as "ordering of the second kind," and it is this configuration which is apparently found for $Mn^{++}$ in MnO and $\alpha$-MnS according to recent measurements of Corliss, Elliot, and Hastings.[13] The $\left(\pi \frac{\pi}{2} \frac{\bar{\pi}}{2}\right)$ configuration consists of $(\pi\ 0\ 0)$ configurations such that the planes of like spin are (120) planes. Measurements by Corliss, Elliot, and Hastings[13] have shown that this configuration is adopted by $Mn^{++}$ in the zinc blende modification of MnS. This configuration has been variously described as "improved ordering of the first kind" or "ordering of the third kind."

We note that $(\pi\ 0\ 0)$ configurations may also be arranged to form a configuration in which each spin has eight like and four unlike nearest neighbors $\left(0 \frac{\pi}{2} \frac{\pi}{2}\right)$ in distinction to the case above.

[13] L. Corliss, N. Elliot, and J. Hastings, *Phys. Rev.* 104, 924 (1956).

Energetically, this case is not favored for any combination of F and AF first- and second-neighbor interactions, nor has an experimental example been found as far as we know.

As illustrated in Fig. 4 for first-neighbor F and second-neighbor AF interactions, the ferromagnetic (0 0 0) configuration is stable for $\rho < 1.0$ and the (0 0 $\pi$) for $\rho > 1.0$. The $\left(\frac{\pi}{2}\frac{\pi}{2}\frac{\pi}{2}\right)$ arrangement has the same energy as the other two for $\rho = 1.0$. This also appears not to be found experimentally.

For the case of AF first- and F second-neighbor interactions only the (0 $\pi$ $\pi$) configuration is energetically favored. This is an AF structure composed of F simple cubic configurations and is a layer structure; the propagation vector for (0 $\pi$ $\pi$) is perpendicular to (100) planes. The (0 $\pi$ $\pi$) configuration has been called "ordering of the first kind" and seems to be the ordering arrangement of $U^{4+}$ in fluorite-type $UO_2$ (ref 14).

It is interesting to point out that the configuration $\left(0\,\frac{\pi}{2}\frac{\overline{\pi}}{2}\right)$, which is made up of (0 $\pi$ $\pi$) configurations, is possibly represented in nature by the AF structure of $Er_2O_3$ (ref 15). This configuration is, however, not energetically favored for isotropic first- and second-neighbor interactions.

A similar compilation has been made for the body-centered cubic lattice and for the hexagonal layer lattice, and the tabulations for these two cases are given in Tables 3 and 4.

---

[14] D. G. Henshaw and B. N. Brockhouse, *Bull. Am. Phys. Soc.* 2, 9 (1957).

[15] M. K. Wilkinson *et al.*, *Bull. Am. Phys. Soc.* 2, 129 (1957).

**Table 3. Ordered Spin Configurations on a Body-Centered Cubic Lattice***

| No. | Oblique Coordinates | Orthogonal Coordinates | Number of Configurations | Neighbors | | | | $E/\lvert\alpha\rvert$ |
|---|---|---|---|---|---|---|---|---|
| | | | | NN | | NNN | | |
| | | | | Like | Unlike | Like | Unlike | |
| 1 | 0 0 0 | 0 0 0; 0 0 0 | 1 | 8 | 0 | 6 | 0 | $4+3\rho$ |
| 2 | $\pi\pi\pi$ | 0 0 0; −(0 0 0) | 1 | 0 | 8 | 6 | 0 | $-4+3\rho$ |
| 3 | $\frac{\pi}{2}\frac{\overline{\pi}}{2}\frac{\overline{\pi}}{2}\left(\frac{\overline{\pi}}{2}\frac{\pi}{2}\frac{\pi}{2}\right)$ | $0\,0\,\pi$; $0\,0\,\pi$ | 6 | 4 | 4 | 4 | 2 | $\rho$ |
| 4 | $0\,0\,\pi\,(\pi\pi 0)$ | $0\,\pi\pi$; $0\,\pi\pi$ | 6 | 4 | 4 | 2 | 4 | $-\rho$ |
| 5 | $\frac{\pi}{2}\frac{\pi}{2}\frac{\pi}{2}\left(\frac{\overline{\pi}}{2}\frac{\overline{\pi}}{2}\frac{\overline{\pi}}{2}\right)$ | $\pi\pi\pi$; $\pi\pi\pi$ | 2 | 4 | 4 | 0 | 6 | $-3\rho$ |
| 6 | $\frac{\pi}{2}\frac{\overline{\pi}}{2}0\left(\frac{\overline{\pi}}{2}\frac{\pi}{2}0;\ 0\,0\,\frac{\pi}{2};\ 0\,0\,\frac{\overline{\pi}}{2}\right)$ | $0\,\frac{\pi}{2}\frac{\pi}{2}$; $0\,\frac{\overline{\pi}}{2}\frac{\overline{\pi}}{2}$ | 12 | 6 | 2 | 4 | 2 | $2+\rho$ |
| 7 | $\frac{\overline{\pi}}{2}\frac{\pi}{2}\pi\left(\frac{\pi}{2}\frac{\overline{\pi}}{2}\pi;\ \pi\pi\frac{\pi}{2};\ \pi\pi\frac{\overline{\pi}}{2}\right)$ | $0\,\frac{\pi}{2}\frac{\pi}{2}$; $-\left(0\,\frac{\overline{\pi}}{2}\frac{\overline{\pi}}{2}\right)$ | 12 | 2 | 6 | 4 | 2 | $-2+\rho$ |
| 8 | $0\,\pi\frac{\pi}{2}\left(0\,\pi\frac{\overline{\pi}}{2};\ \pi\frac{\pi}{2}\frac{\pi}{2};\ \pi\frac{\overline{\pi}}{2}\frac{\overline{\pi}}{2};\ 0\,\frac{\pi}{2}\pi;\ 0\,\frac{\overline{\pi}}{2}\pi;\ \frac{\pi}{2}\frac{\pi}{2}0;\ \frac{\overline{\pi}}{2}\frac{\overline{\pi}}{2}0\right)$ | $\pi\frac{\pi}{2}\frac{\pi}{2}$; $\pi\frac{\pi}{2}\frac{\pi}{2}$ | 24 | 4 | 4 | 2 | 4 | $-\rho$ |

*Equivalent configurations are given in parentheses. The two-sublattice description gives the configurations of the (000) and $\left(\frac{1}{2}\frac{1}{2}\frac{1}{2}\right)$ sublattices in that order.

Table 4. Ordered Spin Configurations on a Hexagonal Layer Lattice

| No. | $\omega_1\,\omega_2\,\omega_3$ | Number of Configurations | Neighbors: NN (parallel to layer) Like | NN (parallel to layer) Unlike | NNN (normal to layer) Like | NNN (normal to layer) Unlike | $E/\lvert\alpha\rvert$ |
|---|---|---|---|---|---|---|---|
| 1 | $0\,0\,0$ | 1 | 6 | 0 | 2 | 0 | $3+\rho$ |
| 2 | $0\,0\,\pi$ | 1 | 6 | 0 | 0 | 2 | $3-\rho$ |
| 3 | $0\,0\,\frac{\pi}{2}$ | 2 | 6 | 0 | 1 | 1 | 3 |
| 4 | $\pi\,\pi\,0$ | 3 | 2 | 4 | 2 | 0 | $-1+\rho$ |
| 5 | $\pi\,\pi\,\pi$ | 3 | 2 | 4 | 0 | 2 | $-1-\rho$ |
| 6 | $\pi\,\pi\,\frac{\pi}{2}$ | 6 | 2 | 4 | 1 | 1 | $-1$ |
| 7 | $\frac{\pi}{2}\,\frac{\pi}{2}\,0$ | 6 | 2 | 4 | 2 | 0 | $-1+\rho$ |
| 8 | $\frac{\pi}{2}\,\frac{\pi}{2}\,\pi$ | 6 | 2 | 4 | 0 | 2 | $-1-\rho$ |
| 9 | $\frac{\pi}{2}\,\frac{\pi}{2}\,\frac{\pi}{2}$ | 12 | 2 | 4 | 1 | 1 | $-1$ |
| 10 | $\frac{\pi}{2}\,\frac{\bar{\pi}}{2}\,0$ | 6 | 4 | 2 | 2 | 0 | $1+\rho$ |
| 11 | $\frac{\pi}{2}\,\frac{\bar{\pi}}{2}\,\pi$ | 6 | 4 | 2 | 0 | 2 | $1-\rho$ |
| 12 | $\frac{\pi}{2}\,\frac{\bar{\pi}}{2}\,\frac{\pi}{2}$ | 12 | 4 | 2 | 1 | 1 | 1 |

## DISCUSSION: LIMITATIONS OF THE CATALOGING SCHEME

It is to be emphasized that we have constructed a method for the enumeration only of certain ordered spin configurations. The method gives all possible ordered configurations corresponding to a single normal mode or, equivalently, to a single propagation vector. It is implicit in our method that there be a single axis of magnetization and a single type of magnetic ion. All the configurations tabulated have the property that all spins have the same numbers of like and unlike neighbors at all distances, but as we have mentioned above, not all such arrangements are counted by our method. There are therefore a large number of possible ordered spin configurations, some of them experimentally observed, which are not contained in our cataloging scheme. However, as we shall illustrate, such configurations may be considered as superpositions of configurations which are contained in our enumeration.

For example, we may cite the *C-E* structure described by Wollan and Koehler[16] in their study of manganese perovskites. The simple cubic point lattice is subdivided into two tetragonal lattices as illustrated in Fig. 5, and on these the $Mn^{3+}$ have a $(\pi\ 0\ \pi)$ configuration; the $Mn^{4+}$ have a

[16] E. O. Wollan and W. C. Koehler, *Phys. Rev.* **100**, 545 (1955).

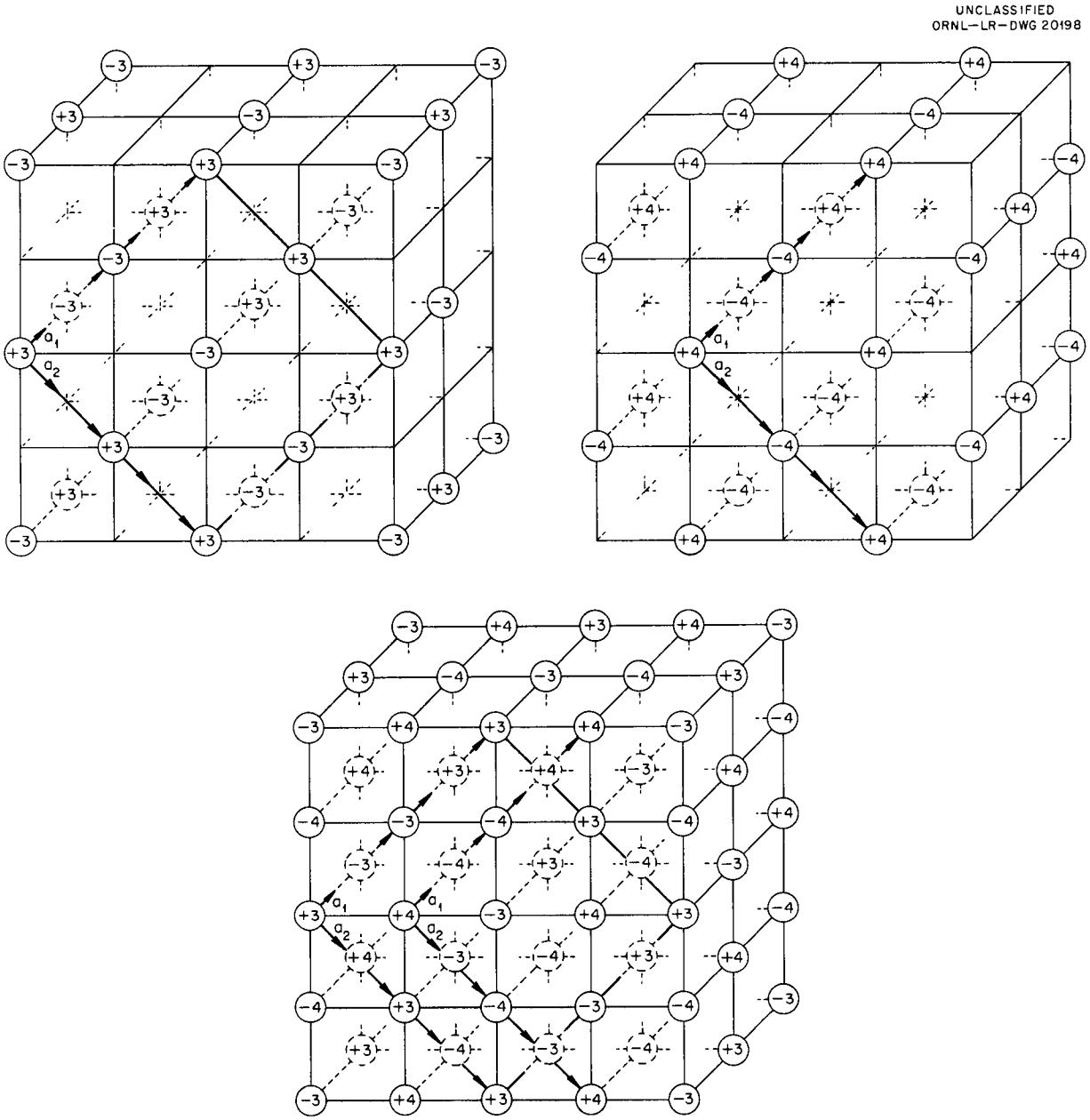


**Fig. 5. Type *C-E* Structure. If tetragonal sublattices are chosen, the configuration is $Mn^{3+}$ ($\pi 0 \pi$); $Mn^{4+}$ ($\pi\pi\pi$).**

($\pi\ \pi\ \pi$) configuration. The $Mn^{3+}$ ions and $Mn^{4+}$ ions separately are represented by single mode configurations, but the over-all arrangement is a superposition of the two. If one disregards the differences in ion type, the arrangement may still be described as a superposition of ($\pi\ 0\ \pi$) and ($\pi\ \pi\ \pi$) configurations, and it will be noted that while the neighbor relation condition is satisfied for first neighbors it fails for second neighbors.

As a second example, consider the face-centered cubic ($0\ 0\ \pi$) configuration (No. 6, Table 2) which is alternatively described as [$\pi\ \pi\ \pi$; $\pi\ \pi\ \pi$; $-(\pi\ \pi\ \pi)$; $\pi\ \pi\ \pi$]. A second configuration may be obtained from this by changing the sign of one of the constituent configurations: thus [$\pi\ \pi\ \pi$; $-(\pi\ \pi\ \pi)$; $-(\pi\ \pi\ \pi)$; $\pi\ \pi\ \pi$]. These two spin arrangements, disregarding moment orientation, have been proposed for $Mn^{++}$ in MnO and $\alpha$-MnS, the first by

Shull, Strauser, and Wollan[17] and the second by Li.[18] Both spin arrangements have equal numbers of like and unlike neighbors for all spins at all distances, and they are energetically degenerate for isotropic first- and second-neighbor interactions. This degeneracy has already been noted by Anderson[19] and Luttinger.[20] In the first-mentioned case the orientations of the four ($\pi\pi\pi$) configurations are such that there exists a single propagation vector; for example, the arrangement is characterized by sheets of like spin alternating in sign along a [111] direction. The second configuration does not correspond to a single mode but must be considered as a superposition of modes. The two types may, in general, be distinguished by single-crystal neutron diffraction data and in favorable cases by powder data. For MnO and $\alpha$-MnS a better explanation of the data is obtained with the first-mentioned configuration.[13]

It is of interest to point out also that no other distinct configuration having the same neighbor relations as the two given above can be found, for all other sign permutations lead to equivalent configurations.

The derivation of other configurations based on the lattices considered here and for other point lattices may be carried out systematically in the manner illustrated above by considering various superpositions. Clearly, if the number of superpositions becomes large, the method loses its simplicity.

### DIFFRACTION EFFECTS

Once a configuration of spins has been given, it is a straightforward matter to calculate the geometrical part of the structure amplitude. Such calculations nave been made for configurations based upon the simple cubic, face-centered cubic, body-centered cubic, and hexagonal layer lattices and will be published in due course elsewhere.

[17] C. G. Shull, W. A. Strauser, and E. O. Wollan, *Phys. Rev.* 83, 333 (1951).

[18] Y. Y. Li, *Phys. Rev.* 100, 627 (1955).

[19] P. W. Anderson, *Phys. Rev.* 79, 705 (1950).

[20] J. M. Luttinger, *Phys. Rev.* 81, 1015 (1951).

## ANTIFERROMAGNETIC STRUCTURE OF IRON-GROUP TRIFLUORIDES

H. R. Child E. O. Wollan W. C. Koehler M. K. Wilkinson

### INTRODUCTION

The trifluorides of the 3*d* transition-group metals crystallize in what may be considered as minor modifications of a cubic structure in which the metal ions lie on the corners of the cube and the fluorine ions are at the center of the cube edges. This arrangement is similar to that of the 3*d* metal ions (M) and the oxygen ions in the perovskites of the form $LaMO_3$, in which the nonmagnetic lanthanum (or other) ion is at the center of the cube. It was thus thought of interest to see whether the antiferromagnetic properties of the trifluorides would be similar to those observed[1,2] in the corresponding perovskite type of compounds.

### CRYSTAL STRUCTURE CONSIDERATIONS

It was a fortunate circumstance that at about the time this investigation was begun the reports of a careful x-ray study by a British group[3,4] of the structure of these compounds had just appeared. Their work shows that the trifluorides of V, Cr, Fe, and Co crystallize with a bimolecular rhombohedral cell of space group $R\,\bar{3}C$, with two metal atoms at 000; $\frac{1}{2}\frac{1}{2}\frac{1}{2}$, and with six fluorine atoms at

$$\pm\left(x, \frac{1}{2}-x, \frac{1}{4}\right);\ \pm\left(\frac{1}{2}-x, \frac{1}{4}, x\right);\ \pm\left(\frac{1}{4}, x, \frac{1}{2}-x\right).$$

The parameter $x$ varies from $-0.164$ in $FeF_3$ to about $-0.12$ for $CrF_3$, the latter having been determined from the neutron data, since no published

[1] E. O. Wollan and W. C. Koehler, *Phys. Rev.* 100, 545 (1955).

[2] W. C. Koehler and E. O. Wollan, *Phys. and Chem. Solids* 2, 100 (1957).

[3] M. A. Hepworth *et al.*, *Acta Cryst.* 10, 63 (1957).

[4] M. A. Hepworth and K. H. Jack, *Acta Cryst.* 10, 345 (1957).

values were available for this compound. The degree of distortion of the structure from cubic symmetry is indicated by the fact that the angle for a unimolecular cell is near 88 deg instead of 90 deg.

The structure of $MnF_3$ has been shown[4] to be of lower symmetry (monoclinic) than the other members of this group, and this may be of interesting significance to the over-all results when the work on the compound is completed.

## RESULTS

The neutron powder diffraction patterns for $CrF_3$, $FeF_3$, and $CoF_3$ show the growth of superlattice reflections at low temperatures. The growth of intensity of reflection of the first pair with decreasing temperature below the respective Néel temperatures is shown in Fig. 1.

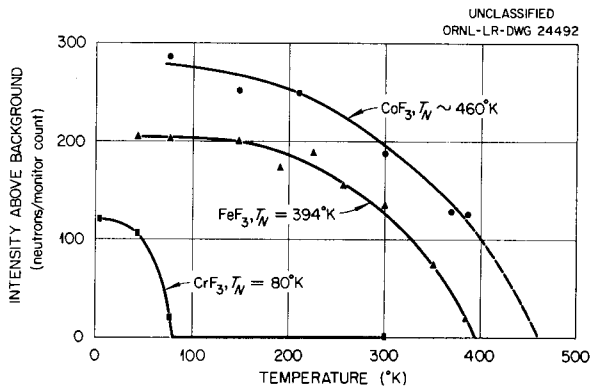


**Fig. 1. Temperature Dependence of Magnetic Reflections from $CrF_3$, $FeF_3$, and $CoF_3$.**

The magnetic reflections observed in all three compounds correspond to what was referred to in the case of the perovskites as the *G*-type structure, the structure in which each metal ion is antiferromagnetically coupled (via the intervening anion) to all six of its nearest neighbors.

A sample diffraction pattern taken below the Néel temperature is shown for $CrF_3$ in Fig. 2. The first two barely resolved peaks of the pattern are of magnetic origin. If the cell were cubic, there would have been a single reflection which would index as the (111). Because of the distortion from cubic symmetry, there are two reflections which, on the rhombohedral cell, index as (111) and (100). The next group of magnetic reflections (221), (210), and ($\bar{1}$11) falls underneath a strong nuclear peak. The intensity associated with these reflections can sometimes be determined with reasonable accuracy from a difference pattern obtained from patterns taken above and below the Néel temperature. A difference pattern over the angular range of interest is shown in the inset in Fig. 2. Such patterns were not obtained for $FeF_3$ and $CoF_3$.

Since the structure of these compounds is distorted from cubic symmetry, it should in principle be possible to obtain information about the orientation of the spins relative to the axes of the rhombohedral cell. The ratio of the intensities of the (111) and (100) reflections, for example, depends strongly on this spin orientation. The calculated ratios of the intensities of these reflections, $P(111)/P(100)$, are given below for three assumed orientations of the spins relative to the rhombohedral axes of the unit cell:

| | Intensity Ratio |
|---|---|
| Parallel to (111) planes (Cr, Fe) | 0.71 |
| Along rhombohedral axis | 0.125 |
| Perpendicular to (111) planes (Co) | 0 |

The related experimental data are shown in Fig. 3, which gives the diffraction patterns over the region of the (111) and (100) magnetic reflections and, incidentally, also over the range of the first nuclear reflection for the three trifluoride compounds. In the case of $CrF_3$, the (111) and (100) reflections are partially resolved; and the ratio of their intensities is found to be close to the value 0.71, which corresponds to the spins being parallel to the (111) planes. In $FeF_3$ these magnetic reflections are not resolved, but the shape of the broad unresolved peak strongly suggests that in this case also the spins are parallel to the (111) planes. In $CoF_3$ the intensity of the (111) reflection is very small. A zero value of this ratio places the spin vector perpendicular to the (111) planes, whereas if the spin vector were along one of the rhombohedral axes, the intensity ratio would be 0.125. The data favor the case of spins perpendicular to the (111) planes.

In the case of the $CrF_3$ sample, intensity measurements of the (111) and (100) reflections were

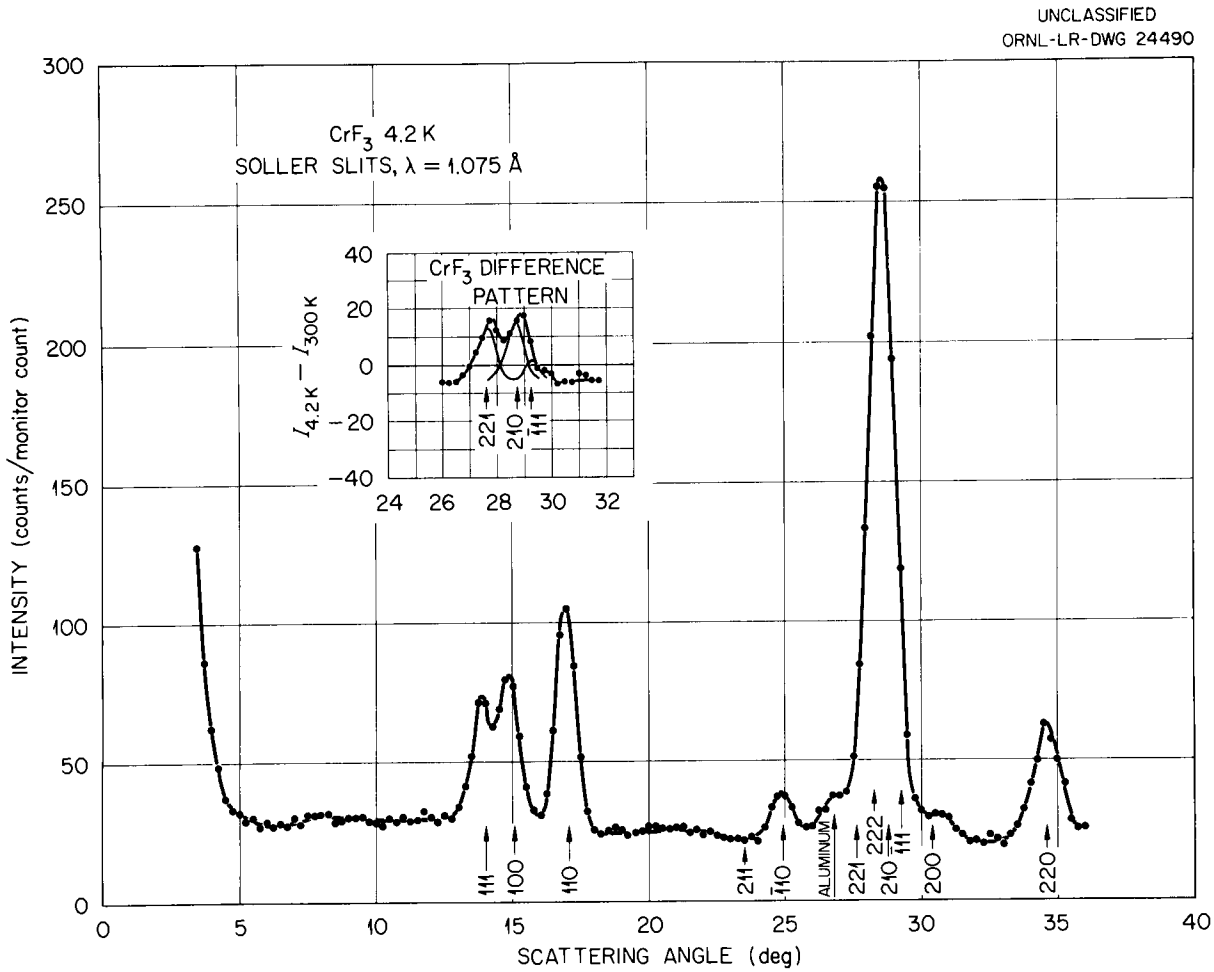


Fig. 2. Low-Temperature Neutron Powder Pattern of $CrF_3$. Inset shows difference pattern $I_{4.2°K} - I_{300°K}$.

made with magnetic fields (~10 kilo-oersteds) applied along the respective scattering vectors. No intensity change was observed for the (111) reflection. This is to be expected, since the spins are parallel to the (111) planes, and any effect would require breaking down the magnetic exchange coupling, and for this, the applied field was much too small. When the field was applied along the scattering vector of the (100) planes, however, the intensity increased by about 50% over the no-field value. This effect can be accounted for on the basis of a reorientation of the spins within the (111) sheets so as to bring them parallel to (100) planes in a larger fraction of reflecting crystallites.

The absolute intensities associated with the magnetic scattering are shown in Table 1, where a comparison is made between the observed intensity at saturation and that calculated for a particular value of the spin of the magnetic ion. In the case of iron and chromium the intensities calculated on the basis of the expected spin only values of 5/2 and 3/2, respectively, for the trivalent ions are seen to be in good accord with the measured values. For cobalt the observed magnetic scattering is larger than that given by the spin only value $S = 2$ for a trivalent cobalt ion. Thus there appears to be some orbital contribution to the magnetic moment in this case.

## DISCUSSION

The fact that the trifluorides of Cr, Fe, and Co develop the same type of antiferromagnetic structure as that of the perovskite compounds $LaCrO_3$

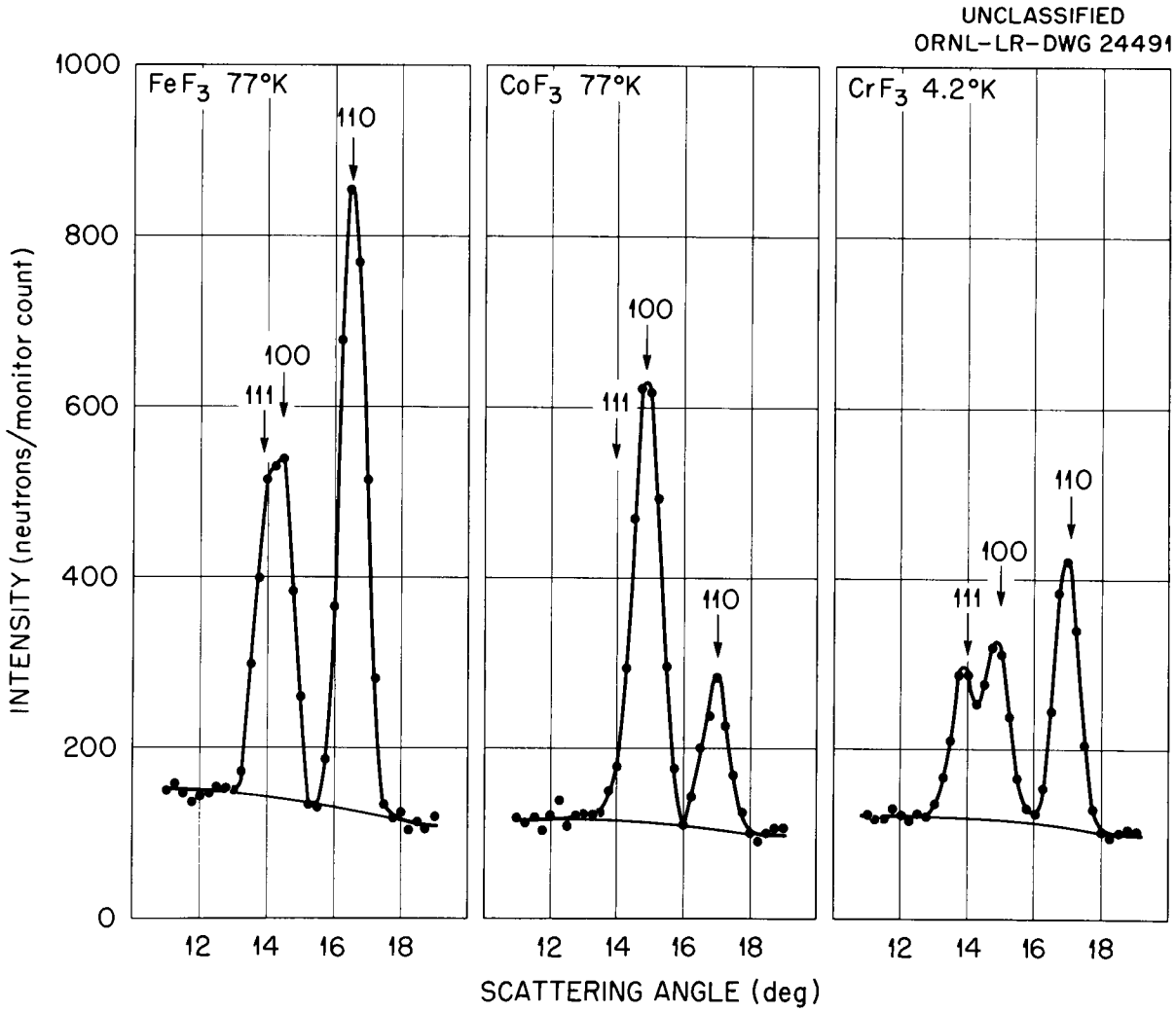


**Fig. 3. Section of Powder Pattern of $FeF_3$, $CoF_3$, and $CrF_3$. The (111) and (100) reflections are magnetic, and (110) is nuclear.**

**Table 1. Comparison of Observed and Calculated Magnetic Intensities**

| Rhombohedral Indices | | $FeF_3$ Calculated ($S = 5/2$) | $FeF_3$ Observed Total Intensity | $CoF_3$ Calculated ($S = 2.2$) | $CoF_3$ Observed Total Intensity | $CrF_3$ Calculated ($S = 3/2$) | $CrF_3$ Observed Total Intensity |
|---|---|---|---|---|---|---|---|
| | 111 | 287 | 272 | 0 | 0 | 140 | 146 |
| | 100 | | | 289 | 289 | 197 | 204 |
| 200<br>222 | Nuclear | 198 | | 367 | | | |
| 210 | Total | 351 | 355 | 579 | 593 | Difference pattern | |
| 221<br>$\bar{1}11$ | Magnetic | 153 | | 266 | | 171 | 176 |

and $LaFeO_3$ suggests that a similar mechanism of indirect exchange is operative in both cases. This is not surprising, since in both cases the the anions are similarly disposed, lying approximately midway between neighboring magnetic ions. The so-called "semicovalent exchange" mechanism proposed by Goodenough and Loeb,[5,6] with which the results on the perovskite compounds showed such striking correlations, would thus seem to be of significance in the similar trifluoride compounds. A comparison of the Néel temperatures for the two types of compounds shows that the effective exchange in the case of iron and chromium trifluorides is weaker than in the corresponding perovskites. On the other hand, $CoF_3$ has a high Néel temperature, whereas $LaCoO_3$ was not observed to order down to 4.2°K.

The authors gratefully acknowledge the work of D. E. LaValle of the Analytical Chemistry Division in preparing the samples used in this study, and of H. L. Yakel and R. M. Steele of the Metallurgy Division, who made x-ray analyses of the preparations.

[5] J. B. Goodenough and A. L. Loeb, *Phys. Rev.* 98, 391 (1955).

[6] J. B. Goodenough, *Phys. Rev.* 100, 564 (1955).

## ATOMIC-BEAM SPECTROSCOPY

J. E. Sherwood

The nuclear spin of $I^{128}$ has been measured by means of the atomic-beam magnetic resonance apparatus.[1] The decay of this 25-min isotope has been examined by Benczer *et al.*,[2] who predict the value of 1 for the ground-state spin.

The atomic-beam source was prepared by irradiating about 50 mg of elemental iodine in the LITR for 20 min. The iodine source was operated at room temperature, and the vapor was passed into the atomic-beam oven, where it was heated to about 400°C to enhance the molecular dissociation. Detection was accomplished by allowing the beam to deposit on a copper tape which had been coated with tincture of iodine. The activity of the spot was then observed by means of a scintillation counter.

Metallic potassium was used to calibrate and align the equipment, the $(f,m) = (2,-1) \rightleftharpoons (2,-2)$ line being observed at 1.80 Mc/sec in the stray field of the deflecting magnets. (The magnets were operated at the field appropriate for iodine.) With this information and with the use of approximations valid for weak fields, calculation showed that the iodine lines

$$(5/2, -1/2) \rightleftharpoons (5/2, -3/2)$$

and

$$(3/2, 1/2) \rightleftharpoons (3/2, -1/2)$$

should appear at 2.87 and 3.51 Mc/sec, respectively, if the nuclear spin is 1. The lines were indeed observed at these frequencies. Final data have not yet been taken, however, because of technical difficulties.

It is planned to continue the work on $I^{128}$ in order to measure the nuclear quadrupole interaction and other nuclear properties.

[1] J. E. Sherwood, *Phys. Semiann. Prog. Rep. Sept. 10, 1955*, ORNL-1975, p 52.

[2] N. Benczer *et al.*, *Phys Rev.* 101, 1027 (1956).

## STUDY OF THE ENERGY LEVELS OF SOME ATOMS AND IONS OF THE SECOND LONG PERIOD

G. W. Charles

The observed energy levels of some atoms and ions of the second long period of the periodic table are being compared with predictions of simple theory, and some of the results are presented.

An interesting result is found with the configuration $4d^9 5s$ of the Pd(I) isoelectronic sequence, which has a possible bearing on the choice between the analyses of Sb(IV) and Te(VII) published by Bloch and Bloch[1] and those published by Schoepfle[2] and modified by Kruger and Shoupp.[3]

A very close fit of the levels of the configuration $4d^9 5s$ to the theory is observed for all the spectra from Pd(I) through Te(VII), including both analyses of the latter spectrum and both analyses of the Sb(VI) spectrum. However, the variation of the parameters, in particular that of $\zeta^{1/4}$, with atomic number $Z$ is smoother with the analysis of Bloch and Bloch than with that of the others. Unfortunately, the fit of the levels of $4d^9 5p$ is not good enough in either case to draw any further conclusion.

The application of the theoretical equations[4] to the levels from $5s4f$ in In(II), Sn(III), and Sb(IV) allows a prediction of the position $5s4f\,^1F_3$ (unknown experimentally) at 227,940 $cm^{-1}$ above $5s^2\ ^1S_0$ in Sb(IV). No experimental data are available to check this prediction. Although very good agreement is noted in In(II), Sn(III), Sb(IV), and Te(V) between the calculated and observed levels from $5s5d$ and from $5s6d$, in Cd(I), the first member of the isoelectronic sequence, the levels taken as $^1D_2$ from these configurations agree well with the calculated positions of $^3D_2$, and vice versa. Very good agreement is noted throughout the entire sequence between observed and calculated positions of the levels from $5s5p$ and $5s6p$. The following predictions are made for I(VI):

| Configuration | Level | Relative Value ($cm^{-1}$) |
|---|---|---|
| $5s5d$ | $^3D_3$ | 252,000 |
| | $^3D_2$ | 250,700 |
| | $^3D_1$ | 250,000 |
| | $^1D_2$ | 258,500 |
| $5s5p$ | $^3P_2$ | 99,500 |
| | $^3P_1$ | 89,000 |
| | $^3P_0$ | 85,500 |
| | $^1P_1$ | 128,100 |

The corresponding lines have not been observed experimentally.

By using parameters calculated by Robinson and Shortley[5] for $5p^2$ of Sn(I), Sb(II), and Te(III), the following predictions are given for levels of $5p^2$ in I(IV):

| Level | Value ($cm^{-1}$) |
|---|---|
| $^3P_0$ | 0 |
| $^3P_1$ | 6,880 |
| $^3P_2$ | 11,040 |
| $^1D_2$ | 22,670 |
| $^1S_0$ | 36,260 |

Similarly, the intervals of the levels of $5p6s$ of I(IV) are predicted to be as follows:

| Interval | Value ($cm^{-1}$) |
|---|---|
| $^3P_1-^3P_0$ | 370 |
| $^3P_2-^3P_1$ | 10,500 |
| $^1P_1-^3P_2$ | 830 |

An attempt to establish the low levels of I(IV) by using these predicted intervals and the line lists

[1] L. Bloch and E. Bloch, *J. phys. radium* **8**, 217 (1937).

[2] G. K. Schoepfle, *Phys. Rev.* 43, 742 (1933).

[3] P. G. Kruger and W. E. Shoupp, *Phys. Rev.* **46**, 124 (1934).

[4] E. U. Condon and G. H. Shortley, *The Theory of Atomic Spectra*, p 271, University Press, Cambridge, 1935.

[5] H. A. Robinson and G. H. Shortley, *Phys. Rev.* 52, 713 (1937).

of Bloch, Bloch, and Felici,[6] and of Bloch and Bloch[7] proved to be fruitless. Also, the attempt to confirm among transitions in the vacuum ultraviolet the intervals between the levels published by Krishnamurty[8] met with no success. The spectrum of I(IV) is probably not well developed in this region.

Excellent agreement is found between the experimental energy levels given by Mack[9] from $5p^3$ of Te(II) and the theoretical equations with the parameters $F_0$ = 6849 cm$^{-1}$, $F_2$ = 1354 cm$^{-1}$, and $\zeta_p$ = 4696 cm$^{-1}$. The predicted value of $^2P^0_{3/2}$ is 23,897 cm$^{-1}$, agreeing very well with 24,033 cm$^{-1}$ listed by Mack[9] as one possibility, along with 22,680 and 25,478 cm$^{-1}$ for this level. The level, 24,033 cm$^{-1}$, also shows more observed combinations than do the other two. The following predictions were made for the intervals among levels from $5p^3$ of I(III):

| Interval | Value (cm$^{-1}$) |
|---|---|
| $^2D^0_{3/2}-{}^4S^0_{3/2}$ | 12,830 |
| $^2D^0_{5/2}-{}^2D^0_{3/2}$ | 3,110 |
| $^2P^0_{1/2}-{}^2D^0_{5/2}$ | 9,420 |
| $^2P^0_{3/2}-{}^2P^0_{1/2}$ | 4,920 |

A search was made for these intervals among the experimental data; nothing conclusive was found.

[6] L. Bloch, E. Bloch, and N. Felici, *J. phys. radium* 8, 359 (1937).

[7] L. Bloch and E. Bloch, *Ann. phys.* 11, 150 (1929).

[8] S. G. Krishnamurty, *Proc. Phys. Soc.(London)* 48, 277 (1936).

[9] J. E. Mack, private communication to P. M. Griffin and K. L. Vander Sluis, Jan. 1957.

## PURITY OF $Hg^{198}$ PRODUCED BY NEUTRON IRRADIATION OF $Au^{197}$[1]

J. R. McNally, Jr.

The neutron irradiation of $Au^{197}$ to produce $Hg^{198}$ for spectroscopic purposes has been discussed by Wiens[2] and by Meggers and others.[3] Recently, Kessler and Meggers[4] reported the vacuum wavelength of the green mercury radiation measured in vacuum and corrected to zero argon carrier-gas pressure as being

$$5462.270240 \pm 0.000008 \text{ Å},$$

relative to 6440.24907 Å for cadmium. The possibility of such extremely high precision raises a question regarding the permissible amount of $Hg^{199}$ in such $Hg^{198}$ standard sources. Figures of 99.6 and 99.9% (ref 5) and 99.7% (ref 6) have been published. Bedford and Crooker[7] report that a gold sample irradiated at very high flux values ($4.6 \times 10^{13}$ neutrons·cm$^{-2}$·sec$^{-1}$) gave an $Hg^{199}/Hg^{198}$ ratio of 0.274.

Given below is the expected impurity as a ratio $Hg^{199}/Hg^{198} = F\sigma/\lambda$, where $F$ is the average flux, $\sigma$ is the cross section[8] of $Au^{198} = 2.6 \times 10^{-20}$ cm$^2$,

[1] The author is indebted to P. S. Baker and J. H. Gillette of the Isotopes Division for discussions on the history and availability of reactor-produced $Hg^{198}$ at ORNL.

[2] J. H. Wiens, *Phys. Rev.* 70, 910 (1946).

[3] See, for example, W. F. Meggers and K. G. Kessler, *J. Opt. Soc. Am.* 40, 737 (1950).

[4] K. G. Kessler and W. F. Meggers, paper 27, Fortieth Annual Meeting Optical Society of America, October 6–8, 1955.

[5] W. F. Meggers and F. O. Westfall, *J. Research Natl. Bur. Standards* 44, 447 (1950).

[6] K. G. Kessler, *Phys. Rev.* 77, 559 (1950).

[7] R. E. Bedford and A. M. Crooker, *Can. J. Phys.* 33, 25 (1955).

[8] R. E. Bedford and A. M. Crooker, *Can. J. Phys.* 33, 492 (1955); R. E. Bell, R. L. Graham, and L. Yaffe, *Can. J. Phys.* 33, 457 (1955). Note: the term $F\sigma_1/\lambda_1$ in the denominator of the equation of Bedford and Crooker should be replaced by $\lambda_2/\lambda_1 a$. Also, the actual value of the cross section will depend on the reactor neutron spectrum; published values range from about 1.6 to $3.8 \times 10^{-20}$ cm$^2$.

and $\lambda$ is the decay constant of $Au^{198} = 0.297 \times 10^{-5}$ $sec^{-1}$:

| Flux | $Hg^{199}/Hg^{198}$ |
|---|---|
| $10^{13}$ | 8.7% |
| $10^{12}$ | 0.87% |
| $10^{11}$ | 0.09% |

Although no definition has been made as to the $Hg^{199}$ tolerance permissible in $Hg^{198}$ standard discharge sources, it has been suggested that a yield of 99.6%, or greater, can be guaranteed by appropriate choice of neutron flux. The first experiments on long-lived tubes[5] were carried out on some 60 mg of 99.84% $Hg^{198}$ obtained by irradiation of gold at Oak Ridge in 1945–1946. In 1949, approximately 420 mg of $Hg^{198}$ was obtained from 373 g of gold irradiated for one year; in 1952, about 1300 mg of $Hg^{198}$ was obtained from 350 g of gold irradiated for about three years at an estimated flux of $5 \times 10^{11}$; a one-year irradiation during 1956–1957 in a flux estimated at $5 \times 10^{11}$ is being completed and is expected[9] to yield about 800 mg of $Hg^{198}$. All three of the early irradiation series yielded $Hg^{198}$ of 99.6% purity or better.

In view of the possible selection of $Hg^{198}$ as a standard light source because of its many advantages,[10] it seems important to include in the definition of such a standard source the isotopic purity of the $Hg^{198}$. The effect of $Hg^{199}$ isotopic impurity in the $Hg^{198}$ will be to introduce possible spurious line shifts because of the overlap of different orders in the interference patterns. By using the wave number data of Burns,[11,12] the overlap cases can be computed in terms of spacers $t$, as $t = \epsilon/2\Delta\sigma$, where $\epsilon$ takes on integral values only and $\Delta\sigma$ is the wave number separation between the $Hg^{198}$ and one of the $Hg^{199}$ components.[13] Table 1 summarizes the situations for various conditions of overlap.

The magnitude of the allowable impurity in the $Hg^{198}$ will be calculated on the basis of 100% in a single $Hg^{199}$ fringe; the correction to the $A$, $B$, or $C$ components can be readily evaluated by multiplying this allowable impurity by the appropriate relative intensity of the component given in Table 1. The calculation will be based on an exponential-type Doppler line broadening, although more rigorous calculations could be made, including instrumental broadening.[14] The line shape, expressed in terms of wavelength intervals, is then

$$I = I_0 e^{-k\delta^2} + I_1 e^{-k(\delta-\delta_1)^2} ,$$

where $I_0$ is the intensity maximum for $Hg^{198}$; $I$, that for $Hg^{199}$; $k$, the Doppler constant for a temperature of 300°K; $\delta$, the wavelength interval in mÅ from the $Hg^{198}$ peak $I_0$; and $\delta_1$, the wavelength separation in mÅ between the $Hg^{198}$ and the $Hg^{199}$ peaks. For mercury 5461 Å, $k$ is approximately 0.11 $mÅ^{-2}$.

[9] J. H. Gillette, Isotopes Division, private communication 1956.

[10] W. F. Meggers, *J. Opt. Soc. Am.* 38, 7 (1948).

[11] K. Burns and K. B. Adams, *J. Opt. Soc. Am.* 42, 56 (1952).

[12] K. Burns and K. B. Adams, *J. Opt. Soc. Am.* 42, 716 (1952).

[13] A similar evaluation can be made by constructing a nomograph. See, for example, J. R. McNally, Jr., *J. Opt. Soc. Am.* 39, 1050 (1949).

[14] J. R. McNally, Jr., P. M. Griffin, and L. E. Burkhart, *J. Opt. Soc. Am.* 39, 1036 (1949).

**Table 1. Fringe Coincidences in the 5461-Å Line for $Hg^{199}$ and $Hg^{198}$**

| Overlap Conditions | $Hg^{199}$ | | |
|---|---|---|---|
| | $A$ (33.3%) | $B$ (60.0%) | $C$ (6.7%) |
| $\sigma$,* $cm^{-1}$ | −0.271 | +0.045 | +0.800 |
| Spacings $t$, mm | 18.5, 36.9, 55.4, 73.8, 92.3, 110.7 | 111.1 | 6.3, 12.5, 18.8, 25.0, 31.3, 37.5, 43.8, 50.0, 56.3, 62.5, 68.8, 75.0, 81.3, 87.5, 93.8, 100.0, 106.3, 112.5 |

*K. Burns and K. B. Adams, *J. Opt. Soc. Am.* 42, 56 (1952); *J. Opt. Soc. Am.* 42, 716 (1952).

The maximum intensity distribution may be obtained by setting $\partial I/\partial\delta = 0$, for which case $\delta$ takes on the specific value(s) $\delta_2$, the wavelength error. This gives an expression involving $I_1$, $I_0$, $k$, $\delta$, and $\delta_2$ as follows:

$$f = \frac{I_1}{I_0} = \frac{\delta_2 e^{-k\delta_2^2}}{(\delta_1 - \delta_2) e^{-k(\delta_1-\delta_2)^2}} ,$$

where $f$ defines the $Hg^{199}$ impurity relative to the $Hg^{198}$; $\delta_2$ will be defined as the limiting wavelength error permissible in the 5461-Å line and as such will be chosen to be 0.008 mÅ, the precision reported by Kessler and Meggers.[4] The maximum tolerable $Hg^{199}$ impurity for any overlap condition, $\delta_1$, will be obtained by $\partial f/\partial\delta_1 = 0$ and will occur for $\delta_1 = \Delta$, the wavelength separation between the two peaks as measured by

$$\Delta = iF_\lambda \pm \Delta\lambda \text{ mÅ} ,$$

where $i$ is an integer corresponding to the difference in orders of the two peaks, $F_\lambda$ is the free spectrum range in mÅ, and $\Delta\lambda$ is the actual wavelength difference of the spectrum lines. We obtain the condition

$$\delta_1 = \Delta = \delta_2 + \sqrt{\frac{1}{2k}} .$$

Thus we obtain the final tolerable impurity fraction:

$$f = \frac{I_1}{I_0} \frac{\delta_2 e^{-k\delta_2^2}}{\sqrt{\frac{1}{2k}}\, e^{-0.5}} \cong 0.77\delta_2 ,$$

where $\delta_2$ is the tolerable wavelength error. Values of $f$ are given in Table 2.

Table 2. Maximum Wavelength Error Introduced by Isotopic Impurity in $Hg^{198}$

| $f$ (%) | Error $\delta_2$ (mÅ) | Relative Distance of Impurity Component (mÅ) |
|---|---|---|
| 7.7 | 0.1 | 2.23 |
| 0.77 | 0.01 | 2.14 |
| 0.62 | 0.008* | 2.14 |
| 0.38 | 0.005 | 2.14 |

*Uncertainty reported by Kessler and Meggers (see ref 4).

It thus appears that even under the worst condition envisaged (all $Hg^{199}$ components falling together about 2 mÅ units away from the $Hg^{198}$ interference fringe peak), the allowable $Hg^{199}$ impurity to produce a fringe shift of less than one-billionth of the wavelength is about 0.4%. In view of the difficulty of measuring fringes to 0.005 mÅ when the half-width is of the order of 5 mÅ, the tolerance figure might well be established at 0.4% $Hg^{199}$ impurity. This requirement does not vitiate the value of 5462.270240 ± 0.000008 Å reported by Kessler and Meggers,[4] because no standard lamps have been made with an $Hg^{199}$ impurity in excess of 0.4%.

## CONCLUSIONS

It may be concluded that a design criterion for $Hg^{198}$ standard lamps may be safely established at an isotopic purity of 99.6% or better. Standard lamps containing $Hg^{198}$ produced in the ORNL Graphite Reactor satisfactorily meet this criterion; however, on this basis, the maximum average neutron flux that may be permitted in the production of $Hg^{198}$ is about $4.6 \times 10^{11}$ neutrons·cm$^{-2}$·sec$^{-1}$ and not $10^{12}$, as previously reported.

## CLASSIFICATION OF SINGLY IONIZED PLUTONIUM, Pu(II)

J. H. Wise[1] P. M. Griffin J. R. McNally, Jr.

The measurements of Zeeman patterns, obtained from a low-current arc between carbon electrodes impregnated with $PuCl_3$ in a magnetic field of 24,470 oersteds with an Echelle-Littrow spectrograph, have been extended beyond those reported by McNally and Griffin.[2] The spectrum region examined by McNally and Griffin was from 2700 to 4775 Å, and more than 330 resolved Zeeman patterns were computed. The present report covers the examination of a new spectroscopic region, which gave partial coverage[3] of the spectrum from 4370 to 6800 Å. One hundred twenty-nine resolved Zeeman patterns were computed, 98 of which were not previously reported. All computations of the $g$ factors were performed by the Oracle with the least-squares routine reported by Vander Sluis.[4]

Preliminary investigation of the computed $g$ factors indicated that about 20 of the newly observed transitions involve the low-energy states of Pu(II). Three of these transitions have the high-energy states which were previously reported by McNally and Griffin; one new high-energy state occurs for three of the observed patterns from transitions satisfying Ritz combinations (21,670.3 $cm^{-1}$; $J = 3/2$; $g = 2.318$); and 14 new high-energy states are indicated by observation of a single Zeeman pattern for each state.

A cursory re-examination of the earlier data revealed the presence of the following two additional high-energy states which are established by the observation, for each state, of two Zeeman patterns from transitions that satisfy Ritz combinations:

| | | |
|---|---|---|
| 28,887.4 $cm^{-1}$ | $J = 1/2$ | $g = 0.120$ |
| 33,389.9 $cm^{-1}$ | $J = 3/2$ | $g = 0.936$ |

[1] Summer employee.

[2] J. R. McNally, Jr., and P. M. Griffin, *Stable Isotopes Semiann. Prog. Rep. Nov. 30, 1956*, ORNL-2236, p 34.

[3] Full coverage was not obtained, since, with the present Echelle-Littrow spectrograph, the separation between orders, at wavelengths larger than about 5000 Å, is greater than the channel height (restricted by the height of the Littrow entrance slit), resulting in part of the spectrum being lost at any particular setting.

[4] K. L. Vander Sluis, *J. Opt. Soc. Am.* 46, 605 (1956).

## INFRARED SPECTRA OF THE ISOTOPICALLY SUBSTITUTED AMMONIA MOLECULES

H. W. Morgan P. A. Staats J. H. Goldstein[1]

Study of the isotopically substituted ammonias began as a routine synthesis and examination of $NT_3$. Contamination by hydrogen, however, produced the weaker bands of $NHT_2$ and $NH_2T$ superimposed on the spectrum of $NT_3$. These weaker bands proved difficult to interpret, and few data were available on the spectra of $NHD_2$ and $NH_2D$ for comparison. Thus the study was extended to all the isotopic ammonias.

Ammonia gas was prepared by the reaction of water and magnesium nitride in an evacuated system, with $T_2O$ and $D_2O$ used for syntheses of the isotopic molecules. The reactions were carried out in the tritium synthesis system previously described.[2] Infrared spectra were recorded on single-beam and double-beam prism spectrometers. Frequencies are considered accurate to ±1 $cm^{-1}$.

The $NH_3$ molecule has six normal modes of vibration. Because of the high symmetry ($C_{3v}$), two pairs of frequencies are degenerate, and only four fundamental bands are observed in the infrared region. Substitution of one or two deuterium or tritium atoms removes the degeneracies, lowering the symmetry to $Cs$. These split pairs are indicated in Table 1 as $s$ and $a$, which refer to the symmetry of the vibrational motions with respect

[1] Consultant, Emory University, Atlanta, Ga.

[2] P. A. Staats, H. W. Morgan, and J. H. Goldstein, *Stable Isotope Research and Production Semiann. Prog. Rep. May 20, 1955*, ORNL-1908, p 4.

Table 1. Summary of Observed and Calculated Frequencies ($cm^{-1}$) for the Fundamental Modes $\nu_3$ and $\nu_4$ of the Ammonia Molecules

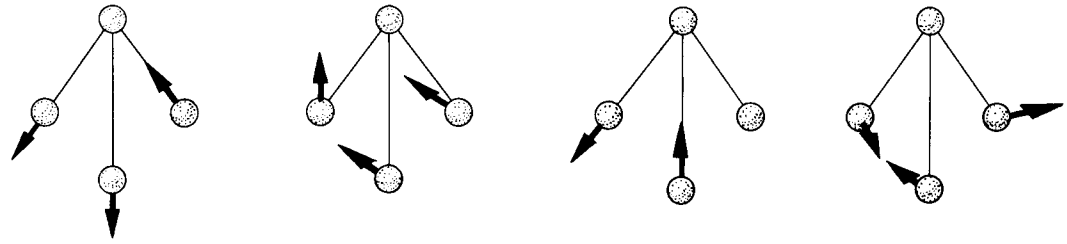

| | $\nu_3$ (s) Asymmetric Stretch | | $\nu_4$ (a) Asymmetric Bend | | $\nu_3$ (a) Asymmetric Stretch | | $\nu_4$ (s) Asymmetric Bend | |
|---|---|---|---|---|---|---|---|---|
| | Observed | Calculated | Observed | Calculated | Observed | Calculated | Observed | Calculated |
| $NH_3$ | 3415* | 3411 | 1627.5* | 1619 | 3415* | 3411 | 1627.5* | 1619 |
| $NHD_2$ | 3402 | 3387 | 1464 | 1476 | 2557 | 2556 | 1177 | 1166 |
| $NHT_2$ | 3400 | 3387 | 1401 | 1382 | 2187 | 2182 | 1077<br>1075 | 1085 |
| $NDH_2$ | 2505 | 2483 | 1380 ± 5 | 1381 | 3411 | 3411 | 1608<br>1594 | 1585 |
| $ND_3$ | 2564* | 2542 | 1191 | 1185 | 2564* | 2542 | 1191 | 1185 |
| $NDT_2$ | 2512 | 2493 | 1114 | 1104 | 2188 | 2178 | | 1014 |
| $NTH_2$ | 2125 | 2098 | | 1291 | 3405 | 3411 | 1599<br>1571 | 1568 |
| $NTD_2$ | 2103 | 2084 | | 1068 | 2572 | 2555 | 1234 | 1252 |
| $NT_3$ | 2187 ± 10 | 2165 | 997 | 988 | 2187 ± 10 | 2165 | 997 | 988 |

*Private communication from E. K. Plyler and W. S. Benedict.

to the one plane of symmetry in these molecules. Since NHDT has no symmetry, its vibrational modes are not comparable in a simple fashion with the other isotopic species.

To unambiguously interpret the absorptions of the mixed isotopic species, such as $NHD_2$, it is necessary to observe the spectra free of bands from other molecules. Because of the rapid exchange in ammonia, any mixed isotopic species is in equilibrium with several other forms, and thus the "pure" species does not exist. To observe the "pure" spectrum, the system shown in Fig. 1 was employed. By proper adjustment of pressures in the four cells, only the absorptions arising from $NHD_2$ are detected. This balancing technique was

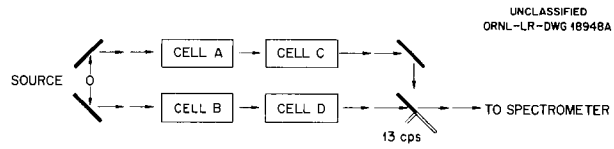


| CELL | $ND_3$ | $NHD_2$ | $NH_2D$ | $NH_3$ | SAMPLE |
|---|---|---|---|---|---|
| A | +9 | +9 | +3 | +0.3 | 75% D |
| B | −9 | −1.5 | −0.1 | 0 | 95% D |
| C | 0 | 0 | 0 | +4.5 | 100% H |
| D | 0 | −0.6 | −2.9 | −4.8 | 84% H |
| | 0 | +6.9 | 0 | 0 | |

UNITS ARE cm Hg PARTIAL PRESSURE

Fig. 1. Study of the $NHD_2$ Spectrum.

used to study $NHD_2$, $NH_2D$, and $ND_3$. It could not be used on tritiated samples because of the difficulties in handling the radioactive samples.

Figure 2 illustrates the effectiveness of this method. The band at 2556 $cm^{-1}$ had been assigned as $\nu_3$ of $ND_3$ by two independent studies at the higher resolution of a grating.[3,4] As can be seen from the lower trace, this $Q$ branch actually arises from $NHD_2$. The true $ND_3$ band center has recently been found by Benedict and Plyler[5] at 2564 $cm^{-1}$. The band $\nu_1$ of $NHD_2$ had been considered to be identical in frequency to $\nu_1$ of $ND_3$, but as shown by this technique it occurs some 41 $cm^{-1}$ lower in frequency. In Fig. 3 are shown overlapping spectra of $\nu_2$ for all the isotopic species, including NHDT. The superimposed bands of $ND_3$ and $NHT_2$ were observed independently in other spectra.

Assuming a valence force field, a normal coordinate analysis was performed. By use of matrix techniques for the Oracle previously reported,[6] the frequencies for the isotopic molecules were predicted. Because of the convenience in calculation, spectroscopic masses were employed to compensate for the anharmonicity of the hydrogen motions. Tables 1 and 2 compare the observed frequencies with those predicted by preliminary calculations. Agreement is considered to be satisfactory.

With the substitution of heavier atoms, the potential barrier for the ammonia inversion is

[3] M. V. Migeotte and E. F. Barker, *Phys. Rev.* **50**, 418 (1936).

[4] J. S. Burgess, *Phys. Rev.* **76**, 1267 (1949).

[5] W. S. Benedict, personal communication.

[6] P. A. Staats, H. W. Morgan, and J. H. Goldstein, *Stable Isotopes Semiann. Prog. Rep. May 20, 1956*, ORNL-2114, p 1.

**Table 2. Summary of Observed and Calculated Frequencies ($cm^{-1}$) for the Fundamental Modes $\nu_1$ and $\nu_2$ of the Ammonia Molecules**

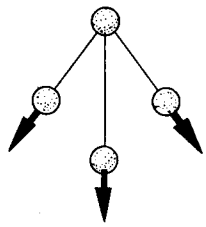

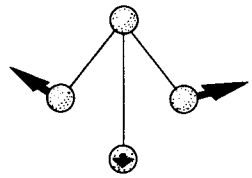

| | $\nu_1$ Symmetric Stretch | | $\nu_2$ Symmetric Bend | |
|---|---|---|---|---|
| | Observed | Calculated | Observed | Calculated |
| $NH_3$ | 3337* | 3334 | 968, 931.5* | 971 |
| $NH_2D$ | 3366 | 3362 | 894, 874 | 895 |
| $NHD_2$ | 2479 | 2459 | 817, 808 | 830 |
| $ND_3$ | 2420 | 2414 | 749, 746 | 746 |
| $ND_2T$ | 2478 | 2470 | 718 | 703 |
| $NDT_2$ | 2061 | 2055 | 686 | 676 |
| $NT_3$ | 2016 | 2006 | 654 | 646 |
| $NT_2H$ | 2055 | 2063 | 748, 744 | 739 |
| $NTH_2$ | 3369 | 3362 | 867, 851 | 865 |

*Private communication from E. K. Plyler and W. S. Benedict.

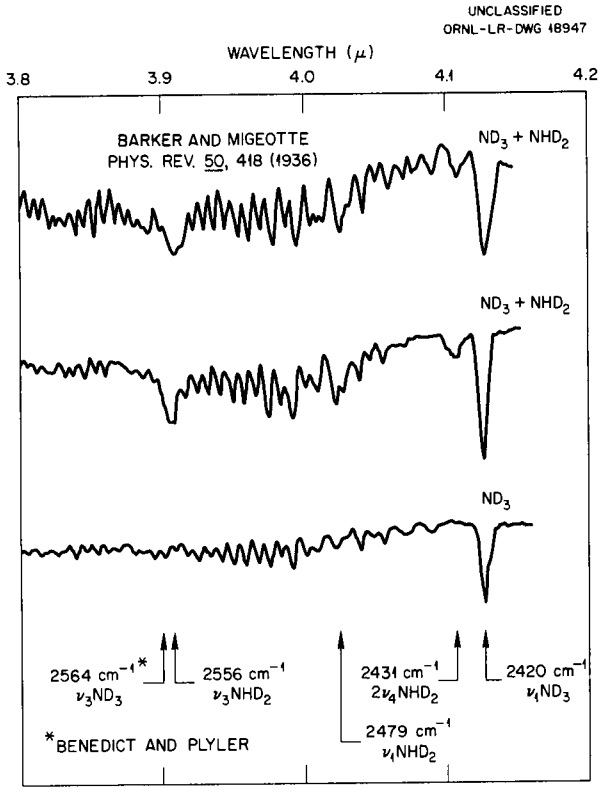


**Fig. 2. The Assignment of $\nu_3$ Fundamentals.**

raised, and the splittings observed in the vibrational bands decrease. This is shown graphically in Fig. 4.

For the preparation of $N^{15}H_3$, 99.3% enriched $HN^{15}O_3$ (ref 7) was converted to $NH_4Cl$ by use of Devarda's alloy. Ammonia gas was generated by the reaction of $NH_4Cl$ and $Ca(OH)_2$. Table 3 presents the observed and calculated frequencies, considered to be in good agreement; $\nu_3$ could not be distinguished from $\nu_1$ at the prism resolution available.

[7] Enriched by the Chemistry Division.

**Table 3. Vibrational Frequencies ($cm^{-1}$) of $N^{15}H_3$**

| Band | $N^{14}$ | $N^{15}$ | Shift | |
|---|---|---|---|---|
| | | | Observed | Calculated |
| $\nu_1$ | 3337 | 3335 | 2 | 3.4 |
| $\nu_2$ | 966.6 | 961.0 | 5.2 | 4.7 |
| | 931.0 | 926.3 | | |
| $\nu_4$ | 1627.5 | 1625.0 | 2.5 | 2.7 |

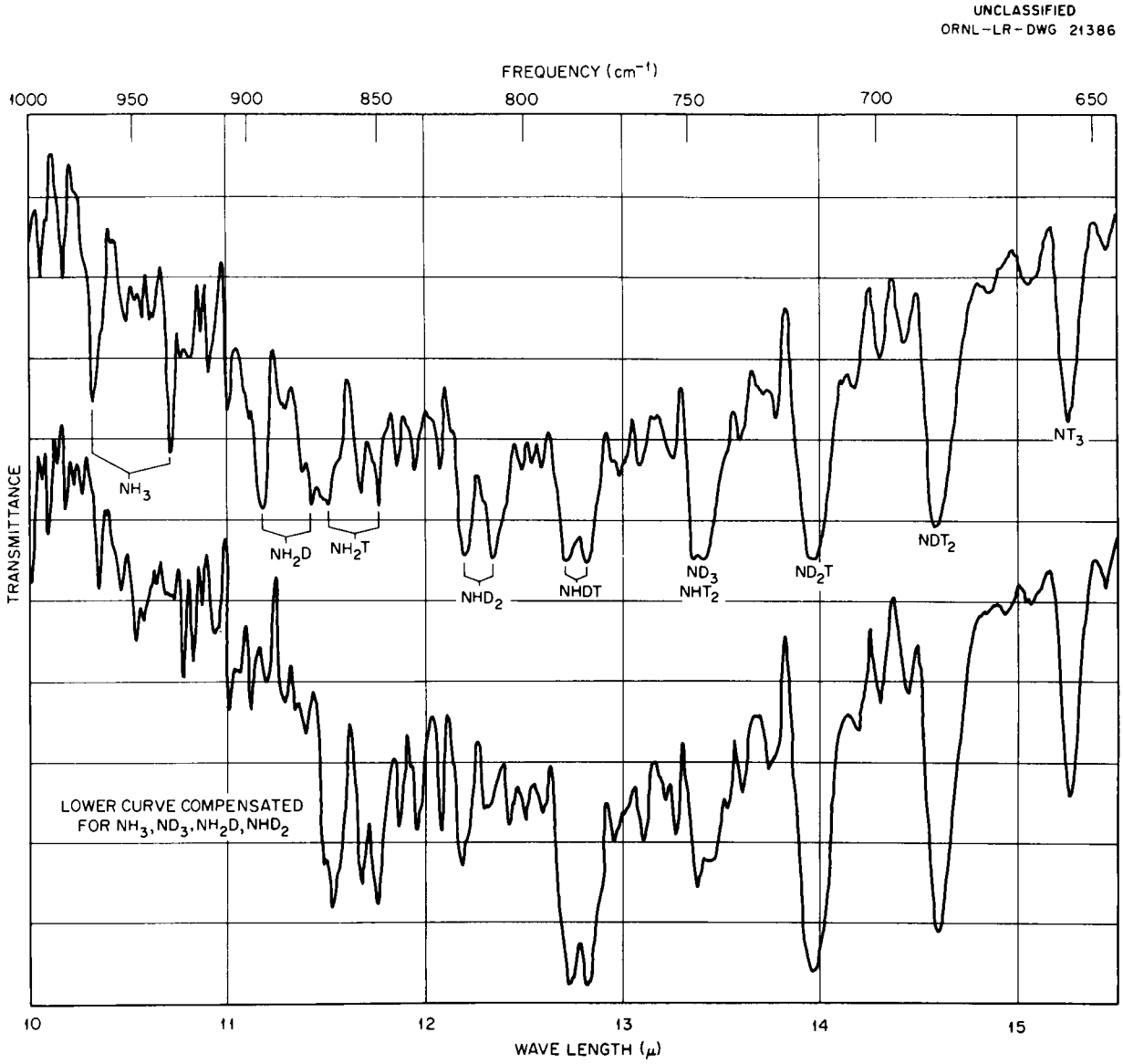


**Fig. 3. The $\nu_2$ Fundamentals for Isotopic Molecules.**

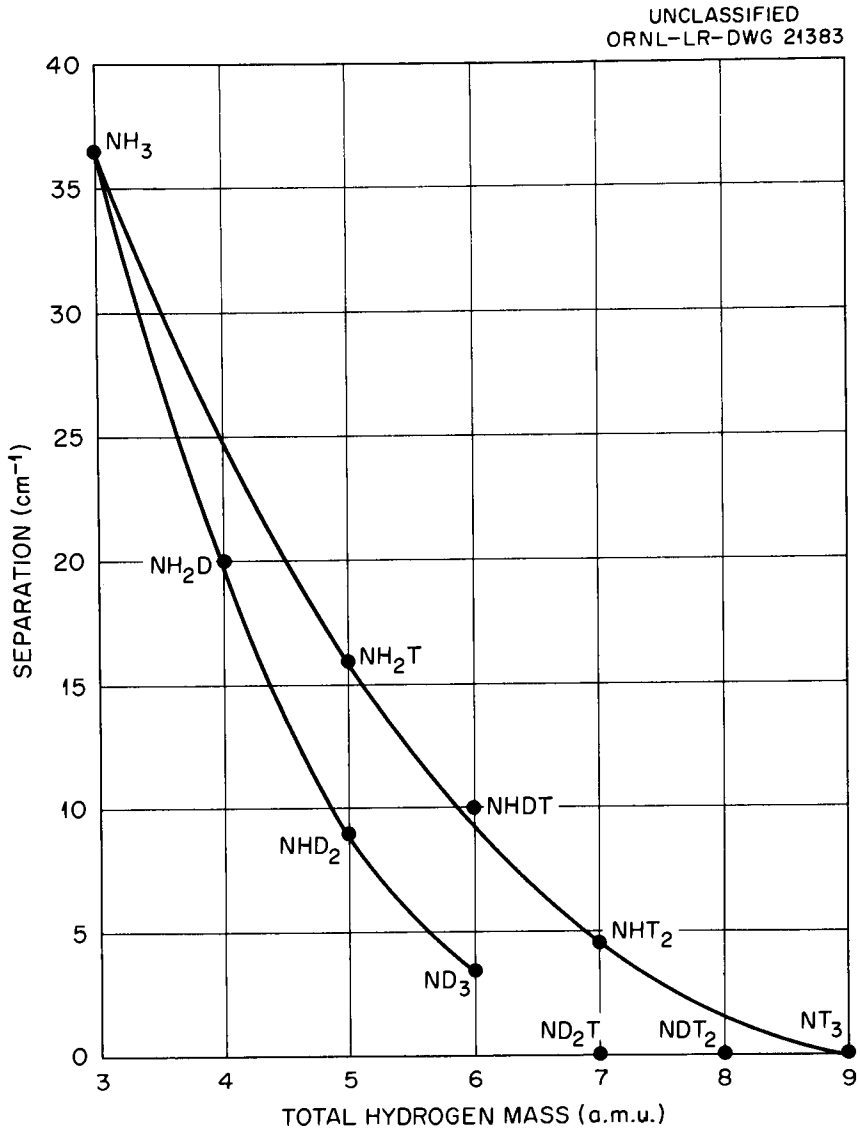


**Fig. 4. Observed Inversion Splittings, $\nu_2$.**

## IMPROVED SWEEPING PULSE GENERATOR AND TIMER FOR MULTICHANNEL ANALYZERS

G. G. Kelley C. C. Harris

The sweeping pulse generator previously reported[1] has been improved and modified for use with analyzers which cover the entire spectrum. Figure 1 is a circuit diagram of the modified device. The most important change is the elimination of the second clipping line. This change permits a signal of sufficient amplitude to be produced with a much lower current than would be necessary otherwise. A pseudo double-differentiated signal is obtained by capacitive coupling between the cathodes of $V_{3a}$ and $V_{3b}$. The signal at the cathode of $V_{3a}$ cuts off $V_{3b}$. During the time this tube is cut off, $C_7$ charges. After the pulse, there is a temporary current through $V_{3b}$ while $C_7$ is discharging to its rest potential. The differentiated signal produced has the rapid fall through zero which is the characteristic of double-differentiated signals required by the pulse-handling circuitry of the MC4 and MC5 analyzers. A further improvement is obtained by rearrangement of the feedback connection in the integrating amplifier. The timer dial is a linear pulse-amplitude control in the pulse generator position. It operates by inserting an adjustable bias between the output and the input.

[1] G. G. Kelley, P. R. Bell, and C. C. Harris, *Phys. Semiann. Prog. Rep. Sept. 10, 1955*, ORNL-1975, p 99.

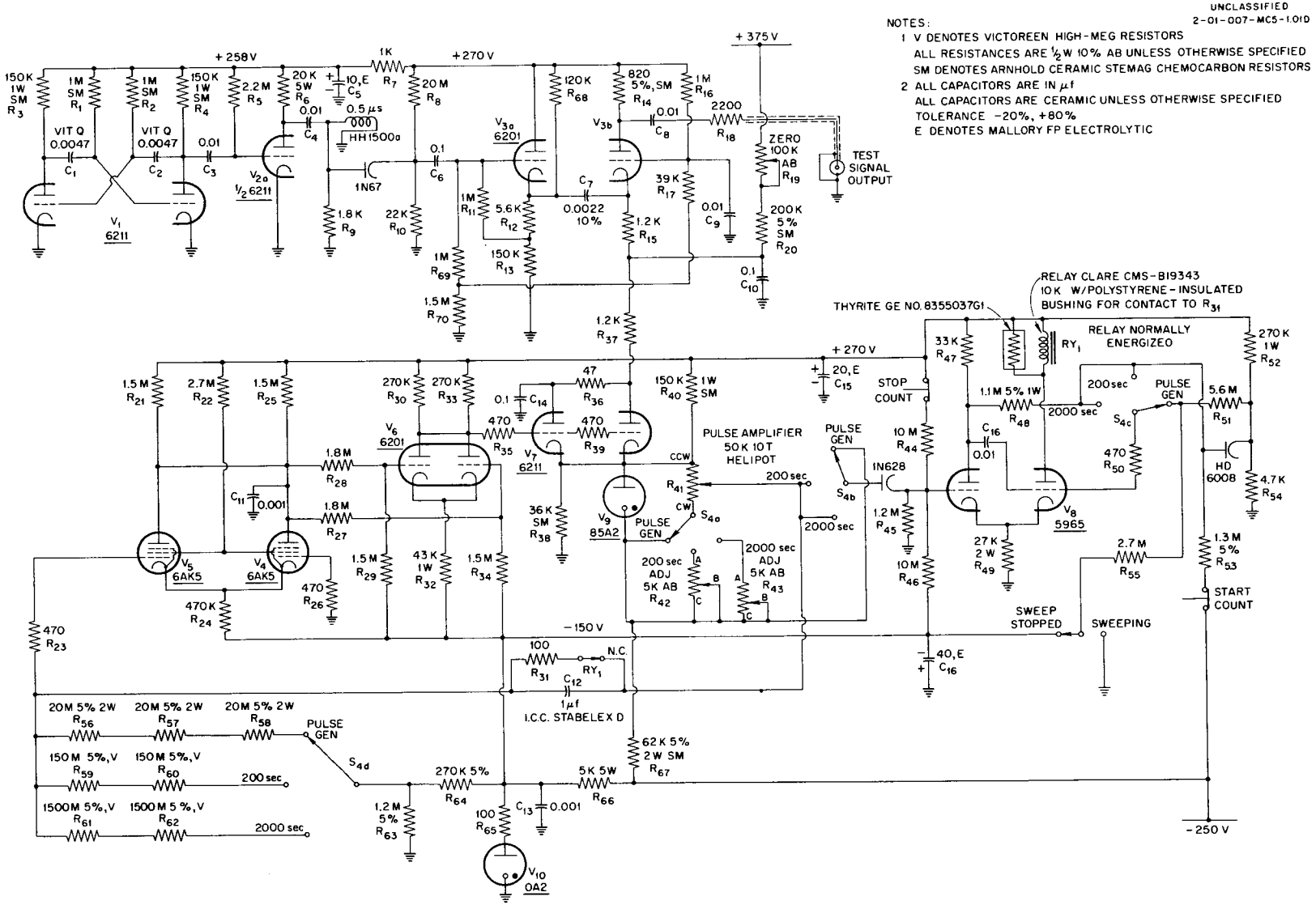


Fig. 1. Circuit Diagram.

## LIFE TESTS OF FILAMENTARY SUBMINIATURE TUBES

C. C. Harris G. G. Kelley

Two of the life tests previously reported[1,2] are in operation. The first (actual operating scalers in an MC4 20-channel analyzer), consisting of 214 CK 5854's and 22 1AG4's, has reached 13,400 hr with four failures. Three of these have been previously reported. At least 1500 hr of remaining life can be predicted for these tubes. The second test, consisting of 120 1AG4's in groups of 40, operated at 50% duty cycle with filament voltages of 1.3, 1.1, and 1.2 v (0.9 v for 6800 hr). This test has reached 23,760 hr, with the number of probable failures in actual scaler operation indicated in Table 1.

One of the original objectives of the life tests was to determine the correct filament voltage for scaler operation. The failure rate has been so low that it has been difficult to draw conclusions, but the failure rate and general appearance of performance data at 23,760 hr show a definite superiority of the 1.1-v group. A valid conclusion is that 1AG4's operated in scaler conditions[3] at $E_f$ = 1.1 v can be considered as 20,000-hr tubes, and that other filamentary subminiature tubes of the same class are useful for at least 15,000 hr.

[1] C. C. Harris, P. R. Bell, and G. G. Kelley, *Phys. Semiann. Prog. Rep. Sept. 10, 1955*, ORNL-1975, p 103.

[2] C. C. Harris and P. R. Bell, *Phys. Semiann. Prog. Rep. March 10, 1956*, ORNL-2076, p 64–65.

[3] C. C. Harris and P. R. Bell, *Rev. Sci. Instr.* 27, 608 (1956).

**Table 1. Probable Failures in Scaler Operation**

| | Failures | | | |
|---|---|---|---|---|
| | in 18,000 hr | | in 23,760 hr | |
| | Incipient | Probable | Incipient | Probable |
| Group A (1.3 v) | 9 | 0 | 6 | 11 |
| Group B (1.1 v) | 1 | 0 | 2 | 0 |
| Group C (0.9–1.2 v) | 0 | 0 | 3 | 1 |

## DEVELOPMENTS IN FOCUSING COLLIMATORS FOR BRAIN TUMOR DIAGNOSIS

J. E. Francis P. R. Bell C. C. Harris

The successful application of gamma-ray spectrometry and focusing collimators to the problem of thyroid scanning leads naturally to the question: How well can this technique be applied to brain tumors?

As a first attempt toward the solution of this problem, the 3-in. focusing collimator was designed. This collimator, containing 61 tapered hexagonal holes, was designed to have the following properties. The focus is at 3 in. from the face of the collimator, with the point of maximum response occurring at approximately $2\frac{3}{4}$ in. from the face of the collimator for 320-kev gamma rays, as shown in Fig. 1. The shielding around the sides is 1 in. thick, as shown in Fig. 2, which should reduce the side radiation to 0.09% of incident radiation for the 364-kev gamma ray and to 4.28% for the 638-kev gamma ray from $I^{131}$, which is the principal isotope, aside from $As^{74}$, that has been used for these studies.

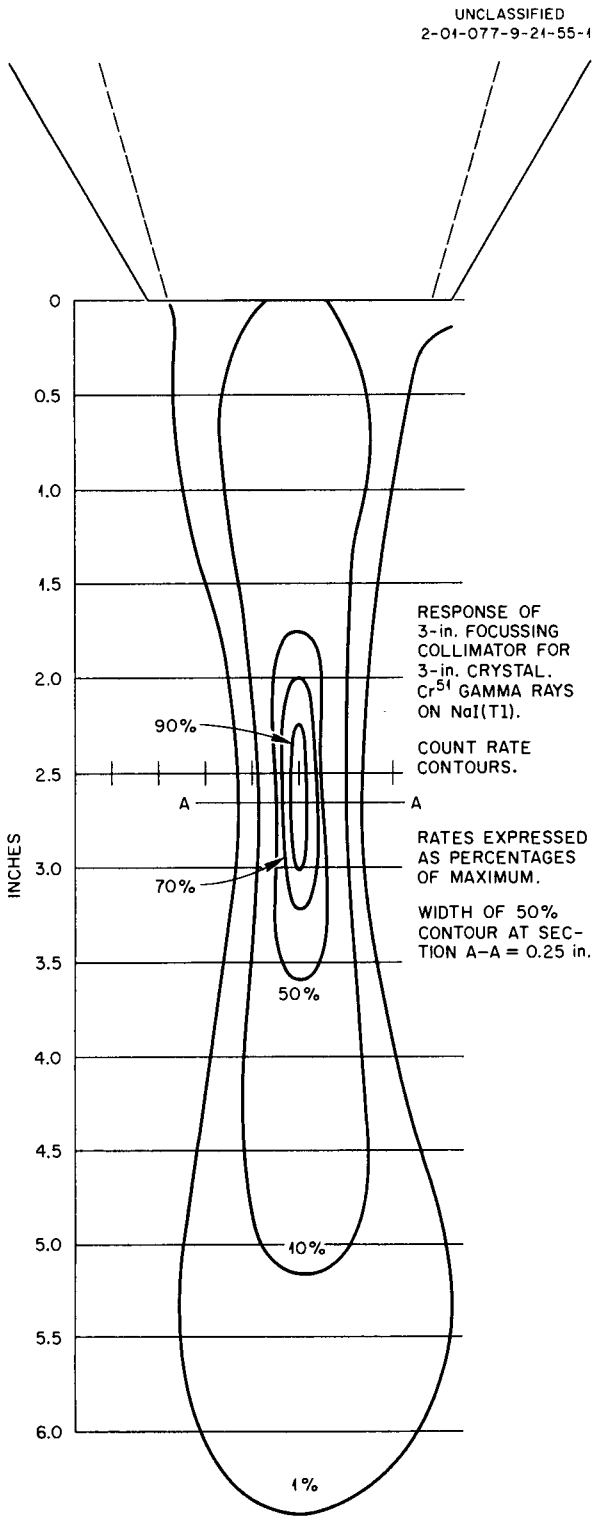


**Fig. 1. Response of 3-in., 61-Hole Lead Collimator for 320-kev Gamma Rays of $Cr^{51}$.**

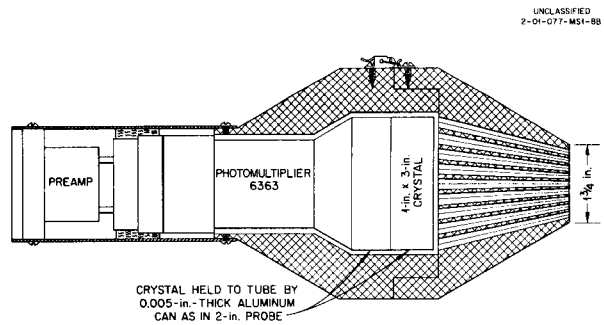


**Fig. 2. The 3-in., 61-Hole Lead Collimator Assembly.**

This collimator was partially field-tested at ORINS, by using it to scan thyroid glands, where it performed very well, as shown in Fig. 3. On the basis of this and similar scans, it was thought that the collimator should work for brain tumors.

The performance of the collimator was also checked for higher-energy gamma rays, in case

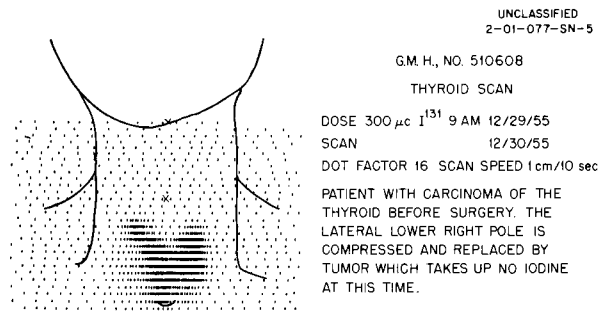


**Fig. 3. Thyroid Scan Showing Carcinoma.**

some isotope should be discovered which would be selectively absorbed by brain tumors. For these higher-energy rays, the resolution of the 3-in. collimator is greatly changed, as shown in Fig. 4, which gives the response for the 1.38-Mev gamma ray of $Na^{24}$ after the addition of another inch of lead shield around the front section of the collimator.

This collimator was then field-tested on patients thought to have brain tumors. The work was done at the National Institute of Health in Bethesda, Maryland, and at the Methodist Hospital in Houston, Texas. It was soon evident that the 1 in. of shielding in the original design was inadequate, since the counting rate increased noticeably when the patient entered the room.

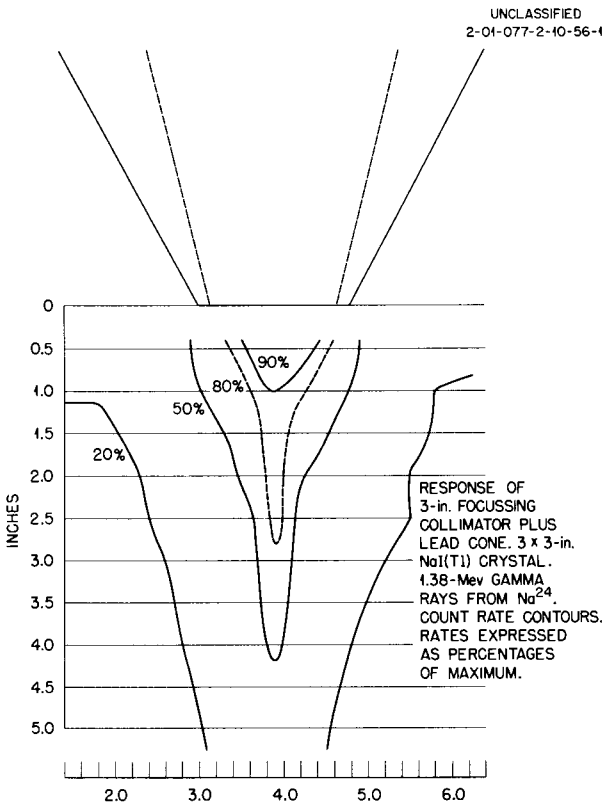


**Fig. 4. Response of 3-in., 61-Hole Lead Collimator for 1.38-Mev Gamma Rays of $Na^{24}$.**

Figure 5 shows the collimator response to a tumor which does have a high uptake of $I^{131}$. This happens to be a metastatic thyroid carcinoma. Although it is an extremely rare type as far as brain tumors are concerned, it does show that if a substance is discovered which would be highly concentrated by a brain tumor, the problem would not be so difficult.

Figures 6 and 7 are scans of different brain tumors which are more typical of what is obtained with the original 61-hole, 3-in. collimator, made of lead. The patient was given radioiodinated human serum albumin intravenously.

From these scans it appears that the detection of a tumor in the brain depends not on its differential uptake but on a breakdown of the "blood-brain barrier." Essentially, one is looking for an increase in the amount of blood which is present, where all the blood might contain the same amount of activity. Rough calculations show that a counting rate of approximately 12 counts/sec would be obtained from 1 ml of blood at the midline if the concentration is 0.1 $\mu$c/ml. This is the concentration for a 500-$\mu$c dose in a patient, assuming 5000 cc of blood.

In order to determine the amount of shielding necessary, the transmissions through two different thicknesses of lead and one of mercury were determined and are shown in Fig. 8. It can be seen that the 1 in. of lead removes most of the 364-kev gamma ray. However, the 638- and the 720-kev gamma rays are not reduced nearly so much, and even with a spectrometer removing most of the 638- and the 720-kev gamma rays, the counts due to the Compton effect in the crystal from the penetration of these rays are the main source of the background. The additional shielding provided by using mercury instead of lead is also indicated by this figure. Since there is a possibility that uses might be found which would require isotopes having harder gamma rays than those of iodine, it was decided to use mercury as a side shield with a collimating insert made of gold. It would be ideal to have the entire collimator made from gold, but the expense is prohibitive.

As an intermediate step before the use of gold, a 19-hole, 3-in. collimator was made from mercury. The focus was still held at 3 in. from the face of the collimator, and the transmission to the crystal from this point was 50%. The tapered hexagonal holes through the mercury were made of foamed polystyrene weighing less than 0.5 g per hole. Scans of a point source of $Cr^{51}$ with the mercury collimator and with the old 3-in. lead collimator show that one obtains three times as many counts with the mercury as with the old collimator. However, all the additional counts lie outside the area shown by the old 3-in. collimator. This indicates that the additional counts are due to a sacrifice in resolution.

The 19-hole mercury collimator was field-tested at the Methodist Hospital, where it performed very well, as shown by Fig. 8. Figure 9 is a scan of a patient having a meningioma. There is evidence of the tumor in both the A.P. view and in the lateral view, and, in addition, a well-circumscribed area of decreased activity is shown which is probably an infarct producing encephalomacia.

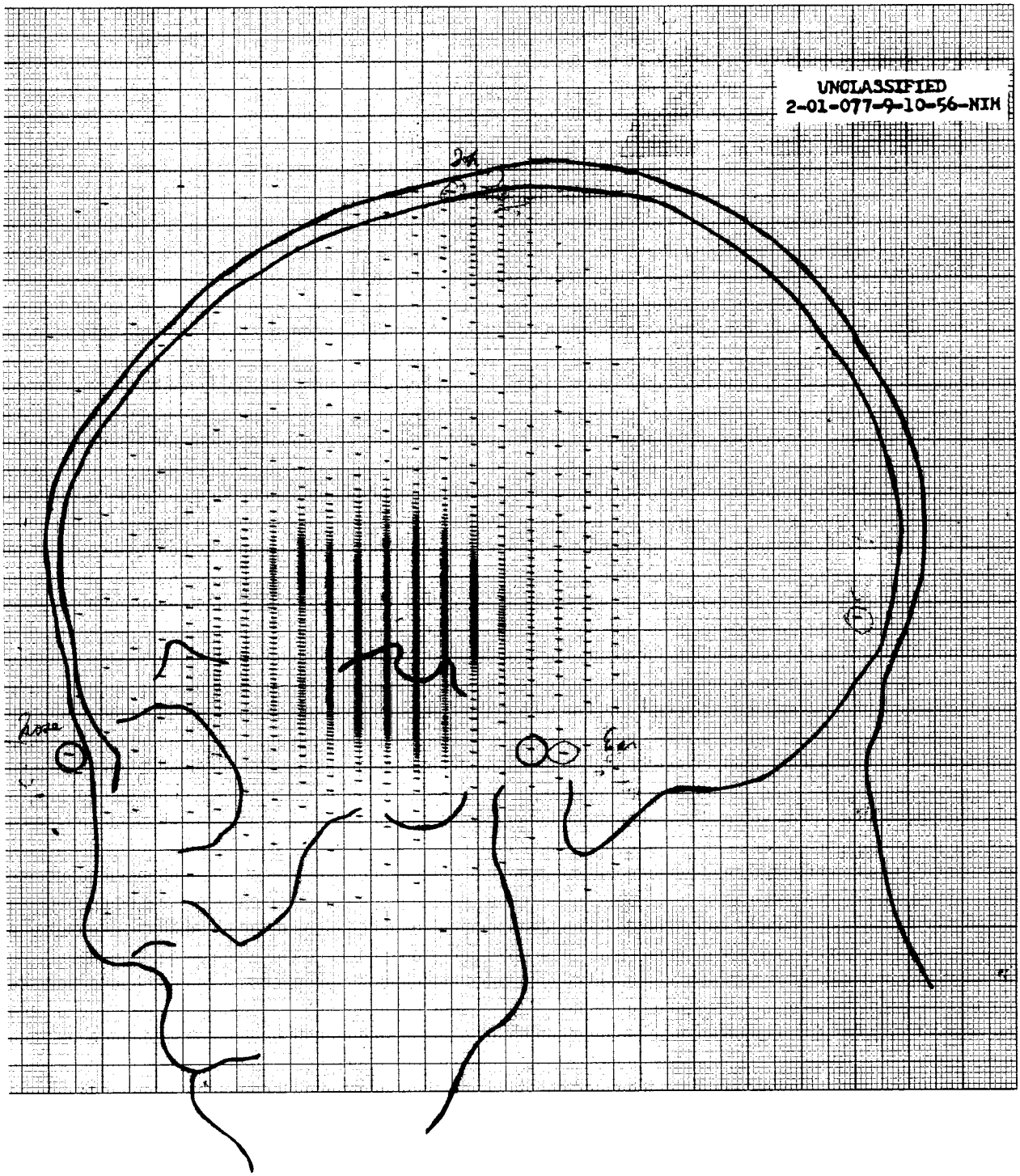


Fig. 5. Brain Scan of Metastatic Thyroid Tumor by Use of 3-in., 61-Hole Lead Collimator.

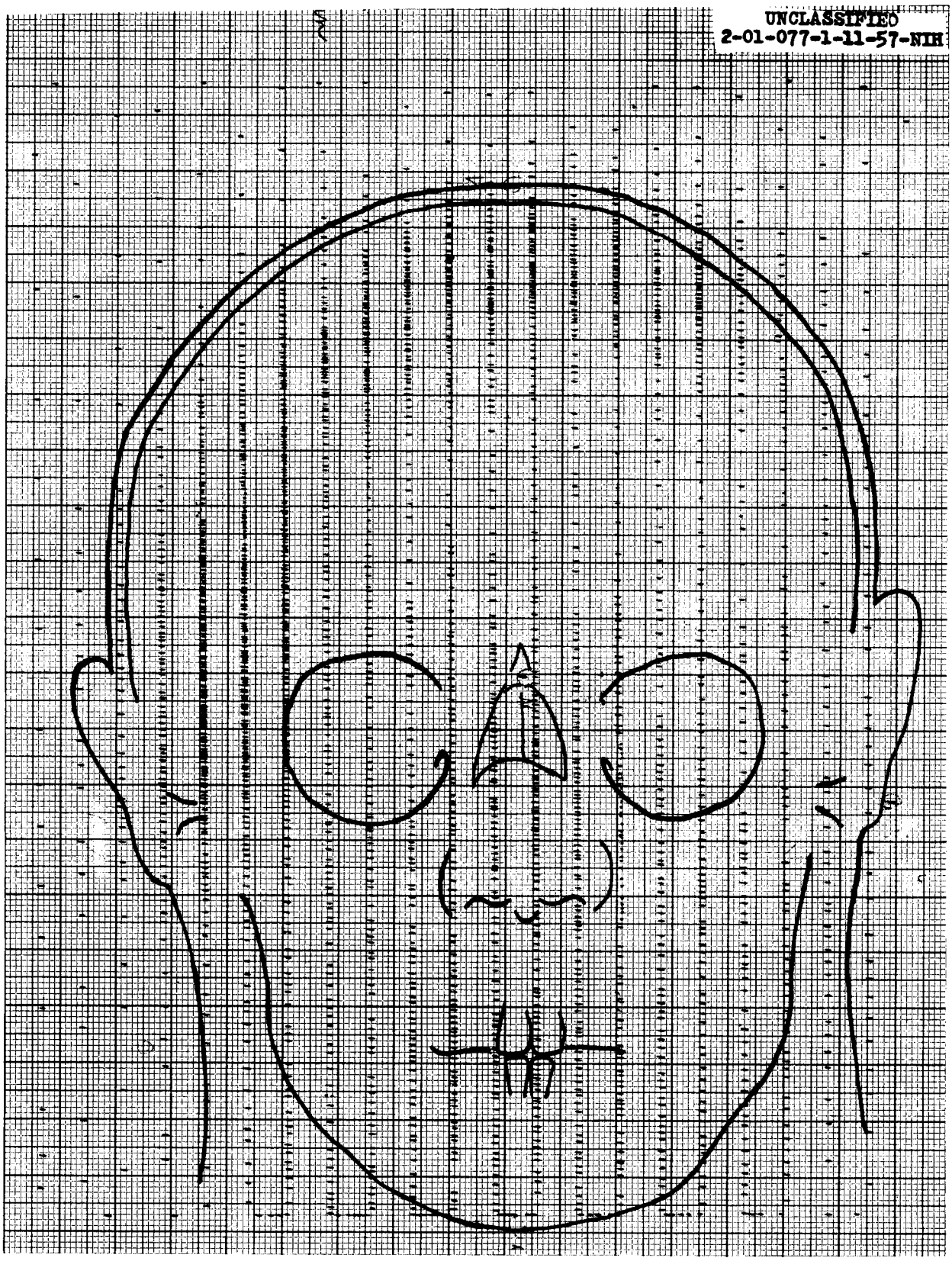


Fig. 6. Brain Scan with 3-in., 61-Hole Lead Collimator.

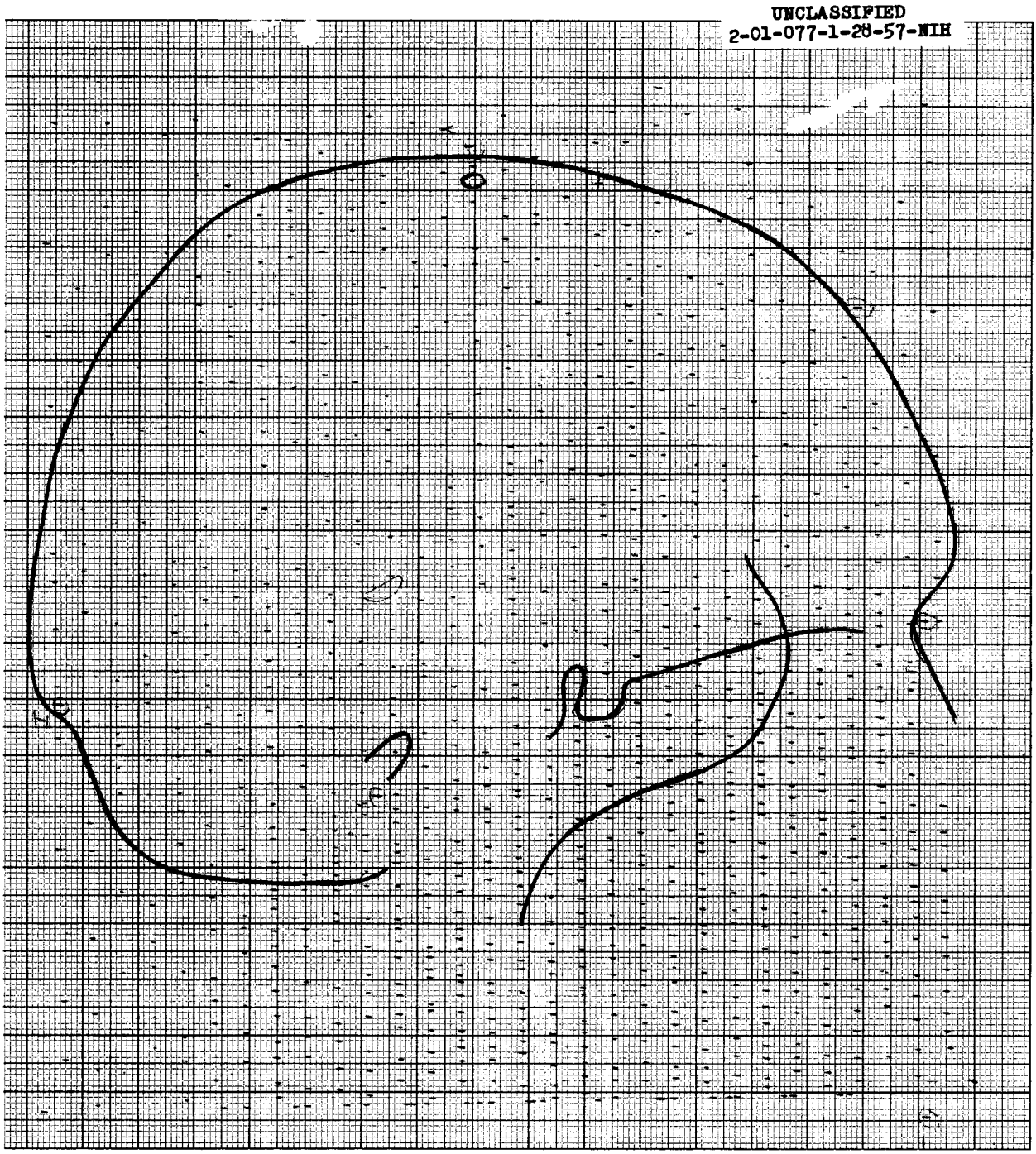


Fig. 7. Brain Scan with 3-in., 61-Hole Lead Collimator.

The infarct could well be the result of the tumor invading the artery supplying this area.

The results of these field tests and the discussions with Dr. M. Shy at the National Institute of Health and Dr. H. Allen at the Methodist Hospital have led to the decision that perhaps the best collimator at this time is one designed to give maximum response for a tumor ½ in. in diameter at a distance of 3 in. Therefore we are presently designing such a collimator.

The new collimator has a gold insert for the focusing part, consisting of 37 hexagonal holes all focused at a distance of 3 in. from the face of the collimator. The transmission to the face of the crystal has been increased from 50% to 60%. Surrounding the crystal and insert will be a shield made of mercury 2 in. thick.

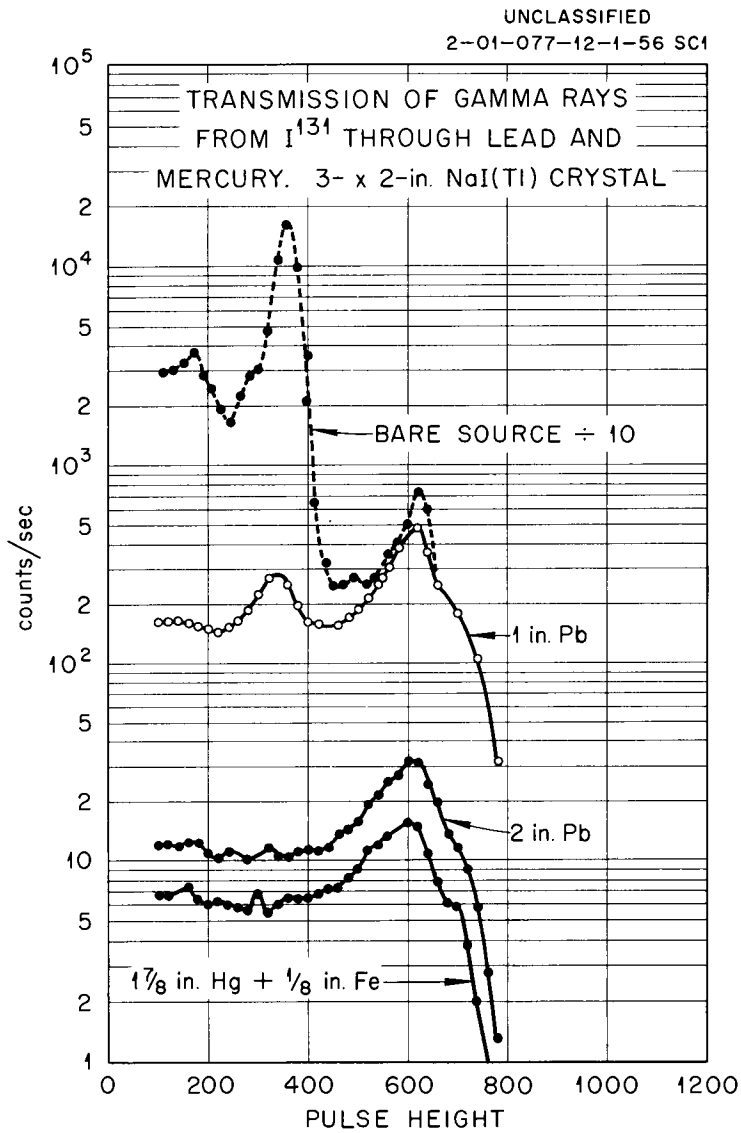


**Fig. 8. Transmission Spectra of $I^{131}$ for Lead and Mercury.**

UNCLASSIFIED
2-01-077-MH57753

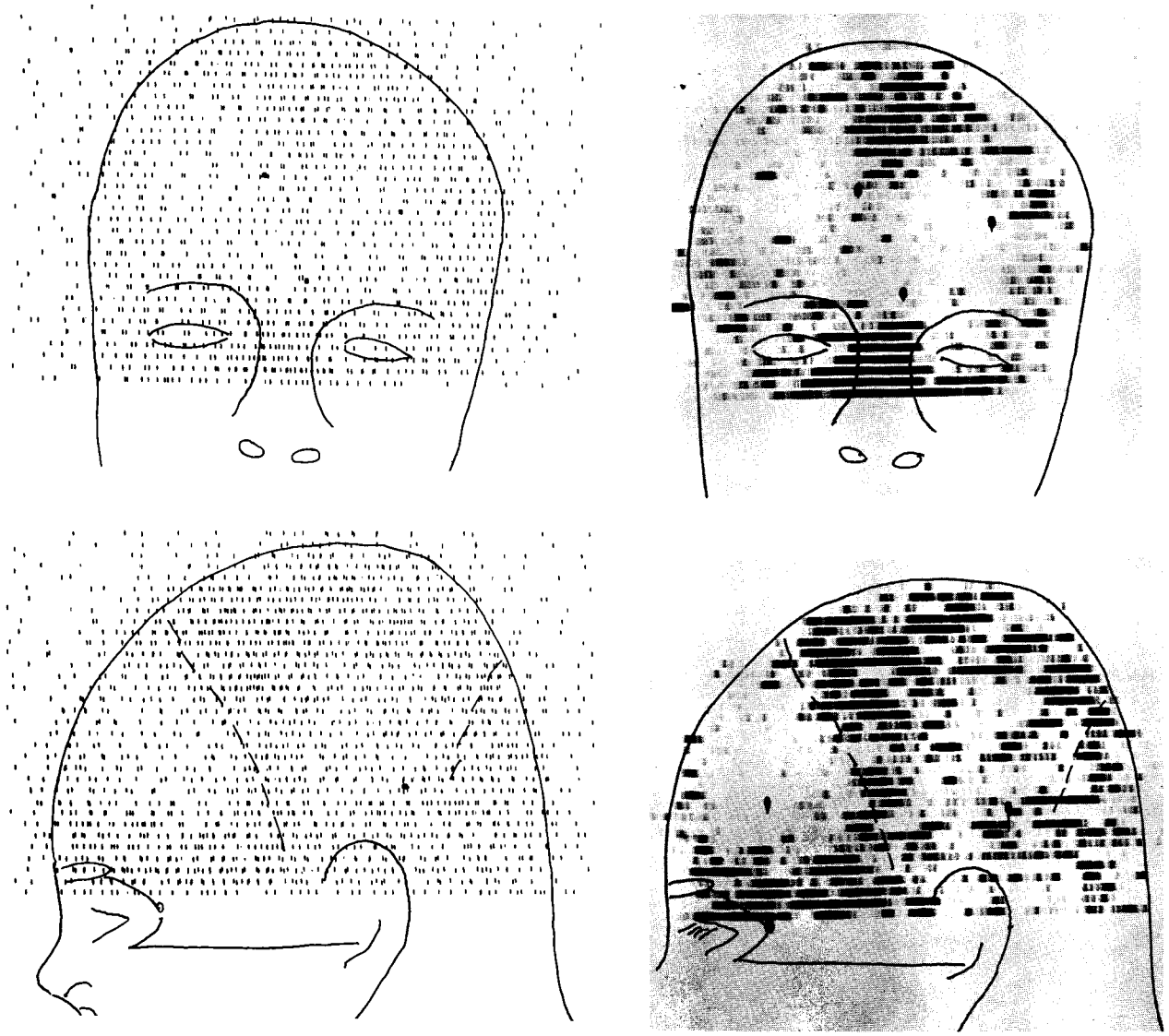

Fig. 9. Brain Scan of Patient with Meningioma by Use of 19-Hole Mercury Collimator.

# DEVELOPMENT OF FAST-PULSE TECHNIQUES FOR MEASUREMENT OF TRANSIT-TIME SPREAD IN PHOTOMULTIPLIER TUBES

H. O. Eason G. G. Kelley

In the interest of evaluation and further improvement of scintillation detectors, a program has been undertaken to make equipment available for accurate measurement of transit time and transit-time spread in photomultiplier tubes. The prospect of significant reduction and closer control of transit-time spread in tubes now in the developmental stage requires that such equipment be extremely stable and capable of measurement to an accuracy of $10^{-9}$ sec or better. The method consists basically of the simultaneous generation of an electrical pulse and a flash of light, illumination of the photocathode with this light flash, placing the electrical outputs of the photomultiplier and pulser in time coincidence by adjustment of relative delay in the two channels, and determination of coincidence counting rate as a function of relative delay. Figure 1 is a block diagram illustrating this method.

The pulser consists of the capsule and operating coil from a Western Electric type 276D mercury relay arranged in a conventional pulser circuit with negative output. The capsule is so positioned with respect to the photomultiplier tube that light from the minute arc formed when the contacts "make" falls upon the photocathode surface. The resultant electrons arriving at the anode are fed to an RC integrating circuit with a time constant of 1 $\mu$sec. A 417A cathode follower provides a low impedance output for the pulse thus formed. This pulse is then amplified and applied to one coincidence input. Direct electrical output of the pulser is suitably delayed by a length of RG/7U coaxial cable and applied to the other coincidence input. The coincidence unit consists of two E-180F pentodes operating as limiters with 17-ma plate current, zero bias, common plate load, and sufficient d-c screen degeneration for stabilization. Under these conditions, a grid signal of approximately 1 v is required for cut-off. The common plate load is composed of a 2-m$\mu$sec shorted stub and its terminating resistor. This stub is formed of two concentric sections of silver-plated brass tubing with air dielectric to prevent degradation of wave form due to losses. A 1N26 silicon diode, suitably biased to eliminate response to singles, operates as a lengthener to provide output. Observation of the plate waveform of the coincidence unit with the aid of an EG&G traveling-wave oscilloscope shows the rise and fall times to be approximately 1 m$\mu$sec for either or both inputs with sufficiently fast input signals. This is corroborated by plotting the output voltage as a function of delay, with both input signals derived from the same source. This curve shows a resolution, that is, transition from 10% to 90% output, of approximately 1 m$\mu$sec.

The attainment of a sufficiently fast coincidence unit still leaves one weak link in the chain – that of providing sufficient amplification between the photomultiplier output and the coincidence unit to accurately signal the arrival of the first photoelectron(s). The Hewlett-Packard 460A distributed amplifier, having a rise time of $2.6 \times 10^{-9}$ sec and a gain of 10, proved to be inadequate for this purpose, even when diodes were used to select the fastest portion of the output signal. A study of available vacuum tubes was then made in order to determine a suitable type for application in a fast-rise distributed amplifier. Of the types investigated, the subminiature type 5840, having characteristics similar to the 6AK5, appears to be best suited to the purpose. It has three cathode leads, close electrode spacing, low input and output capacitances, low lead inductance, and a $G_m$ of 5500 $\mu$mhos when operated near its maximum ratings. In addition, its small physical size permits a compact arrangement and serves to reduce unwanted inductance between sections of the delay line. With the cathode leads soldered directly to the chassis, the equivalent input resistance at the control grid of the 5840 was extrapolated from measurements to be 350 ohms at 600 Mc, as compared with 110 ohms for the 6AK5 at this frequency.

A single-stage distributed amplifier employing six type 5840's has been constructed. The "m-derived" lines are wound on $\frac{1}{8}$-in.-dia forms and have a design cutoff frequency of 600 Mc, with a $Z_0$ of 150 ohms for the grid line and 250 ohms for the plate line. With input from a coaxial mercury pulser, the following output characteristics were

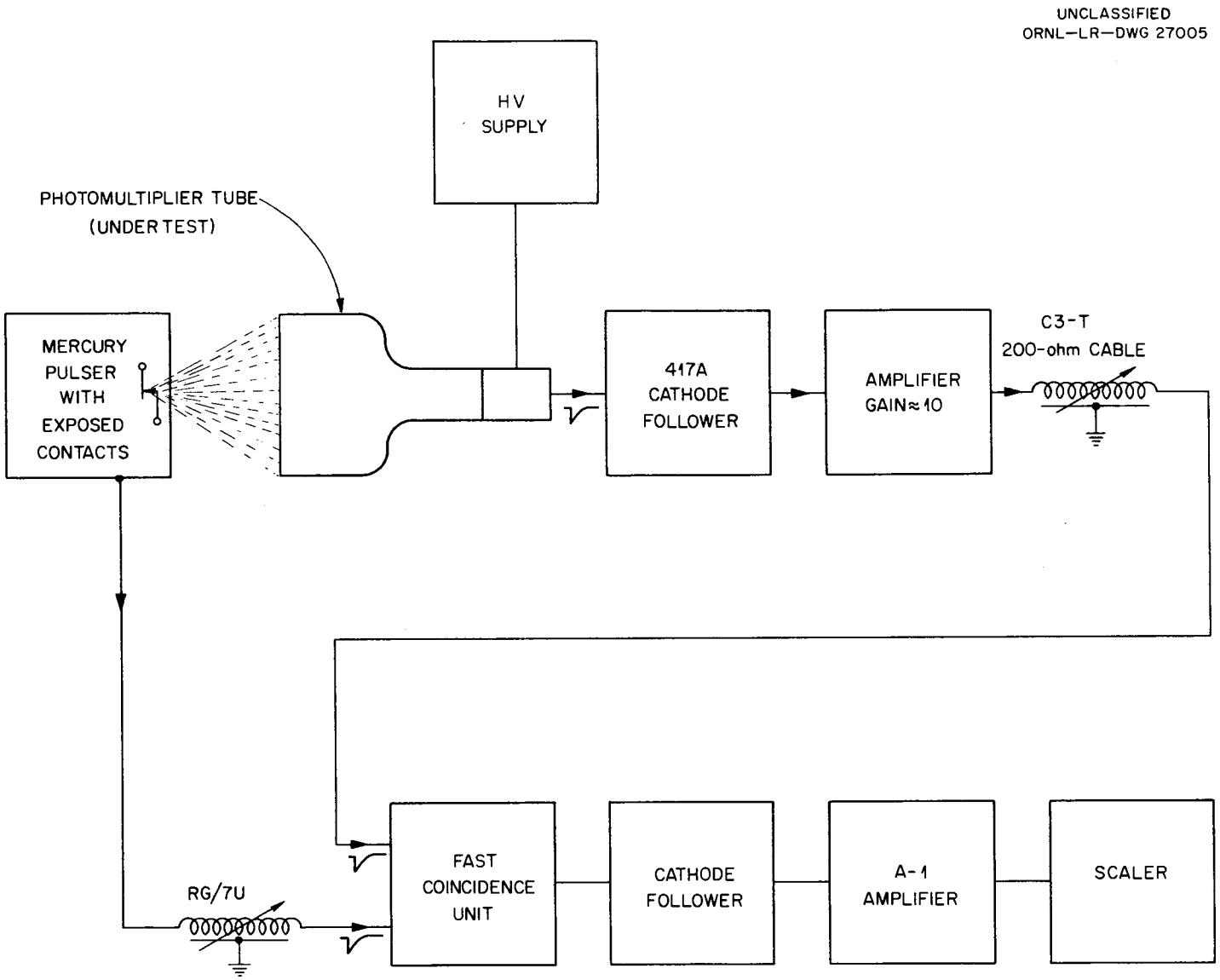


**Fig. 1. Block Diagram Illustrating Method of Measurement of Transit-Time Spread.**

observed with the aid of the EG&G oscilloscope: rise time less than 1 mμsec, voltage gain of four times into a matched load, and combined effects of overshoot and mismatch of the order of 5% of the output voltage. A two-stage amplifier employing similar lines and having eight tubes per stage is being built. This amplifier is expected to have a voltage gain of 20 and a rise time of 1 mμsec, which should be adequate for the intended purpose.

Further work includes completion of the amplifier, investigation of the pulser to determine degree of simultaneity of the light flash and electrical pulse, and the testing of a number of developmental photomultiplier tubes already in hand.

---

## MEDICAL SCANNER

D. P. Hamblen J. E. Francis C. C. Harris G. G. Kelley

The design of an improved mechanical scanner for use with heavy focusing collimators[1] has been completed. In addition, the frame with its carriage has been constructed, and the drive for one coordinate of the two-coordinate scanning plane is in operation.

Mechanical scanners, for the localization of radioactivity in vivo, are available commercially, but they possess certain limitations. The new improved scanner has the following features:

1. It occupies less floor area and at the same time is semiportable. The patient is not surrounded by the apparatus, since the detector and shield are cantilever-mounted from a pedestal.

2. Lead or mercury collimators weighing up to 100 lb can be used. Only light collimators with weights below 50 lb can now be safely handled over patients, whereas the increased use of high-energy gamma rays and attempts at brain tumor localizations have resulted in the construction of collimators with more shielding material.

3. Many more degrees of motion have added to the versatility of the instrument. The patient will be required to assume fewer positions for body scans, and he may be either reclining or sitting. Present machines restrict scans to the horizontal plane, but frequently it becomes necessary to change the patient's body position, thereby running the risk of introducing serious physiological effects.

4. The addition of a servo-controlled system will keep both the scan speed and distance of travel constant. This will eliminate the possibility of introducing artifacts in the recorded data.

5. A greatly improved recording system will provide better scan record interpretation.

[1] J. E. Francis, P. R. Bell, and C. C. Harris, *Nucleonics* 13(11), 82–88 (1955); P. R. Bell and J. E. Francis, *Phys. Semiann. Prog. Rep. Sept. 10, 1955*, ORNL-1975, p 91.

Physics Division progress reports previously issued in this series are as follows:

| | |
|---|---|
| ORNL-325 Supplement | December, January, and February, 1948-1949 |
| ORNL-366 | Period Ending June 15, 1949 |
| ORNL-481 | Period Ending September 25, 1949 |
| ORNL-577 | Period Ending December 15, 1949 |
| ORNL-694 | Period Ending March 15, 1950 |
| ORNL-782 | Period Ending June 15, 1950 |
| ORNL-865 | Period Ending September 20, 1950 |
| ORNL-940 | Period Ending December 20, 1950 |
| ORNL-1005 | Period Ending March 20, 1951 |
| ORNL-1092 | Period Ending June 20, 1951 |
| ORNL-1164 | Period Ending September 20, 1951 |
| ORNL-1278 | Period Ending December 20, 1951 |
| ORNL-1289 | Period Ending March 20, 1952 |
| ORNL-1365 | Period Ending June 20, 1952 |
| ORNL-1415 | Period Ending September 20, 1952 |
| ORNL-1496 | Period Ending December 20, 1952 |
| ORNL-1620 | Period Ending September 10, 1953 |
| ORNL-1705 | Period Ending March 10, 1954 |
| ORNL-1798 | Period Ending September 10, 1954 |
| ORNL-1879 | Period Ending March 20, 1955 |
| ORNL-2076 | Period Ending March 10, 1956 |
| ORNL-2204 | Period Ending September 10, 1956 |
| ORNL-2302 | Period Ending March 10, 1957 |

## PUBLICATIONS

A. V. H. Masket, R. L. Macklin, and H. W. Schmitt, "Cylinder Radiation and Activation," *Rev. Sci. Instr.* **28**, 189 (1957).

A. V. H. Masket, "Solid Angle Contour Integrals, Series, and Tables," *Rev. Sci. Instr.* **28**, 191 (1957).

U. H. Bents, "Neutron Diffraction Study of the Magnetic Structures for the Perovskite-Type Mixed Oxides $La(Mn,Cr)O_3$," *Phys. Rev.* **106**, 225 (1957).

W. C. Koehler and E. O. Wollan, "Neutron-Diffraction Study of the Magnetic Properties of Perovskite-Like Compounds $LaBO_3$," *Phys. and Chem. Solids* **2**, 100 (1957).

F. K. McGowan and P. H. Stelson, "Angular Distribution of Gamma Rays Following Coulomb Excitation in Even-Even Nuclei," *Phys. Rev.* **106**, 522 (1957).

M. E. Rose, *Elementary Theory of Angular Momentum*, Wiley, New York, 1957.

P. H. Stelson and E. C. Campbell, "Cross Section for the $Be^9(n,\alpha)He^6$ Reaction," *Phys. Rev.* **106**, 1252 (1957).

E. D. Klema and R. K. Osborn, "Empirical Determination of Nuclear Shape Factors and Moments of Inertia," *Nuclear Phys.* **3**, 571 (1957).

M. K. Wilkinson, N. S. Gingrich, and C. G. Shull, "The Magnetic Structure of $Mn_2Sb$," *Phys. and Chem. Solids* **2**, 289 (1957).

E. C. Campbell and F. Nelson, "Metastable State of $Ge^{73}$," *Phys. Rev.* **107**, 502 (1957).

R. L. Macklin, N. H. Lazar, and W. S. Lyon, "Neutron Activation Cross Sections with Sb-Be Neutrons," *Phys. Rev.* **107**, 504 (1957).

F. Pleasonton and A. H. Snell, "Ionization Following Internal Conversion in Xenon," *Proc. Roy. Soc.(London)* **A241**, 141 (1957).

A. H. Snell and F. Pleasonton, "Ionization Following Beta Decay in Krypton-85," *Phys. Rev.* **107**, 740 (1957).

L. D. Roberts, book review ("Low Temperature Physics II," vol 15 of *Handbuch der Physik*, ed. by S. Flugge, Springer-Verlag, Berlin, 1956) *Phys. Today* **10**, 32 (1957).

---

## PAPERS PRESENTED AT SCIENTIFIC AND TECHNICAL MEETINGS

*American Physical Society, Southeastern Section Meeting, Lexington, Kentucky, April 4–6, 1957*

J. W. T. Dabbs (invited paper), "Orientation of Actinide Group Nuclei."

M. E. Rose (invited paper), "Conservation Laws in Beta Decay."

A. H. Snell (invited paper), "The Atomic and Molecular Consequences of Radioactivity."

C. F. Barnett, "The Cross Sections for Dissociation of Diatomic Hydrogen Ions."

J. L. Fowler and H. O. Cohn, "Nuclear Potentials for Alpha Particle Nuclei."

J. H. Neiler, J. H. Gibbons, and W. M. Good, "Millimicrosecond Time-of-Flight Measurements of $(d,n)$ Neutrons."

*Instrument Society of America, Atlanta, Georgia, April 12, 1957*

C. C. Harris, "Medical Scintillation Spectrometry."

*Conference on Neutron Age Measurements and Calculations, National Bureau of Standards, Washington, D.C., April 24, 1957*

E. C. Campbell, "Fission Neutron Non-escape Probability in Small $H_2O$-$U^{235}$ Systems."

*American Physical Society Meeting, Washington, D.C., April 25–27, 1957*

R. C. Block, G. G. Slaughter, and J. A. Harvey, "Neutron Resonance Parameters of $Sm^{151}$."

J. W. T. Dabbs, L. D. Roberts, and G. W. Parker, "Magnetic Susceptibility of $NpO_2Rb(NO_3)_3$."

J. H. Gibbons, W. M. Good, and J. H. Neiler, "Kilovolt Neutron Cross Sections by Millimicrosecond Time-of-Flight."

T. A. Green and M. E. Rose, "An Effect of Finite Nuclear Size on the Internal Conversion Coefficients."

C. H. Johnson, A. Galonsky, and J. P. Ulrich, "Cross Sections and Thresholds for $(p,n)$ Reactions in Intermediate Nuclei."

F. K. McGowan and P. H. Stelson, "Coulomb Excitation of States in $_{90}Th^{232}$."

L. D. Roberts, J. W. T. Dabbs, and H. Postma, "Paramagnetic Relaxation in $CuNa(UO_2)_3(C_2H_3O_2)_3 \cdot 9H_2O$ and $Mn(NH_4)_2(SO_4)_2 \cdot 6H_2O$."

*Symposium on Molecular Structure and Spectroscopy, Ohio State University, Columbus, Ohio, June 10–14, 1957*

H. W. Morgan, "Infrared Absorption Spectra of Solid Solutions."

P. A. Staats, H. W. Morgan, and J. H. Goldstein, "The Infrared Spectra of the Deuterium and Tritium Substituted Ammonia Molecules."

*Sixtieth Annual Meeting of the American Society for Testing Materials, Atlantic City, New Jersey, June 16–21, 1957*

J. A. Norris (invited paper), "Spectrographic Determination of Trace Elements in Metals."

*American Physical Society Meeting, Notre Dame, Indiana, June 20–22, 1957*

P. H. Stelson and F. K. McGowan, "Coulomb Excitation of the Second $2^+$ State in Even-Even Medium Weight Nuclei."

*Society of Nuclear Medicine, Oklahoma City, Oklahoma, June 20–23, 1957*

J. E. Francis and P. R. Bell, "Collimators for the Localization of Brain Tumors."

*International Meeting of European Molecular Spectroscopists, Freiburg, Germany, July 9–13, 1957*

H. W. Morgan, "Infrared Absorption Spectra of Solid Solutions."

H. W. Morgan, "The Infrared Spectra of the Deuterium and Tritium Substituted Ammonia Molecules."

*International Congress – International Union of Crystallography, Montreal, Canada, July 10–19, 1957*

W. C. Koehler and H. A. Gersch, "Types of Magnetically Ordered Configurations on Simple Lattices."

W. C. Koehler, E. O. Wollan, M. K. Wilkinson, and J. W. Cable, "Neutron Diffraction Study of Magnetic Ordering in Rare Earth Orthoferrites."

*International Conference on Low Temperatures, Madison, Wisconsin, August 26–31, 1957*

J. W. T. Dabbs, L. D. Roberts, and G. W. Parker, "Fission of Oriented $U^{233}$ Nuclei."

L. D. Roberts, J. W. T. Dabbs, and G. W. Parker, "Alpha Emission from Oriented $U^{233}$ Nuclei."

*International Conference on Neutron Interactions with the Nucleus, Columbia University, New York, New York, September 9–13, 1957*

W. M. Good, J. H. Gibbons, and J. H. Neiler, "Neutron Total Cross Section in the Kilovolt Region."

J. A. Harvey, R. C. Block, and G. G. Slaughter, "Low Energy Neutron Cross Sections of Fission Products."

J. L. Fowler and H. O. Cohn, "Differential Elastic Scattering of Neutrons from Light Nuclei."

*American Chemical Society Meeting, New York, New York, September 9–13, 1957*

A. H. Snell and F. Pleasonton, "The Atomic and Molecular Consequences of Radioactive Decay."

J. E. Worsham, Jr., M. K. Wilkinson, and C. G. Shull, "Neutron Diffraction Observations on the Palladium-Hydrogen and Palladium-Deuterium Systems."

---

## ANNOUNCEMENTS

During this period A. H. Snell, formerly Director of the Division, was appointed Assistant Laboratory Director; J. L. Fowler, formerly Associate Director of the Division, was appointed Director of the Physics Division; W. M. Good and H. B. Willard were appointed Director and Co-Director, respectively, of the High Voltage Laboratory; and P. R. Bell, formerly in charge of the Scintillation Spectrometry and Instrument Development Group, was appointed Associate Director of the newly formed Thermonuclear Experimental Division (TED) – he will also serve as Associate Director of the Laboratory's Sherwood Project.

Additions to the Physics Division staff during this period were as follows: M. M. Gordon (one-year appointment) and R. L. Becker (Theoretical Physics); J. Walter (Reactor Experimental Engineering Division) is on loan to the Low-Temperature Group.

The Spectroscopy Group of the former Stable Isotopes Division became a part of the Physics Division in May of this year. This group, headed by J. R. McNally, Jr., includes G. W. Charles, Z. Combs, H. W. Dunn, P. M. Griffin, H. W. Morgan, J. J. Mundzak, J. A. Norris, S. J. Ovenshine, W. F. Peed, O. B. Rudolph, M. R. Skidmore, P. A. Staats, K. L. Vander Sluis, and G. K. Werner.

Summer personnel during this period included the following research participants and visitors: T. A. Green (Associate Professor, Wesleyan University), L. S. Kisslinger (Assistant Professor, Western Reserve University), M. M. Gordon (summer visitor, University of Florida), and J. J. Murphy (civilian, USAF), Theoretical Physics; G. L. Jenkins (Professor, Stetson University), Velocity Selector; M. S. McCay (Professor, University of Chattanooga) and J. H. Wise (summer visitor, Washington and Lee University), Spectroscopy; A. Meyer (Assistant Professor, University of Florida), Low Temperature; and H. S. Plendl (Assistant Professor, Florida State University), High Voltage.

University students here for the summer were as follows: R. L. Traughber (Stanford University) and J. P. Ulrich (University of Michigan), High Voltage; P. J. Haigh (Carson-Newman College), Theoretical Physics; and J. M. Winter, Jr. (Massachusetts Institute of Technology), Atomic-Beam Spectroscopy.

Transfers: C. F. Barnett (Project Sherwood) transferred to the Thermonuclear Experimental Division.

E. C. Campbell (Scintillation Spectrometry and Instrument Development Group) is on a one-year assignment in Belgium at the Centre d'Etudes pour les Applications de l'Energie Nucleaire (CEAN) for the purpose of participating in physics research at the Mol Laboratories.

*INTERNAL DISTRIBUTION*

1. C. E. Center
2. Biology Library
3. Health Physics Library
4–6. Central Research Library
7. Reactor Experimental Engineering Library
8–19. Laboratory Records Department
20. Laboratory Records, ORNL R.C.
21. A. M. Weinberg
22. L. B. Emlet (K-25)
23. J. P. Murray (Y-12)
24. J. A. Swartout
25. E. H. Taylor
26. E. D. Shipley
27. J. L. Fowler
28. M. L. Nelson
29. A. H. Snell
30. A. Hollaender
31. K. Z. Morgan
32. F. L. Culler
33. M. T. Kelley
34. D. Phillips
35. E. O. Wollan
36. D. W. Cardwell
37. A. S. Householder
38. L. D. Roberts
39. R. B. Briggs
40. R. N. Lyon
41. W. C. Koehler
42. E. P. Blizard
43. M. E. Rose
44. G. E. Boyd
45. W. H Sullivan
46. R. W. Stoughton
47. C. E. Winters
48. W. H. Jordan
49. E. C. Campbell
50. D. S. Billington
51. M. A. Bredig
52. R. S. Livingston
53. C. P. Keim
54. F. C. Maienschein
55. C. E. Clifford
56. R. C. Block
57. C. D. Susano
58. C. J. Borkowski
59. M. J. Skinner
60. M. K. Wilkinson
61. J. W. Cable
62. P. M. Reyling
63. G. deSaussure
64. W. M. Good
65. G. C. Williams
66. F. K. McGowan
67. R. W. Johnson
68. J. R. McNally, Jr.
69. J. L. Gabbard
70. R. A. Charpie
71. G. G. Slaughter
72. Eugene Guth
73. R. W. Peelle
74. P. R. Bell
75. G. G. Kelley
76. C. C. Harris
77. H. G. MacPherson
78. P. H. Stelson
79. J. E. Sherwood
80. W. Zobel
81. R. B. Murray
82. H. B. Willard
83. J. Schenck
84. J. H. Neiler
85. J. A. Harvey
86. C. F. Barnett
87. N. H. Lazar
88. R. R. Dickison
89. A. Simon
90. J. H. Gibbons
91. J. J. Pinajian
92. S. Bernstein
93. F. Pleasonton
94. E. P. Wigner (consultant)
95. H. A. Bethe (consultant)
96. E. Creutz (consultant)
97. L. P. Smith (consultant)
98. R. L. Thornton (consultant)
99. R. F. Christy (consultant)
100. M. Goldhaber (consultant)
101. T. Lauritsen (consultant)
102. J. A. Wheeler (consultant)
103. N. F. Ramsey (consultant)
104. W. R. Brode (consultant)
105. ORNL – Y-12 Technical Library, Document Reference Section

## *EXTERNAL DISTRIBUTION*

106–189. Given external distribution
190–744. Given distribution as shown in TID-4500 (13th ed. rev.) under Physics and Mathematics category (75 copies – OTS)